From Neutrino Physics to Beam Polarisation
–
a High Precision Story at the ILC

Dissertation

zur Erlangung des Doktorgrades
des Department Physik
der Universität Hamburg

vorgelegt von

Benedikt Vormwald

aus Würzburg

Hamburg
2014

Gutachter der Dissertation:	Dr. Jenny List Prof. Dr. Peter Schleper Prof. Dr. James Brau
Gutachter der Disputation:	Dr. Jenny List Prof. Dr. Caren Hagner
Datum der Disputation:	30.01.2014
Vorsitzender des Prüfungsausschusses:	Dr. Georg Steinbrück
Vorsitzende des Promotionsausschusses:	Prof. Dr. Daniela Pfannkuche
Dekan der Fakultät für Mathematik, Informatik und Naturwissenschaften:	Prof. Dr. Heinrich Graener

To my Grandfather.

Zusammenfassung

In der vorliegenden Arbeit betrachten wir die experimentellen Möglichkeiten, ein supersymmetrisches Modell mit bilinear verletzter R-Parität (bRPV SUSY) am International Linear Collider zu untersuchen. In diesem Modell mischen Neutrinos mit den supersymmetrischen Neutralinos, sodass Neutrinoeigenschaften durch die Studie von Neutralinozerfällen untersucht werden können. Diese Zerfälle enthalten typischerweise ein Lepton und ein W/Z-Boson. Als Fallbeispiel konzentrieren wir uns auf die Bestimmung des atmosphärischen Neutrinomischungswinkel θ_{23}, der über die Messung des Verhältnisses der Verzweigungsverhältnisse $\mathrm{BR}(\widetilde{\chi}_1^0 \to W\mu)/\mathrm{BR}(\widetilde{\chi}_1^0 \to W\tau)$ zugänglich ist.
Zu diesem Zweck wird eine detaillierte Detektorsimulation des International Large Detectors für alle Standardmodell-Untergrundprozesse sowie $\widetilde{\chi}_1^0$-Paarproduktion in einem „simplified model“ durchgeführt. Die Studie basiert auf ILC Strahlparameter gemäß des Technical Design Reports bei einer Schwerpunktsenergie von $\sqrt{s} = 500\,\mathrm{GeV}$.
Aus den myonischen $\widetilde{\chi}_1^0$-Zerfällen lässt sich bei einer integrierten Luminosität von $\int L dt = 500\,\mathrm{fb}^{-1}$ die $\widetilde{\chi}_1^0$-Masse mit einer Unsicherheit von $\delta(m_{\widetilde{\chi}_1^0}) = (40(\mathrm{stat.}) \oplus 35(\mathrm{syst.}))\,\mathrm{MeV}$ bestimmen. Das Verhältnis der Verzweigungsverhältnisse kann mit einer Genauigkeit von $\delta(\mathrm{BR}(\widetilde{\chi}_1^0 \to W\mu)/\mathrm{BR}(\widetilde{\chi}_1^0 \to W\tau)) = 2.9\%$ gemessen werden. Hieraus kann wiederum der atmosphärische Neutrinomischungswinkel mit einer Genauigkeit bestimmt werden, die vergleichbar ist mit der moderner Neutrinoexperimente. Damit kann am ILC getestet werden, ob bRPV SUSY für die Neutrinomassengeneration verantwortlich ist.

Wie in der bRPV SUSY-Studie gezeigt wird, ist die Strahlpolarisation ein wichtiger Parameter für Physikanalysen am ILC. Die Strahlpolarisation wird mit Hilfe zweier Compton-Polarimeter pro Elektron-/Positron-Strahl gemessen. Um das Designziel von einer Messgenauigkeit von 0.25% zu erreichen, muss die Detektornichtlinearität der beteiligten Cherenkovdetektoren sehr genau bestimmt werden. Dabei stellen erwartungsgemäß die beteiligten Photomultiplier die Hauptquellen der Detektornichtlinearität dar.
Aus diesem Grund wird eine differentielle Nichtlinearitätsmessung sowie eine Linearisierungsmethode entwickelt. Das Grundprinzip wird in einer Monte-Carlo-Simulation demonstriert. Zudem wird die Simulation dazu verwendet, um Anforderungsparameter für die Entwicklung einer passenden Kalibrationslichtquelle sowie eines geeigneten Testaufbaus zu definieren.
Nach detaillierten Testmessungen wird die Nichtlinearität eines Photomultipliers und dessen Auslesekette auf 1.0% ± 0.1% und 0.4% ± 0.1% in Abhängigkeit des vermessenen Intensitätsbereichs bestimmt. Wir zeigen, dass die gemessene Nichtlinearität genutzt werden kann, um einen unabhängigen Datensatz zu linearisieren. Abschließend wird die mögliche Anwendung der vorgeschlagenen Methode als Nichtlinearitätsüberwachung und Korrekturschema während der ILC Datennahme diskutiert.

Abstract

In this thesis, we investigate the experimental prospects of studying a supersymmetric model with bilinearly broken R parity at the International Linear Collider. In this model, neutrinos mix with the supersymmetric neutralinos such that neutrino properties can be probed by examining neutralino decays, which incorporate usually a lepton and a W/Z boson. As a study case, we focus on the determination of the atmospheric neutrino mixing angle θ_{23}, which is accessible via the ratio of the neutralino branching ratios $\mathrm{BR}(\widetilde{\chi}_1^0 \to W\mu)/\,\mathrm{BR}(\widetilde{\chi}_1^0 \to W\tau)$.
A detailed simulation of the International Large Detector has been performed for all Standard Model backgrounds and for $\widetilde{\chi}_1^0$-pair production within a simplified model. The study is based on ILC beam parameters according to the Technical Design Report for a center-of-mass energy of $\sqrt{s} = 500\,\mathrm{GeV}$.
From muonic $\widetilde{\chi}_1^0$ decays, we find that the $\widetilde{\chi}_1^0$ mass can be reconstructed with an uncertainty of $\delta(m_{\widetilde{\chi}_1^0}) = (40(\mathrm{stat.}) \oplus 35(\mathrm{syst.}))\,\mathrm{MeV}$ for an integrated luminosity of $\int L dt = 500\,\mathrm{fb}^{-1}$. The ratio of branching ratios can be determined to a precision of $\delta(\mathrm{BR}(\widetilde{\chi}_1^0 \to W\mu)/\,\mathrm{BR}(\widetilde{\chi}_1^0 \to W\tau)) = 2.9\%$. Due to this, the atmospheric neutrino mixing angle can be deduced with a precision comparable to modern neutrino experiments. Thus, the ILC is capable to test whether bRPV SUSY is the mechanism of neutrino mass generation.

As also shown in the bRPV SUSY study of this thesis, beam polarisation is an important parameter in physics analyses at the ILC. The beam polarisation is measured with two Compton polarimeters per electron/positron beam. In order to achieve the design goal of an envisaged precision of 0.25%, the detector nonlinearity of the used Cherenkov detectors has to be determined very precisely. Herein, the main source of nonlinearity is expected to originate from the involved photomultipliers.
For this reason, a differential nonlinearity measurement as well as a linearisation method is developed. The working principle is demonstrated in a Monte-Carlo simulation, which is also utilised in order to deduce design parameters for the development of a calibration light source and an appropriate measurement setup.
After extensive test measurements, the nonlinearity is determined using the proposed differential method. We find nonlinearities of the photomultiplier and its read-out chain of $1.0\% \pm 0.1\%$ and $0.4\% \pm 0.1\%$, respectively, depending on the light intensity range. We show that the measured nonlinearity can be used in order to linearise an independent dataset. Finally, a possible application of the developed method in a sliding nonlinearity monitoring and correction scheme during the ILC data taking is outlined.

Contents

1 Introduction

The discovery of the Higgs boson, which was announced on July 4th, 2012 by the ATLAS and CMS experiments, marks a milestone in the history of particle physics. It has been the long-standing missing experimental proof for the Higgs mechanism, which describes the mass generation of elementary particles and has recently been awarded with the Nobel Price. Nevertheless, there still exist several unsolved questions in the field of modern particle physics where observations are not in agreement with the established theory. Among them, the rather light observed Higgs mass calls for a yet unknown mechanism of stabilisation. This is, for instance, offered by supersymmetric extensions of the Standard Model. An at a first glance completely unrelated puzzle is the observation of neutrino oscillations, whose origin is still a mystery.

An attractive way of introducing the observed neutrino phenomenology into the Standard Model is a supersymmetric theory with bilinearly broken R parity (bRPV). This extension of the Standard Model is not only theoretically appealing, but has also experimentally very interesting consequences. Due to R-parity violation, Standard Model neutrinos and supersymmetric neutralinos mix with each other. Additionally, the lightest supersymmetric particle can decay into Standard Model particles. Therefore, one gets direct access to the neutrino sector by studying the properties and decays of the neutralinos. As these properties can be examined very well at a collider, neutrino physics could also be pursued at colliders. The ratio of the branching ratios $\mathrm{BR}(\tilde{\chi}_1^0 \to W\mu)/\,\mathrm{BR}(\tilde{\chi}_1^0 \to W\tau)$, for instance, can be related to the atmospheric neutrino mixing angle in this model. Especially the future International Linear Collider (ILC) offers excellent experimental conditions for studying bRPV SUSY events and in particular neutralino decays. For this reason, it is worthwhile to examine the prospects of bRPV SUSY searches as well as parameter determination at the ILC. This will be addressed in this thesis in a full detector simulation, which takes into account a highly detailed detector model as well as realistic ILC beam parameters.

An outstanding tool at the ILC is the usage of highly polarised electron/positron beams, which can help to enhance signal processes and to suppress backgrounds. Thus, the beam polarisation is a very important parameter which has to be determined as precisely as possible. At the ILC, two Compton polarimeters per beam line are foreseen, which can directly measure the beam polarisation. One of the most important limiting factors of the measurement precision of the polarimeters is

the detector linearity. In order to meet the envisaged precision goal of a systematic uncertainty of the polarisation measurement of $\Delta\mathcal{P}/\mathcal{P} = 0.25\%$, the detector linearity has to be measured on per-mil level as well. This makes a sophisticated detector calibration necessary. At that, it turns out that no absolute calibration is needed, but only the linearity has to be guaranteed. Therefore, a differential measurement of the detector nonlinearity can be utilised in order to linearise the data.
We will investigate the possibility of this kind of polarimeter calibration in simulation studies as well as in real test-stand measurements.

This thesis is organised as follows:

In the first two chapters, we elaborate on the foundations which are of general relevance for this thesis. At this, in *Chapter 2*, we first focus on the global theoretical framework. Starting with a brief review of the Standard Model of Particle Physics, we discuss some of its shortcomings and introduce supersymmetry (SUSY) as a possible extension and solution to some of those problems. In *Chapter 3*, we describe the ILC, which is the experimental basis of the following studies. The experimental features of a linear lepton collider are discussed. We further describe the ILC machine parameters in the light of the achievable luminosity and motivate the importance of beam polarisation. Finally, we explain the most important components of the ILC and the ILC physics case is outlined.

The subsequent part of the thesis is dedicated to the bRPV SUSY study at the ILC. In *Chapter 4*, the current experimental situation of neutrino oscillation measurements is reviewed and bRPV SUSY is introduced. At this, we especially focus on the connection to neutrino physics and the ability to measure the atmospheric neutrino mixing angle at a collider. After briefly commenting on the status of searches for SUSY at the LHC, a simplified model of bRPV SUSY for the ILC is defined. We choose a benchmark point which is used for the following study. The International Large Detector concept, on which the study is based, is described in *Chapter 5*. In *Chapter 6*, we explain the implemented procedure of the simulations of exotic bRPV events. Subsequently, the selection of events comprising the interesting neutralino decays $\widetilde{\chi}_1^0 \rightarrow W\mu$ and $\widetilde{\chi}_1^0 \rightarrow W\tau$ is presented. The selected events are finally analysed in *Chapter 7*. Herein, we show the neutralino mass reconstruction. Additionally, we evaluate the signal significance in the simplified model parameter plane and discuss especially the impact of beam polarisation. Finally, we measure the ratio of the branching ratio $\mathrm{BR}(\widetilde{\chi}_1^0 \rightarrow W\mu)/\,\mathrm{BR}(\widetilde{\chi}_1^0 \rightarrow W\tau)$ and give an interpretation of the findings as a measurement of the atmospheric neutrino mixing angel as suggested by bRPV SUSY. Parts of this study have already been published in References [1–4].

In the second part of this thesis, we focus on polarimetry. In *Chapter 8*, the principles of polarisation measurement are introduced. We also discuss the envisaged precision goals of the ILC polarimeters. It will be shown that the nonlinearity of the involved photodetectors is one of the main components which limits the achievable precision. A linearisation method based on a differential nonlinearity measurement is explained in *Chapter 9*. Here, we work out the theoretical principles of the proposed method and show its potential for linearising data in a Monte-Carlo simulation. We also define design criteria for a real setup. In the subsequent *Chapter 10*, the experimental realisation of the differential nonlinearity measurement is presented. We describe the experimental setup as well as the development of a suitable LED light source. Some emphasis will be put on the characterisation of the setup and the LED driver in order to make sure that the design criteria are fulfilled. Differential nonlinearity measurements are also performed and discussed in this chapter. It will be shown that the method can be utilised in order to linearise experimental data on the envisaged level of precision. In the end of the chapter, we give an outlook of how the linearisation method can be applied during the operation of the ILC polarimeters.

Finally, we conclude in *Chapter 11*.

As it simplifies the reading, we use natural units ($c = \hbar = 1$) for masses and momenta throughout this thesis.

2 Theoretical Foundations

In this chapter, the theoretical foundations of this thesis are described. Section 2.1 gives a brief overview of the Standard Model of Particle Physics. Subsequently, in Section 2.2, we discuss the gauge principle which is the basis of the theoretical formulation of the Standard Model. In Section 2.3, we describe the mechanism of electroweak symmetry breaking. Some of the shortcoming of the Standard Model are outlined in Section 2.4, which motivates the existence of new physics. As one possible extension a new symmetry – supersymmetry – is introduced in Section 2.5. Finally, in Section 2.6, we define the minimal supersymmetric extension of the Standard Model, on which parts of this thesis are based.

2.1 Standard Model of Particle Physics - an Overview

For more than 40 years, the Standard Model of Particle Physics (SM) has been developed, tested and proven to be one of the most successful theories we have. It describes the fundamental building blocks of matter and their interactions in our universe.

All elementary particles which form matter are particles of spin 1/2 – the so-called fermions. “Elementary” in this context means that up to now we have no evidence that those particles have a substructure and volume expansion. They behave as point-like objects. In the Standard Model, there are two types of elementary fermions: Quarks, which form hadrons, and leptons. The quarks subdivide into up- and down-type quarks and the leptons into charged leptons and neutrinos. These particles exist in three generations (also called flavour), which differ only in the particle masses.

Fermions carry an important property called chirality, which is an intrinsic, Lorentz-invariant property of a Dirac spinor. There exist two different chirality eigenstates: left-handed and right-handed fermions (cf. Appendix A for details). In the massless limit, chirality is equal to the helicity, which is the usually measured quantity describing the normalised projection of the particle spin on the direction of motion. For massive particles, however, it is obvious that helicity may flip with respect to

fermions	family			electric charge [e]	colour	weak isospin	
	1	2	3			left-handed	right-handed
leptons	ν_e	ν_μ	ν_τ	0	–	$\frac{1}{2}$	–
	e	μ	τ	-1			0
quarks	u	c	t	$\frac{2}{3}$	r,g,b	$\frac{1}{2}$	0
	d	s	b	$-\frac{1}{3}$			

Table 2.1: Fermions of the Standard Model and their charges.

the particles' chirality in different rest-frames. All fermions except for neutrinos have been observed in both possible helicity states. Table 2.1 gives an overview of the matter particles and their charges in the Standard Model.

In nature we know four fundamental forces: electromagnetism, the strong force, the weak force, and gravity. Gravity is well formulated in the theory of General Relativity, which is a geometric description of space-time. Hence, its structure is significantly different from quantum field theories that are used to describe the other three interactions. This is one of the reasons, why gravity is up to now not part of a consistent formulation of the Standard Model.

All the other interactions between matter particles can be described as the exchange of spin-1 messenger particles. These bosons arise as a direct consequence from gauge theories, which will be discussed in more detail in the next section. In the Standard Model, there exist eight massless gluons, which are the force mediators of the strong force. Gluons couple exclusively to quarks, which are the only matter particles carrying the charge of the strong force – the so-called "colour". The gauge structure of the strong interactions allows for three different colour charges, which are often referred to as red, green and blue. The only matter particles in the Standard Model which carry colour are the quarks. However, due to the behaviour of the strong coupling, quarks always appear in bound, color-neutral states. There exists different ways of forming such color-neutral states: For instance, two-quark systems (mesons) contain one colour and anti-colour and in three-quark systems (baryons) all three colours are present.

The three force carriers of the weak interaction are the $W^\pm$ and Z^0 bosons. $W^\pm$ couples hereby only to the left-handed part of the matter particles and induces a flip in the weak-isospin space, whereas Z^0 can also couple to right-handed fermions.

Finally, the mediator of electromagnetism is the photon, which couples to electrically charged matter particles.

A list of all vector bosons of the Standard Model is given in Table 2.2.

interaction	exchange boson	mass [GeV]
strong	8 gluons (g)	0
weak	$W^{\pm}$	80.385(15)[5]
	Z^0	91.1876(21)[5]
electromagnetic	photon (A)	0

Table 2.2: Vector bosons in the Standard Model.

2.2 The Gauge Principle

The aforementioned vector bosons of the different forces can be described by local gauge theories. The general idea behind gauge theories is to find the Lagrangian $\mathcal{L}$ containing the matter fields of the theory, which stays invariant under a *local* gauge transformation.

The principle of gauge theories will be demonstrated in the following at the example of quantum electrodynamics (QED) and later transferred to the Standard Model Lagrangian.

The Lagrangian of a free electron looks like:

$$\mathcal{L}_{\text{Dirac}} = \overline{\Psi}(x) i\gamma^{\mu}\partial_{\mu}\Psi(x) - m\overline{\Psi}(x)\Psi(x), \quad \text{with} \quad \overline{\Psi}(x) = \Psi^{+}(x)\gamma^{0}, \tag{2.1}$$

where $\Psi(x)$ represents a four-component Dirac spinor (here the electron field) and γ^{μ} are the Dirac matrices. We now apply a $U(1)$ field transformation, which is a phase transformation of the field and leaves the Lagrangian invariant,

$$\Psi(x) \to \Psi'(x) = \mathrm{e}^{-i\alpha}\Psi(x) \quad \text{and} \tag{2.2}$$

$$\overline{\Psi}(x) \to \overline{\Psi}'(x) = \mathrm{e}^{i\alpha}\overline{\Psi}(x). \tag{2.3}$$

However, it is obvious that as soon as the gauge transformation becomes local ($\alpha \to \alpha(x)$), the given Lagrangian is no longer gauge invariant, because of the derivative term in Equation (2.1). The invariance can be recovered by replacing the normal derivative ∂_{μ} by the gauge invariant derivative, which contains a new gauge field A_{μ}

$$\partial_{\mu} \to D_{\mu} = \partial_{\mu} + ieA_{\mu}(x). \tag{2.4}$$

Herein, e is a free parameter, which can be identified as the electron charge – the coupling constant in QED. This constant is an input parameter to the theory and has to be determined from a measurement. The new gauge field transforms like

$$A_{\mu}(x) \to A'_{\mu}(x) = A_{\mu}(x) - \frac{1}{e}\partial_{\mu}\alpha(x). \tag{2.5}$$

Finally, a gauge invariant kinetic term for the newly introduced field has to be added to the QED Lagrangian for completeness:

$$\mathcal{L}_A = -\frac{1}{4} A_{\mu\nu} A^{\mu\nu}, \tag{2.6}$$

$$A_{\mu\nu} = \partial_\mu A_\nu(x) - \partial_\nu A_\mu(x). \tag{2.7}$$

It is important to note that a corresponding mass term for $A_\mu(x)$ is forbidden since this would spoil local gauge invariance again.

In the end, the construction of a locally gauge invariant Lagrangian ends in the introduction of one new massless vector field, which couples to the fermion field with coupling strength e. This new field can be identified as the photon.

The full QED Lagrangian becomes

$$\mathcal{L}_{\text{em}} = \underbrace{\overline{\Psi}(x) i\gamma^\mu \partial_\mu \Psi(x)}_{\text{kinetic term } e} - \underbrace{m\overline{\Psi}(x)\Psi(x)}_{\text{mass term}} - \underbrace{e\overline{\Psi}(x)\gamma^\mu A_\mu(x)\Psi(x)}_{\text{interaction term } e} - \underbrace{\frac{1}{4} A_{\mu\nu} A^{\mu\nu}}_{\text{kinetic term } \gamma} . \tag{2.8}$$

QED with its underlying $U(1)$ gauge symmetry is a nice example for an Abelian gauge theory, which has the consequence that the photon field does not interact with itself. For non-Abelian gauge groups, like $SU(2)$ or $SU(3)$, the new gauge fields can self-interact, as it will be shown in the following. These kinds of gauge theories are also known as Yang-Mills-Theories [6]. As a side remark, it should be mentioned that each gauge symmetry introduces a conserved quantity, following Noether's theorem [7]. In the case of QED, this is the conservation of the electric four-current.

Let us turn now to the full Standard Model Lagrangian. The gauge structure can be summarised as

$$SU(3)_C \times SU(2)_L \times U(1)_Y. \tag{2.9}$$

Herein, $SU(3)_C$ is the gauge group of quantum chromodynamics (QCD), which describes the strong force. QCD was initially developed by Gell-Mann, Fritzsch, and Leutwyler [8] in the 1970s. $SU(2)_L \times U(1)_Y$ represents the gauge group of electroweak interactions, introduced by Glashow [9], Salam [10, 11] and Weinberg [12] about ten years before. The electroweak part of the Lagrangian deconstructs to the electromagnetic and weak force after electroweak symmetry breaking.

The gauge part of the Standard Model Lagrangian reads:

$$\mathcal{L}_{\text{SM,gauge}} = \frac{1}{4} B_{\mu\nu} B^{\mu\nu} - \sum_{a=1}^{3} \frac{1}{4} W^a_{\mu\nu} W^{a,\mu\nu} - \sum_{a=1}^{8} \frac{1}{4} G^a_{\mu\nu} G^{a,\mu\nu} \tag{2.10}$$

with

$$B_{\mu\nu} = \partial_\mu B_\nu - \partial_\nu B_\mu, \tag{2.11}$$

$$W^a_{\mu\nu} = \partial_\mu W^a_\nu - \partial_\nu W^a_\mu - g \sum_{b,c=1}^{3} \varepsilon^{abc} W^b_\mu W^c_\nu, \tag{2.12}$$

$$G^a_{\mu\nu} = \partial_\mu G^a_\nu - \partial_\nu G^a_\mu - g_3 \sum_{b,c=1}^{8} f^{abc} G^b_\mu G^c_\nu. \tag{2.13}$$

The new gauge bosons correspond to the following gauge groups: $U(1)_Y \leftrightarrow B$ with coupling constant g', $SU(2)_L \leftrightarrow W^{1\ldots3}$ with coupling constant g and $SU(3)_C \leftrightarrow G^{1\ldots8}$ with coupling constant g_3. It is clear that for each generator of the corresponding group one gauge field has to be introduced, because the number of generators of a group represents the number of independent base transformations setting up the most general gauge transformation. In general $SU(n)$ has n^2-1 generators. ε^{abc} and f^{abc} are the structure functions of $SU(2)$ and $SU(3)$. From the last terms in Equations (2.12) and (2.13) it becomes visible that for $SU(2)$ and $SU(3)$ the gauge-kinetic terms in Equation (2.10) build up three-point and four-point self-interactions of the gauge bosons. One should note that this self-interaction is dynamically generated by the non-Abelian character of $SU(n)$.

$G^{1\ldots8}$ in (2.10) can directly be identified with the eight gluons listed in Table 2.2. $W^{1,2,3}$ and B, however, cannot be related directly to $W^\pm$, Z^0 and the photon A. From experiments we know that the weak vector bosons are rather heavy. Gauge theories on the other hand only generate massless gauge bosons, as pointed out earlier. Breaking the gauge invariance explicitly, by adding mass terms of the gauge boson $M^2 W^a_\mu W^{a,\mu}$ to the Lagrangian would generate nonrenormalisable divergences for higher orders of perturbation theory.

Furthermore, it turns out that also the fermion masses must not be introduced by an explicit mass term, as it was done in the simple QED example (cf. (2.8)). The different masses for neutrinos and corresponding leptons, e.g., would spoil weak isospin transformations and, therefore, both masses have to be zero.

In fact, the Standard Model, as it has been described so far, cannot account for any particle masses. However, in the following a mechanism is explained, which generates particle masses dynamically by breaking the local electroweak gauge symmetry spontaneously – the Higgs mechanism.

2.3 Electroweak Symmetry Breaking

Let us consider a complex scalar field $\phi = (\phi_1 + i\phi_2)/\sqrt{2}$ with the potential

$$\mathcal{V} = \mu^2 \phi^* \phi + \lambda \left(\phi^* \phi\right)^2. \tag{2.14}$$

Then, the Lagrangian for this field looks like

$$\mathcal{L} = \mathcal{T} - \mathcal{V} = (\partial_\mu \phi)^* (\partial^\mu \phi) - \mu^2 \phi^* \phi - \lambda (\phi^* \phi)^2. \tag{2.15}$$

Note that this Lagrangian is invariant for any global gauge transformation. In order to ensure the stability of the potential and to bind it from below, λ has to be positive. In the case of $\mu^2 > 0$, the Lagrangian represents just two real scalar self-interacting fields ϕ_1 and ϕ_2 with mass $m_{\phi_{1,2}} = \sqrt{2\mu^2}$. The potential has its minimum at $\phi = 0$. However, in the case of $\mu^2 < 0$ the minimum of V is different from zero and lies on a circle defined by

$$\phi_1^2 + \phi_2^2 = v^2, \qquad \text{with} \quad v^2 = -\frac{\mu^2}{\lambda}. \tag{2.16}$$

In this case, the given field definition is inappropriate to describe the properties of the particle, since in a perturbative theory (as it is the Standard Model) fields always have to be expressed as fluctuation over their energetic ground state. For this reason, we expand ϕ around *one* (of the infinite) real minima, chosen without loss of generality to be at $\phi_1 = v$ and $\phi_2 = 0$

$$\phi(x) = \sqrt{\frac{1}{2}} \left(v + \eta(x) + i\xi(x) \right) \tag{2.17}$$

and re-express the Lagrangian in terms of these new field definitions

$$\mathcal{L}' = \frac{1}{2}(\partial_\mu \xi)^2 + \frac{1}{2}(\partial_\mu \eta)^2 + \mu^2 \eta^2 + \text{const.} + \mathcal{O}(\eta^3, \xi^3). \tag{2.18}$$

This transition is called “spontaneous symmetry breaking”, because the symmetry of the Lagrangian is broken by the choice of ground state of the field. It becomes clear from Equation (2.18) that there are two physical fields (η and ξ), of which only η has a mass term with $m_\eta = \sqrt{-2\mu^2}$ (remember that we are discussing the case $\mu^2 < 0$). The massless boson ξ is also called Goldstone boson, according to Goldstone's theorem, which states that for each broken symmetry of a Lagrangian (with respect to the ground state) one massless particle is introduced [13, 14].

We can now move on to a local gauge invariant formulation of Equation (2.15). For simplicity, we choose $U(1)$ as gauge group, but the argumentation works analogously for $SU(2)_L \times U(1)_Y$. In order to make Equation (2.15) gauge invariant under $U(1)$, the normal derivative ∂_μ is replaced by the definition of the covariant derivative D_μ, which contains a gauge field A_μ:

$$\mathcal{L} = (\partial^\mu + ieA^\mu)\phi^* (\partial_\mu - ieA_\mu)\phi - \mu^2 \phi^* \phi - \lambda(\phi^* \phi)^2 - \frac{1}{4} A_{\mu\nu} A^{\mu\nu} \tag{2.19}$$

As before, we expand the scalar field around the real minimum and get

$$\mathcal{L}' = \frac{1}{2}(\partial_\mu \xi)^2 + \frac{1}{2}(\partial_\mu \eta)^2 - v^2 \lambda \eta^2 + \frac{1}{2} e^2 v^2 A_\mu A^\mu - ev A_\mu \partial^\mu \xi - \frac{1}{4} A_{\mu\nu} A^{\mu\nu} + \text{int. terms.} \tag{2.20}$$

As a result, we get one massive scalar boson, one massless Goldstone boson, and a mass term for the gauge boson, which we aimed for. A theory with a massless new particle, however, is not viable, since there is no experimental evidence for an additional massless particle. Higgs [15, 16], Englert, and Brout [17] showed that the unwanted Goldstone boson can be rotated away in order to be absorbed into the new longitudinal degree of freedom of the massive vector boson. The described mechanism of generating mass for the gauge boson is called Higgs mechanism. The most important prediction of this theory is the existence of one massive scalar particle H, which is called the Higgs boson. Its mass, however, is a free parameter and has to be measured.

Applying this mechanism to the Weinberg-Salam model of $SU(2)_L \times U(1)_Y$ of the Standard Model, the vector bosons of the Standard Model are finally generated. However, for this gauge structure a complex Higgs *doublet* is necessary. The gauge eigenstates $W^{1,2}$ are then combined to the massive $W^{\pm}$

$$W^{\pm}_{\mu} = \frac{1}{\sqrt{2}}(W^1_{\mu} \pm W^2_{\mu}), \tag{2.21}$$

with the mass

$$m_W = \frac{1}{2} v g, \tag{2.22}$$

where v is the Higgs vacuum expectation value. The remaining gauge bosons W^3 and B mix to the massive Z^0 and massless photon A

$$\begin{pmatrix} A_{\mu} \\ Z_{\mu} \end{pmatrix} = \begin{pmatrix} \cos(\theta_W) & \sin(\theta_W) \\ -\sin(\theta_W) & \cos(\theta_W) \end{pmatrix} \begin{pmatrix} B_{\mu} \\ W^3_{\mu} \end{pmatrix}. \tag{2.23}$$

Herein, θ_W is the so-called Weinberg angle, which is related to the coupling constants g' and g by

$$\cos(\theta_W) = \frac{g}{\sqrt{g^2 + g'^2}} \qquad \sin(\theta_W) = \frac{g'}{\sqrt{g^2 + g'^2}}. \tag{2.24}$$

The masses of Z and A become

$$m_Z = \frac{1}{2} v \sqrt{g^2 + g'^2} \qquad \text{and} \qquad m_A = 0. \tag{2.25}$$

As mentioned earlier, also the fermions in the Standard Model gain their masses via the Higgs mechanism. Therefore, gauge invariant interaction terms between the Higgs field and the fermions are inserted into the Lagrangian. After electroweak symmetry breaking the Higgs acquires its vacuum expectation value (VEV) $v \neq 0$ and therefore generates dynamically mass terms for the fermions. These Yukawa-type couplings of the Higgs to fermions (which are in the end responsible for the

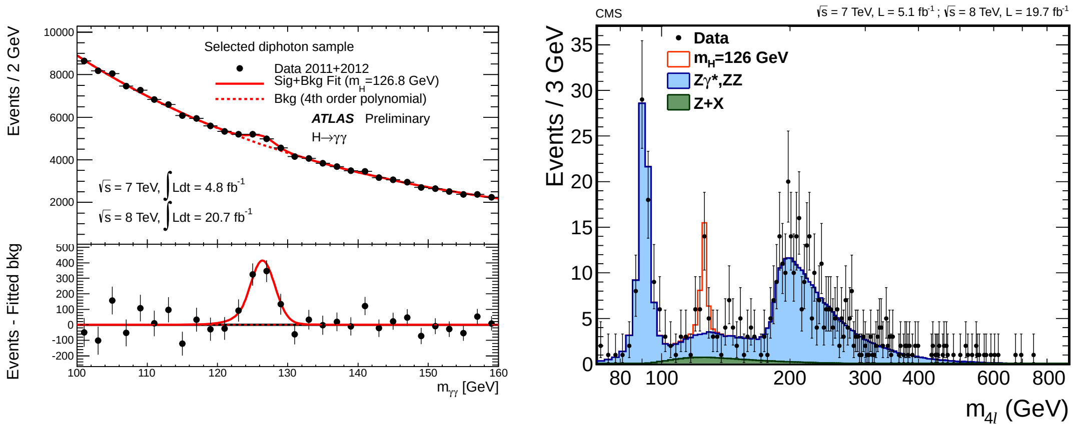

(a) **(b)**

Figure 2.1: (a) Invariant mass distribution of diphoton Higgs candidates measured by the ATLAS detector. Figure taken from [21]. (b) Distribution of the four-lepton invariant mass in the channels $4e$, 4μ, and $2e2\mu$ measured by the CMS detector. Figure taken from [22]. Both figures show the combination of the full $\sqrt{s} = 7$ TeV and $\sqrt{s} = 8$ TeV data samples.

actual mass value) are not predicted, but free parameters of the theory. This is the most unappealing part of the SM theory, since each fermion get its own coupling, which is inserted by hand into the Lagrangian. On the other hand, this fact predicts that the coupling of the Higgs to the different fermions is proportional to their mass, which can be well tested at the ILC.

t' Hooft has shown in 1971 that the presented electroweak gauge theory involving the Higgs mechanism is a renormalizable theory [18], which was awarded with the Nobel price in 1999.

For a long time, the experimental proof of the here described mechanism was missing, but on July 4th, 2012 the two multi-purpose experiments at the Large Hadron Collider (LHC) at CERN, ATLAS and CMS, reported the discovery of the Higgs boson [19, 20]. Figure 2.1a shows the signal in the prominent decay channel of the Higgs $H \rightarrow \gamma\gamma$ (via a top loop) with full statistics of the 2011 and 2012 run of LHC observed by the ATLAS experiment. In this channel the discovery was made. In Figure 2.1b, the invariant mass distribution of four lepton events are shown as measured by the CMS detector. Herein, the Higgs signal originates from the decay mode $H \rightarrow ZZ \rightarrow llll$.

From a combination of different channels, the mass of the boson was determined to

$$m_H = 125.5 \pm 0.2(\text{stat.})^{+0.5}_{-0.6}(\text{syst.})^{[23]} \quad \text{for} \quad \int L dt = 25\,\text{fb}^{-1}. \tag{2.26}$$

The discovery of the Higgs boson is yet another milestone in establishing the Standard Model. However, it is still crucial to measure all the properties of this new particle very carefully in order to test weather it is really the SM Higgs boson. In the other case, it opens the field for many interesting extensions of the Standard Model, like e.g. Supersymmetry (SUSY), which will be introduced in Section 2.5.

2.4 Shortcomings of the Standard Model

In the last section, the great success of the Standard Model was stressed. However, there are also some severe shortcomings. We are going to describe the most prominent ones in this section.

I. Dark Matter A strong evidence for dark matter results from the measurement of the rotation velocity of spiral galaxies [24]. It was observed that the velocity behaviour in dependence of the distance to the galactic center becomes constant in the outer parts of the galaxy. This is in clear disagreement with Kepler's 3rd law assuming that the (observable) light emitting matter was the only matter in the galaxy. With the assumption of additional matter which is non light-emitting (dark), the rotation velocity behaviour can be explained. In fact, the needed dark matter to account for the observations is by a factor of 3 to 10 larger than the visible matter [25].

Another strong evidence for the existence of additional nonvisible matter is the gravitational lensing effect. Following Einstein's General Theory of Relativity, space-time gets distorted by matter. As a consequence, a light trajectory is bent if it traverses areas in the universe with heavily increased matter density. This creates distortions in the picture of the visible sky, which can, in turn, be used to indirectly measure the invisible mass distribution along the light path. Those bending/lensing effects have been identified by astronomers in many examples.

One of the most famous examples and striking hints for the existence of dark matter is the bullet cluster (1E 0657-558) [26]. It shows shows two galaxies right after a head-on collision. From lensing effects, the gravitational potential of the galaxy cluster can be derived. Interestingly, the reconstructed center of gravity differs significantly from the centers of visible matter observed in the X-ray image [27]. This fits well into the picture of galaxies, which are accompanied by a very massive, but only weakly interacting dark matter halo. In the collision of the galaxies, both halos interpenetrated unhinderedly whereas the galactic gas interacts heavily and causes the X-ray emission in the shock cone.

The fraction of nonbaryonic matter in the universe can be measured very precisely as described in the next paragraph.

II. Dark Energy From measurements of the red-shift of galaxies and type 1a supernovae we know that we live in an expanding universe. Moreover, it turns out that our universe accelerates in its expansion. This phenomenon cannot be understood so easily since in fact a deceleration is expected due to gravitational effects between galaxies. In order to meet the experimental observations it is necessary to introduce a vacuum energy density, which is often referred to as "dark energy" [28].

The Planck Collaboration has recently published their measurements of the Cosmic Microwave Background (CMB). From this measurement among other quantities also the fraction of dark energy to the total energy content of the universe can be analysed. According to their measurement, the universe consists of 68.3% of dark energy, 26.8% of dark matter and only 4.9% of baryonic matter [29]. However, only the latter part is described by the Standard Model.

III. Neutrino Masses Neutrinos play a special role in the Standard Model. Up to now, we have only observed neutrinos with negative helicity in contrast to all other particles in the Standard Model, where both helicity states are present. Consequently, neutrinos should be truly massless particles. On the contrary, from the observation of neutrino flavour oscillations, we know experimentally that neutrinos need to be massive. Hence, neutrinos are the first particles, we have already observed that point by their features directly to physics beyond the Standard Model. A possible way to introduce neutrino masses and mixing beyond the Standard Model is discussed in Chapter 4.

IV. Grand Unification One great success of the Standard Model was the unification of electromagnetic and weak force into one single theory at the electroweak scale ($Q \approx 10^2\,\mathrm{GeV}$). The search for more and more general descriptions seem to be a guiding principle in modern physics. Consequently, the next step is to find a theory that unifies the electroweak theory with QCD. This so-called "Grand Unification" is expected to take place at much higher energy scales. However, from renormalisation group equations, which describe the evolution of the coupling constants of the gauge groups at different scales, it is known that the couplings of $SU(3)_C$, $SU(2)_L$ and $SU(1)_Y$ miss each other (cf. Figure 2.2). Therefore, there is no chance to find one common description of all three forces proportional to only one common coupling constant. The existence of new particles can modify the renormalisation group equations in such a way that unification becomes possible. In the case of the presence of additional (non-SM) particles at the TeV scale, the unification scale turns out to be at $Q = 10^{(16 \pm 0.3)}$ [31]. This scale is referred to as GUT scale.

V. Higgs Hierarchy Problem One major problem of the Standard Model Higgs boson is that there exists no symmetry, which prevents the mass from receiving

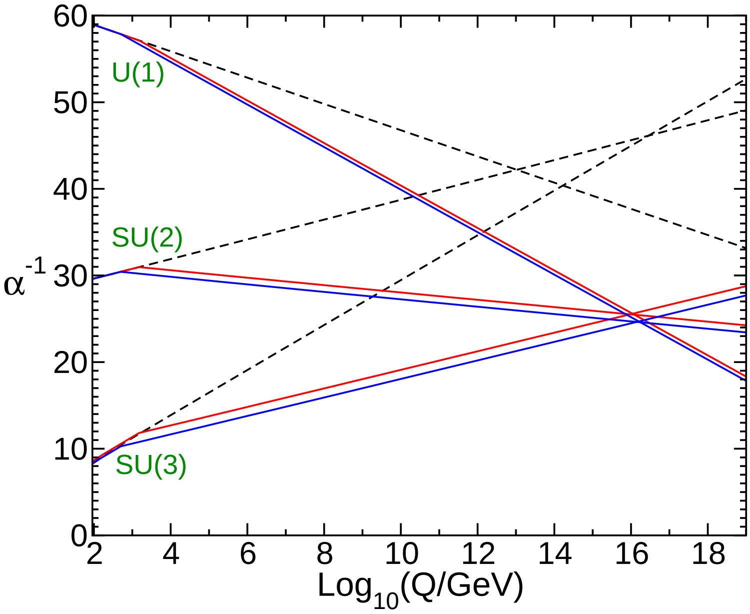

Figure 2.2: Running couplings in dependence of the energy scale for the different gauge groups in the Standard Model without (dashed) and with (solid) a SUSY extension. Gauge unification in the Standard Model is ruled out. Figure taken from [30].

quadratic corrections on higher orders of perturbation theory. This is demonstrated at the example in the following: If the Higgs–fermion interaction term in the Lagrangian looks like $-\lambda_f H\overline{f}f$ (cf. Figure 2.3a), the quantum corrections to the Higgs mass arising from any Standard Model fermion become [30]

$$\Delta m_H^2 = -\frac{|\lambda_f|^2}{8\pi^2}\Lambda_{\mathrm{UV}}^2 + ... \tag{2.27}$$

For the Standard Model being an effective theory, Λ_{UV} denotes the cut-off scale, up to which our current theory is valid. Usually Λ_{UV} is assumed to be around the Planck scale $M_P \approx 10^{19}$. This means that the higher order corrections to the Higgs mass are many orders of magnitudes larger than the expected central value. Therefore, there must be a huge cancellation between tree level and higher loop orders in order to obtain the correct mass (2.26). This is known as the “Higgs hierarchy problem”.

One way to avoid the quadratic dependence of the cut-off scale is to introduce two complex non-SM scalars per Standard Model fermion, which couple to the Higgs like $-\lambda_S|H|^2|S|^2$. These particles also contribute to the loop correction [30]

$$\Delta m_H^2 = \frac{\lambda_S}{16\pi^2}[\Lambda_{\mathrm{UV}}^2 - 2m_S^2\ln(\Lambda_{\mathrm{UV}}/m_S)]. \tag{2.28}$$

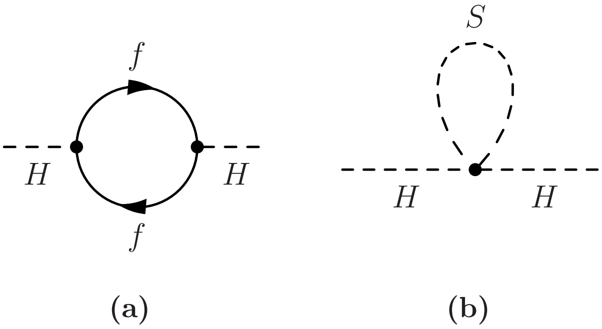

Figure 2.3: Example of Feynman diagrams which lead to a cancellation of the quadratic cut-off scale dependence of the Higgs boson mass loop correction in the case of supersymmetry. (a) Standard Model fermion contribution to Higgs self-energy. (b) Scalar contribution to Higgs self-energy.

The quadratic cut-off dependence finally cancels because of a relative minus sign, if λ_f and λ_S are related to each other. This can be assured by a new fundamental symmetry between fermions and scalars, called Supersymmetry.

2.5 A New Symmetry – Supersymmetry

As indicated in the last sections, symmetries play a very important role in physics. Not seldom they point to new areas of physics long before their discovery. Now we want to turn to another kind of symmetry – the symmetry of space-time, described by the Poincaré group and its algebra. It describes translations, rotations and boosts in the Minkowski space. Coleman and Mandula pointed out in 1967 that it is impossible to find further theories with symmetries that combine space-time and internal symmetries (like aforementioned $SU(n)$ symmetries) in any but trivial way, meaning as direct products [32]. However, a few years later, Haag, Łopuszański and Sohnius showed that there is *one* nontrivial extension, when the normal algebra is extended by anti-commutator relations [33]. This is what is widely known as supersymmetry.

In this theory, the space-time symmetry is extended by a symmetry that is generated by anti-commuting charges and, therefore, the space-time gets extended to a “super-space-time”. All fields (called superfields) are then expressed not only as function of $\vec{x}$ and t, but they also depend on new anti-commuting numbers, the so-called Grassman numbers θ_i (where $\theta_i\theta_j = -\theta_j\theta_i$). Symmetry operations in this superspace include not only the normal space-time transformations, but also additional transformations, generated by the new fermionic (anti-commuting) charges. Mathematically speaking, this corresponds to a $\mathbb{Z}_2$-grading of the Pointcaré algebra in order to arrive at the super algebra. One of the most striking consequences is that the fields of a certain spin S can be rotated into particles with spin $S \pm \frac{1}{2}$ by the fermionic SUSY generator Q [34]:

$$Q\,|\text{SM fermion}\rangle = |\text{SUSY scalar}\rangle \tag{2.29}$$

$$Q\,|\text{SM gauge boson}\rangle = |\text{SUSY fermion}\rangle\,. \tag{2.30}$$

If there is only one such generator Q, one speaks of $N = 1$-supersymmetry, on which we want to focus for the rest of the thesis. However, one should note that there are also extended SUSY theories under study. Especially $N = 4$ offers a connection to string theory.

The generator Q fulfills the following anti-commutator and commutator relations [30]

$$\{Q, Q^\dagger\} = 2\sigma_\mu P^\mu, \tag{2.31}$$

$$\{Q, Q\} = \{Q^\dagger, Q^\dagger\} = 0, \tag{2.32}$$

$$[P^\mu, Q] = [P^\mu, Q^\dagger] = 0. \tag{2.33}$$

Herein, P^μ is the four-momentum generator of the Pointcaré group. Relation (2.33) has very important consequences: The fact that Q commutes with P^μ immediately leads to the fact that the fermionic field ψ and the bosonic fields ϕ belonging to one so-called supermultiplet are mass degenerate since

$$QP^\mu P_\mu\,|\psi\rangle = Qm_\psi^2\,|\psi\rangle = m_\psi^2 Q\,|\psi\rangle = m_\psi^2\,|\phi\rangle \tag{2.34}$$

$$QP^\mu P_\mu\,|\psi\rangle \overset{(2.33)}{=} P^\mu P_\mu Q\,|\psi\rangle = P^\mu P_\mu\,|\phi\rangle = m_\phi^2\,|\phi\rangle\,. \tag{2.35}$$

Thus, it follows $m_\phi^2 = m_\psi^2$. This makes clear that SUSY cannot be an exact symmetry. SUSY partners to fermions of the Standard Model would have exactly the same mass and coupling strength as the fermions itself. This means that we should have already discovered these kind of scalar partners, like e.g. a 0.511 MeV scalar electron. For this reason, SUSY – if it exists – must be a broken symmetry in order to be in agreement with the experimental situation. Mechanisms of SUSY breaking will be discussed in Section 2.6.

The SUSY particle spectrum can be organised in two types of supermultiplets:

Chiral supermultiplets contain one chirality state of a fermion (a two-component Weyl spinor, cf. Appendix A for details on different spinor representations) and its corresponding scalar. The scalar is usually named after the fermion, but with a prefixed “s” indicating the scalar character. A subscribed L or R relates the scalar to the chirality state of the fermion.

Gauge or vector multiplets are formed by a vector boson and its corresponding supersymmetric fermion, whose name gains additionally the suffix “ino”.

In 1974, Wess and Zumino formulated an interacting supersymmetric quantum field theory in four dimensions [35]. In the following, we will give a flavour of how to construct a supersymmetric Lagrangian. Therefore, we start with a free chiral supermultiplet

$$\mathcal{L}_{\mathrm{WZ}}^{\text{chiral,free}} = \partial_\mu \phi_i^* \partial^\mu \phi_i + \chi_i^\dagger i \bar{\sigma}^\mu \partial_\mu \chi_i + F_i^* F_i. \tag{2.36}$$

Herein, ϕ is a complex scalar field, χ represents a left-handed Weyl spinor and $\bar{\sigma}^\mu = (\mathbf{1}, -\sigma_1, -\sigma_2, -\sigma_3)$, with σ_i being the Pauli matrices. The index i indicates different multiplets. F is an auxiliary complex scalar, which adds off-shell two bosonic degrees of freedom to $\mathcal{L}_{\mathrm{WZ}}^{\text{free}}$. This is necessary in order to compensate the two additional fermionic degrees of freedom, which a Weyl spinor gains off-shell. As F has no kinetic term, it disappears on-shell. ϕ has on-shell as well as off-shell the same number of degrees of freedom. It can be shown that Equation (2.36) is invariant under SUSY transformation.

In a next step, we construct the interaction part of the Lagrangian. Therefore, we consider all terms which are renormalizable and preserve SUSY invariance. The interaction part of the Lagrangian can then be written as

$$\mathcal{L}_{\mathrm{WZ}}^{\text{chiral,int}} = W_i(\phi, \phi^*) F_i - \frac{1}{2} W_{ij}(\phi, \phi^*) \chi_i \cdot \chi_j + \text{h.c.}, \tag{2.37}$$

where $W_i = \partial W / \partial \phi_i$ and $W_{ij} = \partial^2 W / \partial \phi_i \partial \phi_j$. The "$\cdot$" denotes the spinor dot product. Due to power counting, we know that W must not depend on any other fields than ϕ and ϕ^*. An extensive discussion about the most general form of W can be found in Reference [36], which finally results in

$$W = \frac{1}{2} M_{ij} \phi_i \phi_j + \frac{1}{6} y_{ijk} \phi_i \phi_j \phi_k. \tag{2.38}$$

Herein, the matrix M_{ij} can be interpreted as a mass and y_{ijk} are Yukawa-like couplings.

We can now investigate the Euler-Lagrange equation for the auxiliary field F_i. The relevant Lagrangian is $\mathcal{L}_{F_i} = F_i F_i^* + W_i F_i + W_i^* F_i^*$, which is also called "$F$ term". Since no derivative $\partial_\mu F_i$ appears, the equation of motion becomes

$$\frac{\partial \mathcal{L}_{F_i}}{\partial F_i} = 0 = F_i^* + W_i \tag{2.39}$$

and, thus,

$$F_i^* = -W_i \qquad \text{and} \qquad F_i = -W_i^*. \tag{2.40}$$

With this result, the auxiliary field can be reformulated and $\mathcal{L}_{F_i}$ simplifies to $\mathcal{L}_{F_i} = -|W_i|^2$. Thus, the full Wess-Zumino Lagrangian of interacting chiral supermultiplets becomes

$$\mathcal{L}_{\mathrm{WZ}}^{\text{chiral}} = \partial_\mu \phi_i^* \partial^\mu \phi_i + \chi_i^\dagger i \bar{\sigma}^\mu \partial_\mu \chi_i - |W_i|^2 - \frac{1}{2}(W_{ij} \chi_i \cdot \chi_j + \text{h.c.}). \tag{2.41}$$

It is worth to insert finally the definition of W to see the structure of interacting supermultiplets:

$$\begin{aligned}
\mathcal{L}_{\mathrm{WZ}}^{\mathrm{chiral}} &= \partial_\mu \phi_i^* \partial^\mu \phi_i + \chi_i^\dagger i \bar{\sigma}^\mu \partial_\mu \chi_i && \text{kinetic terms} \quad (2.42)\\
&- |M_{ij}|^2 \phi_i \phi_i^* - \frac{1}{2}(M_{ij} \chi_i \cdot \chi_i + \text{h.c.}) && \text{mass terms} \quad (2.43)\\
&- \frac{1}{2}(M_{ij} y_{ijk}^* \phi_j \phi_j^* \phi_k^* + \text{h.c.}) && \text{scalar three-point interactions} \quad (2.44)\\
&- \frac{1}{4}|y_{ijk}|^2 \phi_j \phi_k \phi_j^* \phi_k^* && \text{scalar four-point interactions} \quad (2.45)\\
&- \frac{1}{2}(y_{ijk} \chi_i \cdot \chi_j \phi_k + \text{h.c.}) && \text{Yukawa-type interaction} \quad (2.46)
\end{aligned}$$

The appearing mass terms show that fermions and scalars in one supermultiplet are mass-degenerate, what we had already deduced from the superalgebra. Additionally, we can analyse the couplings of the scalar four-point interaction and the Yukawa-type interaction. It turns out that y_{ijk} enters quadratically into the coupling for a four-point interaction as well as linearly into the Yukawa-type coupling. This is exactly the dependence which is needed in order to cancel the quadratic divergences in the Higgs mass (cf. Equations (2.27) and (2.28)).

For a physical theory, also SUSY and gauge invariant gauge supermultiplets have to be constructed. This is a bit more involved, but works in principle analogically to the shown procedure. Thus we give only the result:

$$\mathcal{L}_{\mathrm{WZ}}^{\mathrm{gauge}} = -\frac{1}{4} F_{\mu\nu}^\alpha F^{\mu\nu\alpha} + (\lambda^\alpha)^\dagger \bar{\sigma}^\mu (D_\mu \lambda)^\alpha + \frac{1}{2} D^\alpha D^\alpha \tag{2.47}$$

Herein, $F_{\mu\nu}$ is the field strength tensor, containing the gauge boson field F_μ^α, with α numbering the gauge field of the underlying gauge group (e.g. $\alpha = 1, 2, 3$ for $SU(2)$). λ^α represents the left-handed Weyl spinor of the corresponding supersymmetric fermionic partner of F_μ^α. D^α is a real scalar auxiliary field, needed in order to preserve the bosonic and fermionic degrees of freedom on-shell as well as off-shell. The last term in the Lagrangian is also called "D term". D_μ in Equation (2.47) reflects the covariant derivative.

The final Lagrangian is now the sum of $\mathcal{L}_{\mathrm{WZ}}^{\mathrm{gauge}}$ and a modified version of $\mathcal{L}_{\mathrm{WZ}}^{\mathrm{chiral}}$, with $\partial_\mu \to D_\mu$. A final supersymmetrisation is needed, since there exist also gauge and SUSY invariant terms among combinations of {gauginos, sfermions, fermions} and {sfermions, D fields}. The full SUSY Lagrangian becomes in the end

$$\mathcal{L}^{\mathrm{SUSY}} = \mathcal{L}'^{\mathrm{chiral}}_{\mathrm{WZ}} + \mathcal{L}_{\mathrm{WZ}}^{\mathrm{gauge}} - \sqrt{2} g [(\phi_i^* T^\alpha \chi_i) \cdot \lambda^\alpha + \text{h.c.}] - g(\phi_i^* T^\alpha \phi_i) D^\alpha. \tag{2.48}$$

T^α denotes the α^{th} generator and g the coupling strength of the specific gauge group.

The sum over all F and D terms is called the scalar potential $\mathcal{V}$, which is a positive definite function

$$\mathcal{V} = F_i F_i^* + \frac{1}{2} D^\alpha D^\alpha. \tag{2.49}$$

The full supersymmetric Lagrangian can also be expressed in terms of the superfield formalism, in which for each supermultiplet one superfield is defined, containing all bosonic and fermionic degrees of freedom. The superpotential, which contains all allowed combinations of superfields, describes in this formalism the dynamics of the theory. Together with the underlying gauge structure the full Lagrangian can be derived. For a detailed derivation of the SUSY Lagrangian using the superfield formalism, we refer to Reference [37].

2.6 Minimal Supersymmetric Extension of the Standard Model

In the following, we are going to discuss the Minimal Supersymmetric extension of the Standard Model (MSSM). Table 2.3 shows all chiral supermultiplet in the MSSM and Table 2.4 lists the gauge supermultiplets corresponding to $SU(3)_C \times SU(2)_Y \times U(1)_Y$.

The MSSM superpotential looks like

$$\mathcal{W}^{\mathrm{MSSM}} = y_u^{ij} \overline{u}_i Q_j \cdot H_u - y_d^{ij} \overline{d}_i Q_j \cdot H_d - y_e^{ij} \overline{e}_i L_j \cdot H_d + \mu H_u \cdot H_d, \tag{2.50}$$

where $i, j = 1, 2, 3$ are family indices. Colour indices for the quark superfields are suppressed. $y_{u,d,e}$ are 3×3 matrices representing Yukawa couplings, which are equal to the Yukawa couplings in the Standard Models, since Standard Model physics is also incorporated in Equation (2.50). This leaves us with only one new (in general complex) parameter μ, which can be understood as a supersymmetric Higgsino mass parameter. This is a remarkable result: By adding only one new parameter to the Standard Model, this existing theory could be fully supersymmetrised.

We should mention that the given superpotential could be extended by further SUSY invariant and renormalizable terms, which, however, violate baryon number B and lepton number L.

$$\mathcal{W}^{\Delta L=1} = \lambda_{ijk} L_i \cdot L_j \overline{e}_k + \lambda'_{ijk} L_i \cdot Q_j \overline{d}_k + \epsilon_i L_i \cdot H_u \tag{2.51}$$

$$\mathcal{W}^{\Delta B=1} = \lambda''_{ijk} \overline{u}_i \overline{d}_j \overline{d}_k \tag{2.52}$$

Herein, λ, λ', λ'' are $3\times3\times3$ matrices representing R-parity violating (RPV) Yukawa-like couplings and ϵ_i are dimensionful bilinear RPV parameters.

names		$S=0$	$S=\frac{1}{2}$	$SU(3)_C$	$SU(2)_L$	$U(1)_Y$
squarks, quarks (× 3 families)	Q	$\left(\widetilde{u}_L \quad \widetilde{d}_L\right)$	$(u_L \quad d_L)$	$\mathbf{3}$	$\mathbf{2}$	$+\frac{1}{6}$
	$\overline{u}$	$\widetilde{\overline{u}}_L \equiv \widetilde{u}_R$	$\overline{u}_L \equiv u_R$	$\overline{\mathbf{3}}$	$\mathbf{1}$	$-\frac{2}{3}$
	$\overline{d}$	$\widetilde{\overline{d}}_L \equiv \widetilde{d}_R$	$\overline{d}_L \equiv d_R$	$\overline{\mathbf{3}}$	$\mathbf{1}$	$+\frac{1}{3}$
sleptons, leptons (× 3 families)	L	$(\widetilde{\nu}_L \quad \widetilde{e}_L)$	$(\nu_L \quad e_L)$	$\mathbf{1}$	$\mathbf{2}$	$-\frac{1}{2}$
	$\overline{e}$	$\widetilde{\overline{e}}_L \equiv \widetilde{e}_R$	$\overline{e}_L \equiv e_R$	$\mathbf{1}$	$\mathbf{1}$	$+1$
Higgs, Higgsino	H_u	$(H_u^+ \quad H_u^0)$	$\left(\widetilde{H}_u^+ \quad \widetilde{H}_u^0\right)$	$\mathbf{1}$	$\mathbf{2}$	$+\frac{1}{2}$
	H_d	$\left(H_d^0 \quad H_d^-\right)$	$\left(\widetilde{H}_d^0 \quad \widetilde{H}_d^-\right)$	$\mathbf{1}$	$\mathbf{2}$	$-\frac{1}{2}$

Table 2.3: Chiral supermultiplets and their quantum numbers in the MSSM. Spin-0 particles represent complex scalars and spin-$\frac{1}{2}$ fields are given as left-handed Weyl spinors (cf. A.3.2 for right-handed Weyl spinor nomenclature). The second column gives the superfield symbol of each supermultiplet.

names	$S=\frac{1}{2}$	$S=1$	$SU(3)_C$	$SU(2)_L$	$U(1)_Y$
gluon, gluino	$\widetilde{g}$	g	$\mathbf{8}$	$\mathbf{1}$	0
winos, W boson	$\widetilde{W}^0, \widetilde{W}^\pm$	$W_0, W^\pm$	$\mathbf{1}$	$\mathbf{3}$	0
bino, B boson	$\widetilde{B}$	B	$\mathbf{1}$	$\mathbf{1}$	0

Table 2.4: Gauge supermultiplets and their quantum numbers in the MSSM.

Baryon and lepton number violating terms are new features of the supersymmetric Lagrangian, since in the Standard Model Lagrangian those kind of terms are forbidden by construction. However, the presence of *all* of those terms would lead to proton decay, which has not been observed. The standard procedure in the MSSM in order to suppress these terms is to introduce a new multiplicative quantum number called R parity

$$R = (-1)^{(3B+L+2S)}, \tag{2.53}$$

where S is the spin of the field. Hence, SM particles always carry $R = +1$ and SUSY particles $R = -1$. The conservation of this quantum number has the consequence that all B and L violating terms in the SUSY Lagrangian disappear and the proton remains stable. At a collider, only pairs of supersymmetric particles can be produced. Additionally, the lightest supersymmetric particle (LSP) is stable and cannot further decay into lighter SM particles. In many scenarios the LSP is a neutral, only weakly interacting massive particle (WIMP) and, thus, R-parity conserving (RPC) SUSY offers in many cases naturally a good dark matter candidate. This is often also called the SUSY WIMP miracle.
An alternative to WIMP dark matter is gravitino dark matter as discussed in Reference [38]. It has been shown that in this kind of models the dark matter candidate may decay due to small R-parity violation [39]. Those gravitino decays are usually heavily suppressed by the Planck scale mass and the small RPV coupling, which causes a lifetime of the dark matter candidate that exceeds the life time of the universe. Thus, those models are consistent with cosmology. Decays of the next-to-lightest supersymmetric particle can be used as probes of this kind of models [40–45].

In this thesis, we investigate an R-parity violating (RPV) scenario, which will be introduced in detail in Section 4.2.2. However, for the remainder of the section, we will stick to the R parity conserving (RPC) superpotential.

It has already been pointed out that supersymmetry has still the severe problem that particles and sparticles are mass degenerate. Moreover, the μ term in Equation (2.50) generates automatically a Higgs potential in the Lagrangian

$$|\mu^2|\big((H_u^+)^2 + (H_d^-)^2 + (H_u^0)^2 + (H_d^0)^2\big). \tag{2.54}$$

Unfortunately, by construction, this scalar potential is a positive definite function and does not show the correct sign in the quadratic term in order to make spontaneous symmetry breaking possible (cf. Section 2.3). This is another indication that SUSY must be a broken symmetry: only a broken supersymmetry allows for electroweak symmetry breaking.

From the aesthetic point of view one would hope that SUSY is a spontaneously broken symmetry. This implies that the vacuum is not invariant under SUSY transformations. Since SUSY transformations are related to the momentum operator by Equation (2.31), a broken SUSY theory always corresponds to a nonvanishing energy of the ground state of the Lagrangian. This, in turn, is described as the expectation value of the scalar potential introduced in Equation (2.49). Thus, it is clear that SUSY breaking can only be achieved, if either the F-term or the D-term have a nonvanishing VEV, which is named F term or D term breaking. However, in the MSSM it turns out to be impossible to find a proper form of the F/D term, which could break SUSY spontaneously [30]. This is, why the idea of SUSY breaking via a hidden sector was introduced. Predominantly two possibilities are mentioned and discussed: Gravity/Planck-scale mediated SUSY breaking (PMSB), where new physics near the Planck scale (including gravity) is responsible for the SUSY breaking, and gauge mediated SUSY breaking (GMSB), which breaks SUSY via flavour-blind interactions via a messenger particle.

Our ignorance of the underlying mechanism, however, makes is necessary to insert the SUSY breaking terms explicitly by hand. The approach hereby is to add all possible soft SUSY breaking terms to the Lagrangian. “Soft” in this context means that the introduced couplings should be of positive mass dimension. Those kind of terms prevent us from adding new divergences to the dimensionless couplings established by the unbroken SUSY. Thus, it ensures the stabilisation of the electroweak scale, which was one of the motivations for SUSY.

The soft SUSY breaking terms in the MSSM Lagrangian are given in the following. For the gauginos we get:

$$\mathcal{L}^{\text{gaugino}}_{\cancel{\mathbf{SUSY}}} = -\frac{1}{2}\left(M_3 \widetilde{g}^\alpha \cdot \widetilde{g}^\alpha + M_2 \widetilde{W}^\alpha \cdot \widetilde{W}^\alpha + M_1 \widetilde{B} \cdot \widetilde{B} + \text{h.c.}\right) \tag{2.55}$$

M_3 denotes the gluino mass parameter, M_2 the wino mass parameter and M_1 the bino mass parameter. In general, these parameters can be complex and, thus, be a source for CP violation. Herein, α numbers the gaugino fields depending on the underlying gauge group.
The soft SUSY breaking terms for the scalar partners to the SM fermions are of the form:

$$\mathcal{L}^{\text{squarks}}_{\cancel{\mathbf{SUSY}}} = -\left(\mathbf{m}^2_{\widetilde{\mathbf{Q}}}\right)_{ij} \widetilde{Q}_i^\dagger \cdot \widetilde{Q}_j - \left(\mathbf{m}^2_{\widetilde{\bar{\mathbf{u}}}}\right)_{ij} \widetilde{\bar{u}}_i^\dagger \widetilde{\bar{u}}_j - \left(\mathbf{m}^2_{\widetilde{\bar{\mathbf{d}}}}\right)_{ij} \widetilde{\bar{d}}_i^\dagger \widetilde{\bar{d}}_j \tag{2.56}$$

$$\mathcal{L}^{\text{sleptons}}_{\cancel{\mathbf{SUSY}}} = -\left(\mathbf{m}^2_{\widetilde{\mathbf{L}}}\right)_{ij} \widetilde{L}_i^\dagger \cdot \widetilde{L}_j - \left(\mathbf{m}^2_{\widetilde{\bar{\mathbf{e}}}}\right)_{ij} \widetilde{\bar{e}}_i^\dagger \widetilde{\bar{e}}_j, \tag{2.57}$$

where $\mathbf{m}^2_{\mathbf{X}}$ are Hermitian 3×3 matrices of squared mass parameters for the sfermions of all five chiral supermultiplets and i, j represent family indices.
There are also trilinear couplings, which break SUSY softly:

$$\mathcal{L}^{\text{trilinear}}_{\cancel{\mathbf{SUSY}}} = -\left((\mathbf{a_u})_{ij} \widetilde{\bar{u}}_i \widetilde{Q}_j \cdot H_u - (\mathbf{a_d})_{ij} \widetilde{\bar{d}}_i \widetilde{Q}_j \cdot H_d - (\mathbf{a_e})_{ij} \widetilde{\bar{e}}_i \widetilde{L}_j \cdot H_d + \text{h.c.}\right), \tag{2.58}$$

herein, $\mathbf{a}_{\tilde{\mathbf{X}}}$ are in general complex 3 × 3 Yukawa-like couplings.
Finally, the soft SUSY breaking terms for the Higgsino sector looks like:

$$\mathcal{L}^{\text{Higgs}}_{\cancel{\text{SUSY}}} = -m^2_{H_u} H^\dagger_u \cdot H_u - m^2_{H_d} H^\dagger_d \cdot H_d - (bH_u \cdot H_d + \text{h.c.}) \tag{2.59}$$

The two diagonal squared Higgs mass terms and the off-diagonal b term have the same dimension as μ in the MSSM superpotential. Only with these additional soft SUSY breaking terms, the Higgs potential is able to get a minimum different from zero, as already pointed out before. In the MSSM, two complex Higgs doublets are necessary in order to ensure triangular anomaly cancellations. They are also essential in order to give mass to both the up-type as well as the down-type quarks (in contrary to the Standard Model, where already one Higgs doublet could be used for both). For this reason, the minimisation of the Higgs potential gives two VEVs v_u and v_d – one per Higgs doublet. They obey the relation

$$v^2 = v^2_u + v^2_d = 4m^2_W/g^2 = (246\,\text{GeV})^2. \tag{2.60}$$

In the MSSM Higgs sector, there are in total eight degrees of freedom (d.o.f.), originating from two scalar doublets. After electroweak symmetry breaking, three d.o.f. are transferred into the new longitudinal degrees of freedom of the massive $W^\pm$ and Z^0, whereas the remaining five degrees of freedom form five massive scalar Higgs fields, namely one light Higgs h^0, one heavy Higgs H^0, one pseudo-scalar Higgs A^0 and two charged Higgs $H^\pm$. It should be noted that usually $m^2_{H_u}$, $m^2_{H_d}$ and b are not used for parameterising the Higgs sector, but rather v_u, v_d and m_{A^0}, which is an equivalent choice. Considering additionally Equation (2.60) allows us to describe both VEVs by $\tan(\beta) = v_u/v_d$.

In total, there are in the end 18 parameters from the Standard Model (gauge couplings, fermion masses, ...), one additional parameter to supersymmetrise the SM Lagrangian (μ) and 105 parameters from the soft SUSY breaking, which were introduced in the last paragraphs [46]. Note that when allowing for RPV, there arise even more SUSY parameters. Clearly, those at least 124 free parameters are neither satisfactory nor manageable for SUSY studies. Besides that, this most generic model MSSM-124 is not a viable theory, since it allows for unsuppressed flavour-changing neutral currents and too many sources of CP violation, which is in contradiction to experimental observations [47]. For this reason, phenomenological models are introduced, where the number of parameters are reduced. For a long time, the so-called constrained MSSM (cMSSM) has been a widely studied model since it can be motivated from PMSB. It has only four parameters at a high scale and one sign. The MSSM parameters at the electroweak scale are derived by renormalisation group equations. However, current experimental searches put the cMSSM under severe pressure [48].

A more generic choice is the phenomenological MSSM with 24 real parameters (pMSSM24). Herein, we have the following free parameters: M_1, M_2, and M_3 for the gaugino sector. μ, m_A, and $\tan(\beta)$ for the Higgs sector. $(\mathbf{a_u})_{33} = A_t$, $(\mathbf{a_d})_{33} = A_b$ and $(\mathbf{a_e})_{33} = A_\tau$ as trilinear couplings for the third generation, all other trilinear couplings are zero. The remaining 15 parameters are associated with the five sfermions in the supermultiplets per family, assuming diagonal matrices $\mathbf{m}^2_{\tilde{\mathbf{X}}}$.

After soft SUSY breaking and electroweak symmetry breaking, the electroweak partners of the electroweak gauge bosons and Higgs can mix to the so-called neutralinos and charginos. Since the lightest neutralino plays an important role in the following analysis, we describe the neutralino mixing in particular. The mass term in the Lagrangian can be given in the basis of $\psi_N = (\widetilde{B}, \widetilde{W}^0, \widetilde{H}^0_d, \widetilde{H}^0_u)$ as

$$\mathcal{L}^{\text{neutralino}}_m = -\frac{1}{2}\psi_N^T \mathbf{M_N} \psi_N + \text{h.c.}, \tag{2.61}$$

with the mass matrix being

$$\mathbf{M_N} = \begin{pmatrix} M_1 & 0 & -\frac{1}{\sqrt{2}}g' v_d & \frac{1}{\sqrt{2}}g' v_u \\ 0 & M_2 & \frac{1}{\sqrt{2}}g v_d & -\frac{1}{\sqrt{2}}g v_u \\ -\frac{1}{\sqrt{2}}g' v_d & \frac{1}{\sqrt{2}}g v_d & 0 & -\mu \\ \frac{1}{\sqrt{2}}g' v_u & -\frac{1}{\sqrt{2}}g v_u & -\mu & 0 \end{pmatrix}. \tag{2.62}$$

The mass eigenstates are derived by diagonalising $\mathbf{M_N}$ with an unitary transformation matrix $\mathcal{N}$:

$$\mathcal{N}^* \mathbf{M_N} \mathcal{N}^{-1} = \text{diag}(m_{\tilde{\chi}^0_1}, m_{\tilde{\chi}^0_2}, m_{\tilde{\chi}^0_3}, m_{\tilde{\chi}^0_4}), \tag{2.63}$$

$$\tilde{\chi}^0_i = (\mathcal{N})_{ij}\, \psi_{N,j}. \tag{2.64}$$

By definition, it holds $m_{\tilde{\chi}^0_1} \leqslant m_{\tilde{\chi}^0_2} \leqslant m_{\tilde{\chi}^0_3} \leqslant m_{\tilde{\chi}^0_4}$. Equation (2.64) gives the admixture of the gauginos and Higgsinos to the i^{th} neutralino. Depending on its main contribution, it is characterised as “bino”-like, “wino”-like or “Higgsino”-like.

The electrically charged gauge and Higgs bosons mix to the charginos. For a detailed derivation of all mixing matrices, the interested reader is referred to References [30, 36, 37, 47]. Table 2.5 finally summarises the gauge and mass eigenstates of the SUSY particles in the MSSM.

names	spin	gauge eigenstates	mass eigenstates
Higgs bosons	0	$H_u^0\ H_d^0\ H_u^+\ H_d^-$	$h^0\ H^0\ A^0\ H^\pm$
squarks	0	$\widetilde{u}_L\ \widetilde{u}_R\ \widetilde{d}_L\ \widetilde{d}_R$	(same)
		$\widetilde{s}_L\ \widetilde{s}_R\ \widetilde{c}_L\ \widetilde{c}_R$	(same)
		$\widetilde{t}_L\ \widetilde{t}_R\ \widetilde{b}_L\ \widetilde{b}_R$	$\widetilde{t}_1\ \widetilde{t}_2\ \widetilde{b}_1\ \widetilde{b}_2$
sleptons	0	$\widetilde{e}_L\ \widetilde{e}_R\ \widetilde{\nu}_e$	(same)
		$\widetilde{\mu}_L\ \widetilde{\mu}_R\ \widetilde{\nu}_\mu$	(same)
		$\widetilde{\tau}_L\ \widetilde{\tau}_R\ \widetilde{\nu}_\tau$	$\widetilde{\tau}_1\ \widetilde{\tau}_2\ \widetilde{\nu}_\tau$
neutralinos	1/2	$\widetilde{B}^0\ \ \widetilde{W}^0\ \ \widetilde{H}_u^0\ \ \widetilde{H}_d^0$	$\widetilde{\chi}_1^0\ \widetilde{\chi}_2^0\ \widetilde{\chi}_3^0\ \widetilde{\chi}_4^0$
charginos	1/2	$\widetilde{W}^\pm\ \ \widetilde{H}_u^+\ \ \widetilde{H}_d^-$	$\widetilde{\chi}_1^\pm\ \ \widetilde{\chi}_2^\pm$
gluino	1/2	$\widetilde{g}$	(same)

Table 2.5: Overview of the gauge and mass eigenstates of the SUSY particles in the MSSM. [30]

3 The International Linear Collider

After having described the general theoretical foundations of this thesis, in this chapter we focus on the International Linear Collider (ILC), which defines the experimental basis of the following studies. In Section 3.1, the fundamental principles of a linear lepton collider are discussed. Section 3.2 describes the key parameters of the ILC with respect to the achievable luminosity. A motivation for the usage of beam polarisation is given in the subsequent Section 3.3. In Section 3.4, the most important components of the ILC are outlined. Finally, Section 3.5 summarises the ILC physics case.

3.1 ILC Rudiments

The ILC is a future linear e^+e^- collider based on superconducting radio frequency (SCRF) acceleration technology. Its foreseen center-of-mass energy ranges from 200 GeV to 500 GeV, but also an upgrade to 1 TeV is considered.

In the following paragraphs, we outline some of the rudiments of the International Linear Collider.

3.1.1 History of the ILC

The ILC community is an international collaboration that has emerged from several regional linear collider projects, namely TESLA[1], JLC[2], and NLC[3]. The projects differed mainly in the proposed acceleration technology: for TESLA superconducting acceleration cavities were proposed, whereas the other two projects focused on normal conducting cavities. In September 2004, the International Committee for Future Accelerators (ICFA) recommended the TESLA technology as technology for a future joined international linear collider project [49]. Based on this decision, in

---

[1] TeV Energy Superconducting Linear Accelerator (international consortium based at DESY)

[2] Japanese Linear Collider (Asian)

[3] Next Linear Collider (American)

2005 the Global Design Effort (GDE) was issued in order to bring the different communities together and to work out a detailed technical design for the international linear collider ILC. In 2007, a first Reference Design Report of the ILC [50–53] was released and recently also the evolved Technical Design Report [3, 54–57] was published.

Besides the ILC project, there exists also the CLIC[4] project, mainly developed at CERN. This project relies on a completely different acceleration technology, based on a low energy, high intensity drive beam used for the excitation of the actual accelerating cavities. CLIC has proven the principle of this acceleration technique in a recently published Conceptual Design Report [58]. ILC and CLIC are both organised in the newly founded Linear Collider Community (LCC), which allows for synergies in the developments within the field of linear colliders.

3.1.2 Advantage of *Linear* Colliders

Already in the year 1964, M. Tigner suggested a linear collider approach as the possible way out of the circular collider dilemma [59]. Circular lepton colliders suffer from the large energy loss due to synchrotron radiation, which is proportional to

$$\Delta E \propto \frac{E_{\text{beam}}^4}{R \cdot m^4}, \tag{3.1}$$

where E_{beam} is the beam energy, R is the bending radius of the beam, and m describes the mass of the circulating particle. The small mass of an electron or positron leads to significant energy losses compared to circulating protons, for instance. In order to compensate for these energy losses, either the bending radius of the beam has to be enlarged or more accelerating modules are needed to be installed. However, both options are cost drivers: A cost optimisation shows that for a circular collider costs grow quadratically with the desired beam energy [60].

By contrast, no synchrotron radiation is present for a linear collider, due to $R \to \infty$. However, many acceleration modules have to be installed since the beam passes through the acceleration part only once. As the energy of a linear collider is linearly proportional to the length of the accelerator, the same is true for the costs.

Finally, it turns out that for beam energies beyond about 200 GeV, a linear collider is more cost efficient than a circular collider [60].

---

[4] Compact Linear Collider

collider	$\sqrt{s_{\max}}$	run time
DORIS	11 GeV	1973-1993
PETRA	50 GeV	1978-1986
SLC	100 GeV	1989-1998
LEP	200 GeV	1989-2000
ILC	500 GeV	?

Table 3.1: Overview of energy-frontier lepton colliders and their center-of-mass energy.

3.1.3 Experimental Features of *Lepton* Colliders

ILC lines up with the long and successful history of lepton colliders like DORIS, PETRA, SLC, and LEP. In the past, these colliders contributed significantly in understanding the fundamental mechanisms of physics. At PETRA, for example, the gluon was discovered [61–63], and at LEP and SLC very precise measurements of the Z boson [64] could finally establish the Standard Model of Particle Physics. Table 3.1 summarises different center-of-mass energies of the past energy-frontier lepton colliders and their run times.

During the last years, an extensive physics programme on hadron machines, like the TeVatron and the Large Hadron Collider (LHC), has been carried out. Hadron colliders profit from a large center-of-mass energy reach and are therefore naturally discovery machines. History has proven, that the interplay between lepton and hadron colliders is a fruitful way of addressing questions of modern particle physics. The top quark mass, for instance, has been predicted by LEP experiments only from their sensitivity to quantum corrections in the Z-boson production and at the TeVatron the top quark was finally discovered in the predicted range. However, in the light of the outstanding performance of the LHC, one might well ask why a new lepton collider like the ILC is necessary. Therefore, we want to outline some of the advantages of e^+-e^- collisions in comparison to hadron collisions in the following [3]:

Cleanliness. At LHC energies, the total proton-proton cross section amounts to $\sigma_{\text{tot}} \approx 100\,\text{mb}$. This results in about 30 proton-proton interaction per bunch crossing for the LHC8 beam parameters.
In comparison to that, the dominant source of background at the ILC arises from $\gamma\gamma$ collisions, which have a cross section lower by six orders of magnitudes. Despite of the large luminosity foreseen at the ILC, pile-up plays a subleading role and, thus, the events are usually much clearer. Furthermore, in the collision of elementary particles there are no beam remnants or multi-parton interactions.

Democracy. The total cross section at an hadron collider is completely dominated by soft, nonperturbative QCD processes. Only a small fraction of the total cross section can be attributed to high-momentum transfer processes which are of relevance for further analyses. Those processes are mainly induced by gluon scattering, where the gluon in principle couples equally to all quarks. However, due to the PDF of the proton, heavy particles, like heavy flavour quarks, but also possibly new coloured states, are suppressed in the production. Colour-neutral particles can only be produced in decays of heavy flavour quarks or via direct electroweak production, which has a cross section of several orders of magnitudes below strong production. This indicates that in proton-proton collisions a strong hierarchy of particle production exists. Advanced trigger systems are necessary in order to reduce the high event rates to a processible level and the choice of the trigger biases the recorded data set. Thus, unexpected new physics could in principle be missed.

By contrast, at a lepton collider, the coupling of the photon and Z boson to all particles is (if present at all) of the same order of magnitude and the production rates are mainly limited by the phase space of the reaction. Although the production cross sections are in general smaller than in strong production, there is not such a large hierarchy between Standard Model physics and possible BSM physics. Therefore, detectors at the ILC can be operated in continuous read-out and no trigger is necessary.

Calculability. All the cross sections calculate for the LHC rely on QCD and, therefore, suffer from uncertainties in the nonperturbative regime and parton density functions. Additionally, NLO corrections of QCD cross sections are usually in the order of $\mathcal{O}(30-50\%)$ (see e.g. [65] and references therein). Higher order corrections are very complex calculations especially for multi-parton final states. For this reason, such calculations are not available by default and it is very hard to reduce the theoretical uncertainties below a few percent.
In contrary, processes at the ILC are governed by electroweak production. First order corrections are easier to calculated and those corrections are usually already only at the percent level, which reduces the theoretical uncertainty on the predicted cross sections considerably. Furthermore, electroweak processes are fully perturbative and no uncertainties from PDFs enter. Due to the improved theoretical and experimental precision, also small quantum corrections to the cross section can be observed, which makes the ILC also sensitive to new physics, which is out of the direct kinematic reach of the collider.

Detail. In the collision of elementary particles, like electrons and positrons, the initial state of a reaction is very well defined. This allows for reconstructing all objects in the event on a full four-vector basis and, therefore, the full event topology is accessible. In turn, this makes it possible to improve the reconstruction significantly by using the full kinematic information for fits of reconstructed objects, for instance. Additionally, electron/positron beams can be highly polarised, which gives an excellent tool for studying spin-dependent effects of distinct processes. Therefore, a much more detailed picture of the reaction can be obtained.

3.2 Luminosity at a Linear Collider

The ILC has a specific beam structure: A sequence of N_b bunches form a so-called bunch train, where each bunch contains N particles. These bunch trains are produced with a repetition rate f_{rep}. In the standard ILC scheme, $f_{\text{rep}} = 5\,\text{Hz}$ is foreseen. Assuming Gaussian shaped bunches, the luminosity at the ILC can be described as

$$\mathcal{L} = \frac{N_b N^2 f_{\text{rep}}}{4\pi\sigma_x\sigma_y} H_D, \tag{3.2}$$

where $\sigma_{x,y}$ is the horizontal and vertical bunch size and H_D is an enhancement factor arising from the so-called pinch effect, which causes an additional focusing due to the electromagnetic field of the oppositely charged bunches. H_D depends mainly on the longitudinal bunch size and the focusing strength at the IP, but it is usually in the order of two [52]. The horizontal and vertical bunch size is connected to the corresponding beam emittance $\epsilon_{x,y}$

$$\sigma_{x,y} = \sqrt{\epsilon_{x,y}\beta_{x,y}}\,, \tag{3.3}$$

with $\beta_{x,y}$ being a measure for the focusing strength in the horizontal and vertical axis at the IP. The emittance represents the covered area of a beam in the phase space of the bunch angle and bunch position. It is a conserved quantity in a sequence of electromagnetic lenses. For an accelerated beam, the emittance times the Lorentz factor γ is conserved and, therefore, the emittance itself scales in this case with $1/\gamma$ as the beam energy rises. This effect is also know as adiabatic cooling [66]. In turn, this means that the luminosity intrinsically grows linearly with increasing center-of-mass energy.

A common way of expressing the luminosity at a linear collider makes use of the beam power $P_{\text{beams}} = N_b N f_{\text{rep}} E_{\text{cm}}$, which is proportional to the provided RF power P_{RF}:

$$\mathcal{L} = \frac{1}{4\pi E_{\text{cm}}} \eta_{\text{RF}} P_{\text{RF}} \frac{N}{\sigma_x\sigma_y} H_D \tag{3.4}$$

Herein, η_{RF} is the efficiency factor for transferring RF power into beam power. Usual values for η_{RF} are between $20 - 60\%$ [67]. This factor as well as the maximum RF power is strongly dependent on the chosen accelerator technology.

One important aspect at a linear collider is the energy loss right before the collision due to beamstrahlung, which occurs for strongly focused beams at the IP. The losses can easily become a few percent of the nominal beam energy [55]. The energy loss is proportional to [67]

$$\delta_{\mathrm{BS}} \propto \frac{E_{\mathrm{cm}}}{\sigma_z} \frac{N^2}{(\sigma_x + \sigma_y)^2}, \tag{3.5}$$

with σ_z being the longitudinal expansion of the bunch. Comparing Equations (3.4) and (3.5) shows that for a high luminosity $\sigma_x \sigma_y$ has to be minimised, whereas for small energy losses due to beamstrahlung $(\sigma_x + \sigma_y)$ has to be large. A way to reach both, is to use flat beams, where $\sigma_x \gg \sigma_y$ [66]. In this case, the horizontal bunch size σ_x sets the level of energy loss and the vertical bunch size σ_y has to be made as small as possible in order to reach high luminosities.

Finally, Equation (3.4) can be re-expressed in order to get the final scaling law [5]

$$\mathcal{L} \propto \frac{\eta_{\mathrm{RF}} P_{\mathrm{RF}}}{E_{\mathrm{cm}}} \sqrt{\frac{\delta_{\mathrm{BS}}}{\epsilon_y}} \sqrt{\frac{\sigma_z}{\beta_y}}, \tag{3.6}$$

which allows one to read off directly the requirements for an high luminosity linear collider: The used acceleration technique has to be able to cope with high RF power and especially needs to feature a large acceleration gradient, the efficiency of transferring the RF power onto the beam must be large, the beam needs to have a very small vertical emittance, and the beam needs to be strongly focused at the IP. Table 3.2 shows the beam parameters for the different staging options at the ILC [56]. The total power consumption of the ILC for $E_{\mathrm{cm}} = 500\,\mathrm{GeV}$ amounts to 166 MW, which is comparable to the power consumption of the LHC at CERN [68]. In order to achieve the very high luminosities in the order of $10^{34}\mathrm{cm}^{-2}\mathrm{s}^{-1}$, vertical bunch sizes of a few nanometers are necessary. All the requirements put strong demands on all individual accelerator components, for which an intensive R&D programme is ongoing.

The exact run plan of the ILC depends strongly on the situation of particle physics at the time ILC is ready. However, studies are usually carried out in the three defined staging scenarios of $E_{\mathrm{cm}} = 250\,\mathrm{GeV}, 500\,\mathrm{GeV}, 1\,\mathrm{TeV}$ with the corresponding integrated luminosities of $\int L dt = 250\,\mathrm{fb}^{-1}, 500\,\mathrm{fb}^{-1}, 1000\,\mathrm{fb}^{-1}$ [3]. Due to the intrinsic growth of the luminosity with the beam energy, all three stages correspond to equally long running periods.

3.3 Motivation for Polarised Beams

Some benefits of beam polarisation have already been mentioned. In this section, we focus on the role of beam polarisation in more detail. Thereby, we follow in parts the description in [69].

Center-of-mass energy	E_{cm}	GeV	250	500	1000
Number of bunches per train	N_b		1312	1312	2450
Bunch population	N	$\times 10^{10}$	2.00	2.00	1.74
Average total beam power	P_{beam}	MW	5.9	10.5	27.2
Estimated AC power	P_{AC}	MW	122	163	300
RMS bunch length	σ_z	μm	300	300	250
Electron RMS energy spread	$\Delta p/p$	%	0.190	0.124	0.083
Positron RMS energy spread	$\Delta p/p$	%	0.152	0.070	0.043
Horizontal emittance	$\gamma\epsilon_x$	μm	10	10	10
Vertical emittance	$\gamma\epsilon_y$	nm	35	35	35
IP horizontal beta function	β_x	mm	13.0	11.0	22.6
IP vertical beta function	β_y	mm	0.41	0.48	0.25
IP RMS horizontal bunch size	σ_x	nm	729.5	474.0	481.0
IP RMS vertical bunch size	σ_y	nm	7.7	5.9	2.8
Luminosity	$\mathcal{L}$	$\times 10^{34}\mathrm{cm}^{-2}\mathrm{s}^{-1}$	0.75	1.8	3.6
Average energy loss	δ_{BS}	%	0.97	4.5	5.6

Table 3.2: Excerpt of ILC beam parameters for different center-of-mass energy scenarios. Full beam parameter table can be found in [56].

At the ILC two different production modes are possible: s-channel annihilation or t/u-channel scattering. In the case of t/u-channel production (cf. Figure 3.1a), the chiralities of the incoming electron and positron do not couple directly to each other, but to an exchange particle. Due to the structure of the couplings of this particle to e^+/e^-, a preference for one specific beam polarisation can be introduced, which in turn, can be utilised in order to enhance or suppress processes. In t/u-channel scattering, in principle, all combinations of incoming particle helicities can contribute to the production cross section of a process.

For e^+/e^- annihilation (cf. Figure 3.1b), the helicities of the incoming particles couple directly to each other and, thus, determine the spin of the s-channel propagator. In the usual case of annihilation into vector bosons ($\gamma, Z \Rightarrow J_z = 1$), only the helicity combinations RL and LR give a contribution. The configurations LL and RR would need a scalar particle in the propagator. Since the coupling of the Higgs particle to e^+/e^- is very small, this production mode is negligible in the Standard Model. However, in new physics models also scalar particles could appear unsuppressed in the s-channel, like resonant sneutrino production in R-parity violating scenarios [70]. For this reason, also those “exotic” beam polarisation configurations are of interest.

Figure 3.2 illustrates the possible combinations of (longitudinal) electron and positron helicities for colliding particles. The last column in this table indicates the spin of the exchange particle in case of s-channel annihilation and makes clear that

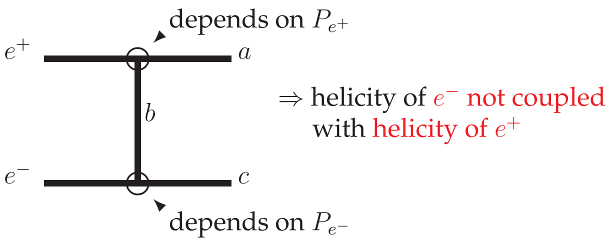

(a) t/u-channel production. The helicities of the incoming beams couple directly to the final state particles. Therefore, in principle, all polarisation configurations can contribute to t/u-channel production.

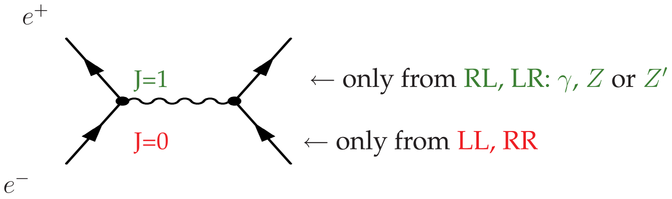

(b) s-channel production. The helicities of the incoming beams are directly coupled. In the Standard Model only the helicity combinations LR and RL give contributions. Annihilation into a Higgs particle is heavily suppressed and, thus, negligible for an e^+e^- collider.

Figure 3.1: Possible production modes at the ILC. Figures taken from [69].

only the RL and LR combinations allow for a vector boson exchange. Additionally, this table gives the weighting factors of each of the individual polarised cross sections to the effective cross section in the case of beam polarisation $(\mathcal{P}_{e^-}, \mathcal{P}_{e^+})$. Herein, $\mathcal{P}_{e^\pm}$ is the polarisation of the corresponding beam, which is defined as

$$\mathcal{P}_{e^\pm} = \frac{N^R_{e^\pm} - N^L_{e^\pm}}{N^R_{e^\pm} + N^L_{e^\pm}}, \tag{3.7}$$

where $N^{R,L}_{e^\pm}$ is the number of electrons/positrons with right/left helicity. Thus, the beam polarisation is the average helicity of an ensemble of individual particles within a beam.

For unpolarised beams all polarised cross sections enter with an equal weight of 1/4 in the effective cross section of a reaction. As soon as beams are polarised, the contributions are weighted according to the beam polarisation, which leads to

$$\begin{aligned} \sigma_{\mathcal{P}_{e^-},\mathcal{P}_{e^+}} = \frac{1}{4}\big(&(1+\mathcal{P}_{e^-})(1+\mathcal{P}_{e^+})\sigma_{RR} + (1-\mathcal{P}_{e^-})(1-\mathcal{P}_{e^+})\sigma_{LL} \\ &+ (1+\mathcal{P}_{e^-})(1-\mathcal{P}_{e^+})\sigma_{RL} + (1-\mathcal{P}_{e^-})(1+\mathcal{P}_{e^+})\sigma_{LR}\big). \end{aligned} \tag{3.8}$$

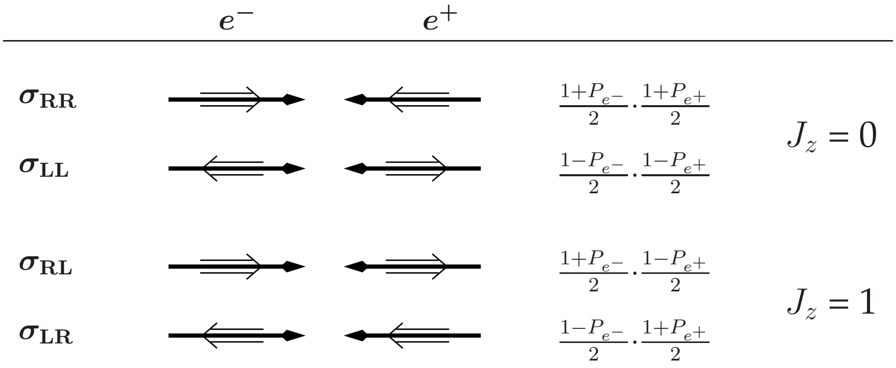

Figure 3.2: Possible helicity combinations of incoming particles for longitudinally polarised beams. The thick arrow depicts the direction of motion and the double arrow indicates the spin orientation of the particle. In the first column the corresponding symbol for the polarised cross section is given and in the fourth column the contribution of the polarised cross section to the total cross section in the case of beam polarisation $(\mathcal{P}_{e^-}, \mathcal{P}_{e^+})$ is indicated. The last column displays the resulting spin of a propagator in the case of s-channel production. Figure taken from [69].

Enhancement of signal processes and suppression of backgrounds is only one of many advantages of beam polarisation. Beam polarisation opens also a wide field of new observables, like all possible asymmetries between the different polarisation combinations of the colliding beams. This can be utilised in order to test the chiral structure of couplings, to determine quantum numbers, and to disentangle parameters in the usually very large parameter space of a new physics model. Especially for studying CP properties, beam polarisation helps to construct meaningful CP-sensitive observables.

In order to illustrate the effect of beam polarisation, we focus on the example of vector boson s-channel production in the following paragraphs. In this case, Equation (3.8) simplifies due to the absence of σ_{RR} and σ_{LL}. After some reformulations (see Reference [69]) we get

$$\sigma_{\mathcal{P}_{e^-},\mathcal{P}_{e^+}} = (1 - \mathcal{P}_{e^-}\mathcal{P}_{e^+})\sigma_0(1 - \mathcal{P}_{\text{eff}} A_{LR}), \tag{3.9}$$

with

$$\sigma_0 = \frac{\sigma_{LR} + \sigma_{RL}}{4}, \tag{3.10}$$

$$A_{LR} = \frac{\sigma_{LR} - \sigma_{RL}}{\sigma_{LR} + \sigma_{RL}}, \tag{3.11}$$

$$\mathcal{P}_{\text{eff}} = \frac{\mathcal{P}_{e^-} - \mathcal{P}_{e^+}}{1 - \mathcal{P}_{e^-}\mathcal{P}_{e^+}}. \tag{3.12}$$

Herein, σ_0 denotes the spin averaged cross section, A_{LR} is the left-right asymmetry of the process, and $\mathcal{P}_{\text{eff}}$ is the effective polarisation in the collision. σ_0 and A_{LR} are properties predicted by theory such that those quantities are interesting to determine. These two quantities can be accessed by performing cross-section measurements of the process with two different polarisation configurations of the beams. At this, between these two configurations, the beam helicity is usually reversed such that the absolute value stays the same, but the sign changes. We obtain [69]:

$$\sigma_{-+} = \frac{1}{4}\big((1 + |\mathcal{P}_{e^-}||\mathcal{P}_{e^+}|)(\sigma_{LR} + \sigma_{RL}) + (|\mathcal{P}_{e^-}| + |\mathcal{P}_{e^+}|)(\sigma_{LR} - \sigma_{RL})\big) \tag{3.13}$$

$$\sigma_{+-} = \frac{1}{4}\big((1 + |\mathcal{P}_{e^-}||\mathcal{P}_{e^+}|)(\sigma_{LR} + \sigma_{RL}) - (|\mathcal{P}_{e^-}| + |\mathcal{P}_{e^+}|)(\sigma_{LR} - \sigma_{RL})\big), \tag{3.14}$$

where “$+-$” indicates the sign of $\mathcal{P}_{e^-}$ and $\mathcal{P}_{e^+}$.

Thus, one can find

$$\sigma_0 = \frac{\sigma_{-+} + \sigma_{+-}}{2(1 + |\mathcal{P}_{e^+}||\mathcal{P}_{e^-}|)} = \frac{N_{-+} + N_{+-}}{2(1 + |\mathcal{P}_{e^+}||\mathcal{P}_{e^-}|) \cdot \int L\mathrm{d}t} \tag{3.15}$$

$$A_{LR} = \frac{1}{\mathcal{P}_{\text{eff}}}\frac{\sigma_{-+} - \sigma_{+-}}{\sigma_{-+} + \sigma_{+-}} = \frac{1}{\mathcal{P}_{\text{eff}}}\frac{N_{-+} - N_{+-}}{N_{-+} + N_{+-}}, \tag{3.16}$$

with N being the number of observed events for the corresponding beam configuration.

Considering Equations (3.15) and (3.16) allows us to draw an important conclusion: In order to determine the cross section of the process and the left-right asymmetry, the beam polarisations of both beams have to be known precisely since this quantity directly enters into the determination of σ_0 and A_{LR}. The beam polarisation $\mathcal{P}_{e^\pm}$ becomes therefore a measurement quantity, which is as important as the beam energy or luminosity, for instance.

Although already one polarised beam would be enough for determining A_{LR}, from error propagation of the uncertainties of the single beam polarisations $\delta\mathcal{P}_{e^\pm}$ in $\mathcal{P}_{\text{eff}}$ (see Equation (3.12)) it becomes clear that $\delta\mathcal{P}_{\text{eff}}/\mathcal{P}_{\text{eff}}$ reduces significantly if both beams are polarised. A 60% polarised positron beam in addition to an 80% polarised electron beam, for instance, reduces the relative uncertainty of $\mathcal{P}_{\text{eff}}$ by a factor of 3 compared to an unpolarised positron beam [69]. For this reason, also a highly polarised positron beam is very important in order to exploit the opportunities of beam polarisation at the ILC the best.

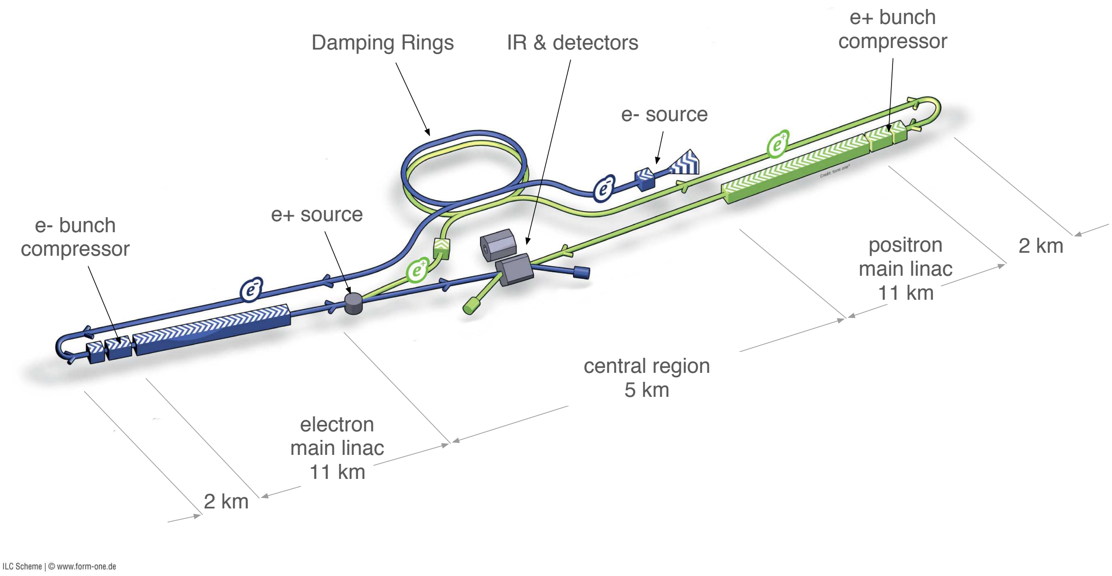

Figure 3.3: Schematic drawing of the ILC including all subsystems. Figure taken from [54].

3.4 ILC Components

Figure 3.3 shows a schematic overview of the ILC with the most important subcomponents. The following sections will describe the main subsystems of the ILC as they are defined in the ILC TDR [56].

3.4.1 Polarised Sources

The electron source consists of a strained GaAs target, which is illuminated by a laser. The chosen material for the photocathode emits naturally 85% polarised electrons with a quantum efficiency of about 0.5%. This meets the ILC baseline design criterion of at least 80% electron beam polarisation. In order to match the band gap in GaAs, the wavelength of the laser has to be $\lambda = 790\,\mathrm{nm}$, which suggests Ti:sapphire for the laser system. In the end of the polarised electron gun, electrons have an energy of 200 keV. The electron gun is followed by a buncher, forming the ILC specific bunch structure, as well as several pre-accelerator.

Polarised positrons are considerably more difficult to acquire in the needed intensity than polarised electrons. Figure 3.4 shows a schematic drawing of the polarised positron source. The fully accelerated electron beam at the end of the main linac[5]

---

[5] linear accelerator

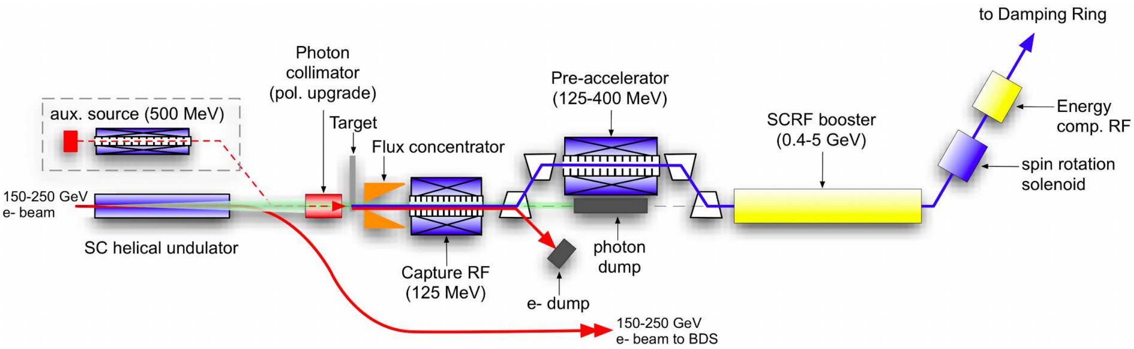

Figure 3.4: Schematic drawing of the positron source at the ILC. Figure taken from [56].

is guided through an about 150 m long helical undulator in order to produce photons, which are shot on a target. The created electron-positron pairs are afterwards coupled into RF cavities, which are located in a solenoid field in order to focus the beam. In a dipole chicane, photons, electrons and positrons are separated, where the first two are dumped and the positrons are further accelerated.

The helical windings of the undulator cause the production of circular polarised photons, which in turn create longitudinally polarised electrons and positrons in the target. In order to reach the foreseen positron beam currents, photon intensity and energy have to be large enough. In the ILC250 staging scenario, the electron beam energy is not sufficient. However, with the extension of the undulator to 231 m and a modification of the flux concentrator, the necessary positron gain can be recovered also for a 125 GeV electron beam [71].

In the baseline design, a positron polarisation of 30% can be reached. An optional upgrade allows for a beam polarisation of up to 60%. The most challenging part of the positron source is the target design. The target has to be very thin ($1.4\,\mathrm{cm} \cong 0.4X_0$) and has to cope with an enormous heat load. Therefore, the current design foresees a spinning wheel with a diameter of 1 m made of titanium alloy.

In addition to the polarised positron source, an unpolarised, low intensity positron source is present, which allows for commissioning runs of the positron beamline also in absence of the electron beam.

Both produced beams, the electron beam and positron beam, leave the source with an energy of 5 GeV. However, at this stage the beam emittance is still much to large and needs to be reduced in the next step. In order to preserve the achieved polarisation of the beams, the beam polarisation vector is rotated from the longitudinal into the vertical beam axis by a spin rotator.

3.4.2 Damping Rings

The damping rings are essential for the performance of the ILC. There exists one damping ring per beam optimised for 5 GeV positron and electron beams and hosted in the same tunnel. As outlined before, only a very small beam emittance allows for the envisaged luminosity goals at the ILC. The damping rings are designed in such a way to reduce the vertical normalised emittance by five order of magnitudes to the targeted 20 nm within only 200 ms. In order to fit a whole bunch train into the 3.2 km damping ring, the pulse has to be compressed by a factor of nine. For the damping, a superferric wiggler of the length of 100 m featuring a peak-field of 2.16 T is installed per beam. The wiggler causes undirected radiation of energy, whereas an RF module accelerates the beam only in beam direction. Thus, the entropy and emittance of the beam is reduced.

The most important effects, which limit the beam emittance, are the fast ion instability (FII) in the case of the electron beam and the electron cloud effect (EC) for the positron beam.
FII denotes the influence of ions created in the collision of the beam with a gas molecule, which then stays in the beam path and affects the following bunches. To minimise this effect, a very low vacuum pressure of 1×10^{-7} Pa is essential.
The EC effect is caused by synchrotron-radiation photons which hit out electrons from the vacuum-pipe walls. Those electrons are then attracted by the positron beam and can lead to a significant disturbance of the electromagnetic field in the bunches, which results in a growing beam emittance. Mitigation methods have been studied, which foresee special coatings of the vacuum pipe wall in order to reduce the EC effect [72].

The damped, low-emittance beams are finally extracted from the damping rings, decompressed again and, still at $E_{\mathrm{beam}} = 5\,\mathrm{GeV}$, transferred for almost 15 km to the beginning of the main linacs.

3.4.3 Main Linacs

After another pre-acceleration from 5 GeV to 15 GeV and bunch compression, the main linacs accelerate the electrons and positrons to a final beam energy of at maximum 250 GeV. Each main linac consists of about 7400 nine-cell niobium cavities (see Figure 3.5) operated at a radio frequency of 1.3 GHz. The cavities are cooled down to a temperature of two Kelvin. At this temperature, niobium becomes superconducting, which allows for a very large effective electric field gradient of up to 31.5 MeV/m. The superconducting technology also leads to an impressive quality factor of the resonator of

$$Q = 2\pi \frac{\text{stored energy}}{\text{lost energy per osciallation periode}} \geqslant 10^{10}. \tag{3.17}$$

Figure 3.5: Nine-cell niobium cavity. About 7400 of these cavities per beam accelerate the electrons and positrons to an energy of up to 250 GeV. Figure taken from [55].

In order to compensate for mechanical deformations originating from the cooling of the material and the strong forces introduced by the RF pulses, a system of mechanical tuners is foreseen. During the last years, intensive R&D has gone into the improvement of the acceleration gradient and the high quality fabrication of the cavities on a large scale. The cavities are embedded in 12.65 m long cryomodules cooled in a liquid helium II bath. Helium in this phase is suprafluid and has a very large heat conductance.

The ILC can greatly benefit from the experience made at FLASH and the European X-ray Free Electron Laser (XFEL), which both are equipped with the same acceleration technology.

3.4.4 Beam Delivery System

The final part of the ILC is the 3.5 km long beam delivery system (BDS). Figure 3.6 shows the design of the electron BDS upstream of the IP. Herein, the vertical axis is considerably zoomed compared to the longitudinal axis such that the deflection angle of the beams due to vertical offsets appear much larger in the figure than they actually are. The black and red vertical lines along the beam line indicate dipole and quadrupole magnets. The undulator at around $x = 500\,\mathrm{m}$ produces the photons for the positron source (see Section 3.4.1). In the so-called dogleg, the electron beam is offset by 1.5 m in order to have enough space for the positron target.

The BDS is equipped with diverse diagnostics tools for beam emittance, beam position, beam energy and beam polarisation. For the beam size measurement, a laser wire system is planned, where four laser beams scan the beam pipe in horizontal and vertical direction. If the laser beam enters the electron beam, Compton-scattered photons are detectable downstream. The system is capable to measure the beam spot size to a precision of $1\,\mu$m. Behind the laser wire chicane a Compton polarimeter is located in which the beam polarisation is measured from the polarisation dependent interaction of the electrons/positrons in the beam with a polarised laser. The envisaged precision of the polarisation measurements amounts to $\Delta\mathcal{P}/\mathcal{P} = 0.25\%$. A detailed description of the measurement principle and the ILC polarimeters is given

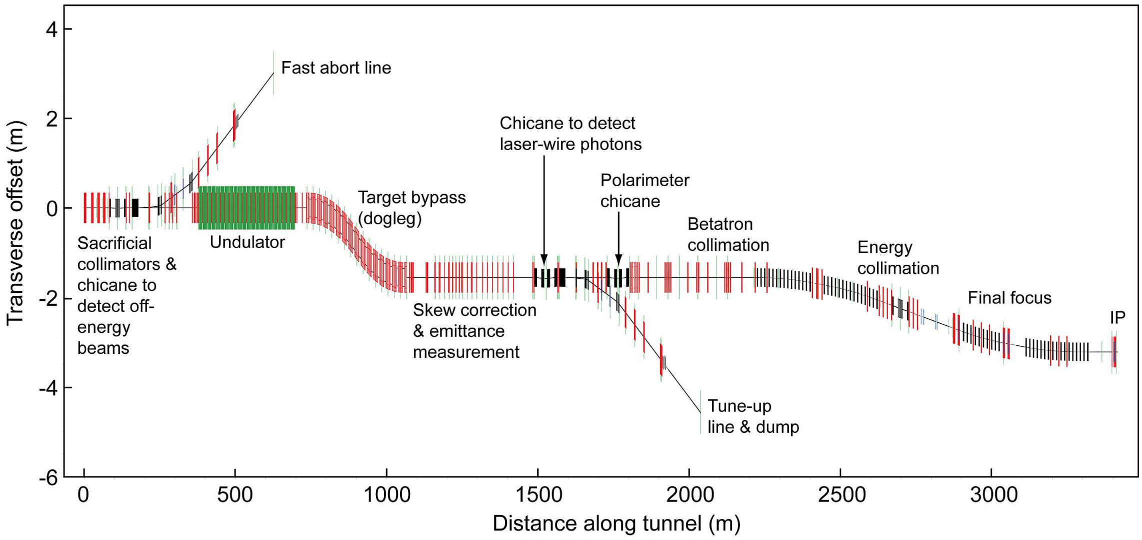

Figure 3.6: Overview of the electron beam delivery system up to the interaction point (IP). Note the different scales of the x- and y-axis. Figure taken from [56].

in Chapter 8. The BDS also contains a system of collimators, which are necessary in order to reduce the beam background at the IP.

The last 500 m before the IP are dedicated to the final-focus system, which focuses the beams to the final beam size of a few nanometers. Therefore, it puts very strong requirements on the alignment of the different magnets of down to some tens of nanometers. In order to ensure stable beam collisions, a fast intra-train alignment correction system is inevitable. The final focus system comprises also sextupoles for correcting for the chromatic aberrations of the system of electromagnetic lenses. Finally, the beams collide at the IP with a crossing angle of 14 mrad, which leaves enough space for two separate extraction lines for the spent beams. However, this crossing angle makes crab cavities necessary, which rotate the colliding bunches by 7 mrad each in order to achieve head-on collisions of the bunches and, thus, restore the luminosity.

The extraction line downstream of the IP is not displayed in Figure 3.6. In contrast to a circular collider, the bunches are very disrupted after the collision because of the strong focusing. Therefore, the beam optics in the extraction lines have to be designed in a way to be able to collect these highly disrupted bunches and guide them to the final beam dumps. Between the IP and the beam dump a second energy spectrometer as well as a second polarimeter are located (cf. Figure 8.4b). This additional downstream instrumentation is necessary in order to obtain information about the collision process. The beam dumps consist of 11 m long, high pressure water targets, which are capable to absorb a power of 18 MW. At this, the main beam dumps are already dimensioned for the 1 TeV ILC upgrade.

Energy [GeV]	Process	Physics Goal
91	$e^+e^- \to Z$	ultra-precision electroweak
160	$e^+e^- \to WW$	ultra-precision W-boson mass
250	$e^+e^- \to ZH$	precision Higgs coupling
350 – 400	$e^+e^- \to t\bar{t}$	top quark mass and couplings
	$e^+e^- \to WW$	precision W-boson couplings
	$e^+e^- \to \nu\bar{\nu}H$	precision Higgs couplings
500	$e^+e^- \to f\bar{f}$	precision search for Z'
	$e^+e^- \to t\bar{t}H$	Higgs coupling to top
	$e^+e^- \to ZHH$	Higgs self-coupling
	$e^+e^- \to \tilde{\chi}\tilde{\chi}$	search for SUSY
	$e^+e^- \to AH, H^+H^-$	search for extended Higgs states
700 – 1000	$e^+e^- \to \nu\bar{\nu}H$	Higgs self-coupling
	$e^+e^- \to \nu\bar{\nu}VV$	composite Higgs sector
	$e^+e^- \to \nu\bar{\nu}t\bar{t}$	composite Higgs and top
	$e^+e^- \to \tilde{t}\tilde{t}^*$	search for SUSY

Table 3.3: Processes to be studied at the ILC at different center-of-mass energies. The ILC offers not only the chance to perform high-precision measurements, but also allows for discoveries of physics beyond the Standard Model. Table taken from [3].

3.5 ILC Physics Case

The physics program at the ILC is clearly focused on precision measurements. Table 3.3 summarises the most relevant processes, which can be studied at different center-of-mass energies at the ILC. In the following, we are going to discuss a selection of those. An extensive summary on the ILC physics case can be found in the Physics Volume of the ILC Technical Design Report [3].

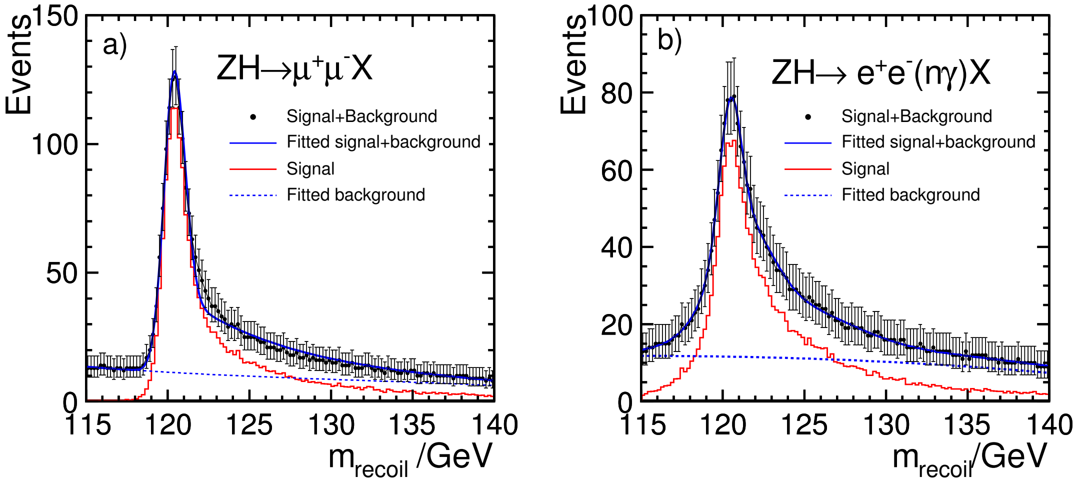

Figure 3.7: Reconstructed recoil mass in the leptonic decay channels of the Z boson for a simulated Higgs-boson mass of $m_H = 120\,\text{GeV}$. In the e^+e^-X channel, energy losses of the electrons due to bremsstrahlungs photons are recovered in the analysis, which leads to a higher selection efficiency, but reduces the resolution. Figures taken from [3].

3.5.1 Higgs Physics

After the discovery of the Higgs boson, one of the main physics goals at the ILC is the measurement of the properties of this new boson to any possible precision in order to establish a complete and distinct picture of electroweak symmetry breaking. At a lepton collider there exist two main Higgs production channels: Higgsstrahlung $e^+e^- \to ZH$ dominates for center-of-mass energies below 450 GeV, whereas W-boson fusion $e^+e^- \to \nu\overline{\nu}H$ becomes important for higher energies.

In the case of Higgsstrahlung production, the mass of the Higgs boson is determined by reconstructing the recoil mass from the decay products of the Z boson. Hereby, the leptonic decay modes of the Z boson are expected to give the most precise reconstruction (see Figure 3.7) [73]. This approach allows for model-independent Higgs studies, since no further assumptions on the Higgs couplings and decays have to be made. For this reason, this method is also sensitive to invisible decay modes of the Higgs boson and, thus, at the ILC the *inclusive* cross section $e^+e^- \to ZH$ can be measured directly and model-independently. A combination of the possible measurements at the ILC allows one to determine the total width of the Higgs boson to a final accuracy of 1.1% [74]. The possible precision of the measurement of the Higgs-boson couplings to Standard Model particles on the sub-percent level is sufficient to discriminate between scenarios of a Standard Model Higgs boson and a Higgs boson of theories with more than one Higgs doublet as in the MSSM [75], for instance.

One of the most important measurements at the ILC is the determination of the (cubic) Higgs self-coupling, which is even in the clean environment of e^+-e^- collisions extremely challenging due to the very small cross section of the processes $e^+e^- \rightarrow ZHH$ and $e^+e^- \rightarrow \nu\overline{\nu}HH$ of below 1 fb. Recent studies show that for the full ILC data set, including the 1 TeV upgrade, the precision reaches $\mathcal{O}(10\%)$ [74].

3.5.2 Top Physics

The top quark plays a special role in the Standard Model. It is the heaviest known elementary particle and, thus, it is the particle which couples the strongest to the Higgs boson. For this reason, loop contributions of the top quark enter in the Higgs sector most strongly. This makes the top quark mass to a very important parameter, not only for the Standard Model, but in particular also for the understanding of electroweak symmetry breaking. The top quark mass together with the Higgs mass determines, for instance, the vacuum stability of the universe [76].

At hadron colliders, it is very difficult to relate the top mass measurement directly to a theoretically well defined quantity and, thus, the precision suffers from undefined theoretical uncertainties. At the ILC, however, the threshold behaviour of $t\bar{t}$ production at $\sqrt{s} \approx 350\,\mathrm{GeV}$ can be analysed in order to extract the so-called $1s$-mass (see Figure 3.8), which can for instance be translated into the top $\overline{MS}$-mass, which is commonly used as theory input. With this technique, a precision of the top mass measurement of $\delta m_t = 100\,\mathrm{MeV}$ is achievable including systematic *and* theoretical uncertainties [77].

Top physics stays interesting beyond the $t\bar{t}$ threshold energy, as the top quark mass can also be measured in the continuum at higher energies with comparable statistical uncertainties. However, in this case, the theoretical uncertainties are not well defined.

Moreover, the ILC also offers a very clean environment for studying forward-backward asymmetries of $t\bar{t}$ production [78]. Due to the high beam polarisation foreseen at the ILC, also the measurement of the left-right asymmetry of $t\bar{t}$ production is accessible. The large Yukawa coupling of the top quark makes it also a very well suited probe for physics beyond the Standard Model.

As a last point to mention here, the coupling of the top quark to the Higgs boson can be investigated in the process $e^+e^- \rightarrow t\bar{t}H$, which is possible for center-of-mass energies beyond 500 GeV. For $\sqrt{s} = 1\,\mathrm{TeV}$ and $\int L dt = 1000\,\mathrm{fb}^{-1}$ the statistical uncertainty of the measurement of the top Yukawa coupling reaches 3.7% [3].

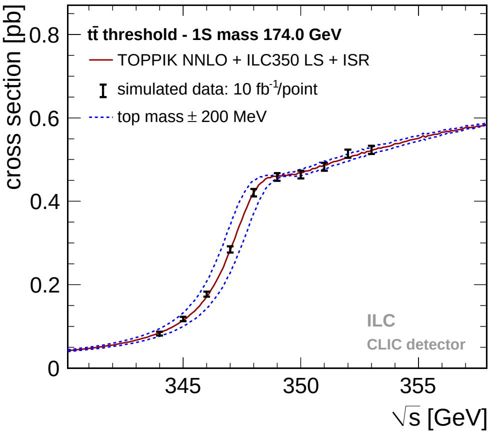

Figure 3.8: Threshold scan of $t\bar{t}$ production. The blue dashed line shows the change in the theory prediction of the threshold behaviour for a changed input top mass by $\pm 200\,\mathrm{MeV}$. A comparison with the error bars of the data points show that theses differences are well resolvable. For the whole scan, a data sample of $\int L dt = 100\,\mathrm{fb}^{-1}$ was assumed. Figure taken from [77].

3.5.3 Beyond Standard Model Physics

If the production of new particles is in the kinematic reach of the ILC, they can be examined with great precision. Thereby, not only production cross sections and masses can be measured on the percent level, but also CP phases [79] or mixing angles [80] are accessible at the ILC, for instance.

Discussing BSM physics, it should be pointed out that the ILC is not only a precision machine, but it also has its own discovery reach. Especially searches for new colour-singlet particles are difficult to carry out at an hadron collider, like the LHC, and several loopholes in the searches can only be closed by a lepton collider. SUSY scenarios which feature a light Higgsino LSP, for instance, can be overlooked at the LHC due to the very soft decay of the next to lightest SUSY particle, which is usually almost mass degenerate with the LSP. However, in the clean environment of the ILC such scenarios are still well observable [81].

We will investigate an R-parity violating SUSY scenario at the ILC in the following study.

4 *R*-Parity Violation and the Connection to Neutrinos

Neutrino oscillations belong to one of the unsolved questions of the Standard Model. In this chapter, we address the question of how neutrino physics can be incorporated in the Standard Model. We start the discussion with an outline of the phenomenology of neutrino oscillations in Section 4.1. Herein, we also discuss the most important neutrino experiments and global neutrino parameter analyses. In Section 4.2, we introduce supersymmetry with bilinearly broken R parity as a theoretical framework, which can describe the neutrino phenomenology. Furthermore, it is a model which can be tested at collider experiments. Therefore, in Section 4.3, we briefly review the status of RPV SUSY searches at the LHC. Finally, we define a benchmark scenario for the ILC study in Section 4.4.

4.1 Neutrino Phenomenology

Although the mechanism behind neutrino mass generation is unknown, neutrino oscillations can be phenomenologically described and the oscillation parameters can be measured, as it will be introduced in this section.

4.1.1 Neutrino Oscillations

A first evidence for neutrino oscillations has been observed in the famous Homestake experiment by Raymond Davis in the 1960s. This radiochemical experiment detected the charged current process

$$\nu_e + {}^{37}\mathrm{Cl} \rightarrow {}^{37}\mathrm{Ar}^{+} + e^{-}. \tag{4.1}$$

The measured electron neutrino flux in the Homestake Gold Mine was considerably reduced compared to the predicted solar electron neutrino flux [82, 83]. This has been known as the “solar neutrino problem”. For more than 30 years this problem kept unsolved, but after many other neutrino experiments it is taken for granted that neutrino oscillations are the reason for the observed deficit (see [5] and references therein).

The presence of oscillations are a direct evidence for nonzero neutrino masses and they arise from the fact that neutrino flavour eigenstates $|\nu_\alpha\rangle$ are not equal to the mass eigenstates $|\nu_i\rangle$. In the case of three neutrino generations, α represents the three flavour states $\{e, \mu, \tau\}$ and i denotes the three mass states $\{1, 2, 3\}$. A unitary transformation $\mathbf{U}$ rotates the two eigensystems into each other:

$$|\nu_\alpha\rangle = \sum_{i=1}^{3} \mathbf{U}_{\alpha,i} |\nu_i\rangle \tag{4.2}$$

Since neutrinos only interact weakly, they are produced in a pure flavour eigenstate. For the propagation in space-time, however, the mass eigenstates are relevant, which evolve with the Hamilton operator:

$$|\nu_i(x_\mu)\rangle = \mathrm{e}^{-i(\hat{P}^\mu x_\mu)} |\nu_i(0)\rangle \tag{4.3}$$

$$\tag{4.4}$$

The produced pure flavour eigenstate propagates therefore in space-time like

$$|\nu_\alpha(x_\mu)\rangle = \sum_{i=1}^{3} \mathbf{U}_{\alpha,i} \mathrm{e}^{-i(P_i^\mu x_\mu)} |\nu_i\rangle , \tag{4.5}$$

where P_i^μ is the four-vector of $|\nu_i\rangle$. If the different mass eigenstates have a different mass, it follows that $P_i \neq P_j$ and, therefore, the different mass eigenstates propagate with a different phase leading to the oscillation phenomena. The detection of the neutrino at the space-time point $x_\mu = (T, L)_\mu$ (at time T after the production and in a distance L) takes place again via a weak interaction and, therefore, the present admixture of a specific flavour in the mass eigenstate is projected out by the measurement

$$\langle \nu_{\alpha'}| = \sum_{j=1}^{3} \mathbf{U}^*_{j,\alpha'} \langle \nu_j| . \tag{4.6}$$

Making use of the orthogonality of the mass eigenstates, the probability, which is the squared transition matrix element, can be expressed as [84]

$$\mathcal{P}(\nu_\alpha \to \nu_{\alpha'}) = |\langle \nu_{\alpha'}|\nu_\alpha(x_\mu)\rangle|^2 = \left| \sum_i \mathbf{U}_{\alpha,i} \mathbf{U}^*_{i,\alpha'} \mathrm{e}^{-i(E_i T - p_i L)} \right|^2 \tag{4.7}$$

$$= \delta_{\alpha\alpha'} + 2\mathrm{Re} \left(\sum_{j>i} \mathbf{U}_{\alpha,i} \mathbf{U}^*_{\alpha,j} \mathbf{U}^*_{\alpha',i} \mathbf{U}_{\alpha',j} \left(1 - \mathrm{e}^{-i\Delta_{ij}}\right) \right) , \tag{4.8}$$

with

$$\Delta_{ij} = (E_i - E_j)T - (p_i - p_j)L \cong \frac{m_i^2 - m_j^2}{2E} T \cong \frac{\Delta m_{ij}^2 L}{2E} \tag{4.9}$$

for neutrinos traveling approximately at the speed of light and $\delta_{\alpha\alpha'} = 1$ for $\alpha = \alpha'$. Equation (4.8) makes clear that only due to the mass difference Δm_{ij} between the mass eigenstates, neutrino oscillations can occur. It also shows that neutrino oscillation experiments are only sensitive to mass differences and not to absolute mass scales. Δ_{ij} describes the phase difference of the mass eigenstate propagation. It is dependent on the neutrino energy, the distance from the production vertex and the actual mass difference between the neutrino mass eigenstates. Given a specific neutrino energy (defined by the production mechanism), the sensitivity of an experiment on neutrino oscillations is influenced by the choice of the distance to the source.

Restricting ourselves to three neutrino generations, the matrix $\mathbf{U}$ is also known as PMNS matrix[1]. As a unitary matrix, it can be described by three Euler angles θ_{12}, θ_{23}, θ_{13}, one Dirac CP phase δ and two Majorana CP phases α_1, α_2. The Majorana phases appear in addition to the Dirac phase, if neutrinos are Majorana particles. However, they do not influence the neutrino oscillation phenomena and, therefore, oscillation experiments are not sensitive to them. In addition to the PMNS matrix, the oscillations are determined by two mass squared differences Δm_{21}^2 and Δm_{31}^2. There are in principle two scenarios for the absolute neutrino masses: in the normal hierarchy ν_1 is the lightest neutrino, whereas in the inverted hierarchy ν_3 is the lightest one.

Because $0 < \Delta m_{21}^2 < |\Delta m_{31}^2|$ and $|\mathbf{U}_{e,3}|^2 = |\sin(\theta_{13})|^2 \ll 1$ [5], the rather complicated oscillation formulae can be approximately decoupled and the parameters Δm_{21}^2 and θ_{21} describe the solar ν_e oscillation, whereas Δm_{31}^2 and θ_{23} are predominantly responsible for atmospheric ν_μ and $\overline{\nu}_\mu$ oscillations. For this reason, the corresponding mass squared differences and neutrino mixing angles are often denoted as

$$\theta_\odot = \theta_{12} \qquad \delta m^2 = \Delta m_\odot^2 = \Delta m_{21}^2 \tag{4.10}$$

$$\theta_{\text{atm}} = \theta_{23} \qquad \Delta m^2 = \Delta m_{\text{atm}}^2 = \Delta m_{31}^2. \tag{4.11}$$

4.1.2 Neutrino Experiments

Many experiments exist measuring neutrino oscillation parameters. In principle, one can distinguish between two types of measurements: Firstly, disappearance measurements, which detect the same neutrino flavour as the neutrino source provides. In this way, the survival probability of the neutrino flavour $\mathcal{P}(\nu_\alpha \to \nu_\alpha)$ as well as

---

[1] Pontecorvo–Maki–Nakagawa–Sakata matrix

the disappearance of the specific flavour into other flavours is accessible. In order to perform such experiments, the neutrino flux of the source has to be known very precisely or two detectors (near and far) are needed for comparing two measured fluxes. Secondly, appearance experiments measure the appearance of other neutrino flavours with respect to the neutrino source.

For studying neutrino oscillations, many different neutrino sources can be exploited. The most famous source, namely the sun, has already been mentioned. Solar neutrino observation has a long-standing history. Current experiments, which are optimised for solar neutrino observation are Borexino [85] or SNO [86], for instance. SNO was the first experiment that could perform flavour dependent neutrino detection. The charged current reaction is only sensitive to electron neutrinos, whereas the neutral current reaction is sensitive to all neutrino flavours. Therefore, the solar neutrino disappearance into other flavours could be proven for the first time by the comparison of the two measured fluxes [87]. The solar neutrino experiments give important input in the determination of the solar mixing angle θ_{12}.

In order to study δm^2, Equation (4.9) suggests a large distance to the neutrino source as well as small neutrino energies. Therefore, a long-baseline (LBL) experiment looking for reactor neutrinos is favourable. KamLAND [88] is such an experiment, which makes important contributions to the determination of δm^2.

Another important source for neutrinos are atmospheric neutrinos, which get produced in the interaction of high energetic cosmic rays with the atmosphere. In order to disentangle possible background, it is important to measure the angular distribution of the incident neutrino flux. Super-Kamiokande is able to measure the neutrino flux in dependence of the zenith angle and it could prove the angular dependent disappearance of muon neutrinos [89]. This is well consistent with $\nu_\mu \leftrightarrow \nu_\tau$ oscillations. Therefore, measurements by Super-Kamiokande contribute significantly to the determination of θ_{23}. Due to the large distance of the neutrino source ($L \approx 10000\,\text{km}$) and the rather large neutrino energy ($E = 1 - 10\,\text{GeV}$), atmospheric neutrino experiments are sensitive to $\Delta m^2 = 10^{-3} - 10^{-4}\,\text{eV}^2$.

Another possibility to study comparable parts of the neutrino oscillation parameter space are offered by long-baseline experiments, where the neutrinos are produced by a high energy proton beam shot on a target. Those experiments are less sensitive ($L = \mathcal{O}(100\,\text{km})$, $E = \mathcal{O}(1\,\text{GeV}) \Rightarrow \Delta m^2 > 2 \cdot 10^{-3}\,\text{eV}^2$), however, they profit from a much better knowledge of the neutrino energy spectrum as well as the distance between the source and the detector. Several such accelerator-based long-baseline disappearance experiments were and are operating, like K2K [90], MINOS [91], and T2K [92]. They mainly constrain the large mass squared difference Δm^2. Although all the results of the disappearance experiments are consistent with $\nu_\mu \leftrightarrow \nu_\tau$ oscillations, they are not sensitive for the ν_τ appearance. However, the long-baseline experiment OPERA [93] is dedicated to this question. The experiment is placed in the Gran Sasso underground laboratory and is designed to detect tau neutrinos in the appearance channel of the muon neutrino beam created at CERN. Up to now, two tau neutrino candidates have been observed with an expected number of signal events of 1.53 ± 0.16 and 0.18 ± 0.02 background events indicating the existence of $\nu_\mu \leftrightarrow \nu_\tau$ oscillations. The absence can be excluded at 2.40σ [94].

For a long time it was not clear, whether the last remaining neutrino mixing angle θ_{13} is unequal to zero. Recently, in short-baseline (SBL) reactor experiments like Double Chooz, Daya Bay, or RENO, θ_{13} could be measured to be nonzero in the disappearance channel of electron antineutrinos [95–97]. This year, the T2K collaboration reported the first observation of electron neutrino appearance in a muon neutrino beam, which confirms $\theta_{13} \neq 0$ on a significance level of 7.3σ [98].

4.1.3 Global Neutrino Parameters

As outlined in the last sections, the many different neutrino experiments are sensitive to very different parts of the 3ν oscillation parameter space. For this reason, it is very favourable to combine the present data and perform a global analysis of the oscillation parameters [99–101]. It should be noted that the three flavour neutrino oscillation model is the minimal model, which can describe all the present neutrino data [5].

In Figure 4.1, the results of the global fit carried out in Reference [99] are depicted. Neutrino data by all the different introduced experiments went into the fit as available after *Neutrino 2012* conference[2]. The six subfigures show the six parameters of the three flavour neutrino oscillation model for normal (blue solid line) and inverted (red dashed line) hierarchy. On the y-axis of the subfigures, the distance of the parameter point to the best fit point is given in numbers of standard deviations. The location of the dip down to zero indicates therefore the best fit point. The more linear and symmetric the curves are, the better the parameter uncertainty is described by a Gaussian [99]. We observe that all parameters are constrained rather well, except for the CP phase δ, where no constraints exist above the 2σ level. For the parameter $\sin^2(\theta_{23})$, a second dip is visible, which reflects the degeneracy of this mixing angle between the first ($0 < \theta_{23} < \pi/4$) and second ($\pi/4 < \theta_{23} < \pi/2$) octant. Although in this fit the first octant is slightly preferred, this bias is not very significant and comparisons with other global analyses [100, 101] show even smaller biased results towards the first octant. Table 4.1 gives the numerical values for the best fit point as well as the 1σ range in case of the normal hierarchy.

---

[2] During writing of this thesis an update of Reference [99] has been published, which includes the 2013 results of the reactor experiments Daya Bay and RENO, as well as the new results of the LBL accelerator experiments T2K and MINOS [102]. For the interpretation of the results of the performed ILC study in this thesis, we still refer to the results quoted in Reference [99]

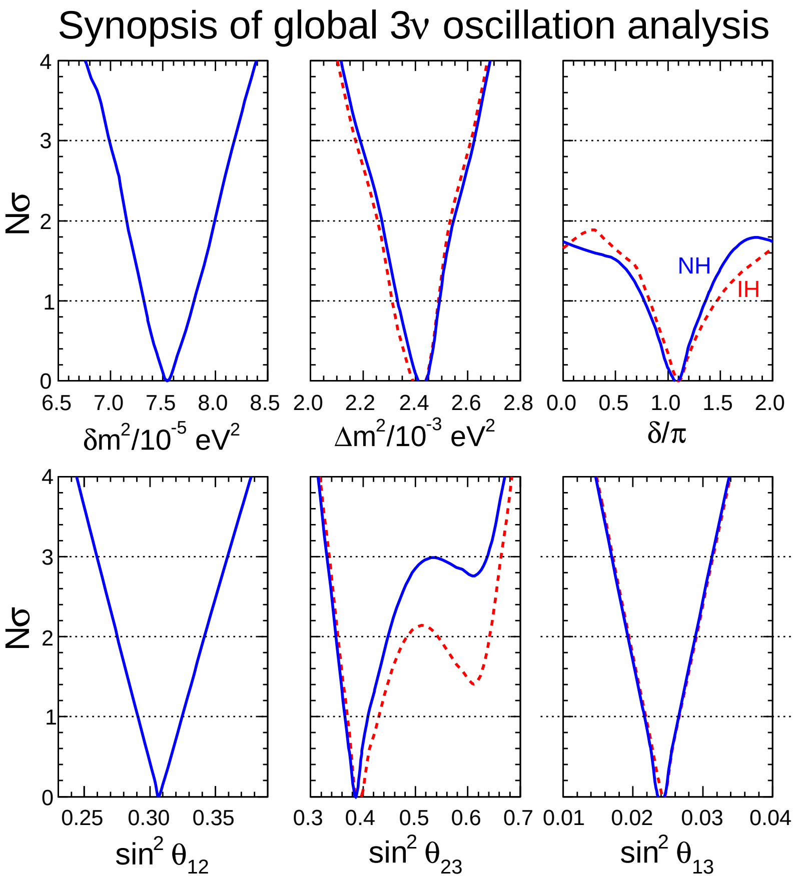

Figure 4.1: Results of the global three neutrino oscillation analysis performed in Reference [99]. It shows the constraints of the individual parameters in terms of standard deviations for the normal (solid blue line) and inverted (rad dashed line) mass hierarchy. Figure taken from [99].

From this global neutrino oscillation analysis a few conclusions can be drawn: The parameters δm^2, Δm^2, $\sin^2(\theta_{12})$, $\sin^2(\theta_{13})$, and $\sin^2(\theta_{23})$ are constrained very well with a relative uncertainty of $\mathcal{O}(1-10\%)$, where the atmospheric mixing angle is by far the most uncertain parameter. Besides this, there are still a few unknowns, like the CP phase, the θ_{23} octant choice, and the mass hierarchy. Thereby, $\sin^2(\theta_{13}) \neq 0$ allows in the future to access the CP phase in neutrino oscillation experiments. In order to increase the precision of $\sin^2(\theta_{23})$ in the future, the disappearance channel in LBL accelerator experiments will be important [102]. In the Conceptual Design Report of the LBNE project [103], a targeted precision of θ_{23} of 0.7° is quoted. This would mean an improvement of about a factor of two compared to the above discussed results of the global neutrino data analysis.

parameter	best fit	1σ range
$\delta m^2/10^{-5}$ eV^2	7.54	7.32 – 7.80
$\Delta m^2/10^{-3}$ eV^2	2.43	2.33 – 2.49
$\sin^2(\theta_{12})/10^{-1}$	3.07	2.91 – 3.25
$\sin^2(\theta_{23})/10^{-1}$	3.86	3.65 – 4.10
$\sin^2(\theta_{13})/10^{-2}$	2.41	2.16 – 2.66
δ/π	1.08	0.77 – 1.36

Table 4.1: Numerical results of the global three neutrino oscillation analysis performed in Reference [99]. It gives the best-fit values and allowed 1σ ranges for the 3ν mass-mixing parameters in the normal hierarchy.

4.2 Neutrinos beyond the Standard Model

After having introduced the phenomenological aspects of neutrino physics, we want to focus on the theoretical description in the context of a bigger theoretical framework in this section.

Neutrinos *only* interact weakly and the weak force only couples to left-handed particles. This means that two of the four degrees of freedom of a Dirac spinor describing a neutrino are not relevant (ν_R, $\overline{\nu}_L$). Following simplicity arguments, this fact suggests that neutrinos are not described the best by Dirac spinors [104]. In 1937, Ettore Majorana introduced a special type of spinors [105], which is invariant under charge conjugation and, so, exhibit a reduced number of degree of freedom (cf. Appendix A.3). Up to now, we have not found any elementary particle being a Majorana fermion, but neutrinos are considered as possible candidates (as well as neutralinos in SUSY).

4.2.1 Seesaw Mechanism

It is sort of a puzzle, why neutrinos are that light compared to their charged lepton partners in the same isospin doublet. A nice way to explain this is the so-called “seesaw” mechanism [106–110]. Thereby, a right-handed Majorana-type neutrino singlet N_R, which is supermassive ($m_M \approx m_{\mathrm{GUT}}$), is added to the Lagrangian. Together with the left-handed neutrino, which is present in the SM, a Dirac mass term can be formed, so that the mass terms in the Lagrangian become [84]:

$$\begin{aligned}-\mathcal{L}^{\nu}_{\mathrm{mass}} &= m_D\overline{\nu_L}N_R + \frac{1}{2}m_M\overline{N^c_L}N_R + \text{h.c.}\\ &= \frac{1}{2}\left(\overline{\nu_L}\,\overline{N^c_L}\right)\begin{pmatrix}0 & m_D\\ m_D & m_M\end{pmatrix}\begin{pmatrix}\nu^c_R\\ N_R\end{pmatrix} + \text{h.c.} \qquad (4.12)\end{aligned}$$

Herein, m_D is assumed to be of the order of the other charged leptons.

Diagonalisation of the mass matrix leads to one very light neutrino ($m_1 \approx m_D^2/m_N$)[3] and one very heavy ($m_2 \approx m_M$). This explains the name of the mechanism: The heavier the right handed neutrino becomes, the lighter gets the left-handed one. In a pure Standard Model, which is just extended by the superheavy right-handed neutrino, this approach enormously destabilises the electroweak scale, because of the huge mass of N_R [111] as discussed in Section 2.4. In SUSY, however, the right-handed neutrino gets accompanied by a scalar partner and thus only a logarithmic cut-off dependence remains. This is also known as SUSY Type-1-Seesaw mechanism. There exist also other types of SUSY-Seesaw mechanisms whose description is beyond the scope of this work.

4.2.2 SUSY with Bilinear *R*-Parity Violation

Another, very elegant way of introducing neutrino masses and their mixings in the context of SUSY is via R-parity violation. As pointed out before, R parity is a discrete $\mathbb{Z}_2$ symmetry, which is introduced in the MSSM in order to save the proton from fast decay. However, as demonstrated in Reference [112], it exists also a (gauge-anomaly free) discrete $\mathbb{Z}_3$ symmetry, which is called baryon parity and also keeps the proton stable. Thereby, baryon parity only forbids the baryon number violating terms in the superpotential (2.52) and allows for the lepton number violating terms (2.51).

In the following, we will consider a model where only the bilinear R-parity violating (bRPV) terms are present. This has been theoretically widely studied in the literature [113–115]. The superpotential in this case reads

$$\mathcal{W}^{\text{bRPV}} = \mathcal{W}^{\text{MSSM}} + \epsilon_i L_i \cdot H_u. \tag{4.13}$$

Herein, i denotes the family and ϵ_i is a dimensionful coupling, comparable with the μ term in the RPC superpotential. Additionally, there arise also new soft SUSY breaking terms

$$\mathcal{L}^{\text{bRPV}}_{\cancel{\text{SUSY}}} = \mathcal{L}^{\text{MSSM}}_{\cancel{\text{SUSY}}} + B_i \epsilon_i \widetilde{L}_i H_u, \tag{4.14}$$

where B_i is the equivalent to b of the RPC soft SUSY breaking Lagrangian of the Higgs sector. The broken R parity has the important consequence that also an odd number of SUSY particles can be produced at a collider and that the LSP can decay into SM particles.

If one compares the down-type Higgs supermultiplet H_d and the lepton superfield L in Table 2.3, one notices that both superfields have the same quantum numbers.

---

[3] at this point arises a minus sign, which can be absorbed into a phase

This is the reason, why for RPV new terms appear, where L replaces H_d. As a consequence this leads to new mixings of the particles compared to the MSSM: The neutral Higgs sector mixes with sneutrinos, the charged Higgs sector with sleptons, the charged leptons with charginos and the neutrinos with neutralinos.

Often it is claimed that the bRPV terms in Equation (4.13) can be rotated away into trilinear terms by a field redefinition and, thus, are physically irrelevant. However, this is not entirely true, since this does not work for the soft SUSY breaking terms [116].

Finally, we arrive at six new free parameters arising from the bRPV extension of the MSSM. In this model, the three sneutrinos acquire a VEV $\langle\widetilde{\nu}_i\rangle = v_i$. By convention ϵ_i and v_i are chosen as independent parameters and B_i are derived from them.

We now want to turn to the connection between bRPV and neutrino masses. Therefore, we examine the mass matrix of the neutral fermions, where we follow the derivation of Reference [117]. Because of the aforementioned mixing of neutralinos and neutrinos, the basis of neutral fermions becomes

$$\psi_N^{\text{bRPV}} = (\widetilde{B}, \widetilde{W}^0, \widetilde{H}_d^0, \widetilde{H}_u^0, \nu_e, \nu_\mu, \nu_\tau) \tag{4.15}$$

and, thus, the mass matrix can be written as

$$\mathbf{M}_{\mathbf{N}}^{\text{bRPV}} = \begin{pmatrix} \mathbf{M_N} & \mathbf{m}^T \\ \mathbf{m} & 0 \end{pmatrix}, \tag{4.16}$$

with

$$\mathbf{m} = \begin{pmatrix} -\frac{1}{2}g'v_1 & \frac{1}{2}gv_1 & 0 & \epsilon_1 \\ -\frac{1}{2}g'v_2 & \frac{1}{2}gv_2 & 0 & \epsilon_2 \\ -\frac{1}{2}g'v_3 & \frac{1}{2}gv_3 & 0 & \epsilon_3 \end{pmatrix}. \tag{4.17}$$

Herein, $\mathbf{M_N}$ is the usual MSSM neutralino mass matrix (cf. Equation (2.62)) and $\mathbf{m}$ arises from the bRPV parameters. In Equation (4.16), one can see very nicely a seesaw-like mass matrix, but without involving the GUT scale. For this reason, bilinear R-parity breaking is also often referred to as weak-scale seesaw mechanism [118].

The mass matrix can be diagonalised by

$$\mathcal{N}^* \mathbf{M}_{\mathbf{N}}^{\text{bRPV}} \mathcal{N}^{-1} = \text{diag}(m_{\tilde{\chi}_1^0}, m_{\tilde{\chi}_2^0}, m_{\tilde{\chi}_3^0}, m_{\tilde{\chi}_4^0}, m_{\nu_e}, m_{\nu_\mu}, m_{\nu_\tau}). \tag{4.18}$$

For small RPV parameters a perturbative diagonalisation of $\mathbf{M}_{\mathbf{N}}^{\text{bRPV}}$ can be performed. The matrix ξ is introduced, which is used to approximate $\mathcal{N}$:

$$\xi = \mathbf{m} \cdot \mathbf{M_N}^{-1} \qquad \forall \xi_{ij} \ll 1 \tag{4.19}$$

$$\begin{aligned}
\xi_{i1} &= \frac{g' M_2 \mu}{2\det(\mathbf{M_N})}\Lambda_i & \xi_{i2} &= -\frac{g M_1 \mu}{2\det(\mathbf{M_N})}\Lambda_i \\
\xi_{i3} &= -\frac{\epsilon_i}{\mu} + \frac{(g^2 M_1 + g'^2 M_2) v_u}{4\det(\mathbf{M_N})}\Lambda_i & \xi_{i4} &= -\frac{(g^2 M_1 + g'^2 M_2) v_d}{4\det(\mathbf{M_N})}\Lambda_i,
\end{aligned} \tag{4.20}$$

where Λ_i are the so-called alignment parameters

$$\Lambda_i = \mu v_i + v_d \epsilon_i. \tag{4.21}$$

At leading order the mixing matrix $\mathcal{N}$ is obtained:

$$\mathcal{N}^* = \begin{pmatrix} N^* & 0 \\ 0 & V_\nu^T \end{pmatrix} \begin{pmatrix} 1 - \frac{1}{2}\xi^\dagger \xi & \xi^\dagger \\ -\xi & 1 - \frac{1}{2}\xi \xi^\dagger \end{pmatrix} \tag{4.22}$$

The second part of (4.22) brings $\mathbf{M}_\mathbf{N}^{\mathrm{bRPV}}$ into block-diagonal form $\mathbf{M}_\mathbf{N}^{\mathrm{bRPV}} = \mathrm{diag}(\mathbf{M_N}, \mathbf{m}_{\mathrm{eff}})$, where

$$\mathbf{m}_{\mathrm{eff}} = \frac{M_1 g^2 + M_2 g'^2}{4\mathrm{det}(\mathbf{M_N})} \begin{pmatrix} \Lambda_e^2 & \Lambda_e \Lambda_\mu & \Lambda_e \Lambda_\tau \\ \Lambda_\mu \Lambda_e & \Lambda_\mu^2 & \Lambda_\mu \Lambda_\tau \\ \Lambda_\tau \Lambda_e & \Lambda_\tau \Lambda_\mu & \Lambda_\tau^2 \end{pmatrix}. \tag{4.23}$$

Finally, the first part of (4.22) diagonalises $\mathbf{M_N}$ and $\mathbf{m}_{\mathrm{eff}}$:

$$N^* \mathbf{M_N} N^\dagger = \mathrm{diag}(m_{\tilde{\chi}_1^0}, m_{\tilde{\chi}_2^0}, m_{\tilde{\chi}_3^0}, m_{\tilde{\chi}_4^0}) \tag{4.24}$$

$$V_\nu^T \mathbf{m}_{\mathrm{eff}} V_\nu = \mathrm{diag}(0, 0, m_\nu) \tag{4.25}$$

This leaves us in the end with one neutrino mass on tree level

$$m_\nu = \frac{M_1 g^2 + M_2 g'^2}{4\mathrm{det}(\mathbf{M_N})} |\vec{\Lambda}|^2. \tag{4.26}$$

Parametrising the neutrino mixing matrix as

$$V = \begin{pmatrix} 1 & 0 & 0 \\ 0 & \cos(\theta_{23}) & -\sin(\theta_{23}) \\ 0 & \sin(\theta_{23}) & \cos(\theta_{23}) \end{pmatrix} \begin{pmatrix} \cos(\theta_{13}) & 0 & -\sin(\theta_{13}) \\ 0 & 1 & 0 \\ \sin(\theta_{13}) & 0 & \cos(\theta_{13}) \end{pmatrix} \tag{4.27}$$

gives directly access to two neutralino mixing angles

$$\tan(\theta_{13}) = -\frac{\Lambda_e}{\sqrt{\Lambda_\mu^2 + \Lambda_\tau^2}} \quad \text{and} \tag{4.28}$$

$$\tan(\theta_{23}) = -\frac{\Lambda_\mu}{\Lambda_\tau}. \tag{4.29}$$

It is important to note that Equations (4.28) and (4.29) only depend on the alignment parameters, which arise only from nonzero RPV parameters. The remaining two neutrino masses as well as the remaining mixing angle θ_{12} are obtained taking into account one-loop calculations [117, 119].

An interesting feature of this model is the fact that the left-handed part of the $\widetilde{\chi}_1^0 - W - l_i$–coupling is approximately proportional to the corresponding alignment parameter Λ_i:

$$\mathcal{O}_{\widetilde{\chi}_1^0 W l_i} \simeq \Lambda_i \cdot f(M_1, M_2, \mu, v_d, v_u) \propto \Lambda_i, \tag{4.30}$$

where $f(M_1, M_2, \mu, v_d, v_u)$ is a function of soft SUSY breaking parameters. The full expression can be found in [118]. Combining Equation (4.30) with Equation (4.28) or Equation (4.29) makes clear that neutrino mixing angles can be determined from the measurement of neutralino branching ratios:

$$\tan^2(\theta_{13}) \simeq \frac{\mathcal{O}^2_{\widetilde{\chi}_1^0 We}}{\mathcal{O}^2_{\widetilde{\chi}_1^0 W\mu} + \mathcal{O}^2_{\widetilde{\chi}_1^0 W\tau}} = \frac{\mathrm{BR}(\widetilde{\chi}_1^0 \to We)}{\mathrm{BR}(\widetilde{\chi}_1^0 \to W\mu) + \mathrm{BR}(\widetilde{\chi}_1^0 \to W\tau)} \tag{4.31}$$

$$\tan^2(\theta_{23}) \simeq \frac{\mathcal{O}^2_{\widetilde{\chi}_1^0 W\mu}}{\mathcal{O}^2_{\widetilde{\chi}_1^0 W\tau}} = \frac{\mathrm{BR}(\widetilde{\chi}_1^0 \to W\mu)}{\mathrm{BR}(\widetilde{\chi}_1^0 \to W\tau)}. \tag{4.32}$$

It has to be added that relation (4.32) is only exact on tree level. Due to loop contributions, further SUSY parameter dependencies enter. However, this can be addressed by additional parametric uncertainties, as it is going to be discussed in Section 7.4.

The presented derivation has shown that the neutrino sector can be probed at a collider experiment. Therefore, it is the aim of this thesis to investigate the potential of detecting bRPV SUSY at the ILC and to study the possible precision in measuring the atmospheric mixing. Before we enter the discussion of the bRPV study at the ILC, we review the status of SUSY searches with respect to (bilinear) R-parity violation at the LHC in the next section.

4.3 Status at the LHC

In proton-proton collisions, the main SUSY production modes are squark or gluino production. These particles decay subsequently via cascades down to the lightest supersymmetric particle. In case of R-parity violation, the LSP further decays into Standard Model particles. Therefore, in contrast to the RPC case, the LSP does not escape the detector unobservedly such that the missing energy in RPV SUSY events is significantly lowered. This makes modified search strategies for RPV SUSY necessary.

The ATLAS collaboration performed a dedicated search for bRPV SUSY in the framework of the cMSSM [120]. In this analysis, the bRPV parameters have been fitted to neutrino data and are therefore not free model parameters. All possible production modes within this model have been taken into account. The analysis could exclude a large area of the cMSSM parameter plane reaching up to $m_{1/2} \approx 600\,\mathrm{GeV}$ or $m_0 \approx 1.2\,\mathrm{TeV}$ for a data sample of $\int L dt = 4.7\,\mathrm{fb}^{-1}$ and a center-of-mass energy of $\sqrt{s} = 7\,\mathrm{TeV}$. However, most parts of the excluded parameter space result only from the coloured particle spectrum at a specific parameter point.

Besides this RPV SUSY search, which is embedded in a high-scale SUSY model, a large number of RPV SUSY searches have been performed in simplified models by the ATLAS and CMS collaborations [121–128]. Many of them assume strong production, which dominates for not too heavy squarks or gluinos, and, for this reason, the derived limits are mostly limits on the coloured sector. The electroweak sector keeps rather untested. Exclusion limits are usually quoted in the $m_{\tilde{g}} - m_{\tilde{\chi}^0_1}$ plane. For gluino masses larger than 900 GeV the neutralino mass is unconstrained [121].

Recently, the LHC experiments demonstrated that they are also sensitive to searches in direct electroweak production channels for the RPC [129–134] as well as for the RPV [135] case. In Reference [135], one nonvanishing trilinear RPV coupling has been assumed. Since the direct $\tilde{\chi}^0_1$-pair production has a very small cross section at the LHC, the production of a chargino pair is considered, where both charginos decay via the LSP into Standard Model particles. The derived limits in the $m_{\tilde{\chi}^\pm_1} - m_{\tilde{\chi}^0_1}$ parameter plain depend strongly on the type and strength of the RPV coupling. However, under most optimistic assumption, chargino masses up to 750 GeV are probed.

If the RPV couplings are small, the LSP can become rather long-lived, which allows for searches for displaced vertices. In Reference [136] a search at the ATLAS detector is presented. This analysis assumes squark-pair production where both squarks decay into a quark and the LSP. The LSP is long-lived and decays at a displaced vertex into two quarks and a muon with a branching fraction of 50%. This decay can be induced by a nonvanishing trilinear RPV coupling λ' or by bRPV, for instance. Figure 4.2 shows the upper limits at 95% CL on the cross section of long-lived LSP production via squarks with respect to the LSP lifetime. Three different scenarios for the squark and LSP mass are examined: MH and ML denote scenarios with medium-mass squarks ($m_{\tilde{q}} = 700\,\mathrm{GeV}$) and a heavy neutralino ($m_{\tilde{\chi}^0_1} = 494\,\mathrm{GeV}$) or a light neutralino ($m_{\tilde{\chi}^0_1} = 108\,\mathrm{GeV}$), respectively. HL assumes a heavy squark ($m_{\tilde{q}} = 1000\,\mathrm{GeV}$) and a light neutralino. The horizontal lines indicate the production cross sections for the two considered squark masses. In the MH and ML scenarios,

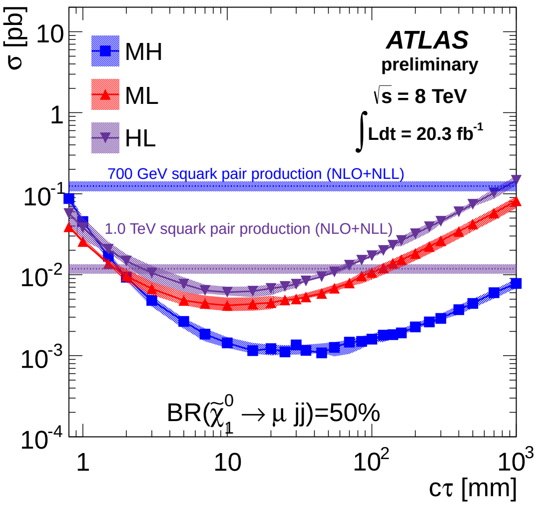

Figure 4.2: Upper limits at 95% CL on the cross section of long-lived neutralino production via squarks. Three scenarios for the squark and LSP mass are depicted: MH ($m_{\tilde{q}} = 700\,\mathrm{GeV}$, $m_{\tilde{\chi}_1^0} = 494\,\mathrm{GeV}$), ML ($m_{\tilde{q}} = 700\,\mathrm{GeV}$, $m_{\tilde{\chi}_1^0} = 108\,\mathrm{GeV}$), and HL ($m_{\tilde{q}} = 1000\,\mathrm{GeV}$, $m_{\tilde{\chi}_1^0} = 108\,\mathrm{GeV}$). The horizontal lines indicate the production cross section in the case of $m_{\tilde{q}} = 700\,\mathrm{GeV}$ and $m_{\tilde{q}} = 1000\,\mathrm{GeV}$. Taken from [136].

displaced vertices can be excluded for the whole displayed range of $c\tau$. However, in the HL scenario, there are still allowed ranges ($c\tau < 2.5\,\mathrm{mm}$ and $c\tau > 70\,\mathrm{mm}$), where the analysis is not yet sensitive. For even larger squark masses, the production cross section drops and the exclusion limits become weaker.

To conclude, the coloured sector of SUSY is intensively probed at the LHC and recent results suggest that if SUSY is realised in nature, coloured particles have to be at the multi-TeV scale. However, the electroweak sector of SUSY, especially in the case of RPV, can still be rather light and electroweakinos can still be in the kinematic range of the ILC. Therefore, searches for direct electroweakino production are essential in order to constrain the parameter space which is relevant for the ILC.

4.4 A Benchmark Scenario for the ILC

In this section, we discuss a simplified model of the bRPV MSSM in the context of the ILC. In order to cope with the large number of parameters of this model, we identify the most important ones for the experimental study and define a simplified model.

4.4.1 LSP Production and the Role of Polarisation

The possible production mechanism of LSPs at the ILC depends on the character of the particle. We can distinguish the following three limits:

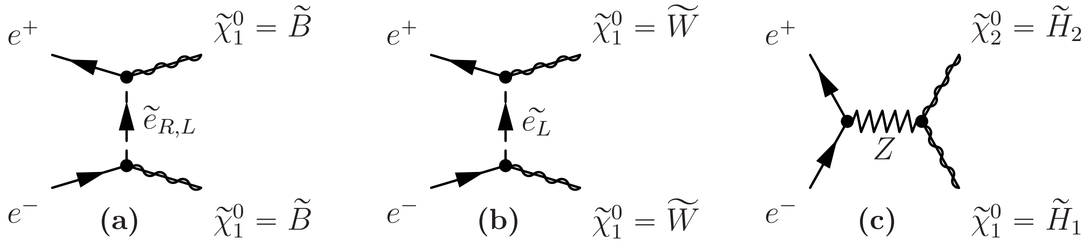

Figure 4.3: Possible production channels in dependence of different LSP characters.

- In the case of the LSP being a pure bino, only t/u-channel production is possible, mediated predominantly via a virtual selectron (cf. Figure 4.3a).
- For the pure wino case, the situation is comparable to the pure bino case, but only the left selectron is possible as exchange particle (cf. Figure 4.3b), since there exist no coupling between right selectrons, right-handed electrons, and the wino. It should be noted that in principle all charged scalars may occur in the t/u-channel as exchange particles, since they possess a selectron admixture due to the bRPV terms in the Lagrangian. However, for small bRPV parameters, which are necessary to describe neutrino physics correctly, these diagrams are negligible. The production cross sections of these two production channels depend clearly on the corresponding selectron mass and LSP mass. Typical production cross sections are of the order of 100 fb for selectron masses of $m_{\widetilde{e}} < 500\,\text{GeV}$.
- If the LSP is a Higgsino, only the associate production of a $\widetilde{\chi}_1^0$ together with a $\widetilde{\chi}_2^0$ is possible via a s-channel Z-boson exchange (cf. Figure 4.3c). Usually, in this kind of scenarios, $\widetilde{\chi}_1^0$ and $\widetilde{\chi}_2^0$ are close in mass and the $\widetilde{\chi}_2^0$ decays into $\widetilde{\chi}_1^0$. Thereby, the decay products are rather soft such that experimentally the situation is comparable to direct LSP-pair production. The cross section for this production mode is about 100 fb – 200 fb [137].

From now on, we will focus on a simplified scenario, in which we assume the LSP being a pure bino. We further assume that all other SUSY particles are heavy (around the multi-TeV scale), except for the right selectron. This is a worst case scenario since a lighter left selectron would only increase the production cross section. Additional available production channels due to a lighter sparticle spectrum also only increases the number of examinable LSP decays. Thus, the production cross section in this scenario is parametrised only by the LSP mass $m_{\widetilde{\chi}_1^0}$ and the right selectron

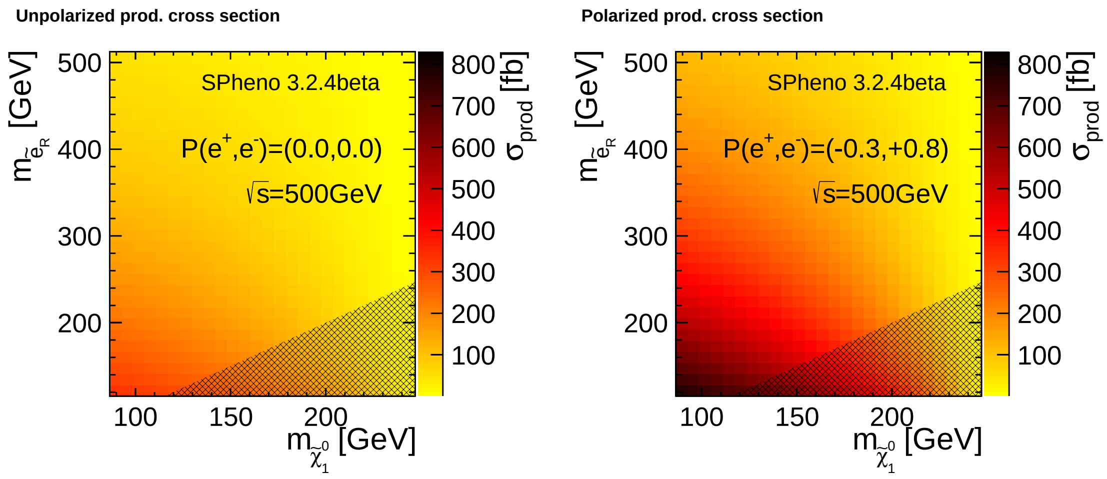

(a) (b)

Figure 4.4: Production cross section of bino pairs at the ILC500 in the described simplified model for unpolarised (a) and polarised (b) incoming beams. Beam polarisation can significantly enhance the production cross section. The shaded area shows the region of the parameter space where the selectron becomes the LSP.

mass $m_{\tilde{e}_R}$. All bRPV parameters are fitted to neutrino data and are therefore no free parameters of the model. Also the SUSY Higgs sector has been adjusted in order to be in agreement with the current Higgs mass. Technically, this simplified model is realised as a pMSSM24 (cf. Section 2.6) where the parameters are chosen correspondingly to the above description. Figure 4.4 shows the production cross section of bino pairs in the defined simplified model. The cross section is maximal for light LSPs and selectrons and drops for heavier masses. For unpolarised e^+/e^- beams the maximal cross section amounts to about 320 fb for $m_{\tilde{\chi}_1^0} = 100\,\text{GeV}$ and $m_{\tilde{e}_R} = 120\,\text{GeV}$.

As elaborated in Section 2.5, supersymmetry associates each chiral degree of freedom of a positron/electron with a selectron partner

$$e^-_{L,R} \leftrightarrow \tilde{e}^-_{L,R} \leftrightarrow e^+_{R,L}. \tag{4.33}$$

Therefore, we can identify helicity configurations of the incoming positron and electron, which give nonvanishing contributions to the production cross section:

$\sigma_{RL} = \quad \sigma$

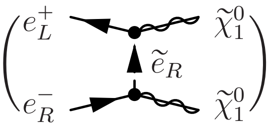

$\sigma_{LR} = \quad \sigma$

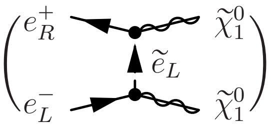

(4.34)

In the introduced scenario, the second graph is suppressed due to the large mass of the left selectron such that $\sigma_{LR} \approx 0$.

As described in Section 3.3, beam polarisation is a useful tool to either enhance or suppress a corresponding diagram. In the case of the t/u-channel, the specific helicity structure of the coupling of the selectron to electron/positron causes this effect. The effective production cross section is calculated using Equation (3.8). In the considered scenario, this equation simplifies to

$$\sigma \approx \frac{1}{4}(1+\mathcal{P}_{e^-})(1-\mathcal{P}_{e^+})\sigma_{RL}. \tag{4.35}$$

Herein, $\mathcal{P}_{e^-}$ and $\mathcal{P}_{e^+}$ denote the polarisation of the electron and positron beam, respectively.

Figure 4.4b shows the effect of a 30% left-handed polarised positron beam and 80% right-handed polarised electron beam. This polarisation is in agreement with the baseline polarisation of the ILC [56]. According to Equation (4.35), the cross section is enhanced by a factor of 2.34 compared to the unpolarised case.

4.4.2 LSP Decay

The decay of the lightest supersymmetric particle in the bRPV model is solely governed by the additional RPV terms in the Lagrangian. Small RPV parameters, which are motivated from neutrino physics, lead to considerable decay lengths of the neutralinos of up to kilometers for very light LSPs. In this case, the RPV scenario would not be distinguishable from RPC SUSY, since most of the neutralinos would escape the detector unobservedly like stable neutral particles. However, there is still a chance to observe such events at the ILC from radiative LSP-pair production down to production cross sections in the order of 10 fb, as shown in Reference [138].

In this study, we are, however, interested in the region of parameter space where the on-shell W-boson decay of the neutralino is possible. This implies that $m_{\tilde{\chi}_1^0}$ is larger than m_W. In this case, the decay length in the simplified scenario is between 100 μm and 10 cm, which is depicted in Figure 4.5. A comparison with the impact parameter resolution of the International Large Detector (ILD) in Figure 5.3a shows that the this detector is well suited for measuring such displaced vertices.

Relaxing the simplifications on the remaining sparticle spectrum and allowing for lighter masses can decrease the decay length, but not much less than 100 μm [118]. The reason for this are additional decay modes, which become less suppressed in this case. This results in a larger decay width of the LSP.

In the bRPV model, three different types of on-shell 2-body decays of the LSP are possible:

$$\tilde{\chi}_1^0 \rightarrow W^{\pm} l^{\mp} \tag{4.36}$$

$$\tilde{\chi}_1^0 \rightarrow Z^0 \nu \tag{4.37}$$

$$\tilde{\chi}_1^0 \rightarrow h^0 \nu \tag{4.38}$$

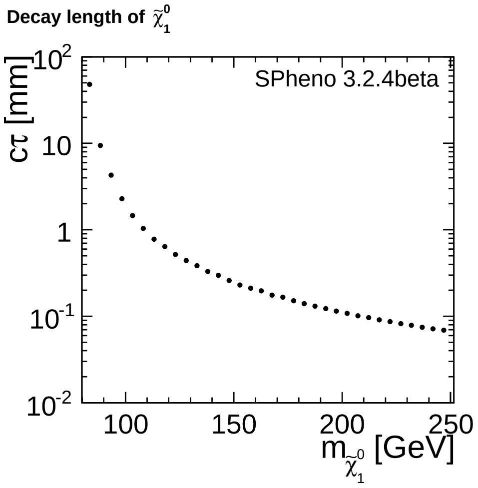

Figure 4.5: Decay length of the LSP in dependence of its mass in the simplified model. For a light spectrum of the remaining sparticles the decay length can be smaller.

The branching ratios for the decay modes in the simplified model are drawn in dependence of the LSP mass in Figure 4.6a . Herein, $\tilde{\chi}_1^0 \to W^\pm l^\mp$ is always the dominant decay. The branching ratios of the different leptonic final states $W^\pm l_i^\mp$ are proportional to the corresponding alignment parameter Λ_i (cf. Equation (4.30)). For this reason, we are interested in measuring these branching ratios of the LSP in this study. For $m_{\tilde{\chi}_1^0} \gg m_Z$ the ratio between the W-boson decay mode and the Z decay mode is about two. The Higgs decay mode starts to enter for $m_{\tilde{\chi}_1^0} > m_{h^0}$.

In the case of a lighter sparticle spectrum, also three-body decays may become important. This is depicted in Figure 4.6b which shows the fraction of three-body decays in the example of light staus. In this parameter scan, $m_{\tilde{\tau}_{L,R}}$ have been lowered significantly such that they become close to the LSP mass. The fraction of three-body decays is calculated as

$$f_{\mathrm{3BD}} = 1 - f_{\mathrm{2BD}}, \text{with} \tag{4.39}$$

$$f_{\mathrm{2BD}} = \mathrm{BR}(\tilde{\chi}_1^0 \to W^\pm l^\mp) + \mathrm{BR}(\tilde{\chi}_1^0 \to Z^0 \nu) + \mathrm{BR}(\tilde{\chi}_1^0 \to h^0 \nu). \tag{4.40}$$

Close to the on-shell condition $m_{\tilde{\chi}_1^0} = m_{\tilde{\tau}}$, there is a significant contribution from three-body decays arising from off-shell intermediate staus. The increase of three-body decays for $m_{\tilde{\chi}_1^0} < m_W$ stem from off-shell W-boson decays.

For the following detector study, we will stick to the simplified model, where three-body decays are not present. However, three-body decays, if present, may become an additional source for background in the analysis.

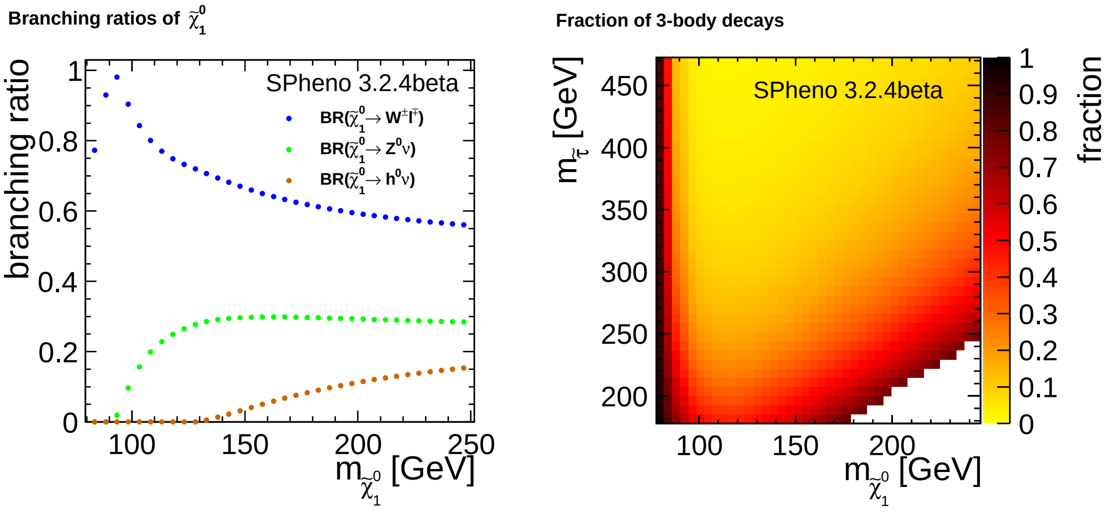

(a)

(b)

Figure 4.6: (a) Branching ratios in the simplified model. (b) Three-body decays become relevant for a lighter sparticle spectrum, like e.g. light staus.

4.4.3 Benchmark Point

For the subsequent analysis, we choose the following benchmark point in the simplified model

$$m_{\tilde{\chi}_1^0} = 98.5\,\text{GeV} \tag{4.41}$$

$$m_{\tilde{e}_R} = 280.0\,\text{GeV}. \tag{4.42}$$

At this, the selected LSP mass at the parameter point is a worst case scenario, where $m_{\tilde{\chi}_1^0}$ is close to $m_{W/Z}$. This is most challenging, since the main background is expected to peak around $m_{W/Z}$. Furthermore, the decay products of the LSP into a W/Z boson and a lepton become rather soft, due to the small mass difference between the LSP and the corresponding boson.

The production cross section at the chosen parameter point for a beam polarisation of $\mathcal{P}(e^-, e^+) = (80\%, -30\%)$ and a center-of-mass energy of $\sqrt{s} = 500\,\text{GeV}$ amounts to

$$\sigma = 344\,\text{fb}. \tag{4.43}$$

From the fit of the bRPV parameters to the neutrino oscillation data performed by `SPheno 3.2.4beta`[4], the nonvanishing branching ratios are predicted to

$$\mathrm{BR}(\tilde{\chi}_1^0 \to W^\pm e^\mp) = 0.002 \tag{4.44}$$
$$\mathrm{BR}(\tilde{\chi}_1^0 \to W^\pm \mu^\mp) = 0.427 \tag{4.45}$$
$$\mathrm{BR}(\tilde{\chi}_1^0 \to W^\pm \tau^\mp) = 0.472 \tag{4.46}$$
$$\mathrm{BR}(\tilde{\chi}_1^0 \to Z^0 \nu) = 0.098. \tag{4.47}$$

The very small value of the $(W^\pm e^\mp)$ decay mode arises from the small neutrino mixing angle θ_{13}[5]. Three-body decay modes are negligible at this benchmark point. However, differing from this benchmark point, we have also studied the impact of nonvanishing contributions of three-body decays, which will be commented on in the end of Chapter 6.

For the decay length of the LSP at the parameter point we find

$$c\tau = 2.26\,\mathrm{mm}. \tag{4.48}$$

Before continuing with the discussion of the details of the Monte-Carlo event generation with respect to this benchmark point as well as the detector simulation, we will firstly introduce the detector concept in the next chapter.

---

[4] `SPheno` assumes a real PMNS matrix

[5] In the used `SPheno` version, the input values of the neutrino parameters for the fit are taken from Reference [139], which does not include the more recent measurements of θ_{13}.

5 The International Large Detector Concept

The following analysis is based on the International Large Detector (ILD). For this reason, this chapter summarises the most important aspects of the detector concept as well as the software framework. In Section 3.5, we have given already an overview of the most important key measurements foreseen at the ILC. These intended measurements define the design goals of the ILD subdetectors as discussed in Section 5.1. Section 5.2 introduces the concept of Particle Flow, which is pursued at the ILD and, therefore, influences significantly the detector design. All the subdetector components are outlined in Section 5.3 covering the vertex detectors, trackers, calorimeters as well as the outer detector region. The chapter is closed with a brief description of the software framework for event simulation and reconstruction in Section 5.4.

5.1 Design Goals

It is clear that the quoted precision of the diverse intended measurements implies the need of excellent detectors. As a result of optimisation studies a set of design goals have been formulated for the International Large Detector concept (ILD):

Many measurements rely on heavy flavour tags. Top quarks, for instance, decay predominantly into bottom quarks and a W boson. For this reason, excellent b-tagging performance is essential for studying top events. But also for the analysis of the coupling of the Higgs boson to SM fermions it is crucial to be able to discriminate e.g. $H \to b\bar{b}$ from $H \to c\bar{c}$ and $H \to \tau^+\tau^-$ by a powerful heavy flavour tag, which makes use of the lifetime information of the different fermions. Therefore, the precision in reconstructing secondary vertices is a key ingredient to the flavour tagging performance and the following design goal for the impact parameter has been formulated:

$$\sigma_{r\Phi} = 5\,\mu\text{m} \oplus \frac{10}{p(\text{GeV})\sin^{3/2}(\theta)}\,\mu\text{m} \tag{5.1}$$

In order to achieve the best reconstruction performance, the ILD pursues the concept of Particle Flow, which means that each particle in the detector is reconstructed

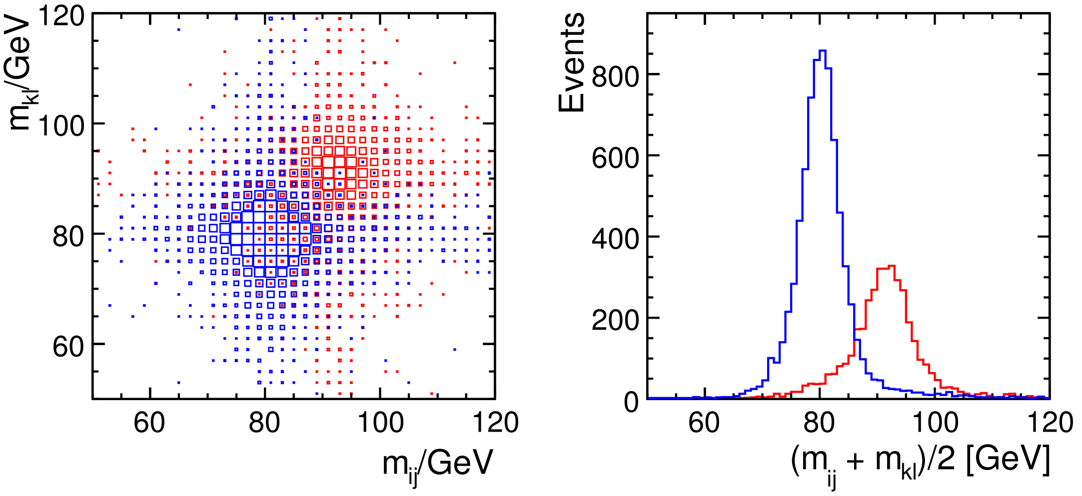

Figure 5.1: High performance tracking and calorimetry allows for a separation between $e^+e^- \rightarrow ZZ$ and $e^+e^- \rightarrow WW$ events. Figure taken from [3].

individually by the detector component that gives the best resolution. Details on Particle Flow will be discussed in Section 5.2. The Particle Flow concept demands on the one hand a highly segmented calorimeter, on the other hand a very precise tracking system. The targeted momentum resolution at the ILD amounts to

$$\sigma_{1/p_t} = 2 \times 10^{-5}\,\mathrm{GeV}^{-1} \oplus \frac{1 \times 10^{-3}}{p_t \sin(\theta)}. \tag{5.2}$$

A broad variety of analyses at the ILC rely on the reconstruction of invariant masses from jets. Due to this, the jet energy resolution plays a key role in the performance of the future experiment. The discrimination between hadronic W-boson and Z-boson decays are used as benchmark scenario. Taking the natural width of W and Z boson into account, a separation is possible if the jet energy resolution is

$$\sigma_E/E = 3 - 4\%, \tag{5.3}$$

which defines the design goal at the ILD. This resolution corresponds to a stochastic term in classical calorimetry of about $30\%/\sqrt{E(\,\mathrm{GeV})}$ for 100 GeV jets. It is clear that this is beyond the capability of classical hadronic calorimetry. However, Particle Flow calorimetry can reach this goal.

Figure 5.1 shows the reconstructed mass of two di-jet systems m_{ij} and m_{kl} in fully hadronic $e^+e^- \rightarrow \nu\nu ZZ$ and $e^+e^- \rightarrow \nu\nu WW$ events assuming the jet energy resolution given in (5.3). It is nicely demonstrated that a discrimination between hadronic W and Z bosons is possible.

5.2 The Particle Flow Concept

The idea of Particle Flow is explained in detail in Reference [140]. It is motivated by the knowledge of the composition of jets [141]: 62% of the energy of a jet is carried by charged particles, 27% by photons, about 10% by neutral, long-lived hadrons and only a small fraction of 1.5% by neutrinos. Thus, a large fraction of the jet energy is usually measured by the combined electromagnetic and hadronic calorimeter. The jet energy resolution is thereby limited by the rather poor energy resolution of the hadronic calorimeter, which typically amounts to $> 55\%/\sqrt{E(\,\mathrm{GeV})}$ [140]. Particle Flow relies on the fact that the four-momenta of all the visible (charged) particles in a jet can be reconstructed individually in the tracking detector and the corresponding calorimeter cluster is ignored. Thus, an imaging calorimeters which features a very fine granularity is necessary in order to be able to discriminate calorimeter clusters belonging to the individual tracks. The photon energy is reconstructed precisely by the electromagnetic calorimeter and only 10% of the energy content of a jet originating from neutral hadrons is measured in the hadronic calorimeter.

Assuming an energy resolution of $15\%/\sqrt{E(\,\mathrm{GeV})}$ for the electromagnetic and $55\%/\sqrt{E(\,\mathrm{GeV})}$ for the hadronic calorimeter, would allow for an overall jet energy resolution of $19\%/\sqrt{E(\,\mathrm{GeV})}$ [140]. This, however, assumes a perfect association of all energy deposits in the calorimeter to the different reconstructed particles. It is clear that in reality confusion between clusters lowers the achievable resolution. There exist two main sources for errors [142]:

Cluster Merging. A calorimeter cluster of a neutral particle close to a cluster of a charged particle cannot be resolved and is merged with the cluster of the charged particle. Since for charged particles the associated cluster is removed and the energy is measured from the track, this results in missing energy.

Cluster Splitting. A calorimeter cluster of a charged particle is not recognised as one cluster and only a part is associated to a track. The remaining part is reconstructed as a neutral fake-hadron. This leads to double counting of energy, since the track energy of the charged particle also comprises the energy fraction which is misreconstructed as neutral hadron.

Thus, for the jet energy resolution an additional term has to be added which takes the confusion probabilities into account.

The overall jet energy resolution can then be written as

$$\begin{aligned}\sigma_{\mathrm{jet}} &= f_{X^\pm}\cdot\sigma_{X^\pm}\oplus f_\gamma\cdot\sigma_\gamma\oplus f_{h^0}\cdot\sigma_{h^0}\oplus\sigma_{\mathrm{confusion}} && (5.4)\\ &= f_{X^\pm}\cdot\sigma_{\mathrm{tracking}}\oplus f_\gamma\cdot\sigma_{\mathrm{ECAL}}\oplus f_{h^0}\cdot\sigma_{\mathrm{HCAL}}\oplus\sigma_{\mathrm{PFA}}, && (5.5)\end{aligned}$$

where f is the energy fraction within a jet originating from a charged particle ($X^\pm$), a photon (γ) or neutral hadron (h^0).

Equation (5.5) shows that the obtained jet energy resolution consists of much more than just the calorimeter energy resolutions. In the Particle Flow reconstruction, the tracking performance as well as the pattern recognition performance of the algorithms enter to a large extend and, thus, this demands outstanding performance in *all* subsystems and reconstruction software. In order to minimise the confusion term, the capability of topological cluster reconstruction in the calorimeters is at least as important as the bare energy resolution of the calorimeters.

5.3 The ILD Concept

The ILD concept is one of two planned detector concepts at the International Linear Collider. It has arisen from the earlier GLD[1] [143] and LDC[2] [144] detector proposals. The detailed baseline design of the ILD has been optimised for the ILD Letter of Intent [145] and has been updated recently in the Detector Volume of the ILC TDR [57]. In addition to that, a slightly modified design of the ILD detector concept exists, which is adapted to the needs of the CLIC linear collider [146].

The second detector concept foreseen at the ILC is SiD[3], which is smaller in size and bases its tracking solely on silicon detectors [57]. Both detectors are going to be operated at the ILC in "push-pull" mode.

Figure 5.2 shows a schematic overview of the ILD concept as well as a quadrant view, which specifies the different subdetector systems. ILD in its current design has a diameter of about 16 m and a length of about 13 m. The detector is designed as a multi-purpose detector optimised for Particle Flow reconstruction. This demands a great performance in the spacial resolution of all detector components. The whole detector is embedded in a superconducting solenoid, providing a magnetic field of 3.5 T. No hardware based trigger is foreseen for the ILD and, thus, the detector is operated in continuous readout.

In order to minimise the need for external detector cooling, many hardware components pursue the concept of power pulsing. Power pulsing makes use of the beam structure at the ILC. A typical bunch train is 1 ms long and, therefore, in the 5 Hz scheme of the ILC, most of the detector components can be switched of in between the trains.

In the following, we give an overview of the different subsystems based on the latest description of ILD published in the Detector Volume of the ILC TDR [57].

---

[1] Gaseous Large Detector

[2] Large Detector Concept

[3] Silicon Detector

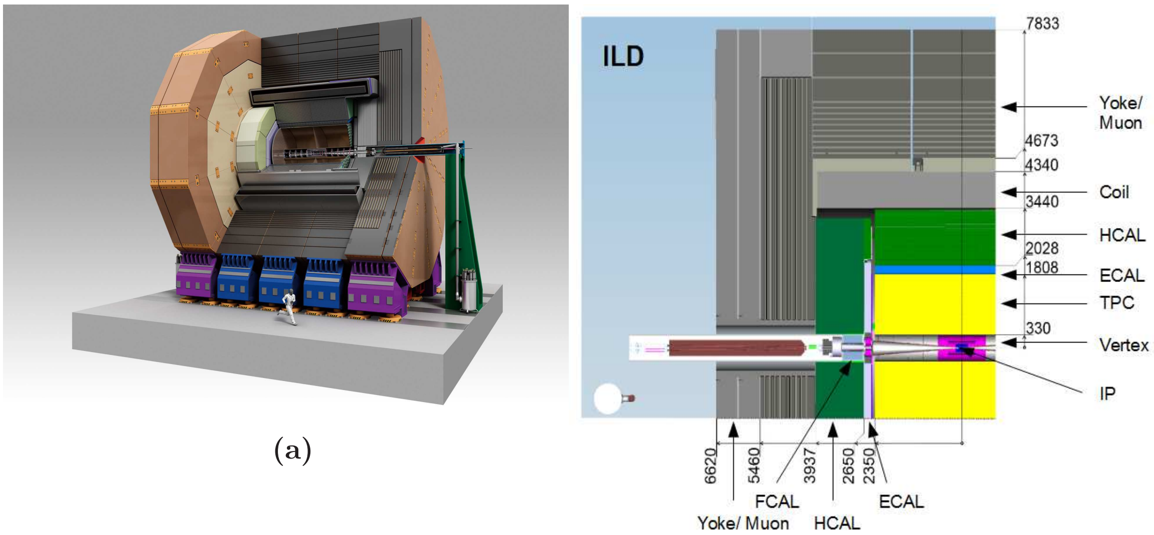

(a)

(b)

Figure 5.2: (a) Schematic drawing of ILD. (b) Quadrant view of ILD. The interaction point is in the lower right corner. Dimensions are given in mm. Figures taken from [57].

5.3.1 Vertex Detectors

In order to achieve the design goal for the impact parameter resolution (5.1), very stringent hardware requirements for the vertex detector have been defined [57]:

- a spatial resolution near the interaction point better then $3\,\mu$m
- a material budget below 0.15% of a radiation length per detector layer
- a first detector layer located at a radius of 16 mm
- a pixel occupancy not exceeding a few percent

There exist two concepts for the vertex detector (VTX). The baseline design foresees three cylindrical and concentric double layers of silicon pixel detectors within a distance of 60 mm with respect to the beam axis. This design allows for the measurement of six space-points per track. An alternative concept suggests five equally spaced single-sided layers, resulting in the measurement of five space-points per track.

Currently, three technical options for the sensors are under discussion, which have proven to have the potential to meet the design specifications: CMOS Pixel Sensor, Fine Pixel CCD sensors, and Depleted Field Effect Transistor sensors. For all options, intense R&D programs are ongoing, since not yet all requirements are fulfilled. However, some sensors are already in a stage that they are going to come

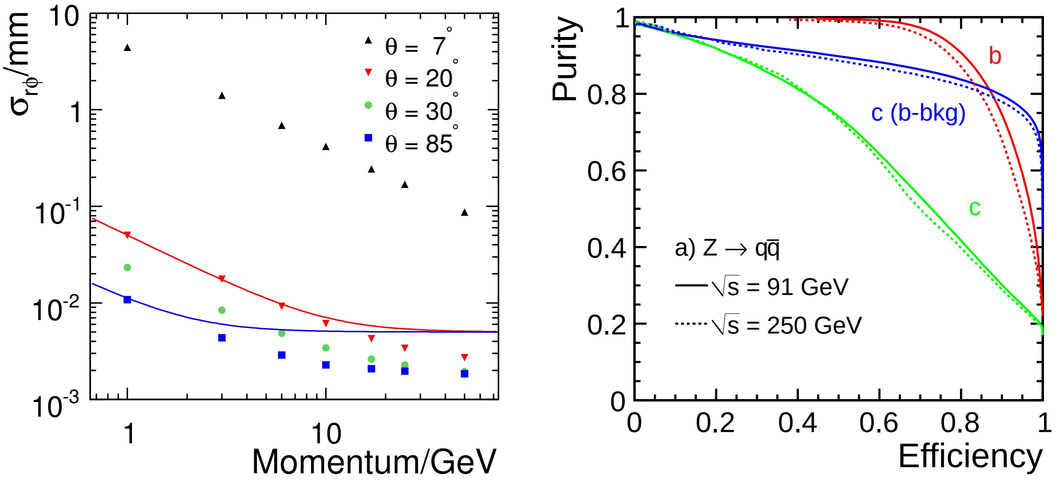

(a)

(b)

Figure 5.3: (a) Impact parameter resolution resulting from a GEANT 4-based detector simulation. The solid lines show the design goal for different incident angles of the track with respect to the beam axis. (b) Flavour tagging performance for $Z \rightarrow q\overline{q}$. Figures taken from [3].

into operation in other experiments. The CMOS pixel sensor “MIMOSA-28” [147], for example, is going to be used in the vertex detector of the STAR experiment at BNL [148].

The extremely tight material budget makes very thin sensitive ladders of $\mathcal{O}(50\,\mu\mathrm{m})$ necessary, which implies an involved design of the support structures. A detailed mechanical model of the vertex detector is implemented in the detector simulation.

Figure 5.3a shows the resulting performance of the vertex detector derived from a full GEANT 4-based detector simulation. The achieved impact parameter resolution even exceeds the design goal formulated in (5.1), which is indicated as solid lines in Figure 5.3a for different incident angles. The resolution is almost one order of magnitude better than at the ATLAS detector [149] and by a factor $2-4$ better than the impact parameter resolution achieved at the OPAL detector [150].

This leads to an excellent flavour tagging performance. Figure 5.3b shows the efficiency versus purity of flavour tagged jets in hadronic Z-boson decays at a center-of-mass energy of $\sqrt{s} = 91\,\mathrm{GeV}$ and $\sqrt{s} = 250\,\mathrm{GeV}$. The different colours indicate the discrimination of b-jets from $udsc$-jets (red), c-jets from $udsb$-jets (green), and c-jets from b-jets (blue).

5.3.2 Tracking Concept

The ILD is based on a hybrid tracking system. The central part of the tracking consists of a time projection chamber (TPC), which is surrounded by layers of silicon detectors – the so-called silicon envelope. Additionally, in the very forward direction a silicon forward tracker is foreseen.

5.3.2.1 Silicon Tracking

The silicon tracking concept is developed within the SiLC Collaboration [151]. It can be subdivided into the barrel system and the end-cap system:

In the barrel region two detector components are planned. The Silicon Inner Tracker (SIT) is located between the vertex detector and the TPC. The Silicon External Tracker (SET) is placed between the TPC and the electromagnetic calorimeter. Those two components link the vertex detector to the TPC and the TPC to the calorimeter, respectively. The precise measurement of additional space-points outside the TPC by the SIT and SET helps to increase the momentum resolution. In particular, the reconstruction of low-p_t tracks benefits from the SIT. Both barrel silicon detectors can be used to monitor and calibrate the TPC, which is expected to be very sensitive to temperature and atmospheric pressure variations.

The barrel system is complemented by two end-cap detector components: The Endplate Tracking Detector (ETD) is located between the TPC endplates and the forward calorimeter. Therefore, it completes the silicon envelope of the TPC.

For center-of-mass energies of $\mathcal{O}(500\,\mathrm{GeV})$, forward tracking is much more important compared to LEP energies [152]. Therefore, also the very forward direction is instrumented with the Forward Tracking Detector (FTD). It consists of seven sensitive discs arranged perpendicular to the beam axis. The first disk is placed in a distance of 220 mm and the last disk 2250 mm with respect to the interaction point. This large lever arm is necessary to obtain a good momentum resolution also in the very forward direction. The system covers an angular range of up to $|\cos(\theta)| = 0.996$.

For the SIT, SET, ETD as well as for the last five disks of the FTD, silicon strip sensors are going to be used. The first two disks, which are closest to the interaction point are foreseen to be instrumented with pixel detectors for occupancy reasons. The options discussed there are the same as for the vertex detector.

The silicon detectors have a very good time resolution compared to the bunch-structure at the ILC and, thus, they are used to time-stamp the tracks.

The front-end electronics is provided by an ASIC[4], which comprises analog to digital conversion as well as a first digital data processing. Therefore, the amount of data transferred out of the detector is minimised.

---

[4] Application Specific Integrated Circuit

5.3.2.2 Time Projection Chamber

The TPC is the main tracker in the ILD concept and constitutes the major difference to the SiD concept. It consists of a large gas-filled volume with a diameter of about 3.6 m and a length of about 5 m. The central cathode is situated in the middle of the chamber, whereas the read-out pad modules are located at the end-plates and act as anodes. The support structure works as field cage ensuring a very homogeneous electric field within the TPC volume. A charged particle traversing the volume ionises the gas. The homogeneous electric field guides the electrons to the readout-pad.

The great advantage of a TPC is the fact that a very large number of 3D-space-points are measured. Its light-weight design and, therefore, small material budged supports the performance of the calorimeter and the Particle Flow reconstruction. The point resolution, which is achievable with the current design of the TPC, amounts to less than $100\,\mu$m. The double hit resolution, which is a measure of how well parallel tracks with respect to the z axis can be separated, is less than 2 mm. Another advantage of the TPC is the ability to measure the energy loss $\mathrm{d}E/\mathrm{dx}$ of a charged particle due to specific ionisation, which gives a powerful tool for particle identification [153].

In order to measure a track, the signal drift electrons have to be amplified. Currently, two technical options for the gas amplification system are considered: Micromegas [154] and Gas Electron Multipliers (GEM) [155]. R&D programmes for both options are ongoing within the LCTPC collaboration [156] and both concepts have been proven to be applicable.

One of the limiting factors of the precision of the TPC are field distortions. One topic under extensive study is the effect of ions in the drift volume of the TPC. It has been shown that mostly ion back drifts from the amplification region are problematic in terms of the precision. Therefore, concepts with active ion gating are currently under investigation.

5.3.2.3 Performance

The performance of the ILD tracking system is summarised in Figure 5.4. The track efficiency in Figures 5.4a and 5.4b is determined from a full detector simulation of the process $t\bar{t} \rightarrow 6$ jets at $\sqrt{s} = 500\,\mathrm{GeV}$ and $\sqrt{s} = 1\,\mathrm{TeV}$. Figure 5.4a shows the track reconstruction efficiency in dependence of the track momentum. For tracks with $p > 1\,\mathrm{GeV}$, the efficiency becomes almost 100%. The slight degradation of the efficiency for low-momentum tracks originates from the larger pair background at $\sqrt{s} = 1\,\mathrm{TeV}$. Figure 5.4b visualises angular dependence of the track reconstruction at ILD. The reconstruction efficiency is almost 100% even for large values of

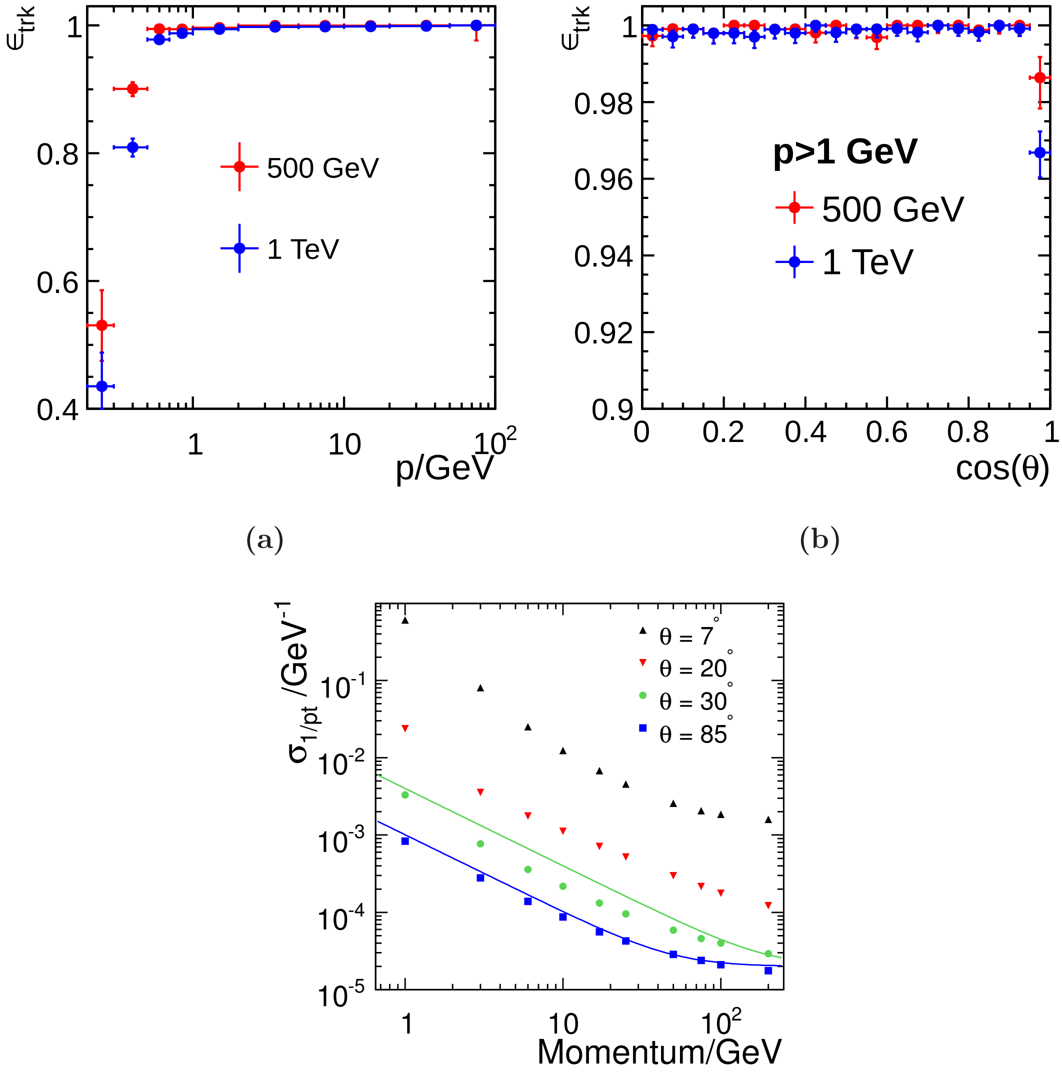

(a) **(b)**

(c)

Figure 5.4: Track efficiency in $t\bar{t} \rightarrow 6$ jets events at $\sqrt{s} = 500\,\text{GeV}$ and $\sqrt{s} = 1\,\text{TeV}$ as a function of (a) the track momentum and (b) the polar angle. The efficiency for low-momentum tracks for $\sqrt{s} = 1\,\text{TeV}$ is slightly reduced due to the larger pair background. (c) Achievable momentum resolution at the ILD. The solid lines depict the design goal for different polar angles. Figure taken from [3].

$\cos(\theta)$, which stresses the very good forward tracking performance of ILD. Finally, in Figure 5.4c, the momentum resolution in dependence of the particle momentum is shown. The solid lines indicate the envisaged momentum resolution for different incident angles formulated in the design goal (5.2). It is visible that the tracking design goal is fulfilled.

5.3.3 Calorimetry

An imaging calorimeter, which allows for a topological reconstruction of events, is the main ingredient in the Particle Flow Concept. ILD posses different calorimeter subsystems. In the barrel as well as in the forward region there is an electromagnetic calorimeter (ECAL) and an hadronic calorimeter (HCAL). Both foreseen systems are sampling calorimeters developed in the CALICE collaboration [157]. The subsystems are going to be described in more detail in the next subsections.

The forward region is additionally instrumented with a luminosity calorimeter (LCAL), a beam calorimeter (BCAL), and a low-angle hadronic calorimeter (LHCAL) developed in the FCal collaboration [158]. The LCAL acts as luminosity monitor. By reconstructing the rate of Bhabha scattered electrons/positrons the luminosity can be measured. Even more forward directed, the BCAL measures the beamstrahlung pairs produced in each bunch crossing. This measurement allows for a bunch-per-bunch estimate of the instantaneous luminosity as well as further beam parameters [159].

In total, the calorimeter system will have of the order of $\mathcal{O}(10^8)$ readout channels. This large number comprises several challenges. It is clear that a compact detector design is only possible if the readout and front-end electronics are integrated into the sensitive detector layers to a large extend. For this reason, one main effort is the development of ASICs for the different calorimeter systems which feature auto-triggering and zero-suppression, and fully digital output in order to reduce the amount of transferred data. Another critical point is the power consumption. Therefore, all the ASICs are required to support power-pulsing.

5.3.3.1 Electromagnetic Calorimeter

For the ECAL, tungsten has been chosen as absorber material. This material has a radiation length of $X_0 = 3.5\,\mathrm{mm}$ and a nuclear interaction length of $\lambda_I = 99\,\mathrm{mm}$. The rather large ratio λ_I/X_0 is ideal for an electromagnetic calorimeter, since it causes early electromagnetic showers and late hadronic showers in the calorimeter. Tungsten also features a rather small Molière radius of $R_M = 9\,\mathrm{mm}$, which allows for a good separation of close-by electromagnetic showers. Longitudinally, the ECAL is segmented into 30 layers in order to ensure the best energy resolution. The total

ECAL thickness corresponds to about $24X_0$. As a result of optimisation studies, the ECAL is transversely segmented into cells of $5 \times 5\,\mathrm{mm}^2$.

Currently, two technical options are taken into account as active layer: Silicon pin diodes are available in the targeted segmentation size, are easy to operate, and can directly be used as sensors. This is the so-called Silicon-Tungsten option. Another option foresees scintillator strips of the size $5 \times 45\,\mathrm{mm}^2$ read out with silicon photomultipliers. In an alternating arrangement of the strips, the targeted segmentation size can also be reached in this setup.

Both concepts were tested and validated in various testbeam campaigns [160, 161]. For the Silicon-Tungsten option, for example, an energy resolution of $\frac{(16.69\pm0.13)\%}{\sqrt{E(\,\mathrm{GeV})}} \oplus (1.09 \pm 0.06)\%$ has been achieved in testbeam operation [162].

5.3.3.2 Hadronic Calorimeter

In the Particle Flow Concept, the HCAL is only used to measure the energy of neutral hadrons very precisely. But in order to separate energy deposits of charged and neutral hadrons, also the HCAL has to be highly segmented. As absorber material, stainless steel has been chosen. Because of its stiffness it can directly act as support material of the active layers, which reduces the dead regions of the detector.

For the HCAL, two different concepts have been developed. The *analog* HCAL represents a sampling calorimeter, consisting of scintillation tiles and photosensors. The full analog information is preserved for the analysis. Optimisation studies have suggested tile sizes of $3 \times 3\,\mathrm{cm}^2$ and a longitudinal segmentation into 48 layers, which corresponds to six interaction lengths. This fine granularity is only possible because small silicon photomultipliers are used as photosensors.

The second concept is called the *semidigital* HCAL. Hereby, gaseous detectors are used for the active layers and the signal per cell is returned on a 2 bit digitisation level. Compared to a purely binary calorimeter version, the semidigital approach relaxes the requirements on the cell size. The best compromise between cell occupancy and cell size turns out to be $1 \times 1\,\mathrm{cm}^2$.

It has been shown in testbeam campaigns that both concepts are viable options [163, 164].

5.3.3.3 Performance

The overall jet-reconstruction performance of the ILD has been obtained by performing a full detector simulation of hadronic Z decays into light quarks (u,d,s) based

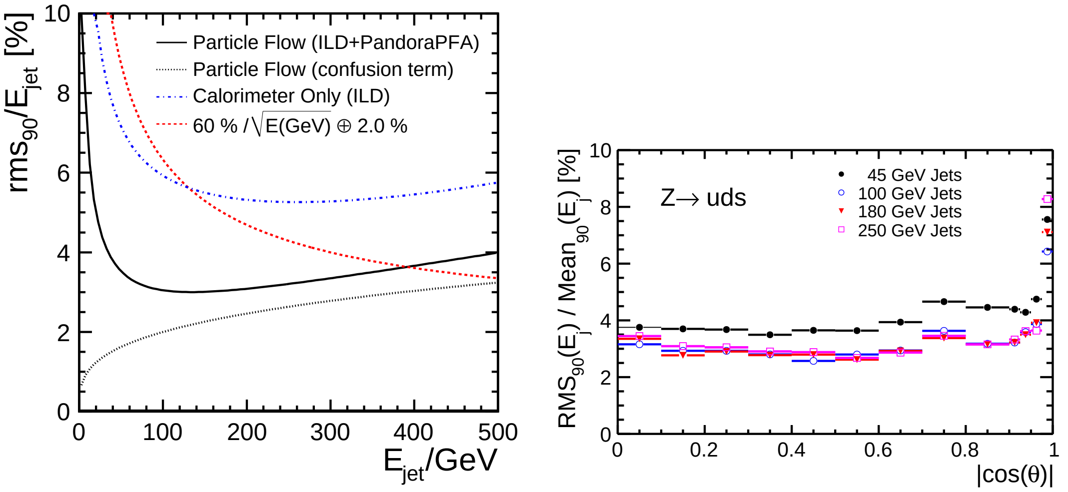

(a) **(b)**

Figure 5.5: Jet energy resolution: (a) Different contributions to jet energy resolution in dependence of the jet energy. The confusion term limits the ILD jet energy resolution for high energetic jets. Figure taken from [140]. (b) Angular dependence of the jet energy resolution. The design aim of a jet energy resolution of 3 – 4% is fulfilled. Figure taken from [57]. Please note that both figures are based on different software versions such that they are not completely compatible.

on the AHCAL option. The result is depicted in Figure 5.5a. Herein, the dotted blue line shows the jet energy resolution resulting only from the calorimeters. The increase for high jet energies originates from the leakage of high energy jets out of the relatively thin HCAL in ILD. Thus, it performs in this region worse than an assumed typical stochastic and constant term (red dotted line). Particle Flow reconstruction, however, results in a much better performance (solid black line) and is mostly limited for high energetic jets by the confusion term introduced in Section 5.2 (dotted black line). Figure 5.5a shows the contribution of the confusion term to the overall jet energy resolution achievable at ILD. For jet energies as expected at the ILC, Particle Flow reconstruction yields a significant improvement over classical calorimetry.

In Figure 5.5b, the jet energy resolution for different jet energies in dependence of the polar angle of the jet thrust axis is shown. The achievable resolution is well in agreement with the design goal.

5.3.4 Outer Detector Region

The outer part of the detector consists of a superconducting solenoid and an iron return yoke. Hereby, the return yoke fulfills different tasks:

The inner most region is segmented into ten layers of steal, each separated by 10 cm in the barrel and 14 cm in the end-cap region. The gaps in between are instrumented with scintillator strips and silicon photomultipliers, like in the AHCAL option, but also resistive plate chambers are considered as alternative for the sensitive layer. Thus, the inner most part of the yoke acts as a tail catcher, measuring tails of hadronic showers of the HCAL. It has been shown that the tail catcher further improves the jet energy resolution.

The outer part of the return yoke comprises additional three sensitive layers spaced by 60 cm. Together with the first part it serves as muon detector.

The whole yoke also works as main mechanical frame of ILD. Because of its big amount of steel it helps to achieve the radiation safety requirements, which foresee the ILD to be a self-shielding detector during operation. One of the main purposes of the yoke is the flux return of the magnetic field, which is needed in order to reduce the fringe field to a maximum of 50 G in a distance of 15 m from the interaction point. This is one of the design requirements in order to avoid interference of the magnetic fields of the two detectors in the underground hall.

The magnet design involves a superconducting solenoid providing a magnetic field of $3.5-4.0$ T. It is complemented by the anti-DID[5], which consists of two additional dipole magnets modulating the magnetic flux inside the detector in order to guide low energetic beam background out of the detector. This becomes necessary due to the crossing angle of both beams (cf. Chapter 3).

5.4 Software Chain

For a future experiment, hardware design as well as prototyping are essential. But also proper software tools have to be developed, which allow for Monte-Carlo simulation and reconstruction of physics events. At this, the ILD software is more elaborate than for any previous experiment before the actual project start. This high level of detail is demanded by the Particle Flow concept and allows the detector optimisation based on physics goals.

In the following section, we describe briefly the ILD software framework.

---

[5] detector integrated dipole

5.4.1 Event Generation

In order to generate Monte-Carlo events, `Whizard 1.95` [165] is used as event generator. `Whizard` was initially developed for physics at a linear collider. Thus, it is well adaptable to the specific needs at the ILC. It can handle a collider specific beam spectrum, initial state radiation, and beam polarisation.

`Whizard` uses internally `O'Mega` [166] as matrix element generator. This tool allows for the computation of helicity amplitudes for any possible process in a given model. `O'Mega` is written in a very efficient way such that also rather complicated final states with many contributing diagrams, like 2 → 6 processes, can be computed very resource efficiently. As output `O'Mega` produces compilable `FORTRAN` code, which is the input for a user specific `Whizard` event generator incorporating the defined processes.

In the ILD software chain, `Whizard` is employed for the event generator of the hard interaction. For the simulation of the fragmentation and hadronisation, `PYTHIA 6.4.22` is called internally. Hereby, the OPAL `PYTHIA` tune is used [167].

The standard output format of the event generation step is `stdhep` [168].

5.4.2 Event Data Model

The ILC event data model is defined in the `LCIO` package [169]. It declares data structures for all possible data which can arise in an event. `LCIO` is designed in order to be capable to serve as data model for the whole life-cycle of an experiment at the ILC, from simulation to real data taking.

`LCIO` provides classes for very low level data, like detector hits, but also more evolved structures like calorimeter clusters and tracks. It also serves as data model for event reconstruction and offers data structures for reconstructed objects, particle IDs etc.

Monte-Carlo data from event simulation are present as MCParticles in the data model. There exist dedicated tools to convert `stdhep` data into the `LCIO` format. There are recently discussions ongoing for supporting `LCIO` natively by the event generator `Whizard`.

All the `LCIO` objects are collected per each event in object collections of a certain object type, which serve as input for all algorithms in the software chain. `LCIO` data can be persistently stored in the “slcio” format.

5.4.3 Detector Simulation

The detector simulation is implemented in the software package `Mokka` [170], which is based on the GEANT 4 framework [171, 172]. `Mokka` is part of `iLCsoft` – a collection of linear collider related software tools. A very realistic model of the ILD detector exists, which allows for involved ILD performance studies as well as physics analyses. All subdetectors have been implemented at a high level of detail including dead material, mechanical support structures, electronics, cabling, and gaps. Three different detector models are defined, which differ in the combination of ECAL and HCAL option (cf. Section 5.3.3) [57]:

name	HCAL option	ECAL option
`ILD_o1_v05`	analog	Silicon-Tungsten
`ILD_o2_v05`	semi-digital	Silicon-Tungsten
`ILD_o3_v05`	analog	Scintillator-Strip

For the following study, option `ILD_o1_v05` has been used.

For this thesis, the ILD detector simulation has been extended in order to be able to emulate also the response of exotic long-lived particles. Since this is not a default feature, this will be described in Section 6.1.2 in more detail.

5.4.4 Background Overlay

Considering the strong electromagnetic fields during an ILC bunch collision, the ILC can also be understood as a photon collider. Therefore, an important background that has to be considered is the $\gamma\gamma \rightarrow$ hadrons background. Figure 5.6a shows a schematic Feynman diagram. These events involving virtual or real photons are simulated and considered as additional SM background. In the soft-collinear limit of the photons, however, the cross section diverges and one enters a nonperturbative QCD regime of hadron production [173]. The cross section for this low-p_t $\gamma\gamma$-events become so large that in average $\langle N \rangle = 1.2$ events take place per bunch crossing for the instantaneous luminosity foreseen at ILC500. For this reason, those events act as pileup to any other hard process and, thus, have to be taken into account for a realistic simulation.

Therefore, $\gamma\gamma \rightarrow$ hadrons events are generated with `PYTHIA`, which models those events well, and the detector response is simulated by `Mokka`. In the detector simulation, the actual z position of the interaction point is smeared by a Gaussian with $\sigma_z = 300\,\mu$m according to ILD500 bunch parameters. Any event of a hard process is overlaid with an Poissonian distributed number of $\gamma\gamma \rightarrow$ hadrons events (in average

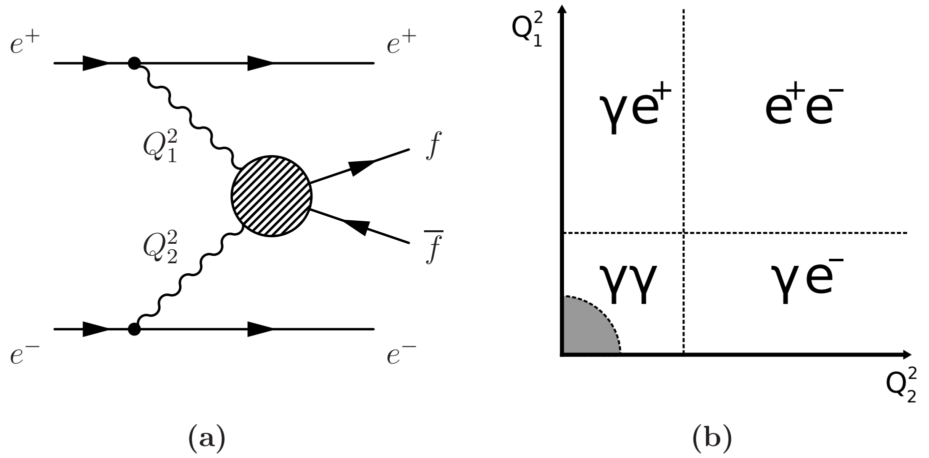

(a) **(b)**

Figure 5.6: (a) Schematic Feynman diagram of $\gamma\gamma \rightarrow f\overline{f}$. In the soft-collinear limit of the photons, the nonperturbative regime is entered. (b) $\gamma\gamma$ and γe events are additional background samples. For low-p_t photons (shaded area) the cross section becomes so large that low-p_t $\gamma\gamma$-events act as pileup to any other hard process.

$\langle N \rangle$) before the reconstruction step is performed in order to simulate the effect of the pileup.

At the time of the Monte-Carlo mass production for the ILC TDR a slightly too large number $\langle N \rangle = 1.7$ had been estimated, which results in a too conservative estimation of the $\gamma\gamma \rightarrow$ hadrons background in the samples used in this analysis. Nevertheless, it turns out that the impact is negligible (cf. Section 6.2.2).

5.4.5 Standard Event Reconstruction and Analysis

The event reconstruction and analysis tools are implemented in the `Marlin` framework [174], which is also part of `iLCsoft`. The software is organised in so-called processors that work on collections of `LCIO` objects in the events.

Recently, a lot of effort was put into the re-implementation of the ILD tracking software. It comprises processors for pattern recognition in the TPC (`Clupatra`) and for the forward tracking (`FwdTracking`), a track fitter, based on a Kalman filter (`KalTest`) and a tool to combine the single track segments into the final output tracks (`FullLDCTracking`). The new tracking software is much more resource efficient and, therefore, well capable to deal also with high multiplicity environments as expected for events at the ILC1000, for instance.

The Particle Flow Algorithms (PFA) are implemented in the package `PandoraPFANew`, which contains more than 60 advanced algorithms for calorimeter cell clustering, track-cluster-matching and re-clustering [140, 142]. A lot of software engineering has gone into `PandoraPFANew` in order to disentangle geometry, algorithms and steering in the software. As final result the `Marlin` interface `MarlinPandora` returns a list of Particle Flow Objects (PFO) including a first particle identification. Those PFOs are the basis for more advanced analyses.

For the vertex finding, the packages `LCFIVertex` [175] and `LCFIPlus` are used. Both packages provide secondary vertex finding, jet clustering, and flavour tagging based on artificial neuronal networks and multivariate analysis methods, respectively. The secondary vertex finding is ran by default in the standard event reconstruction. Whereas the other algorithms can be employed by the user if needed for the specific analysis.

The package `MarlinReco` offers many preimplemented processors for user specific event reconstruction and analysis. However, also new user processors can be easily implemented by inheriting from the `Marlin` processor class. Processors are configured via input parameters, which are set by an XML steering file. This file also defines the order of the processor execution.

For easy data analysis the processor `LCTuple` exists, which dumps the `LCIO` event collection into lightweight ROOT trees [176].

6 Bilinear RPV SUSY Study – Simulation and Event Selection

One of the main goals of the bRPV SUSY analysis performed in this thesis is to measure the ratio of branching ratios of LSP decays into $W\mu$ and $W\tau$, since this measurement allows one to determine the neutrino atmospheric mixing angle. The bRPV SUSY event generation and simulation is described in Section 6.1. In Section 6.2, the signal classes are defined and the $\gamma\gamma$ background removal as well as a first event preselection is performed. Finally, in Section 6.3, the event selection is presented.

6.1 Event Simulation

The event simulation of the signal events comprises two challenges: Firstly, we describe the event generation of the exotic bRPV SUSY model with the event generators `Whizard` and `PYTHIA`. Secondly, the implementation of long-lived $\widetilde{\chi}^0_0$ in the detector simulation `Mokka` is presented.

6.1.1 From a Model to Generated Events

In order to generate physics events, the specific model has to be implemented in `Whizard`. The `Whizard` software package is already delivered with the most frequently used models, like the Standard Model or the R-parity conserving MSSM. However, in order to generate events for a more exotic model, like the bRPV MSSM, some effort has to be made in defining the event generator model files.

6.1.1.1 Model File Generation

A suitable computing tool for model file generation is `Sarah` [177, 178]. `Sarah` is a Mathematica package [179] for studying ($N = 1$) supersymmetric models. The package needs as input the structure of the gauge sector of a model. At this, `Sarah` can deal with any direct sum of $SU(n)$ and $U(1)$. Moreover, the particle content,

symbol	meaning	approximate correspondence
$\{n_1, n_2, n_3, n_4, n_5, n_6, n_7\}$	neutral fermion	$\{\nu_1, \nu_2, \nu_3, \widetilde{\chi}^0_1, \widetilde{\chi}^0_2, \widetilde{\chi}^0_3, \widetilde{\chi}^0_4\}$
$\{e^\pm_1, e^\pm_2, e^\pm_3, e^\pm_4, e^\pm_5\}$	charged fermion	$\{e^\pm, \mu^\pm, \tau^\pm, \widetilde{\chi}^\pm_1, \widetilde{\chi}^\pm_2\}$
$H^\pm_i$	charged scalars	parameter point dependent

Table 6.1: Naming scheme of particles within the bRPV SUSY model.

i.e. all irreducible representations of the chiral superfields and their corresponding quantum numbers have to be defined. From this, `Sarah` calculates automatically the gauge interactions. All matter interactions have to be entered by the definition of a superpotential. Additionally, a few further definitions of the VEVs, gauge fixing, etc. have to be made.

Based on this information, `Sarah` provides symbolic calculations on tree level for masses, tadpole equations, all vertices, and two-loop renormalisation group equations, for instance. It also tests the defined model automatically for gauge anomalies or charge conservation. This makes this programme a useful tool for model building.

However, `Sarah` also provides interfaces for generating model files for other HEP programs, like `CalcHep`, `FeynArts/FormCalc` or `Whizard`. For this reason, this package is also very useful for performing phenomenological and simulation studies of exotic models.

Recently, a new version of `Sarah` was published (version 4.0), which extends these features also to non-SUSY models.

For the generation of the bRPV MSSM `Whizard` model files, `Sarah 3.0.beta5` has been used in this analysis. This version already contains a definition of the bRPV MSSM model. Thus, the `Whizard` model files can be generated easily. After inserting the model files into the `Whizard` file structure, the model can be used to define processes and, thus, a bRPV MSSM version of `Whizard` can be built.

6.1.1.2 Naming Scheme

As already pointed out in Section 4.2, bRPV introduces mixing among SUSY and Standard Model fields in the lepton and Higgs sector. This is reflected in the naming scheme of the different particles within `Sarah`, as summarised in Table 6.1.

For the neutral and charged fermions, an approximate correspondence between the bRPV mass eigenstates and the usual MSSM mass eigenstates can be given if the bRPV parameters are small. The charged scalars comprise the sleptons and charged Higgs boson ordered by their masses. Since the individual masses of the sleptons and the charged Higgs boson are parameter point dependent, no general relation exists.

In spite of the special naming, the original particle character of the individual mass eigenstates remains almost unchanged. For this reason, we use the more comprehensive and familiar MSSM naming scheme in the following, i.e. n_4 will always be called $\tilde{\chi}_1^0$, for instance.

6.1.1.3 Cross Section Validation

In order to validate the generated model files, we have chosen an arbitrary SUSY model point (SPS1a'). All SUSY parameters (masses, mixing angles, couplings) have been evaluated at this point with the spectrum generator `SPheno 3.1` [180, 181], as bRPV MSSM is directly implemented in `SPheno`. For this specific parameter point, we have derived the production cross sections for all production channels (excluding squarks) with the modified `Whizard` version. `SPheno` also provides an independent routine to calculate the production cross sections of SUSY particles within the bRPV MSSM. Thus, a comparison between the results of `SPheno` and the bRPV version of `Whizard` is possible in order to cross-check and validate the `Whizard` implementation.

We have set the center-of-mass energy for the cross-section calculation to $\sqrt{s} = 2\,\text{TeV}$ in order to enable all targeted production channels.

It has to be noted that `SPheno` and `Sarah` use a different definition of particle mixing matrices, which makes a careful treatment of the `SPheno` input parameter in `Whizard` necessary.

The results of the comparison are shown in Table 6.2.

The difference between the cross section calculated by `SPheno` and the cross section obtained from the bRPV `Whizard` version generated with `Sarah` is shown in the last column of Table 6.2. Here, Δ is defined as the relative deviation of both results

$$\Delta = \frac{\sigma_{\text{Sarah}} - \sigma_{\text{SPheno}}}{\sigma_{\text{Sarah}}} \cdot 100\%. \tag{6.1}$$

Except for a few outliers, the deviations are below one percent. The strong deviation in some of the processes are understood and can be traced back to missing contributions in the cross section calculation in `SPheno` [182]. Since the cross section calculation comprises many aspects of a model, the good agreement between both programs consolidates the reliance in the `Sarah` generated model files.

Process	σ_{Sarah} [fb]	δ_{Sarah} [%]	σ_{SPheno} [fb]	Δ [%]
$e_1^- e_1^+ \to n_1 n_1$	1.475×10^4	1.05×10^{-1}	6.255	$1. \times 10^2$
$e_1^- e_1^+ \to n_2 n_2$	4.269×10^3	9.9×10^{-2}	6.255	9.99×10^1
$e_1^- e_1^+ \to n_3 n_3$	1.937×10^3	1.05×10^{-1}	6.255	9.97×10^1
$e_1^- e_1^+ \to n_4 n_4$	3.285×10^1	2.57×10^{-2}	3.289×10^1	-1.23×10^{-1}
$e_1^- e_1^+ \to n_4 n_5$	1.141×10^1	2.51×10^{-2}	1.141×10^1	-1.41×10^{-2}
$e_1^- e_1^+ \to n_4 n_6$	6.61×10^{-1}	2.06×10^{-2}	6.608×10^{-1}	2.21×10^{-2}
$e_1^- e_1^+ \to n_4 n_7$	1.409	2.26×10^{-2}	1.409	-8.67×10^{-3}
$e_1^- e_1^+ \to n_5 n_5$	1.855×10^1	2.14×10^{-2}	1.854×10^1	7.57×10^{-2}
$e_1^- e_1^+ \to n_5 n_6$	1.545	1.37×10^{-2}	1.545	9.29×10^{-3}
$e_1^- e_1^+ \to n_5 n_7$	2.376	1.43×10^{-2}	2.375	3.58×10^{-2}
$e_1^- e_1^+ \to n_6 n_6$	4.174×10^{-3}	1.47×10^{-2}	4.175×10^{-3}	-1.12×10^{-2}
$e_1^- e_1^+ \to n_6 n_7$	1.038×10^1	5.69×10^{-3}	1.039×10^1	-1.88×10^{-2}
$e_1^- e_1^+ \to n_7 n_7$	8.225×10^{-2}	2.71×10^{-2}	8.223×10^{-2}	2.47×10^{-2}
$e_1^- e_1^+ \to e_1^+ e_1^-$	1.286×10^9	2.79×10^1	2.985×10^1	$1. \times 10^2$
$e_1^- e_1^+ \to e_2^+ e_2^-$	2.985×10^1	2.86×10^{-2}	2.985×10^1	-1.26×10^{-2}
$e_1^- e_1^+ \to e_3^+ e_3^-$	2.987×10^1	2.77×10^{-2}	2.985×10^1	6.57×10^{-2}
$e_1^- e_1^+ \to e_4^- e_4^+$	4.648×10^1	2.16×10^{-2}	4.649×10^1	-9.75×10^{-3}
$e_1^- e_1^+ \to e_4^- e_5^+$	2.848	1.65×10^{-2}	2.849	-2.3×10^{-2}
$e_1^- e_1^+ \to e_5^- e_4^+$	2.848	1.6×10^{-2}	2.849	-2.55×10^{-2}
$e_1^- e_1^+ \to e_5^- e_5^+$	2.886×10^1	6.42×10^{-3}	2.886×10^1	-8.86×10^{-3}
$e_1^- e_1^+ \to h_1 Z$	3.101	1.82×10^{-2}	3.157	-1.83
$e_1^- e_1^+ \to h_2 A_2^0$	2.992	1.18×10^{-2}	2.992	-2.03×10^{-2}
$e_1^- e_1^+ \to h_3 A_3^0$	2.99	1.09×10^{-2}	2.989	$3. \times 10^{-2}$
$e_1^- e_1^+ \to h_4 A_4^0$	1.859×10^2	2.97×10^{-2}	2.989	9.84×10^1
$e_1^- e_1^+ \to h_5 A_5^0$	2.329	1.18×10^{-2}	2.328	3.88×10^{-2}
$e_1^- e_1^+ \to H_2^+ H_2^-$	6.903	9.78×10^{-3}	6.905	-3.17×10^{-2}
$e_1^- e_1^+ \to H_2^+ H_7^-$	2.498×10^{-1}	1.06×10^{-2}	2.499×10^{-1}	-1.74×10^{-2}
$e_1^- e_1^+ \to H_3^+ H_3^-$	7.077	9.11×10^{-3}	7.08	-3.57×10^{-2}
$e_1^- e_1^+ \to H_3^+ H_6^-$	1.410×10^{-3}	1.03×10^{-2}	1.41×10^{-3}	-2.01×10^{-2}
$e_1^- e_1^+ \to H_4^+ H_4^-$	1.114×10^2	4.67×10^{-2}	1.114×10^2	-1.38×10^{-2}
$e_1^- e_1^+ \to H_4^+ H_5^-$	8.79	5.82×10^{-2}	8.784	6.43×10^{-2}
$e_1^- e_1^+ \to H_5^+ H_4^-$	8.778	5.85×10^{-2}	8.784	-6.29×10^{-2}
$e_1^- e_1^+ \to H_5^+ H_5^-$	8.204×10^1	3.08×10^{-2}	8.211×10^1	-7.75×10^{-2}
$e_1^- e_1^+ \to H_6^+ H_3^-$	1.410×10^{-3}	9.21×10^{-3}	1.41×10^{-3}	1.23×10^{-2}
$e_1^- e_1^+ \to H_6^+ H_6^-$	7.258	1.05×10^{-2}	7.262	-5.37×10^{-2}
$e_1^- e_1^+ \to H_7^+ H_2^-$	2.498×10^{-1}	$1. \times 10^{-2}$	2.499×10^{-1}	-3.7×10^{-2}
$e_1^- e_1^+ \to H_7^+ H_7^-$	6.963	1.05×10^{-2}	6.962	1.68×10^{-2}
$e_1^- e_1^+ \to H_8^+ H_8^-$	5.643	9.95×10^{-3}	5.644	-1.67×10^{-2}

Table 6.2: Comparison between cross sections calculated by `SPheno 3.1` and `Whizard` based on model files provided by `Sarah 3.0.beta5`. For comparison, an arbitrary SUSY parameter point has been chosen. The center-of-mass energy has been set to $\sqrt{s} = 2\,\text{TeV}$ in order to ensure all channels to be kinematically allowed. The large deviations in some processes are understood and traced back to missing contributions within the calculation by `SPheno`.

6.1.1.4 LSP Decay

`Whizard` is only used for generating the hard process, which does not include the decay of the SUSY particles. In the following, we will focus only on LSP-pair production. In bRPV SUSY, the lightest supersymmetric particle decays into Standard Model particles. These decays are carried out by `PYTHIA`. The factorisation of production and decay is possible because the LSP width in bRPV models is usually very small ($\Gamma_{\tilde{\chi}_1^0} = \mathcal{O}(10^{-14}\,\text{GeV})$) and, thus, the narrow-width approximation is applicable [183]. The error introduced by this method is estimated to be $\mathcal{O}(\Gamma/m)$ and, therefore, negligibly small for LSP masses of some GeV.

In order to enable `PYTHIA` to decay the LSP properly, the SUSY parameters have to be transferred to `PYTHIA`. To this end, `PYTHIA` provides an interface to read in a SUSY Les Houches Accord (SLHA) file [184, 185], which is a standardised file format for sharing SUSY parameters among different programs. It contains the numerical values for the mixing matrices, decay widths and branching fractions of SUSY particles. Since `PYTHIA` is called internally by `Whizard` for hadronisation and fragmentation, we have had to modify the `PYTHIA` interface in order to read in and use the SLHA file before.

Finally, we obtain proper bRPV Monte-Carlo (MC) events as result, which are the basis of a full ILD simulation.

6.1.2 Long-lived Neutralinos within the ILD Simulation

Due to its small decay width, the LSP is rather long-lived. This introduces some difficulties in the detector simulation since these exotic long-lived particles have to be tracked for a finite distance by GEANT. Triggered by the needs of the bRPV analysis, we have developed a generic routine for `Mokka` for transferring the lifetime information from the Monte-Carlo generator to the detector simulation.

The algorithm enters in the place where the MC truth information of `MCParticles` is translated into the GEANT 4 object structure of `G4PrimaryParticles`. `MCParticles` as well as `G4PrimaryParticles` are organised in a tree structure holding information about mother and daughter particles associated with the specific particle. The MC truth tree, however, includes the whole event history from the initial hard interaction down to the hadronisation. There are intermediate states that are clearly of no interest for the detector simulation. However, taking into account only entries which are flagged as final state particles in the MC truth list would ignore intermediate unstable particles which decay into stable particles in some distance from the actual primary vertex. A better approach is to use the generator lifetime information. The developed recursive algorithm loops over the MC truth history

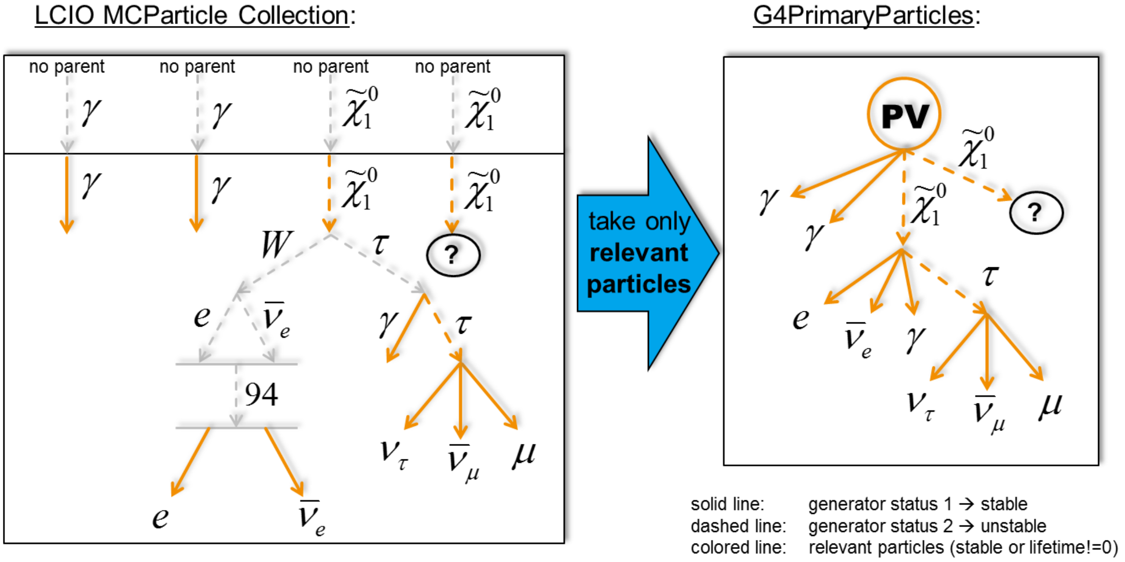

Figure 6.1: Translation of Monte-Carlo truth to Geant primary particles. A detailed description is given in the text.

and concatenates all particles which are either flagged as stable (generator status 1) or unstable (generator status 2), but have a lifetime unequal to zero.

Figure 6.1 shows a typical example of a bRPV event of $e^+e^- \to \tilde{\chi}_1^0\tilde{\chi}_1^0$ and the subsequent decays. The left box depicts the MC truth tree. Herein, the first row represents entries in the MC truth list originating from the `Whizard` part of the event generation. It is a general feature that `Whizard` always adds two photons to the actual demanded process, which takes care of initial state radiation (ISR). If no ISR is present in a specific event, the photons just carry no energy. These first lines in the MC truth history are present only for documentation of the production process by `Whizard`. Nevertheless, they are of importance, as they are the starting point for the algorithm in order to find the relevant particles for the detector simulation.

The second and following lines in the left box of Figure 6.1 show the part of the MC truth list written by `PYTHIA`. Both photons are taken over by `PYTHIA`, but now flagged as stable objects. Therefore, they get directly assigned to the tree of `G4PrimaryParticles` (see right box of Figure 6.1). The situation is more interesting for the neutralinos. The generator assigned to both neutralinos a lifetime. For that reason, although they are unstable, they are added to the `G4PrimaryParticle` tree. In the left branch of the LSP decay the W-boson decays promptly, so it is left out in the `G4PrimaryParticle` tree. The same is true for the two decay products since they first form an intermediate internal generator state (PDG ID 94) before they become stable particles. The right branch of the LSP decay shows a bremsstrahlungs process, where a photon is emitted from a τ lepton. So, also the first τ lepton is

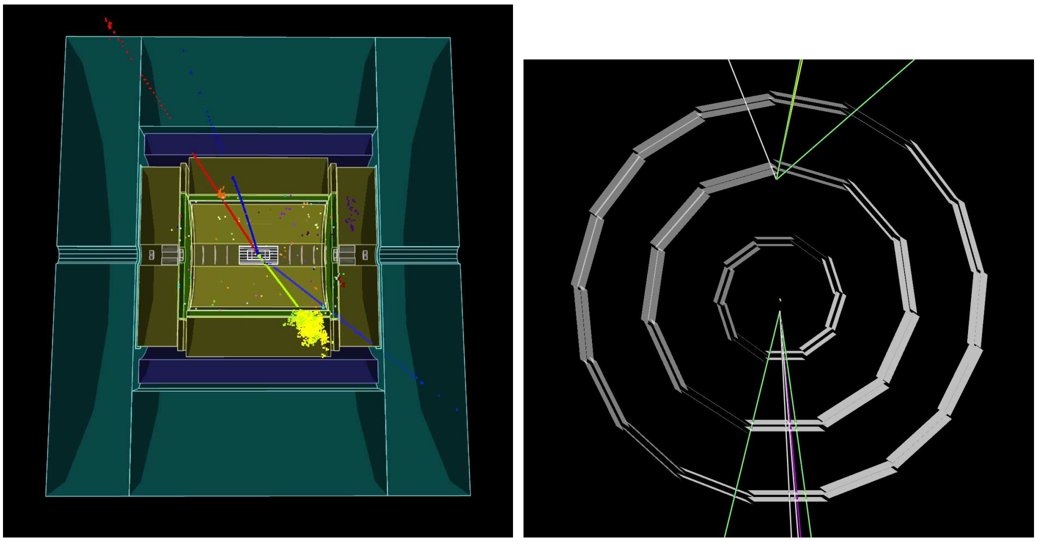

(a) (b)

Figure 6.2: Event display of a leptonic bRPV event in ILD. (a) Side view of ILD showing the simulated detector interaction. (b) Transversal view, zoomed into the interaction region. The three concentrical double layers represent the VTX detector. The inner layer is situated 16 mm away from the interaction point. The lines display the Monte-Carlo truth information of the simulated particle (green: charged particle, purple: neutral hadron, yellow: photon, white: neutrino). A clear displacement of the vertices is visible.

left out. The second τ lepton, however, has to be considered, since it flies a certain distance before it decays into stable particles.

The resulting tree of `G4PrimaryParticles` is finally associated to a primary vertex (PV), which is the starting point for the actual GEANT 4 simulation. Although the assigned momenta will change in the simulation due to scattering processes and the presence of a magnetic field, for instance, the ongoing decay chain is fully predetermined by the `G4PrimaryParticle` tree.

As a last step, new exotic particles that are going to be tracked by GEANT have to be registered in the `G4ParticleTable`. Within `Mokka` this can be easily done. A text file that contains the ID, name, charge, mass, total width, and lifetime of the exotic particle has to be provided and be enabled in the `Mokka` steering file.

Figure 6.2 shows finally an event display of a properly simulated bRPV event:

$$e^+e^- \rightarrow \tilde{\chi}_1^0\tilde{\chi}_1^0 \rightarrow (\mu^+W^-)(\mu^+\nu_{\mu^-}\tau^+) \rightarrow (\mu^+\mu^-\gamma\overline{\nu}_\mu)(\mu^+\nu_\mu\overline{\nu}_\tau\pi^0\pi^+). \qquad (6.2)$$

In the side view of the ILD (Figure 6.2a) the different detector subcomponents and the specific simulated detector response is visible. In the upper hemisphere one can observe two escaping muons originating from the first $\widetilde{\chi}_1^0$ decay and in the lower hemisphere one muon and the one-prong τ decay from the other $\widetilde{\chi}_1^0$ decay is present. For the muons, the MIP[1] trace is depicted in the calorimeters, whereas an hadronic shower is displayed for the hadronic τ decay. A zoom into the interaction region (Figure 6.2b) shows the Monte-Carlo truth information of the simulated particles, which confirms that the displaced vertices have been successfully introduced by the described new long-lived exotic particle treatment.

6.1.3 Data Samples

Initially, for the event generation, an mSUGRA motivated SUSY point has been used ($m_0 = 220\,\mathrm{GeV}$, $m_{1/2} = 250\,\mathrm{GeV}$, $\tan(\beta) = 10$, $\mathrm{sgn}(\mu) = +$, $A_0 = -300\,\mathrm{GeV}$). In total, 38000 bRPV events $e^+e^- \rightarrow \widetilde{\chi}_1^0\widetilde{\chi}_1^0$ have been generated, which corresponds to an integrated luminosity of $\int L dt = 100\,\mathrm{fb}^{-1}$. A center-of-mass energy of $\sqrt{s} = 500\,\mathrm{GeV}$ and a beam polarisation of $\mathcal{P}(e^-, e^+) = (-30\%, 80\%)$ has been chosen for the analysis.

The mSUGRA point does not agree with the current measurement of the Higgs mass and features a too light coloured particle spectrum. For this reason, the generated events have been reinterpreted in the framework of the benchmark scenario (cf. Section 4.4), where the Higgs sector and coloured sector are adapted correspondingly, but the relevant parameters, like $m_{\widetilde{\chi}_1^0}$ and $m_{\widetilde{e}_R}$, are kept equal. Since the predicted production cross section and branching ratios at the benchmark point differ slightly from the originally produced mSUGRA point, the simulated events have been reweighted with respect to the new parameter point. The SUSY Les Houches Accord parameter files for the mSUGRA point and the benchmark point can be found in Appendix B.

It has to be noted that the decay length for the simulated mSUGRA point is slightly larger and amounts to $c\tau = 4.18\,\mathrm{mm}$. The decay length cannot be easily adapted to the correct value at the parameter point in the simplified model. Therefore, we have accepted this slightly too large value. However, since we are not going to exploit the lifetime information in this analysis, the effect should be negligible.

The simulated events have been overlaid with $\gamma\gamma \rightarrow$ hadrons background, where we have decided to also choose a too large number of overlay events per bRPV event in order to be consistent with the already produced Standard Model background samples (see discussion in Section 5.4.4). The simulated and overlaid bRPV events have finally been reconstructed by the standard reconstruction described in Section 5.4.5.

For the following analysis, the signal sample is accompanied by Standard Model background samples, which have been produced for the ILC TDR [57]. The Standard Model background is subdivided into several subsamples discriminated by the

---

[1] minimum ionising particle

	$\mathcal{P}(e^-, e^+)$		
w_h^{pol}	$(0\%, 0\%)$	$(+80\%, -30\%)$	$(+80\%, -60\%)$
w_{RR}^{pol}	0.25	0.315	0.180
w_{RL}^{pol}	0.25	0.585	0.720
w_{LR}^{pol}	0.25	0.035	0.020
w_{LL}^{pol}	0.25	0.065	0.080

Table 6.3: Weighting factors for typical beam polarisations at the ILC. The weighting factors for the opposite sign in the polarisation can be obtained for an exchange of $R \leftrightarrow L$.

number of fermions in the final state and the production mode (cf. also Figure 5.6b). We have considered the following subsamples:

nf (ee): $e^+e^- \to n$ fermions, with $n \in \{2, 4, 6\}$
4f ($\gamma\gamma$): $\gamma + \gamma \to 4$ fermions
5f (eγ): $e^\pm + \gamma \to 5$ fermions

Since the event topology of the subsamples 2f ($\gamma\gamma$) and 3f (eγ) are very different from the signal events and, therefore, play a negligible role, those have not been considered.

All the individual SM background subprocess samples p are available for all allowed helicity combinations $h \in \{RR, RL, LR, LL\}$ of the incoming electron and positron. In order to adapt the available statistic of the individual subprocesses to the envisaged integrated luminosity, a luminosity weighting is performed

$$w_{p,h}^{\mathrm{lumi}} = \frac{\sigma_{p,h} \cdot \int L \mathrm{d}t}{N_{p,h}^{\mathrm{prod}}}, \tag{6.3}$$

where $\sigma_{p,h}$ is the helicity cross section of the subprocess p, $N_{p,h}^{\mathrm{prod}}$ the number of produced events of the subprocess p with a certain helicity combination h, and $\int L dt$ denotes the targeted integrated luminosity.

In addition to the luminosity weighting, the different helicity combinations of the individual subprocesses are weighted according to Equation (3.8) in order to obtain the desired polarisation. Table 6.3 contains the weighting factors for typical beam polarisations at the ILC.

This leaves us finally with the overall weighting factor

$$w_{p,h} = w_{p,h}^{\mathrm{lumi}} \cdot w_h^{\mathrm{pol}}, \tag{6.4}$$

which is used to scale the SM background samples correctly to the design parameters of the study.

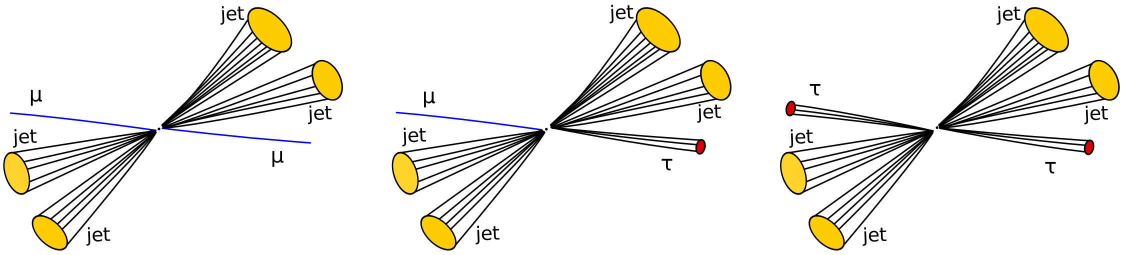

(a) $\mu\mu$ event **(b)** $\mu\tau$ event **(c)** $\tau\tau$ event

Figure 6.3: Event topologies of the signal events.

6.2 Event Preparation

In the following, the event selection is presented in detail. We start with the general event preparation, which includes $\gamma\gamma \to$ hadrons background removal as well as a first event preselection.

6.2.1 Event Topology and Signal Classes

In order to be able to measure the ratio of the two branching ratios, it is especially important to separate the different signal decay modes. Therefore, we define three signal event classes, which reflect the different possible final states in LSP pair-produced events involving the signal decays: $\mu\mu$ class, $\mu\tau$ class, and $\tau\tau$ class (cf. Figure 6.3). The classes are named after the corresponding present final state leptons. All events which contain at least one non-signal-like decay are treated as background.

In the analysis, we consider only hadronic W-boson decays such that there exist no major source of missing energy in the events, except for the neutrino in the τ decay, which is unavoidable. By doing this, we also profit from the larger branching fraction of the W boson into hadrons (68%) compared to the fraction into leptons (32%). It has already been discussed that the ILD detector is very well suited for reconstructing the W-boson mass in the hadronic channel because of the very good performance of Particle Flow (cf. Figure 5.1).

Thus, the events, we are looking for, have six visible objects in the final state. Two pairs of jets reconstruct to two W bosons and, each W-boson candidate together with one of the remaining objects reconstructs the LSP mass, accordingly. The event selection can be tailored very accurately to this described topology in order to select signal events and to distinguish the different event classes to high precision. This will be discussed in much more detail in Section 6.3.

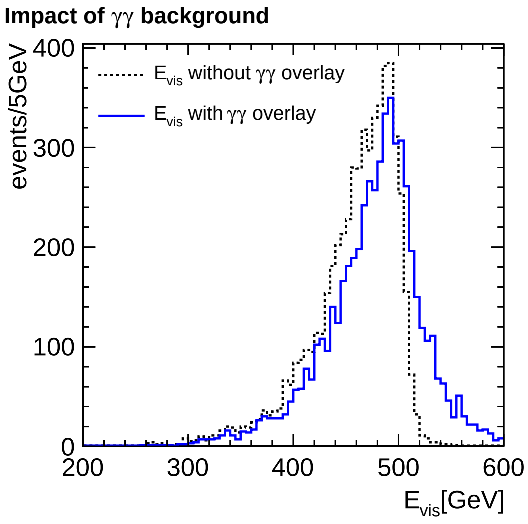

(a)

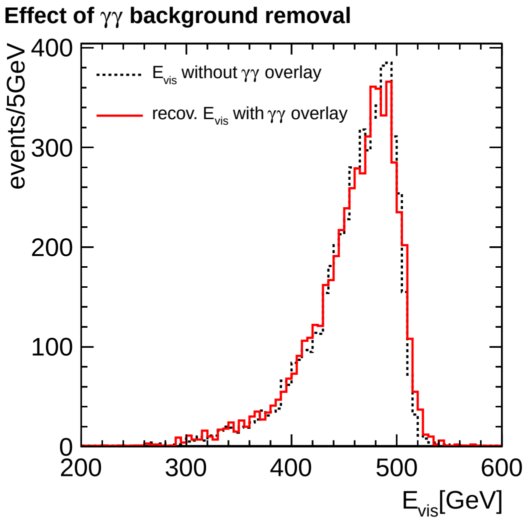

(b)

Figure 6.4: (a) Effect of $\gamma\gamma \to$ hadrons background overlay on the visible energy in the bRPV SUSY signal sample. (b) Recovered visible energy in the event after $\gamma\gamma \to$ hadrons background removal procedure, as described in the text.

6.2.2 $\gamma\gamma$ Overlay Removal

The effect of the overlay of $\gamma\gamma \to$ hadrons events is depicted in Figure 6.4a. This figure shows the distribution of the total visible energy per event for the bRPV SUSY signal sample without (dotted black line) and with (solid blue line) $\gamma\gamma \to$ hadrons overlay. It is observable that the overlay shifts the visible energy considerably to higher energies, which would have a severe impact on the analysis.

The produced hadrons are very forward directed, low-p_t objects. A strategy for removing this forward contribution is borrowed from hadron collider analyses: At an hadron collider there is typically a large forward directed background originating from the beam remnants that does not belong to the actual hard process. For this reason, at hadron colliders usually *exclusive* jet algorithms are used in the analyses. Exclusive in this context means that not all reconstructed objects in an event are clustered to jets associated to the hard process. Instead, two additional beam jets are built up, which absorb the beam remnants. These beam-jets are discarded and, thus, the original event is recovered.

We use this technique as well, and choose an exclusive k_T jet clustering algorithm [186, 187] with the clustering parameter $R = 1.3$. This value has been found to be optimal in other studies [188]. As termination condition for the clustering process, the algorithm is forced to find six jets in an event, since this reflects best the targeted signal-event topology. If the k_T jet algorithm does not converge, the event is directly rejected because it implies that the event is in no way compatible with a six-final-state topology. The found jets are in a next step again decomposed into the single Particle Flow Objects, which are used for the further analysis.

The comparison of the visible energy in the bRPV SUSY signal sample after the background removal procedure (solid red line) with the non-overlayed sample (dotted black line) is depicted in Figure 6.4b. It illustrates that the situation without overlay can be almost restored.

6.2.3 Preselection

In a next step, we perform a preselection in order to reduce both, the Standard Model as well as the LSP background.

A very good observable in order to reduce backgrounds is the visible energy. The distribution of this variable for the different samples is shown in Figure 6.5a. In order to better understand the Standard Model background, we have broken down the sample into different subcategories, as described in Section 6.1.3. LSP BG denotes the bRPV SUSY events in which at least one LSP decay is non-signal like and LSP SIG displays finally the targeted signal events.

One eye-catching feature of Figure 6.5a is the long tail of the 2f and 4f samples well beyond the actual collision energy of $\sqrt{s} = 500\,\text{GeV}$. This originates from the fact that in those samples the described $\gamma\gamma \rightarrow$ hadrons background removal procedure does not work efficiently. The request for six jets causes also many forward, low-p_t hadrons to be wrongly clustered into jets associated with the hard process instead of being associated to the beam jets. For the other subsamples whose final state topology is closer to a real six-jet configuration, the removal procedure performance gets restored, which results in a steeply falling edge at around $\sqrt{s} = 500\,\text{GeV}$.

It is visible that the distribution of the 6f sample, which consists predominantly of $e^+e^- \rightarrow t\bar{t}$ events, has a similar shape as the signal event sample and peaks also at $\sqrt{s} = 500\,\text{GeV}$. These events are very signal-like and are going to play an important role as SM background especially in the $\tau\tau$ channel, as we will see later.

Finally, an upper cut on the visible energy was chosen at $E_{\text{vis}} = 550\,\text{GeV}$ in order to remove the tails in the 2f and 4f events. For the minimal visible energy, $E_{\text{vis}} = 350\,\text{GeV}$ has been chosen. In this first preselection cut, 4f ($\gamma\gamma$) and 5f (eγ) events can be removed efficiently, since due to the involved photon the total energy in the event is typically lower than 350 GeV.

As a second variable for the preselection the number of reconstructed Particle Flow Objects (PFOs) has been considered, which is plotted in Figure 6.5b. The first bin

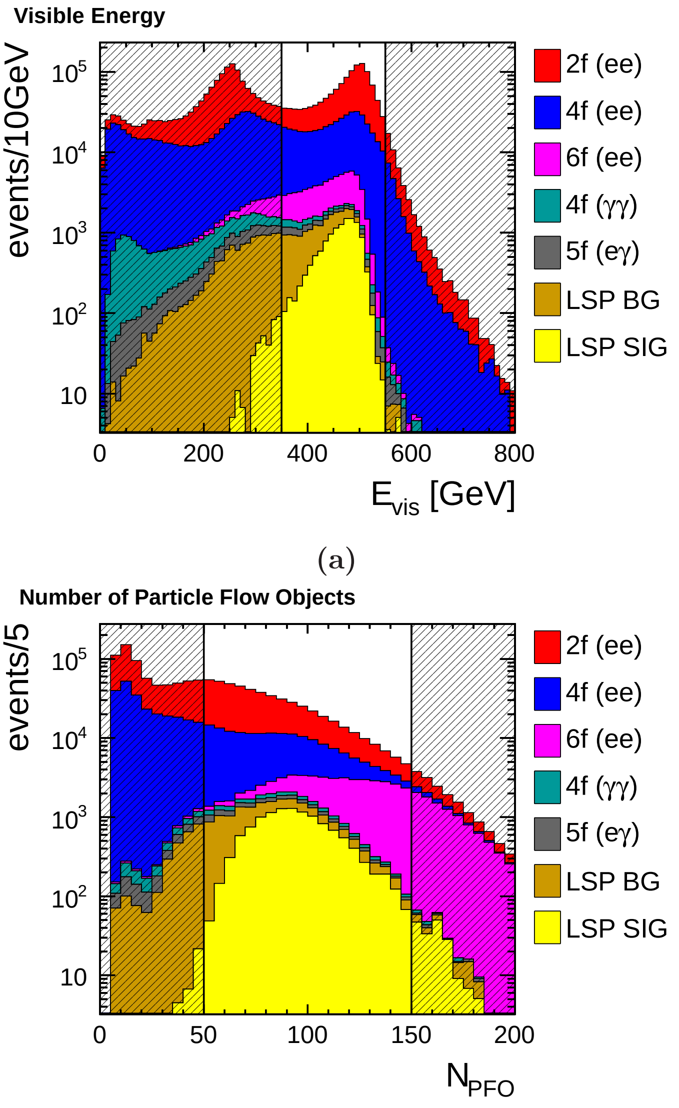

(b)

Figure 6.5: Distribution of events with respect to the visible energy (a) and the number of reconstructed objects (b) for the Standard Model background (see text for details), LSP background (LSP BG), and LSP signal (LSP SIG). The nonshaded areas show the selected events by the preselection cuts.

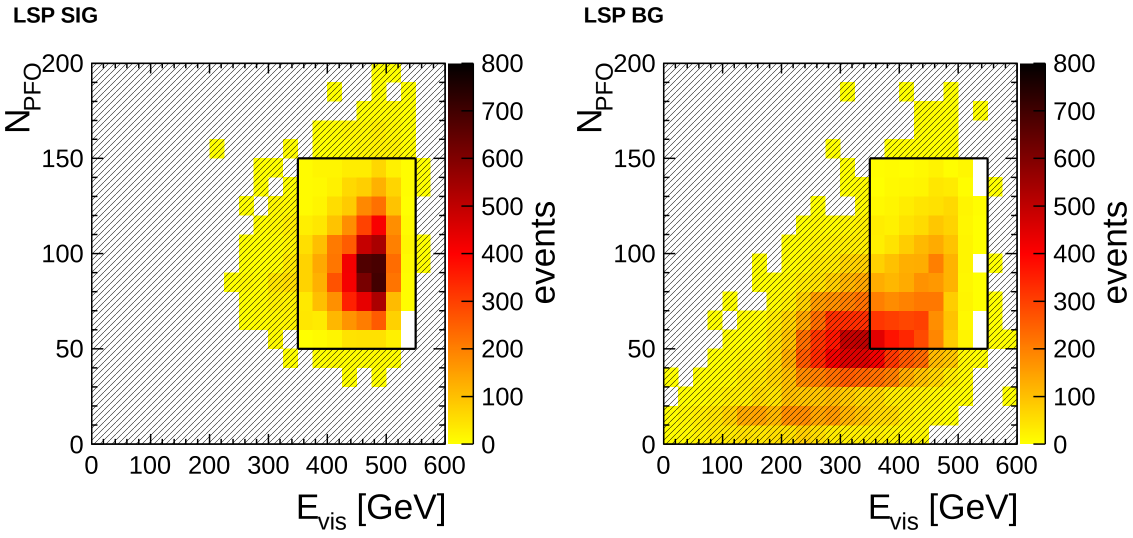

(a)

(b)

Figure 6.6: Distribution of events with respect to the visible energy and the number of reconstructed objects for (a) LSP signal and (b) LSP background. The nonshaded areas show the selected events by the preselection cuts.

in this histogram is empty since at least six reconstructed PFOs are necessary to let the six-jet k_T algorithm converge. It is visible that six fermion events prefer a larger particle multiplicity per event compared to the signal events. Therefore, an upper cut at $N_{\mathrm{PFO}} = 150$ has been set. Also a lower cut at $N_{\mathrm{PFO}} = 50$ can be applied, which removes the Standard Model events with mainly leptonic final states (e.g. leptonic Z-boson decays).

Figure 6.6 shows the event distribution with respect to both used cut variables in a two-dimensional histogram for the LSP signal sample and the LSP background sample. Is is clearly visible that both presented cuts select a large fraction of the signal events (cf. Figure 6.6a), whereas the LSP background peaks mostly in other areas of the two-dimensional plane (cf. Figure 6.6b). The concentration of events with low PFO multiplicities, for instance, can be attributed to events, where both LSPs decay to a W boson and a lepton and both W bosons decay subsequently into leptons. This results in very few objects in the event and a significantly reduced visible energy due to the involved neutrinos. A small peak is also observable in the center of the selected area. This arises from events in which both LSPs decay into Z bosons which further decay fully hadronically. However, the LSP background peaks majorly at $E_{\mathrm{vis}} = 340\,\mathrm{GeV}$ and $N_{\mathrm{PFO}} = 50$, which arises from all combinations of the leptonic and hadronic W/Z-boson decays.

The preselection is summarised quantitatively in the cut flow table 6.4. The selection efficiencies for Standard Model background and LSP background amounts to 16%

cut	Standard Model samples 2f (ee)	4f (ee)	6f (ee)	4f ($\gamma\gamma$)	5f (eγ)	**SM BG**
no cut	1840474	1117014	49857	20972	8949	**3037266**
k_T algorithm convergence	1775441	967780	49849	20411	8829	**2822309**
$350\,\text{GeV} \leqslant E_{\text{vis}} \leqslant 550\,\text{GeV}$	759338	349255	40526	3262	3185	**1155566**
$50 \leqslant N_{\text{PFO}} \leqslant 150$	334921	123931	31366	2415	2306	**493467**
efficiency	0.182	0.111	0.629	0.115	0.258	**0.162**

cut	**LSP BG**	bRPV SUSY samples $\mu\mu$	$\mu\tau$	$\tau\tau$	**LSP SIG**
no cut	**21516**	2878	6238	3502	**12618**
k_T algorithm convergence	**21345**	2878	6238	3502	**12618**
$350\,\text{GeV} \leqslant E_{\text{vis}} \leqslant 550\,\text{GeV}$	**9866**	2811	6061	3364	**12235**
$50 \leqslant N_{\text{PFO}} \leqslant 150$	**7198**	2772	5946	3307	**12026**
efficiency	**0.335**	0.963	0.953	0.944	**0.953**

Table 6.4: Cut flow table for the event preselection.

and 34%, respectively, whereas the LSP signal is selected with an efficiency of 95%. It is worth noting that the signal efficiencies are almost the same for all three signal event classes. Overall, with this preselection, the signal to background ratio has been enhanced roughly by a factor of six.

6.3 Event Selection

After the $\gamma\gamma$-background removal and event preselection, in this section, we focus on the actual event selection in the different selection classes as defined in Section 6.2.1.

6.3.1 Object Definitions

The event selection relies on reconstructed muons and jets. For this reason, we are going to give a short description of the definition of both objects in the following.

6.3.1.1 PFO Muons

The muon identification used for the selection is provided by the Pandora Particle Flow Algorithms. It is based on track and cluster information in all parts of the detector. The muon candidate is seeded by a muon like MIP[2] cluster in the calorimeters. If a track can be associated, all the particle properties are measured from this

---

[2] minimum ionising particle

track, like momentum, energy, and charge. The MIP cluster is removed from the list of clusters for the further particle finding process in order to avoid double counting of energy by the Particle Flow Algorithms. The decision whether a reconstructed pattern is a muon, is cut-based. In this analysis, the standard configuration of Pandora PFA has been used, which is part of the standard reconstruction chain.

6.3.1.2 Durham Jets

For the jet clustering in the event selection, the Durham jet clustering algorithm [189] is used. This algorithm is designed especially for e^+-e^- collisions. It runs over all Particle Flow Objects (PFO) of an input collection and calculates the distance between two particles k and l defined as

$$y_{kl} = 2\,(1 - \cos(\theta_{kl}))\,\frac{\min(E_k^2, E_l^2)}{E_{\mathrm{CM}}^2}, \tag{6.5}$$

where θ_{kl} is the angle between both particles, $E_{k,l}$ the energy of the individual particles k, l and E_{CM} the center-of-mass energy of the event. The two particles with the smallest y_{kl} are merged into a new pseudo particle. For the recombination, the so-called E scheme is used, which derives the momentum and energy of the pseudo particle as the sum of the two original four-vectors $p_k^\mu + p_l^\mu$. The algorithm continues iteratively merging particles until the targeted number of jets is reached. In contrast to the exclusive k_T jet algorithm described earlier, this algorithm combines all present particles into the final jets and no beam jets are formed.

Finally, the algorithm provides two output parameters $y_{n,n+1}$ and $y_{n-1,n}$, where n is the number of targeted jets. $y_{n,n+1}$ is the distance between (pseudo) particle n and $n+1$ before merging into a new pseudo particle. On the contrary, $y_{n-1,n}$ is the distance between the closest (pseudo) particles in the current n-jet configuration. For a stable n-jet configuration, one expects $y_{n-1,n}$ to be large and $y_{n,n+1}$ to be small.

6.3.2 Selection Procedure

In this section, we first discuss the selection procedure. The final selection efficiencies of the event classes are presented in the subsequent section.

During the selection, each event is first tested against the $\mu\mu$ class, then against the $\mu\tau$ class and finally against the $\tau\tau$ class.

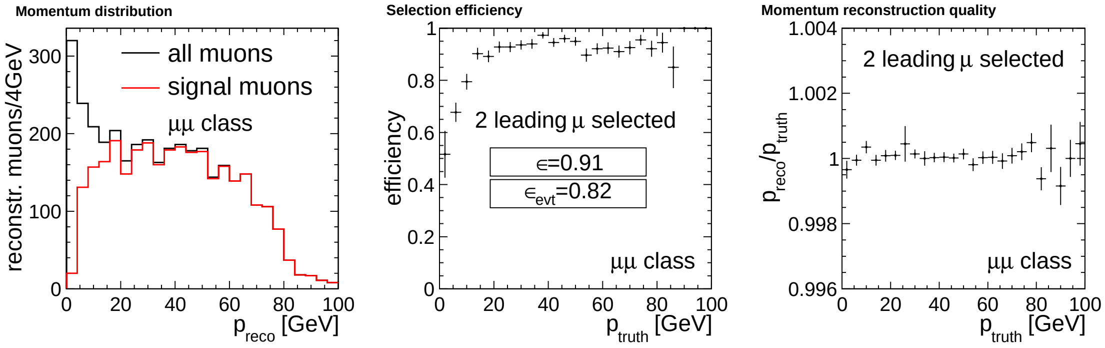

(a) **(b)** **(c)**

Figure 6.7: Muon selection in the $\mu\mu$ selection class based on a pure $W\mu W\mu$ signal sample. (a) Momentum spectrum of all selected signal muon candidates (black) and correctly selected signal muons (red). (b) Combined muon reconstruction efficiency and selection probability of a signal muon. In 82% of all cases, both signal muons are correctly selected by selecting the two leading muons of an event. (c) Reconstruction quality of signal muon momentum. The deviations between true and reconstructed muon momentum are below 0.5‰.

6.3.2.1 $\mu\mu$ Class

In the $\mu\mu$ class, we consider events with at least two reconstructed muons. From the muons we select the two most energetic ones and consider them as signal muon candidates which originate from the LSP decay.

In order to study the quality of the selection, we firstly consider a pure $W\mu W\mu$ signal sample. Figure 6.7a shows the reconstructed momentum spectrum of all signal muon candidates. The red line indicates the correctly selected signal muons. Therefore, the ratio of both distributions defines the purity of the selected signal muon sample. It can be observed that the purity of the sample is very low for low momentum muons. In this area, many signal muon candidates stem originally from decays of heavy flavour quarks which are produced in W/Z-boson decays. However, for reconstructed momenta larger than 15 GeV, the purity reaches almost 100%. The momentum spectrum of the correctly selected signal muon candidates shows a box-like shape, which corresponds to the decay kinematics of a two-body decay. The calculated endpoints for an 100 GeV LSP at a center-of-mass energy of $\sqrt{s} = 500$ GeV are [3.4; 80.1] GeV, where the edges are smeared out due to the beam-energy spread, initial state radiation, and the natural width of the involved W boson in the LSP decay.

Figure 6.7b shows the combined reconstruction efficiency and selection probability for signal muons defined as

$$\epsilon = \frac{\text{number of correctly selected signal muon candidates}}{\text{number of true signal muons}}. \tag{6.6}$$

In the low momentum region this efficiency is reduced. This can be understood because per event only the two most energetic muons are selected. Thus, for low-momentum signal muons it is rather likely that a muon from a heavy-flavour decay is wrongly selected and the actual signal muon is rejected. For signal muon momenta larger than 15 GeV, the selection efficiency of a single signal muon is beyond 90%, which is the intrinsic reconstruction efficiency for (any) PandoraPFO muon. The efficiency of selecting both signal muons correctly in the individual events is determined to $\epsilon_{\text{evt}} = 0.82$, which is in agreement with ϵ^2. Figure 6.7c shows the reconstruction quality of the selected muon momenta. The deviations from the true muon momentum is well below 0.5‰ over the whole momentum range.

The two selected muons are removed from the list of PFOs. In a next step, the remaining particles are used as input for the jet clustering, where we force the algorithm to form four jets. Out of these four elements we build all possible combinations of double pairs and evaluate the invariant mass in order to find two W-boson candidates. The two W-boson candidates which are closest to the real W-boson mass are chosen for the further analysis. Additionally, it is required that both W-boson candidates fulfill

$$\chi^2_{W_i} = \left(\frac{m_{\text{reco},i} - m_W}{\sigma}\right) < 2, \tag{6.7}$$

in order to remove backgrounds. Herein, σ is a resolution factor and has been chosen to be $\sigma = 5\,\text{GeV}$. This factor yields the optimum for the selection (cf. Section 7.1.1 for the actually determined resolution).

The reconstructed di-jet mass in the pure $W\mu W\mu$ signal sample is depicted in Figure 6.8a. It shows a very clear peak at m_W. The nonshaded area corresponds to the selection $\chi^2_W < 2$. In Figure 6.8b, the true and reconstructed momentum spectrum are depicted for the selected W-boson candidates. Both curves are well in agreement. Again, the momentum spectrum has two edges due to the two-body decay kinematic, which are consistent with the expected endpoints at $[149.7; 233.2]\,\text{GeV}$. Figure 6.8c shows the energy reconstruction quality of the W-boson candidates. In the region of high statistics ($p_W > 100\,\text{GeV}$), the ratio $E_{\text{reco}}/E_{\text{truth}}$ is very close to one and deviations are below 1%.

The selected muon and W-boson candidates are combined in a last step such that both μW pairs form two $\widetilde{\chi}^0_1$ candidates. The combination in which both resulting

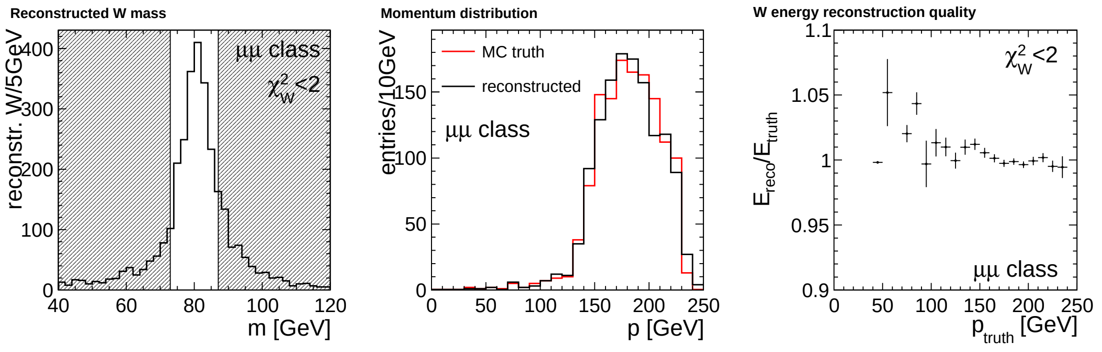

(a) **(b)** **(c)**

Figure 6.8: W-boson reconstruction in the $\mu\mu$ selection class based on a pure $W\mu W\mu$ signal sample. (a) Reconstructed W-boson mass. The shaded area indicates the rejected W-boson candidates for the further LSP-mass reconstruction. (b) Comparison between the reconstructed (black) and true (red) momentum spectrum of the W bosons. (c) Reconstruction quality of the W-boson energy. Deviations between true and reconstructed energy are below 1% in the high-statistics range ($p_W > 100\,\mathrm{GeV}$).

$\tilde{\chi}^0_1$ candidates are closest in mass is chosen. For the final selection of the event, it is required that

$$\chi^2_{\mathrm{eqm}} = \left(\frac{m_{\mathrm{reco},1} - m_{\mathrm{reco},2}}{\sigma}\right)^2 < 2. \tag{6.8}$$

If the event passes the selection, it is counted as $\mu\mu$ event, otherwise, it is tested in the next step against the $\mu\tau$ topology.

6.3.2.2 $\mu\tau$ Class

In this class, we require to find at least one reconstructed muon and select the most energetic one as signal muon. In the case of a pure $W\mu W\tau$ signal sample, the muon selection efficiency ϵ for a single signal muon amounts to 87% and is therefore slightly reduced compared to the $\mu\mu$ class (cf. Figure 6.9b). This can be understood by looking at the momentum distribution of the muons in events with at least one reconstructed muon. The background of non-signal muons is much larger. Therefore, the selection efficiency is reduced, because it is more likely to select the wrong muon as signal muon. However, since there is only one signal muon required in this event class, ϵ_{evt} is larger than in the $\mu\mu$ class.

The following procedure is comparable to the $\mu\mu$ class selection: The selected muon is removed from the PFO list and the remaining particles are clustered by a Durham

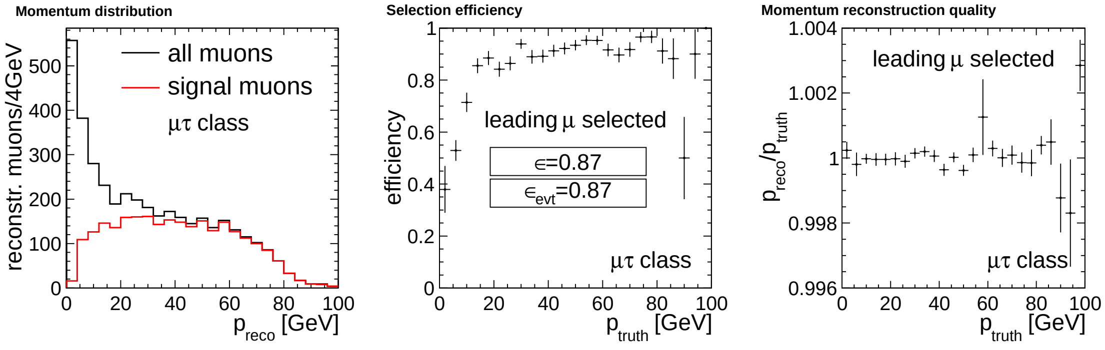

(a) (b) (c)

Figure 6.9: Muon selection in the $\mu\tau$ selection class based on a pure $W\mu W\tau$ signal sample. (a) Momentum spectrum of all selected signal muon candidates (black) and correctly selected signal muons (red). (b) Combined muon reconstruction efficiency and selection probability of a signal muon. In 87% of all cases the signal muon is selected correctly by selecting the leading muon of an event. (c) Reconstruction quality of signal muon momentum. The deviations between true and reconstructed muon momentum are below 0.5‰.

jet clustering algorithm. Thereby, the algorithm is forced to find in this case five jets where the fifth jet is the τ candidate. This assumption is reasonable since τ leptons decay in about 65% of the cases hadronically [5]. However, there is also still a chance that leptonic τ decays get clustered into a one-track jet, if the decay lepton is isolated enough. We then select the jet with the smallest number of constituents and consider it as τ candidate. For the remaining four jets, we repeat the strategy for finding two W-boson candidates as in the $\mu\mu$ class.

The reconstructed mass of the W-boson candidates for a pure $W\mu W\tau$ signal sample is depicted in Figure 6.10a. One observes that there is a larger tail towards lower masses, which results from imperfect jet clustering in the busier event. It can happen that also PFOs are clustered in the τ jet which actually belong to the W boson. This can also be seen in the reconstruction quality of the W-boson energy (cf. Figure 6.10c), which is degraded compared to the situation in the $\mu\mu$ selection class. Again, only W-boson candidates which feature $\chi^2_{W_i} < 2$ are further processed in the analysis. The momentum spectrum of the selected W-boson candidates reproduces well the box-like true spectrum (cf. Figure 6.10b).

The relaxation of the muon criterion in this event class causes significantly larger Standard Model background. Therefore, in this class additional cuts are set in order to reduce the background. To this end, Figure 6.11 shows the event distributions for the complete LSP signal sample (LSP SIG), the LSP background sample (LSP BG), and the Standard Model background sample after the $\mu\mu$ class selection. For the τ

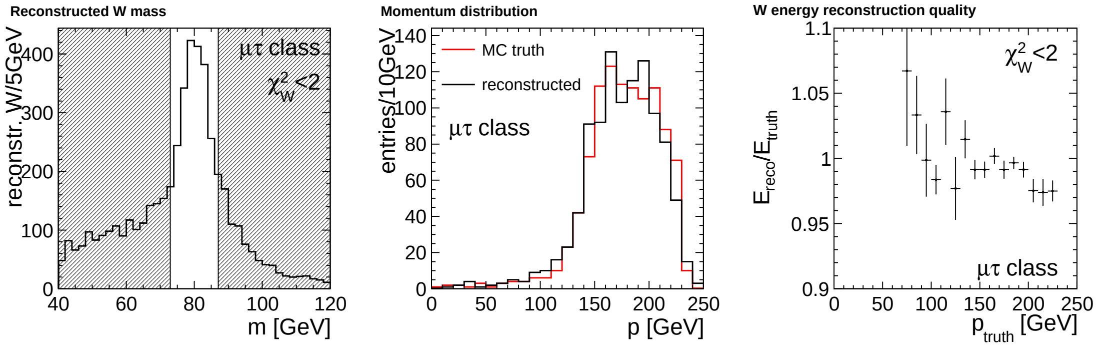

(a) (b) (c)

Figure 6.10: W-boson reconstruction in the $\mu\tau$ selection class based on a pure $W\mu W\tau$ signal sample. (a) Reconstructed W-boson mass. The shaded area indicates the rejected W-boson candidates for the further LSP-mass reconstruction. The wash-out of the distribution towards lower masses originates from imperfect jet clustering. (b) Comparison between the reconstructed (black) and true (red) momentum spectrum of the W bosons. (c) Reconstruction quality of the W-boson energy. The reconstructed energy is reduced due to assignments of PFOs originating originally from the W-boson decay to the τ jet.

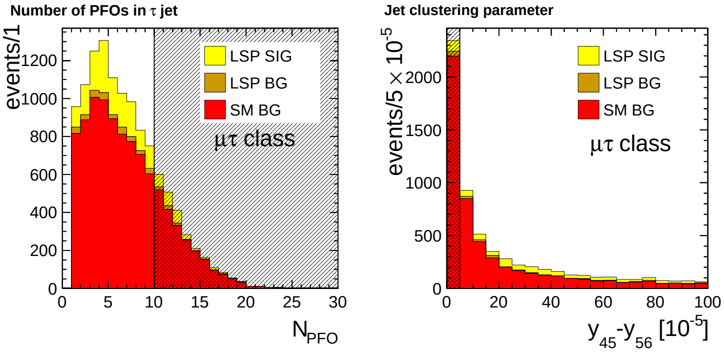

(a) (b)

Figure 6.11: Event distributions for the complete LSP signal sample (LSP SIG), the LSP background sample (LSP BG), and the Standard Model background sample after the $\mu\mu$ class selection. (a) Number of PFOs in the τ jet. A cut on the maximum number of constituents helps to reduce Standard Model background. (b) The jet parameter $y_{45} - y_{56}$ is a measure of how well a five-jet configuration describes the event. Small values are rejected.

jet it is required that the number of PFOs is smaller than ten (cf. Figure 6.11a). Additionally, the τ jet must not contain a muon. This helps a lot to reduce in particular the $t\bar{t}$ Standard Model background, which is very similar in the event topology compared to the signal events. Additionally, we use a cut on the jet-collection parameters y_{56} and y_{45}. The distribution of $y_{45} - y_{56}$ is depicted in Figure 6.11b. Events which are not well described by a five-jet configuration are expected to peak at small values of $y_{45} - y_{56}$. Therefore, we select only events that fulfill

$$y_{45} - y_{56} > 5 \times 10^{-5}. \tag{6.9}$$

Finally, the muon, τ and W-boson candidates are combined to form two $\tilde{\chi}_1^0$ candidates, like in the $\mu\mu$ class. If $\chi^2_{\mathrm{eqm}} < 2$ the event is counted as $\mu\tau$ event, otherwise we continue with the test of the $\tau\tau$ class.

6.3.2.3 $\tau\tau$ Class

In the $\tau\tau$ class, no muon is removed and the whole event is directly clustered into a six-jet configuration by a Durham jet clustering algorithm. The two jets with the smallest number of constituents are treated as τ jets and removed from the event. From the remaining four jets two W-boson candidates are derived, like in the $\mu\mu$ and $\mu\tau$ class. As before, the W-boson candidates which fulfill $\chi^2_{W_i} < 2$ are selected. The corresponding control plots for the W-boson reconstruction in the $\tau\tau$ class are given in Figure 6.12. A striking feature is the systematically reduced energy reconstruction of the selected W-boson candidates in Figure 6.12c. This results again from problems in the jet clustering due to the very busy environment of a six-jet event. An explicit τ-reconstruction would probably improve the result since at the moment too many PFOs are associated to the τ-jets.

As already in the $\mu\tau$ class, we require that both τ jets contain less than ten constituents. Figure 6.13 shows the event distributions for the complete LSP signal sample (LSP SIG), the LSP background sample (LSP BG), and the Standard Model background sample after the $\mu\mu$ class, and the $\mu\tau$ class selection.

The distribution of number of PFOs in the largest τ jet is depicted in Figure 6.13a. We also cut on the jet-collection parameter $y_{56} - y_{67} < 5 \times 10^{-5}$ in analogy to the $\mu\tau$ event class (cf. Figure 6.13b).

The two τ candidates and W-boson candidates are then combined into two $\tilde{\chi}_1^0$ candidates following the same procedure as in the $\mu\mu$ and $\mu\tau$ class. If condition (6.7) is fulfilled, this event is counted as $\tau\tau$ event. Otherwise the event is finally rejected.

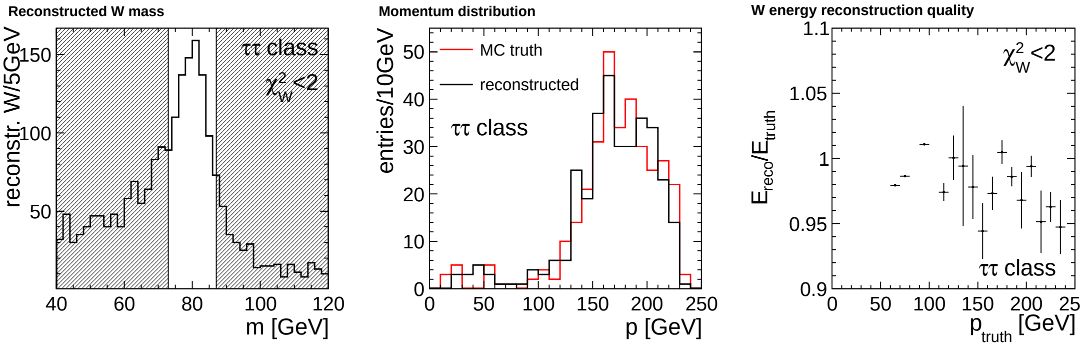

(a) (b) (c)

Figure 6.12: W-boson reconstruction in the $\tau\tau$ selection class based on a pure $W\tau W\tau$ signal sample. (a) Reconstructed W-boson mass. The shaded area indicates the rejected W-boson candidates for the further LSP-mass reconstruction. The wash-out of the distribution towards lower masses originates from imperfect jet clustering. (b) Comparison between the reconstructed (black) and true (red) momentum spectrum of the W bosons. (c) Reconstruction quality of the W-boson energy. The reconstructed energy is reduced due to assignments of PFOs originating originally from the W-boson decay to the τ jets.

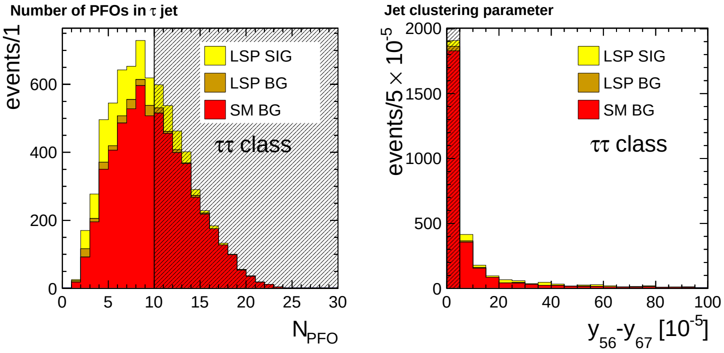

(a) (b)

Figure 6.13: Event distributions for the complete LSP signal sample (LSP SIG), the LSP background sample (LSP BG), and the Standard Model background sample after the $\mu\mu$ and $\mu\tau$ class selection. (a) Number of PFOs in the largest τ jet. A cut on the maximum number of constituents helps to reduce Standard Model background. (b) The jet parameter $y_{56} - y_{67}$ is a measure of how well a six-jet configuration describes the event. Small values are rejected.

6.3.3 Event Selection Summary

The result of the event selection is presented in Figure 6.14. It shows the reconstructed mass of the LSP candidates in the $\mu\mu$, $\mu\tau$, and $\tau\tau$ channel. For all three channels, a clear signal peak around the expected LSP mass is observable. The main remaining background arises from WW and ZZ events and, therefore, peak around $m_{W/Z}$.

Table 6.5 gives an quantitative summary of the whole event selection. The Standard Model background can be suppressed very efficiently by a factor of $10^{-4} - 10^{-5}$, whereas the tailored event class selection is most efficient for the corresponding signal events. An analysis of the remaining LSP background has shown that most of the remaining events consist of one signal-like LSP decay and one LSP decay involving a Z boson. As described in Section 4.4.3, three-body decays are negligible at the studied benchmark point. However, the selection procedure has also been applied to a sample in which three-body decays of the LSP are sizable. We have found that the LSP background originating from these three-body decays is suppressed by about a factor of 10 in the presented selection procedure.

Among the signal classes, the $\tau\tau$ channel has, as expected, the smallest efficiency. A state-of-the-art τ identification could certainly help to improve the efficiency in the corresponding classes. Since this study is a first estimate of the prospects of studying bRPV LSP decays at the ILC, not all possible improvements of the event selection have yet been exploited.

The $\mu\mu$ channel features a very good selection efficiency of about 32%. However, it can also be seen that in this selection class there are also contributions from $W\mu W\tau$ and $W\tau W\tau$ signal events. The τ decays in 17% of the cases like $\tau \rightarrow \mu\overline{\nu}_\mu\nu_\tau$ and, thus, produces a fake muon. Therefore, it is clear that in the $\mu\mu$ selection class also a fraction of the $W\mu W\tau$ and $W\tau W\tau$ signal events is selected. The same argumentation is true for the contributions of $W\tau W\tau$ signal events in the $\mu\tau$ selection class.

Based on this selection, we are now able to analyse the events further, which will be the subject of the next chapter.

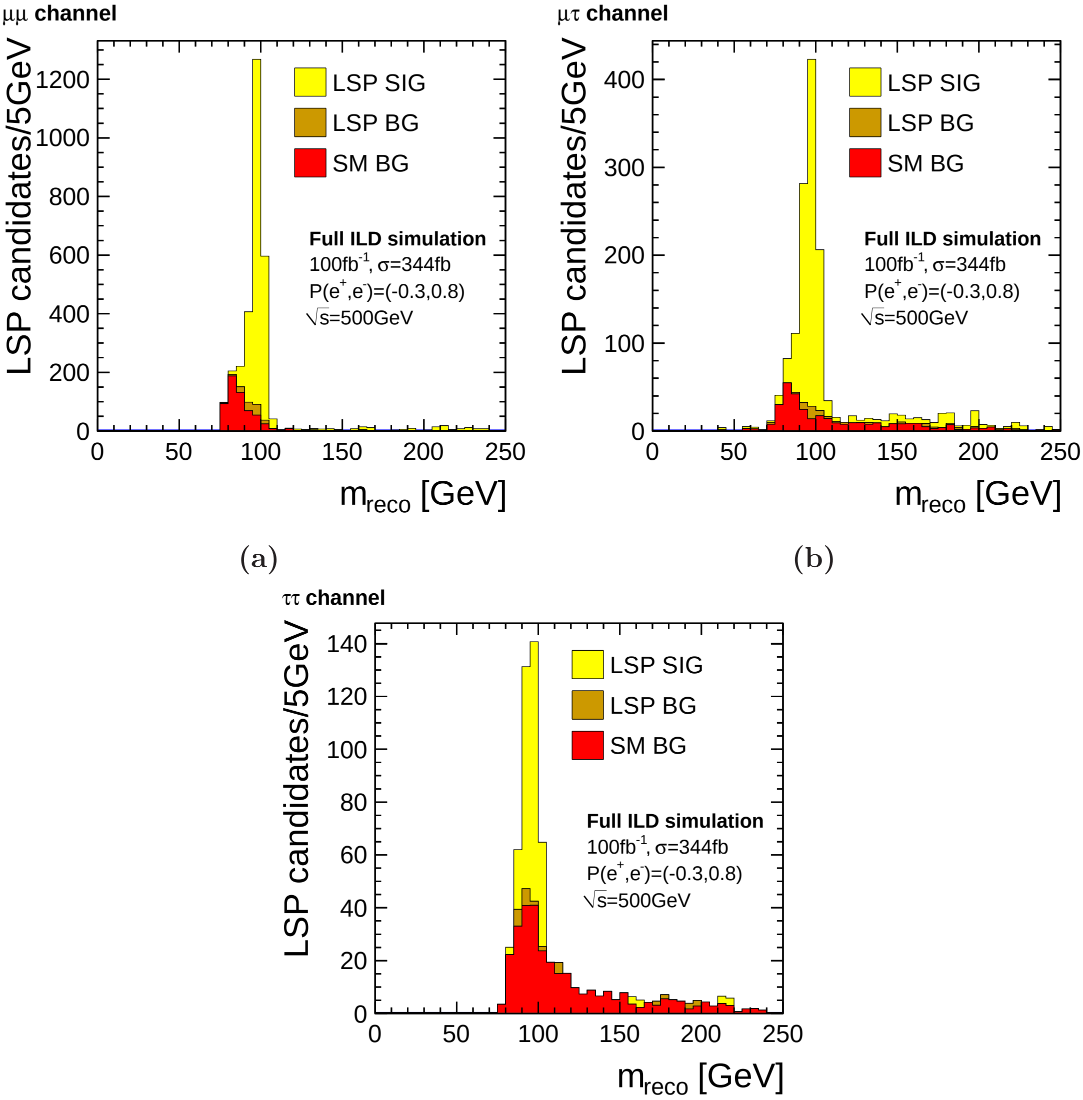

(a)

(b)

(c)

Figure 6.14: Invariant mass distribution of the LSP candidates in the (a) $\mu\mu$ class, (b) $\mu\tau$ class and (c) $\tau\tau$ class

cut	LSP SIG			LSP BG	SM BG
	$\mu\mu$	$\mu\tau$	$\tau\tau$		
no cut	2878	6238	3502	21516	3037266
preselection	2772	5946	3307	7198	493467
$\mu\mu$ selection	913	204	37	59	298
$\epsilon_{\mu\mu}$	0.317	0.033	0.011	2.74×10^{-3}	9.81×10^{-5}
$\mu\tau$ selection	16	451	87	29	175
$\epsilon_{\mu\tau}$	0.006	0.072	0.025	1.35×10^{-3}	5.76×10^{-5}
$\tau\tau$ selection	0	2	127	14	160
$\epsilon_{\tau\tau}$	0.000	0.000	0.036	0.65×10^{-3}	5.27×10^{-5}

Table 6.5: Cut flow table for the full event selection.

7 Bilinear RPV SUSY Study – Analysis and Results

After having discussed the event selection of bRPV events in the previous chapter, we present the analysis of the selected events in the following sections. Hereby, we first focus on the precision measurement of the LSP mass in Section 7.1, the discovery reach of bRPV LSP decays at ILD in Section 7.2, and the measurement of the ratio of branching ratios $\mathrm{BR}(\tilde{\chi}_1^0 \to W\mu)/\,\mathrm{BR}(\tilde{\chi}_1^0 \to W\tau)$ in Section 7.3. Also sources of systematic uncertainties are discussed in this chapter. In Section 7.4, we finally interpret our findings as measurement of the atmospheric neutrino mixing angle. The chapter is closed with an outlook on perspectives of this analysis.

7.1 LSP Mass and Resolution

From the reconstructed mass distributions of the LSP candidates in Figure 6.14, we estimate the precision of the LSP mass measurement.

7.1.1 Measurement

For performing a high precision measurement of the LSP mass, the $\mu\mu$ channel is best suited, since it has the cleanest event topology and no sources of missing energy. This results in a very precise reconstruction of all involved objects, as demonstrated in Section 6.3.2.1.

Figure 7.1 shows the reconstructed LSP mass distribution for an integrated luminosity of $\int L dt = 100\,\mathrm{fb}^{-1}$ in the $\mu\mu$ channel. The Standard Model background has been subtracted, but its fluctuations have been taken into account in the bin errors. From the fit of a Gaussian to the distribution, the LSP mass can be extracted to

$$m_{\tilde{\chi}_1^0}^{\mathrm{fit}} = (98.401 \pm 0.092(\mathrm{stat.}))\,\mathrm{GeV}. \tag{7.1}$$

Since the tail of the mass distribution is slightly washed out towards lower masses due to misreconstructions, this part of the distribution has been omitted in the

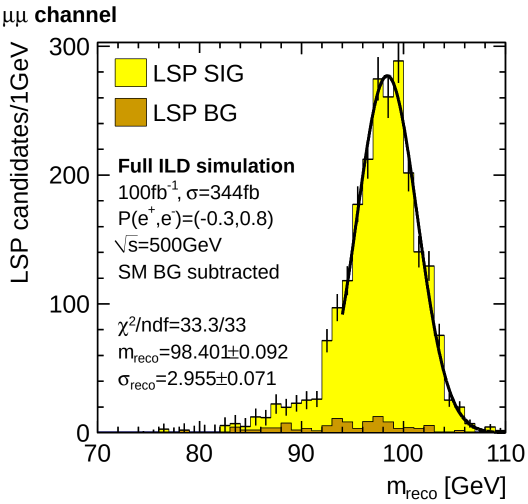

Figure 7.1: Mass reconstruction of the LSP in the $\mu\mu$ channel. In the distribution the Standard Model background has been subtracted, but fluctuations have been taken into account for the bin errors. The obtained result is in very good agreement with the input mass used for the simulation.

fit. The obtained result for the LSP mass is within the statistical error in very good agreement with the theoretical input value of the studied benchmark point $m_{\tilde{\chi}_1^0}^{\mathrm{theo}} = 98.48\,\mathrm{GeV}$.

The natural width of the LSP is so small (cf. Section 4.4.3) that the observable width of the distribution corresponds directly to the detector resolution. It can be determined to $\sigma_{\tilde{\chi}_1^0}^{\mathrm{fit}} = 3\,\mathrm{GeV}$, which is in very good agreement with the ILD design goals discussed in Chapter 5.

For completeness, in Figure 7.2 the reconstructed LSP mass in the other event classes is depicted. As expected, the performance is not as compelling as in the $\mu\mu$ channel. The obtained reconstructed mass is shifted towards lower masses with respect to the input mass by 0.9 GeV and 1.5 GeV, respectively. This can be attributed to the involvement of the τ lepton in the channels, which entails the presence of at least one neutrino in the event. A tau reconstruction algorithm, which is capable for correcting the missing energy in the collinear approximation, could help to recover the expected value of the invariant mass. This could be done, for instance, in a kinematic fit of the event.

7.1.2 Systematic Uncertainties

For the quoted statistical error of the fitted LSP mass of only a few MeV, it is clear that also sources of systematic uncertainties have to be considered and discussed. In

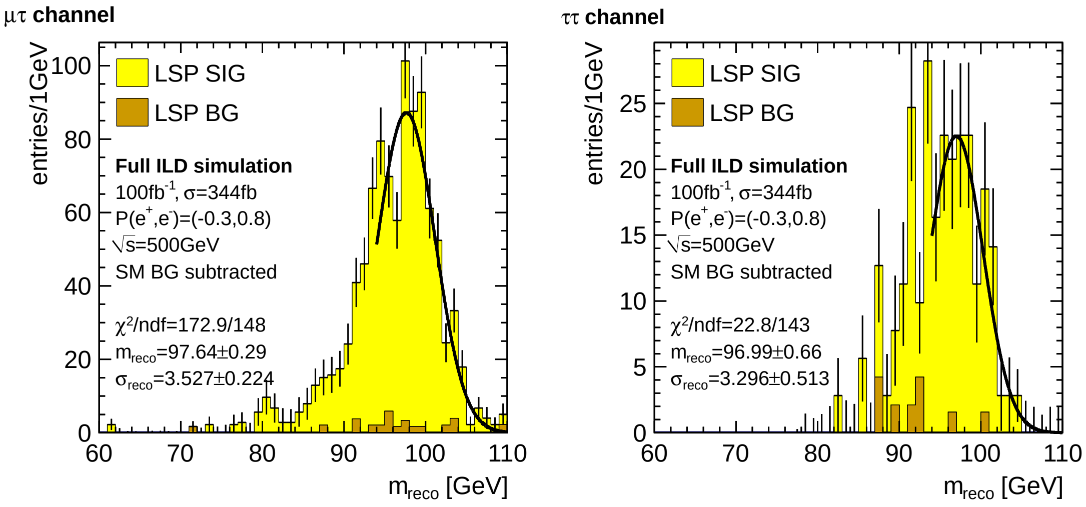

Figure 7.2: Mass reconstruction of the LSP in the $\mu\tau$ and $\tau\tau$ channel. The extracted LSP mass in both channels is slightly shifted towards lower masses with respect to the simulated input LSP mass. This is due to the involved τ lepton, which introduces at least one neutrino.

the reconstruction of the LSP mass, three main sources of systematic uncertainties can be identified: Uncertainties from the muon-momentum scale calibration, the jet-energy scale calibration and the Standard Model background modelling.

For a fully correct derivation of the systematic uncertainties of the muon momentum and the jet energy calibration, the reconstructed muon momenta and jet energies in all signal and background events had to be varied by the uncertainty on the muon-momentum scale $\delta|\vec{p}_\mu|$ and the jet-energy scale δE_{jet}. Subsequently, the selection and analysis step had to be repeated with those rescaled values and compared to the unscaled result. However, in the following , we will give an estimate of the systematic uncertainty on the LSP-mass reconstruction derived from analytic error propagation, which is possible under a few simplifying assumptions on the event kinematics. The scale uncertainties $\delta|\vec{p}_\mu|$ and δE_{jet} are estimated from Standard Model control samples.

The invariant mass of the LSP determined from a decay into a W boson (which further decays hadronically) and a muon is given by

$$\begin{aligned} m^2_{\tilde{\chi}^0_1} &= (p_{\mu,\mu} + p_{W,\mu})^2 \\ &= m^2_\mu + 2\,(E_\mu E_W - |\vec{p}_\mu||\vec{p}_W|\cos(\sphericalangle \vec{p}_\mu, \vec{p}_W)) + m^2_W, \\ &\cong 2|\vec{p}_\mu|(E_W - |\vec{p}_W|\cos(\sphericalangle \vec{p}_\mu, \vec{p}_W)) + m^2_W, \qquad (7.2) \end{aligned}$$

where $p_{\mu/W,\mu}$ is the four-momentum of the muon/W boson and $E_{\mu/W}$ the corresponding energy.

We now express Equation (7.2) in terms of jet energies and muon momentum. As a simplification, we assume $E_{\mathrm{jet1}} = E_{\mathrm{jet2}} = E_{\mathrm{jet}}$.

After some transformations we arrive at

$$m^2_{\tilde{\chi}^0_1} = A \cdot |\vec{p}_\mu| E_{\mathrm{jet}} + B \cdot E^2_{\mathrm{jet}}, \tag{7.3}$$

$$\tag{7.4}$$

with

$$A = 2\left(2 - \cos(\sphericalangle \vec{p}_\mu, \vec{p}_W)\sqrt{2 + 2\cos(\sphericalangle \vec{p}_{\mathrm{jet1}}, \vec{p}_{\mathrm{jet2}})}\right) \quad \text{and} \tag{7.5}$$

$$B = 2\left(1 - \cos(\sphericalangle \vec{p}_{\mathrm{jet1}}, \vec{p}_{\mathrm{jet2}})\right). \tag{7.6}$$

Thus, the systematic uncertainty on the LSP-mass reconstruction becomes

$$\delta(m^2_{\tilde{\chi}^0_1})^2 = ((AE_{\mathrm{jet}})\delta|\vec{p}_\mu|)^2 + ((A|\vec{p}_\mu| + 2BE_{\mathrm{jet}})\delta E_{\mathrm{jet}})^2 \quad \text{or} \tag{7.7}$$

$$\delta(m_{\tilde{\chi}^0_1})^2 = \frac{1}{4m^2_{\tilde{\chi}^0_1}}\left(((AE_{\mathrm{jet}})\delta|\vec{p}_\mu|)^2 + ((A|\vec{p}_\mu| + 2BE_{\mathrm{jet}})\delta E_{\mathrm{jet}})^2\right). \tag{7.8}$$

$$= \delta(m_{\tilde{\chi}^0_1})^2_{E_{\mathrm{jet}}} + \delta(m_{\tilde{\chi}^0_1})^2_{|\vec{p}_\mu|}, \tag{7.9}$$

with the different contributions due to the uncertainties of the μ momentum and jet energy reconstruction of

$$\delta(m_{\tilde{\chi}^0_1})_{|\vec{p}_\mu|} = \frac{AE_{\mathrm{jet}}}{2m_{\tilde{\chi}^0_1}}\delta|\vec{p}_\mu| \quad \text{and} \tag{7.10}$$

$$\delta(m_{\tilde{\chi}^0_1})_{E_{\mathrm{jet}}} = \frac{A|\vec{p}_\mu| + 2BE_{\mathrm{jet}}}{2m_{\tilde{\chi}^0_1}}\delta E_{\mathrm{jet}}. \tag{7.11}$$

Typical values for the jet energies and muon momentum can be read off from Figure 6.7a and 6.8b. The average opening angles have been calculated analytically:

$$\langle|\vec{p}_\mu|\rangle = 40\,\mathrm{GeV} \qquad \cos(\sphericalangle \vec{p}_\mu, \vec{p}_W) = 0.86 \qquad A = 0.85 \tag{7.12}$$

$$\langle E_{\mathrm{jet}}\rangle = \langle E_W\rangle/2 = 100\,\mathrm{GeV} \qquad \cos(\sphericalangle \vec{p}_{\mathrm{jet1}}, \vec{p}_{\mathrm{jet2}}) = 0.68 \qquad B = 0.64 \tag{7.13}$$

This gives the following prefactors for the contributions of the muon-momentum scale and the jet-energy scale

$$\delta(m_{\tilde{\chi}^0_1})_{|\vec{p}_\mu|} = 0.42\,\delta|\vec{p}_\mu| \quad \text{and} \tag{7.14}$$

$$\delta(m_{\tilde{\chi}^0_1})_{E_{\mathrm{jet}}} = 0.81\,\delta E_{\mathrm{jet}}. \tag{7.15}$$

The muon-momentum scale as well as the jet-energy scale can be calibrated using leptonic and hadronic Z-boson decays. The Z-boson mass was very precisely measured at LEP and SLC with an uncertainty of only 2.3 MeV [5] and, therefore, this quantity is very well suited for the calibration. The unpolarised cross section of $e^+e^- \to Z \to \mu^+\mu^-$ for a center-of-mass energy of $\sqrt{s} = 500\,\mathrm{GeV}$ is 2.5 pb, which corresponds to $N_{\mu\mu} = 12.5 \times 10^5$ events for an integrated luminosity of $\int L dt = 500\,\mathrm{fb}^{-1}$. Therefore, the statistical uncertainty on the measured Z-boson mass amounts to $1/\sqrt{N_{\mu\mu}} = 0.09\%$. For the hadronic decay mode of the Z boson, the cross section is by a factor of ten larger, resulting in a statistical uncertainty on the mass calibration of $1/\sqrt{N_{q\bar{q}}} = 0.03\%$. These uncertainties represent an ultimate limit given by the size of the potential control sample. It does not take into account time-dependent effects.

We now can derive a relation which connects the calibration uncertainty to the uncertainty on the muon-momentum scale and jet-energy scale, respectively.

The invariant mass of two fermions forming a Z boson can be expressed as

$$m^2_{\mathrm{inv,lep}} = 2|\vec{p}_{\mu 1}||\vec{p}_{\mu 2}|(1 - \cos(\alpha_{12})) = 4 \cdot |\vec{p}_{\mu 1}||\vec{p}_{\mu 2}| \tag{7.16}$$

$$m^2_{\mathrm{inv,had}} = 2E_{\mathrm{jet1}}E_{\mathrm{jet2}}(1 - \cos(\alpha_{12})) = 4 \cdot E_{\mathrm{jet1}}E_{\mathrm{jet2}}. \tag{7.17}$$

For simplicity, we assume for this estimate back-to-back decays.

Error propagation gives

$$\delta(m^2_{\mathrm{inv,lep}}) = 4 \cdot (|\vec{p}_{\mu 1}|\delta(|\vec{p}_{\mu 2}|) + |\vec{p}_{\mu 2}|\delta(|\vec{p}_{\mu 1}|)) = 8 \cdot |\vec{p}_{\mu}|\delta(|\vec{p}_{\mu}|) \tag{7.18}$$

$$\delta(m^2_{\mathrm{inv,had}}) = 4 \cdot (E_{\mathrm{jet1}}\delta E_{\mathrm{jet2}} + E_{\mathrm{jet2}}\delta E_{\mathrm{jet1}}) = 8 \cdot E_{\mathrm{jet}}\delta E_{\mathrm{jet}}. \tag{7.19}$$

Since $|\vec{p}_\mu| = \frac{1}{2}m^2_{\mathrm{inv,lep}}$ and $E_{\mathrm{jet}} = \frac{1}{2}m_{\mathrm{inv,had}}$, the relative uncertainty on $|\vec{p}_\mu|$ and E_{jet} simplifies to

$$\frac{\delta|\vec{p}_\mu|}{|\vec{p}_\mu|} = \frac{1}{8 \cdot |\vec{p}_\mu|^2}\delta(m^2_{\mathrm{inv,lep}}) = \frac{2m_{\mathrm{inv,lep}}}{8 \cdot |\vec{p}_\mu|^2}\delta(m_{\mathrm{inv,lep}}) = \frac{m^2_{\mathrm{inv,lep}}}{4 \cdot |\vec{p}_\mu|^2}\frac{\delta(m_{\mathrm{inv,lep}})}{m_{\mathrm{inv,lep}}} = \frac{1}{\sqrt{N_{\mu\mu}}} \tag{7.20}$$

$$\frac{\delta E_{\mathrm{jet}}}{E_{\mathrm{jet}}} = \frac{1}{\sqrt{N_{q\bar{q}}}}. \tag{7.21}$$

Now we can evaluate Equations (7.14) and (7.15), and we obtain

$$\delta(m_{\tilde{\chi}^0_1})_{|\vec{p}_\mu|} = 15\,\mathrm{MeV} \qquad \text{and} \qquad \delta(m_{\tilde{\chi}^0_1})_{E_{\mathrm{jet}}} = 24\,\mathrm{MeV}. \tag{7.22}$$

An additional source of systematic uncertainties arises from the Standard Model background modelling. As visible in Figure 6.14a, the invariant mass distribution of the remaining Standard Model background shows a steeply falling edge for LSP masses smaller then 105 GeV. The Standard Model subtraction relies on a correct

source	calibration process	cross section	$1/\sqrt{N}$@500 fb^{-1}	effect on $m_{\tilde{\chi}_1^0}$
$\lvert\vec{p}_\mu\rvert$ scale	$Z \to \mu^+\mu^-$	2.5 pb	0.09%	15 MeV
E_{jet} scale	$Z \to q\bar{q}$	25 pb	0.03%	24 MeV
background modelling	$WW \to$ hadrons	7 pb	0.05%	20 MeV
total				$\sim$ 35 MeV

Table 7.1: Main sources for systematic uncertainties on the LSP-mass reconstruction. The largest contribution in the current estimate arises from the muon-momentum scale calibration.

modelling of this slope and, thus, any uncertainty connected to the Standard Model background modelling could enter into the LSP mass determination. The ILC, however, offers many possibilities to study electroweak background processes. Especially, the most important remaining background of W-boson-pair production has a cross section of several pico-barn, which allows for many possibilities of tuning the modelling of the process. Therefore, we assume that the residual effect from subtracting the SM background on the LSP-mass reconstruction is less than

$$\delta(m_{\tilde{\chi}_1^0})_{\text{BG}} = 20\,\text{MeV}. \tag{7.23}$$

Systematic errors on beam energy, beam polarisation or luminosity do not influence the mass reconstruction and, thus, do not enter into the overall uncertainty of the LSP mass measurement. A summary of all relevant sources of systematic uncertainties are listed in Table 7.1.

The total systematic uncertainty on the LSP-mass reconstruction is estimated to

$$\delta(m_{\tilde{\chi}_1^0})_{\text{syst}} = \sqrt{\delta(m_{\tilde{\chi}_1^0})^2_{\lvert\vec{p}_\mu\rvert} + \delta(m_{\tilde{\chi}_1^0})^2_{E_{\text{jet}}} + \delta(m_{\tilde{\chi}_1^0})^2_{\text{BG}}} = 35\,\text{MeV}. \tag{7.24}$$

Thus, the final total uncertainty on the measured LSP mass scaled to an integrated luminosity of $\int L dt = 500\,\text{fb}^{-1}$ is found to be

$$\delta(m_{\tilde{\chi}_1^0}) = (40(\text{stat.}) \oplus 35(\text{syst.}))\,\text{MeV}. \tag{7.25}$$

7.2 Signal Significance

The large signal to background ratio in the selection classes raises directly the question of the signal significance. In this section, we analyse the significance and evaluate the discovery potential of the presented selection in the parameter plane of the simplified model.

7.2.1 Choice of Significance Estimator

In order to make a discovery, the "Standard-Model-only" hypothesis has to be ruled out. Therefore, we test how likely it is to observe N or more events expecting only B Standard Model events. In the case of a Monte-Carlo study, the number of observed events is set to the predicted number of events from Monte-Carlo simulations: $N = S + B$, where S describes the number of bRPV SUSY events. The underlying statistic of event counts is the Poissonian statistic and, therefore, the probability can be expressed as

$$p = P(n \geqslant N|B) = \sum_{n=N}^{\infty} \frac{B^n}{n!} \mathrm{e}^{-B}. \tag{7.26}$$

The significance of an excess over Standard Model background is usually quoted in units of standard deviations of a normal distribution m rather than a probability value p. However, both are related via

$$1 - p = \operatorname{erf}\left(\frac{m}{\sqrt{2}}\right). \tag{7.27}$$

Herein, erf(x) represents the error function, which is the integral of a standard normal distribution in the limits $[-\infty; x]$. We finally obtain

$$m = \sqrt{2}\,\operatorname{erf}^{-1}\left(P(n < N|B)\right) = \sqrt{2}\,\operatorname{erf}^{-1}\left(\sum_{n=0}^{N-1} \frac{B^n}{n!} \mathrm{e}^{-B}\right). \tag{7.28}$$

The calculation of Equation (7.28) is slow and numerically rather unstable, since the argument of the inverse error function is usually very small. Therefore, it is useful to use a significance estimator, which reproduces the actual value of the significance.

A widely used estimator is the ratio $m = S/\sqrt{B}$. This estimator, however, is known to overestimate the significance for small backgrounds. Another estimator, which we are going to use in the following, is based on a likelihood ratio

$$Q = \frac{P(n = N|S + B)}{P(n = N|B)} = \left(\frac{S}{B} + 1\right)^N \mathrm{e}^{-S}. \tag{7.29}$$

This ratio compares the probability of observing N events between the "background-only" hypothesis and the "signal-plus-background" hypothesis. The estimator is defined as

$$m = \sqrt{2 \ln Q} = \sqrt{2N \ln\left(\frac{S}{B} + 1\right) - 2S}. \tag{7.30}$$

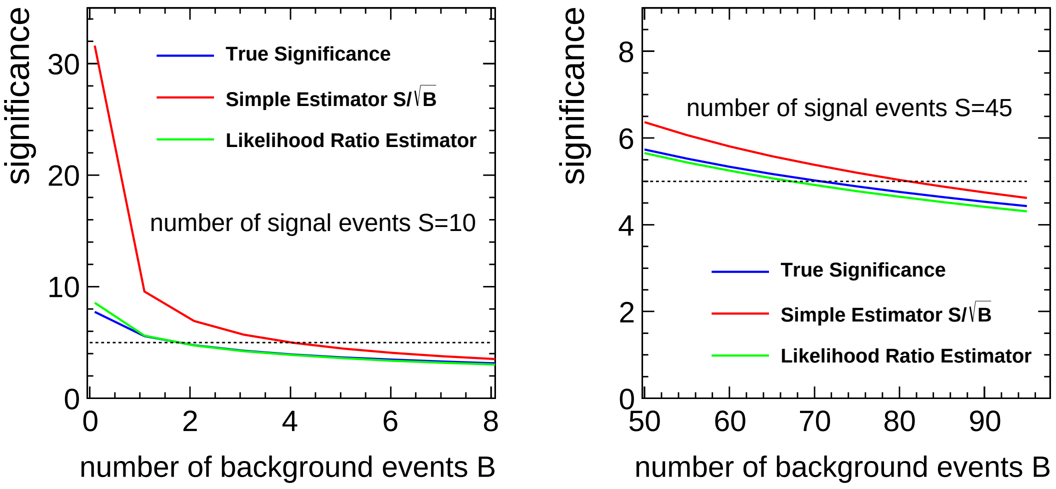

(a) (b)

Figure 7.3: Comparison of significance estimators in different regimes of background events: (a) The simple $S/\sqrt{B}$ estimator overrates the significance for low backgrounds strongly, whereas the likelihood based estimator is close to the actual true significance. (b) Also in the regime of moderate background the likelihood based estimator performs better.

The performance of both estimators with respect to the true significance (7.28) is illustrated in Figure 7.3. We have studied two different regimes, which are of relevance for the following analysis. Figure 7.3a depicts the resulting significance for low backgrounds. It is visible that the simple estimator strongly overestimates the significance for very few background events, whereas the likelihood ratio estimator performs outstanding well. In Figure 7.3b, the scenario of a moderate number of background events compared to the number of signal events is presented. Also here, the likelihood ratio estimator is very close to the true significance. The dashed line in both figures shows the 5σ level needed for a discovery.

For this reason, we employ the likelihood ratio estimator for the following significance estimates.

7.2.2 Signal Significance at the Benchmark Point

The measurement of the LSP mass in the $\mu\mu$ channel allows us to define a signal region. We only select events where both reconstructed LSP masses are within the range $m^{\text{fit}}_{\tilde{\chi}^0_1} \pm 3\sigma^{\text{fit}}_{\tilde{\chi}^0_1}$. This reduces the Standard Model background further and we finally get the following event selection matrix for $\int L\mathrm{d}t = 100\,\mathrm{fb}^{-1}$:

$$\mathbf{N} = \begin{array}{c} \\ N^{\text{sel}}_{\mu\mu} \\ N^{\text{sel}}_{\mu\tau} \\ N^{\text{sel}}_{\tau\tau} \end{array} \begin{array}{c} \begin{array}{ccccc} N^{\text{true}}_{\mu\mu} & N^{\text{true}}_{\mu\tau} & N^{\text{true}}_{\tau\tau} & N^{\text{true}}_{\text{LSP BG}} & N^{\text{true}}_{\text{SM BG}} \end{array} \\ \begin{pmatrix} 858 & 173 & 11 & 40 & 69 \\ 16 & 410 & 45 & 17 & 67 \\ 0 & 2 & 107 & 4 & 60 \end{pmatrix} \end{array} \tag{7.31}$$

In the different rows, the event counts of selected events per selection class are given. The columns indicate the decomposition of those events into their true origin.

We can now derive the significance of the selected events with respect to the background expectation. For this purpose, we count also the LSP BG events as signal events, since they give also an excess with respect to the pure Standard Model hypothesis. Thus, we obtain for the number of signal and background events in the different classes

$$S_i = \sum_{j=1}^{4} \mathbf{N}_{ij} \qquad\qquad B_i = \mathbf{N}_{i5}, \tag{7.32}$$

with $i \in \{1, 2, 3\}$ denoting the individual selection classes and $j \in \{1...5\}$ denoting the true origin.

For an integrated luminosity of $\int L\mathrm{d}t = 100\,\mathrm{fb}^{-1}$, the signal significance becomes:

	m
$\mu\mu$ class	65.7
$\mu\tau$ class	37.0
$\tau\tau$ class	11.8

Assuming that the signal and background event numbers scale linearly with the integrated luminosity taken at the ILC, we can derive the minimum amount of data needed in order to make a 5σ discovery of the bRPV SUSY LSP decay in the different channels (cf. Figure 7.4). In the $\mu\mu$ channel, for instance, a discovery can already be made with a data set of $\int L\mathrm{d}t = 0.6\,\mathrm{fb}^{-1}$, which is acquired within less than a day at full ILC500 running. Even in the low-performing $\tau\tau$ channel a data set of only $\int L\mathrm{d}t = 16\,\mathrm{fb}^{-1}$ is sufficient to make a 5σ discovery.

7.2.3 Signal Significance in the Simplified Model Parameter Plane

In a next step, we leave the single benchmark point and interpret our findings in the two-dimensional parameter plane of the simplified model described in Section 4.4.

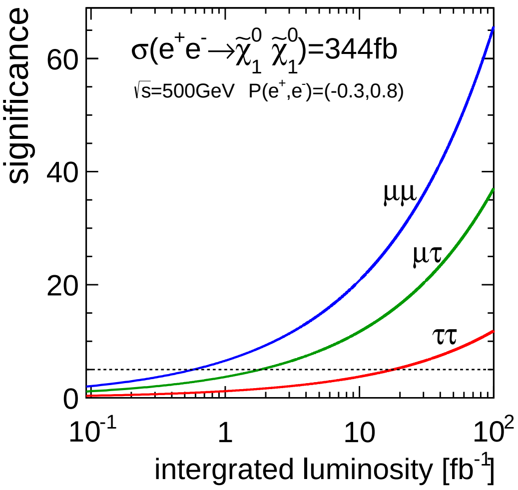

Figure 7.4: Signal significance as a function of the integrated luminosity at the studied benchmark point. A 5σ discovery of the bRPV LSP decay of the LSP in the $\mu\mu$ channel is possible very early.

Therefore, we assume that the selection efficiencies of the different event classes stay unchanged for different LSP masses. This is a conservative assumption, since in the case of a heavier LSP, the reconstruction and selection would benefit from stronger boosted decay objects of the LSP.

In order to find the 5σ discovery contours in the parameter plane, the number of signal events S is derived from the LSP-pair production cross section calculated by `SPheno` and the corresponding branching ratios at the point in the parameter space multiplied with the efficiency for reconstructing events in the corresponding event class. The number of background events is directly extracted from the Standard Model background shown in Figure 6.14. We require that the reconstructed mass of both LSP candidates lie within a signal range of $\pm 3\sigma^{\mathrm{fit}}_{\tilde{\chi}^0_1}$ around the true LSP mass. For the significance calculation, the likelihood ratio based estimator is used.

The result is depicted in Figure 7.5 for an integrated luminosity of $\int L dt = 500\,\mathrm{fb}^{-1}$ and a center-of-mass energy of $\sqrt{s} = 500\,\mathrm{GeV}$. It is visible that in the $\mu\mu$ selection the bRPV decay of the LSP can be discovered for selectron masses of up to 1.5 TeV in a large range of LSP masses. In the $\mu\tau$ channel, the presented selection is sensitive to selectron masses of up to 700 GeV and even in the poor $\tau\tau$ channel a discovery can be made for not too heavy LSPs and selectron masses of below 400 GeV. This is a remarkable result, since we can test in this simplified model selectron masses well beyond the direct kinematic reach of both ILC500 and ILC1000. Even if we assume a reduction of the signal-like LSP decays modes by 90% (e.g. induced by a very light stau, see Figure 4.6b), we can still probe the parameter space up to selectron masses of about 800 GeV for the presented event selection procedure.

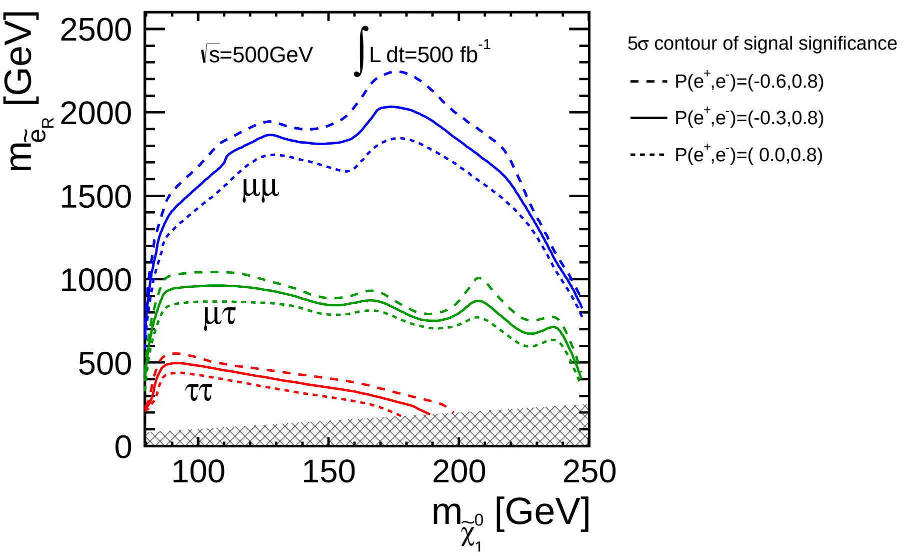

Figure 7.5: 5σ contour of signal significance in the $\mu\mu$ (blue), $\mu\tau$ (green), and $\tau\tau$ (red) selection class based on an integrated luminosity of $\int L dt = 500\,\mathrm{fb}^{-1}$. The differently dashed lines show the impact of various positron polarisations. Thereby, a larger positron polarisation helps to increase the sensitivity.

The general trend for a degraded significance towards lower LSP masses is caused by the Standard Model background that is concentrated around $m_{W/Z}$. In this region we expect $\mathcal{O}(60)$ background events. For large LSP masses, the background is almost vanishing, but also the signal is small since the cross section drops in this region, which also results in a drop of the significance. As already discussed, both regimes are well modelled by the used significance estimator (cf. Section 7.2.1).

Furthermore, Figure 7.5 also demonstrates the effect of positron polarisation. The solid lines indicate the baseline design polarisation of 30% polarised positrons. An upgrade to 60% would increase the production cross section and, thus, the sensitivity. In the $\mu\mu$ channel, for instance, this would lead to an increase of the sensitivity in the selectron mass by up to 200 GeV.

7.3 Measurement of Ratio of Branching Ratios

After having discussed the high precision mass measurement of the LSP and the discovery reach of the analysis, we are going to perform the measurement of the ratio of the two LSP branching ratios $\mathrm{BR}(\tilde{\chi}^0_1 \to W\mu)$ and $\mathrm{BR}(\tilde{\chi}^0_1 \to W\tau)$, which is one of the important motivations for studying this bRPV model.

7.3.1 Efficiency Matrix

In order to determine the ratio of branching ratios of the LSP decay, it is necessary to unfold the different contributions ending up in the selection classes.

Therefore, we build an 3×3 efficiency matrix based on the event matrix $\mathbf{N}$ (cf. Equation (7.31)) which takes care of migration of events into other classes:

$$(\mathbf{E})_{ij} = \frac{(\mathbf{N})_{ij}}{N_j^{\mathrm{true}}} = \begin{pmatrix} 0.2981 & 0.02767 & 0.003224 \\ 0.005566 & 0.06576 & 0.012892 \\ 0.0000 & 0.0003591 & 0.03062 \end{pmatrix}_{ij} \tag{7.33}$$

$$\delta\mathbf{E} = \begin{pmatrix} 0.0015 & 0.00014 & 0.000016 \\ 0.000028 & 0.00033 & 0.000065 \\ 0.0000 & 0.0000018 & 0.00015 \end{pmatrix}, \tag{7.34}$$

with $i, j = \{\mu\mu, \mu\tau, \tau\tau\}$. N_j^{true} denotes the number of simulated Monte-Carlo events in the different signal classes before any selection. The statistical error on the entries in the efficiency matrix follows the binomial statistics. However, we assume that the Monte-Carlo statistics which is used in order to derive the efficiencies at the time of the ILC running is going to be large enough such that statistical errors are negligible. The dominant source of error on the entries in the efficiency matrix comes from the systematic uncertainty on the Monte-Carlo description of the model and the event migration, which is estimated to be less then 0.5% (cf. discussion of systematic errors later in Section 7.3.3).

This efficiency matrix can be inverted in order to reconstruct the true number of events in the three event classes:

$$\mathbf{E}^{-1} = \begin{pmatrix} 3.381 & -1.4240 & 0.2436 \\ -0.2869 & 15.364 & -6.438 \\ 0.003364 & -0.18018 & 32.73 \end{pmatrix} \tag{7.35}$$

The error on the inverted efficiency matrix is calculated as

$$\delta(\mathbf{E}\mathbf{E}^{-1}) = \delta\mathbb{1} \tag{7.36}$$

$$\delta\mathbf{E}\mathbf{E}^{-1} + \mathbf{E}\delta\mathbf{E}^{-1} = 0 \tag{7.37}$$

$$\delta\mathbf{E}^{-1} = -\mathbf{E}^{-1}\delta\mathbf{E}\mathbf{E}^{-1}. \tag{7.38}$$

Thus, numerically we get

$$\delta\mathbf{E}^{-1} = \begin{pmatrix} -0.017 & 0.0071 & -0.0012 \\ 0.0014 & -0.077 & 0.032 \\ -0.000017 & 0.00090 & -0.16 \end{pmatrix}. \tag{7.39}$$

For the actual measured and selected number of events, we assume that the Standard Model background can be estimated and subtracted with an accuracy of 0.05% based on Monte-Carlo samples (cf. Section 7.1.2 and Table 7.1). Also the LSP background can be predicted once the LSP mass is known, which is possible at a very early stage, as discussed before. In the case no other SUSY particle has directly been found at the ILC except for the LSP, contaminations of the event selection originating from three-body decays can be neglected. The LSP mass then defines the relative branching ratio of the LSP decay modes involving a W, Z, or Higgs boson (cf. Figure 4.6a). The latter two influence the number of LSP background events. After all, we assume that the LSP background can be predicted and subtracted with an accuracy of 0.5% (cf. Section 7.3.3).

The vector of selected signal events finally becomes

$$\vec{N}^{\text{sel}}_{\text{sig}} = \begin{pmatrix} N^{\text{sel}}_{\mu\mu} - \langle N^{\text{MC}}_{BG,\mu\mu}\rangle \\ N^{\text{sel}}_{\mu\tau} - \langle N^{\text{MC}}_{BG,\mu\tau}\rangle \\ N^{\text{sel}}_{\tau\tau} - \langle N^{\text{MC}}_{BG,\tau\tau}\rangle \end{pmatrix} \tag{7.40}$$

$$\delta\vec{N}^{\text{sel}}_{\text{sig}} = \begin{pmatrix} \sqrt{N^{\text{sel}}_{\mu\mu} + \delta\langle N^{\text{MC}}_{BG,\mu\mu}\rangle^2} \\ \sqrt{N^{\text{sel}}_{\mu\tau} + \delta\langle N^{\text{MC}}_{BG,\mu\tau}\rangle^2} \\ \sqrt{N^{\text{sel}}_{\tau\tau} + \delta\langle N^{\text{MC}}_{BG,\tau\tau}\rangle^2} \end{pmatrix}. \tag{7.41}$$

The error on the number of selected events comprises the Poissonian error on the number of selected events and the uncertainty on the Monte-Carlo background estimation. However, the latter contribution is much smaller compared to the first one and, thus, can be neglected.

The reconstructed number of events in the event classes can then be evaluated by

$$\vec{N}^{\text{reco}} = \mathbf{E}^{-1}\vec{N}^{\text{sel}}_{\text{sig}} \tag{7.42}$$

$$\delta N^{\text{reco}}_i = \sqrt{\sum_{j=1}^{3}\left((\vec{N}^{\text{sel}}_{\text{sig}})_j(\delta\mathbf{E}^{-1})_{ij}\right)^2 + \sum_{j=1}^{3}\left((\mathbf{E}^{-1})_{ij}(\delta\vec{N}^{\text{sel}}_{\text{sig}})_j\right)^2}. \tag{7.43}$$

Those event counts are used now to determine $\text{BR}(\tilde{\chi}^0_1 \to W\mu)/\,\text{BR}(\tilde{\chi}^0_1 \to W\tau)$.

7.3.2 Measurement of $\text{BR}(\tilde{\chi}^0_1 \to W\mu)/\,\text{BR}(\tilde{\chi}^0_1 \to W\tau)$

There exist three different ways of deducing the ratio of $\text{BR}(\tilde{\chi}^0_1 \to W\mu)$ and $\text{BR}(\tilde{\chi}^0_1 \to W\tau)$ from the three observed event counts:

$$\frac{\text{BR}(\tilde{\chi}^0_1 \to W\mu)}{\text{BR}(\tilde{\chi}^0_1 \to W\tau)} = \frac{2N^{\text{reco}}_{\mu\mu}}{N^{\text{reco}}_{\mu\tau}} = \frac{2N^{\text{reco}}_{\mu\tau}}{N^{\text{reco}}_{\tau\tau}} = \sqrt{\frac{N^{\text{reco}}_{\mu\mu}}{N^{\text{reco}}_{\tau\tau}}}, \tag{7.44}$$

because for the expected number of events the following relations hold

$$N_{\mu\mu} = N_{\tilde{\chi}_1^0\tilde{\chi}_1^0} \cdot \mathrm{BR}(\tilde{\chi}_1^0 \to W\mu)^2 \tag{7.45}$$

$$N_{\mu\tau} = N_{\tilde{\chi}_1^0\tilde{\chi}_1^0} \cdot 2\,\mathrm{BR}(\tilde{\chi}_1^0 \to W\mu) \cdot \mathrm{BR}(\tilde{\chi}_1^0 \to W\tau) \tag{7.46}$$

$$N_{\tau\tau} = N_{\tilde{\chi}_1^0\tilde{\chi}_1^0} \cdot \mathrm{BR}(\tilde{\chi}_1^0 \to W\tau)^2, \tag{7.47}$$

where $N_{\tilde{\chi}_1^0\tilde{\chi}_1^0} = \sigma(e^+e^- \to \tilde{\chi}_1^0\tilde{\chi}_1^0) \cdot \int L dt$ is the number of produced LSP pairs.

We obtain the following three results at the studied benchmark point. The uncertainties are scaled to an integrated luminosity of $\int L dt = 500\,\mathrm{fb}^{-1}$:

$$\frac{2N_{\mu\mu}^{\mathrm{reco}}}{N_{\mu\tau}^{\mathrm{reco}}} = 0.923 \pm 0.035 \tag{7.48}$$

$$\frac{2N_{\mu\tau}^{\mathrm{reco}}}{N_{\tau\tau}^{\mathrm{reco}}} = 0.891 \pm 0.060 \tag{7.49}$$

$$\sqrt{\frac{N_{\mu\mu}^{\mathrm{reco}}}{N_{\tau\tau}^{\mathrm{reco}}}} = 0.907 \pm 0.026 \tag{7.50}$$

Special care must be taken for the error calculation. Inspecting Equation (7.43) shows that the errors of the reconstructed number in the event classes are not uncorrelated, which has to be taken into account in the error propagation. The results are also depicted in Figure 7.6. Herein, the dashed line indicates the input value for the simulation, $\mathrm{BR}(\tilde{\chi}_1^0 \to W\mu)/\mathrm{BR}(\tilde{\chi}_1^0 \to W\tau) = 0.9035$. All three results are within their statistical errors in very good agreement with the actual input value. The most precise single result is achieved in (7.50), which can be attributed to the square root in the relation.

A possibility of improving further the uncertainty on the ratio of the two branching ratios is by a constrained fit, which utilises that (7.44) is an over-constrained system of equations. However, it is not expected that this gives an exceedingly large improvement in the achievable precision compared to the result obtained in (7.50). As we will see in Section 7.4, the final achievable precision of the measurement of the atmospheric neutrino mixing angle is limited by parametric uncertainties. Therefore, we continue the discussion with result given in Equation (7.50).

Figure 7.7 depicts the expected relative uncertainty in measuring the ratio of the two branching ratios in dependence of the integrated luminosity taken at ILC500. For an integrated luminosity of $\int L dt = 100\,\mathrm{fb}^{-1}$, the achievable precision is about 6%, which scales down to 2.9% for $500\,\mathrm{fb}^{-1}$ or even 2.1% for $1000\,\mathrm{fb}^{-1}$. The relative uncertainty in the limit $\int L dt \to \infty$ becomes 0.32%. This can be understood as the systematic uncertainty on the measurement of $\mathrm{BR}(\tilde{\chi}_1^0 \to W\mu)/\mathrm{BR}(\tilde{\chi}_1^0 \to W\tau)$ originating from the systematic uncertainty of the efficiency matrix.

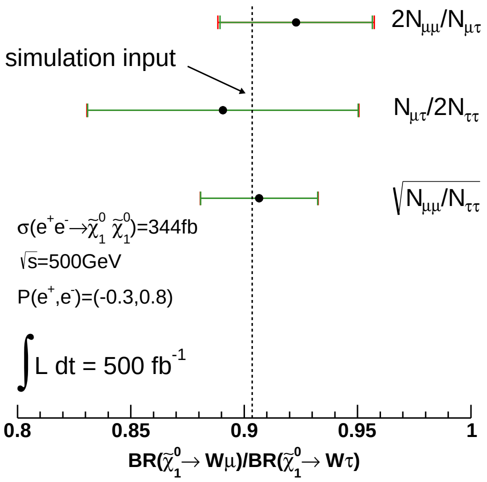

Figure 7.6: Results of the extraction of $\mathrm{BR}(\tilde{\chi}_1^0 \to W\mu)/\mathrm{BR}(\tilde{\chi}_1^0 \to W\tau)$ using the reconstructed event counts of the different event classes. The total uncertainty (red error bars) is completely dominated by the statistical uncertainty (green error bars). The vertical dashed line shows the simulated input value. All measurements agree within the statistical errors with the simulated value at the benchmark point. The presented errors are scaled according to an integrated luminosity of $\int Ldt = 500\,\mathrm{fb}^{-1}$.

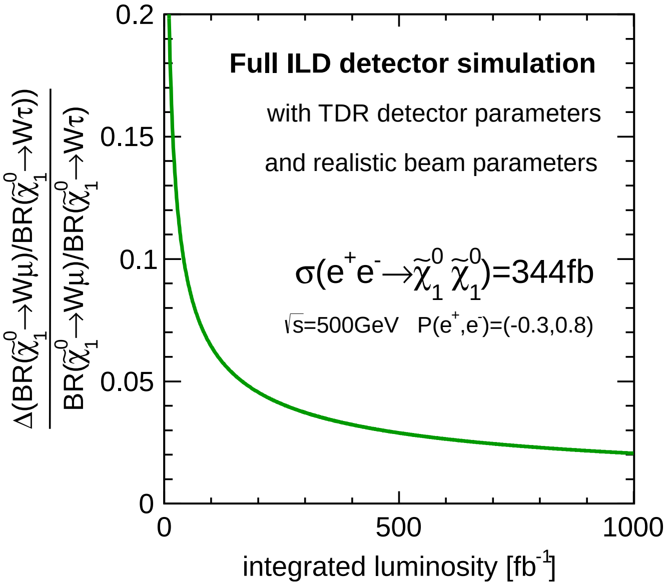

Figure 7.7: Achievable measurement precision of the ratio of the two branching ratios $\mathrm{BR}(\tilde{\chi}_1^0 \to W\mu)$ and $\mathrm{BR}(\tilde{\chi}_1^0 \to W\tau)$ in dependence of the integrated luminosity taken at ILC500.

	control process	cross section	$1/\sqrt{N}$@500 fb^{-1}
μ / τ ID with $Z/W \to$ jets	$ZZ \to ll q\bar{q}$	225 fb	0.3%
	$WW \to l\nu_l q\bar{q}$	2.5 pb	0.09%
W-boson reconstruction	$WW \to$ hadrons	7 pb	0.05%
total			$\sim$ 0.5%

Table 7.2: Possible control samples to verify efficiencies and purities obtained from Monte-Carlo simulation; l denotes either a μ or a τ. The largest contribution originates from the limited statistics of the SM control sample for verifying the migrations between the $\mu\mu$, $\mu\tau$ and $\tau\tau$ classes.

7.3.3 Systematic Uncertainties

As shown in Equation (7.44), the measurement of the ratio of branching ratios reduces to the measurement of the ratio of two event numbers in the different event classes. For this reason, all systematic uncertainties that factorise with the number of events, like uncertainties on beam polarisation or beam energy, cancel out in this calculation. The same is valid for those reconstruction effects which affect all selection classes simultaneously, like uncertainties on the jet-energy scale, for instance.

The main source of uncertainty is expected to arise from the extraction of selection efficiencies and purities for the different selection classes from Monte-Carlo data. Hence, it is very important to validate the efficiencies and purities for the lepton identification as well as the W-boson reconstruction with real data.

A well suited process for doing this is $e^+e^- \to ZZ \to l^+l^-q\bar{q}$ with $l = \{\mu, \tau\}$. It allows one to study μ + jets and τ + jets events under comparable experimental conditions. The unpolarised cross section for the process at a center-of-mass energy of $\sqrt{s} = 500\,\mathrm{GeV}$ amounts to 225 fb. Assuming a data set corresponding to an integrated luminosity of $\int L dt = 500\,\mathrm{fb}^{-1}$, the statistical uncertainty in comparing measured data with Monte-Carlo data becomes 0.3%. Another process which could be used for studying selection efficiencies is $e^+e^- \to WW \to l\nu_l q\overline{q'}$ with $l = \{\mu, \tau\}$. This process has a significantly larger cross section of 2.5 pb and, therefore, the statistical uncertainty for 500 fb^{-1} amounts to 0.09%.

A control process for the W-boson reconstruction efficiency could be $e^+e^- \to WW \to$ hadrons, which has a very large cross section of 7 pb such that the statistical uncertainty for 500 fb^{-1} is 0.05%.

Table 7.2 summarises the possible control samples. Overall, we assume that the uncertainty on the selection efficiencies can be controlled below 0.5%. Further uncertainties originating from background subtraction are well below the expected Poissonian fluctuations in the event classes and can therefore be neglected.

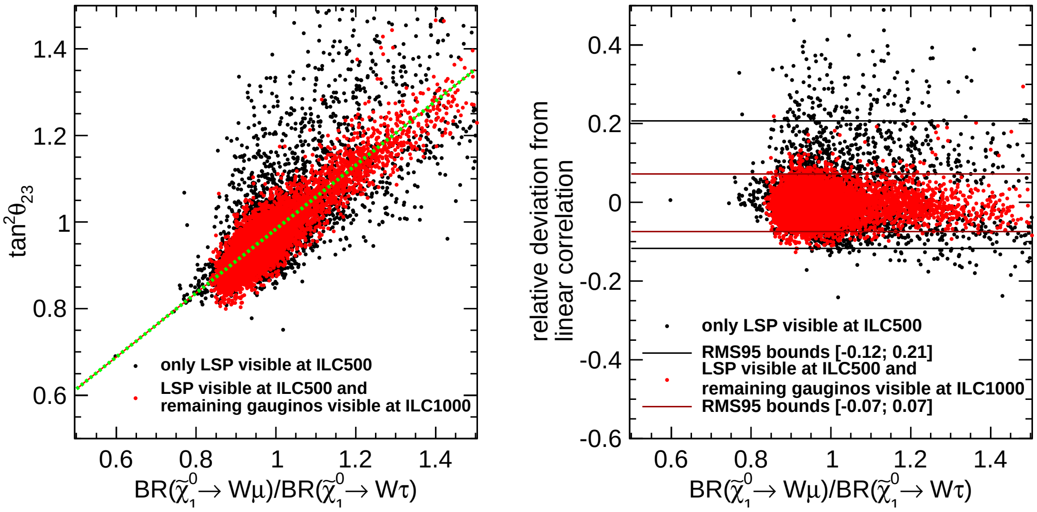

(a)

(b)

Figure 7.8: Random scan in the SUSY parameter space for two scenarios. Each dot represents a viable SUSY parameter configuration. (a) Correlation between atmospheric mixing angle and ratio of branching ratios. (b) Relative deviation from linear correlation. The horizontal lines indicate the corresponding RMS95 bounds.

7.4 Neutrino Interpretation

Finally, the measured ratio of branching ratios is translated into a measurement of the atmospheric mixing angle according to Equation (4.32):

$$\tan^2(\theta_{23}) \simeq \frac{\mathrm{BR}(\tilde{\chi}^0_1 \to W\mu)}{\mathrm{BR}(\tilde{\chi}^0_1 \to W\tau)} = R \tag{7.51}$$

This relation is valid at tree level. For higher orders of perturbation theory, there enter additional dependencies on other SUSY parameters, which have to be considered as parametric uncertainties. In order to study these residual parametric uncertainties, we define two scenarios: Firstly, only the LSP is directly observable at the ILC500 and the masses of all other SUSY particles are randomly chosen to be larger than 300 GeV. Secondly, the remaining three neutralinos are kinematically accessible at the ILC1000.

Figure 7.8 shows for both scenarios a SUSY parameter scan of about 6000 random data points provided by [190]. In Figure 7.8a, the correlation between the ratio of branching ratios with the atmospheric mixing angle is depicted. The black data points correspond to a viable set of SUSY parameters in the first scenario and the red points show viable parameter configurations in the more restricted scenario. It is observable that the linear correlation between the two axes becomes narrower with increasing knowledge of the sparticle spectrum. The green dashed line is a fitted first order polynomial to the data points of scenario one.

The relative deviation from the fitted straight line is plotted in Figure 7.8b. In order to estimated the parametric uncertainty on Equation (7.51), we evaluate the RMS95 bounds of the projection of the data points onto the y-axis. We find that in scenario one 95% of the random points deviate at maximum between −12% and 21% from a linear behaviour. For scenario two, this reduces to a range between −7% and 7%. However, it has to be noted that the point density cannot be interpreted as a probability density, since there is no well defined measure and *any* point represents a viable supersymmetric scenario. In the following, we are going to consider a parametric uncertainty of ±17% and ±7%, according to the two scenarios.

Thus, we can rewrite Equation (7.51) as

$$\tan^2(\theta_{23}) = a \cdot \frac{\mathrm{BR}(\tilde{\chi}_1^0 \to W\mu)}{\mathrm{BR}(\tilde{\chi}_1^0 \to W\tau)} = a \cdot R, \tag{7.52}$$

where the parameter a accounts for the parametric dependency. The central value of a is set to 1, but the parametric uncertainty is included in $\delta a = \{0.07, 0.17\}$.

Usually the neutrino mixing angle is quoted as $\sin^2(\theta_{23})$. Therefore, we transform Equation (7.52) into

$$\sin^2(\theta_{23}) = \frac{\tan^2(\theta_{23})}{1+\tan^2(\theta_{23})} = \frac{a \cdot R}{1 + a \cdot R}. \tag{7.53}$$

For the uncertainty we find

$$\delta \sin^2(\theta_{23}) = \sqrt{\frac{\delta R^2 + \delta a^2 R^2}{(1+R)^4}}. \tag{7.54}$$

Finally, the relative uncertainty $\delta \sin^2(\theta_{23}) / \sin^2(\theta_{23})$ is depicted in Figure 7.9a in dependence of the integrated luminosity. It is clearly visible that the uncertainty is dominated by the parametric uncertainty. The ultimate achievable experimental precision for an integrated luminosity of $\int L dt = 500\,\mathrm{fb}^{-1}$ on $\sin^2(\theta_{23})$ amounts to 1.5%. We can now compare the measurement precision with current measurements at neutrino experiments. In Figure 7.9b, the red solid line indicates the current best fit value $\sin^2(\theta_{23})$ extracted from current neutrino oscillation data [99]. The dashed red lines show the corresponding 1σ interval. The overlaid measurement uncertainty at the ILC demonstrates that the ILC is capable to decide whether the measured LSP decay rates are compatible with the directly measured neutrino mixing under the assumption of bRPV. Therefore, the ILC can test whether neutrino

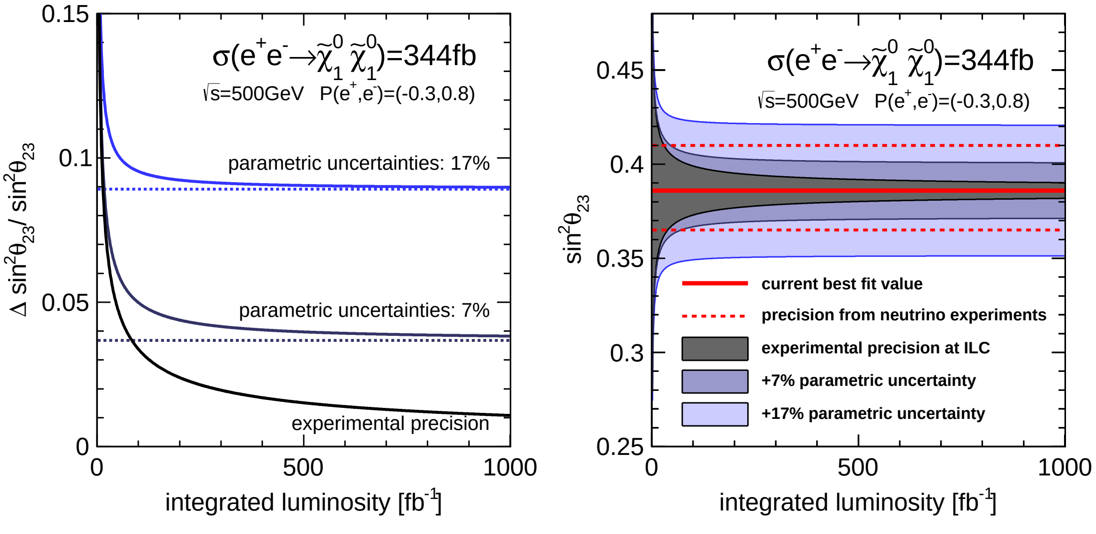

(a) (b)

Figure 7.9: Precision of the measurement of the atmospheric mixing angle at the ILC. (a) Relative uncertainty assuming different parametric uncertainties on the relation between ratio of branching rations and atmospheric neutrino mixing angle. (b) Comparison between achievable precision at the ILC and the precision at current neutrino experiments assuming present best fit value [99] as central value.

mixing is introduced by bRPV SUSY. Future improvements in the measurement of the atmospheric neutrino mixing angle at neutrino experiments like the LBNE (see Section 4.1.3) would further sharpen the comparison between the both independent measurements. Furthermore, if bRPV SUSY is realised in nature, the measurement of the ratio of branching ratios $\mathrm{BR}(\tilde{\chi}_1^0 \rightarrow W\mu)/\,\mathrm{BR}(\tilde{\chi}_1^0 \rightarrow W\tau)$ could contribute to the determination of the octant of θ_{23} for nonmaximal mixing.

7.5 Further Perspectives

As shown in the last section, experimental improvements are not urgent at the current status of the parametric uncertainties. However, in this section, we comment on several options for further improvements of the presented analysis.

As aforementioned, Regarding the lepton identification a dedicated tau finding algorithm would certainly help to increase the selection efficiency of the $\mu\tau$ and $\tau\tau$ channel. Such an algorithm can make use of the decay properties of τ leptons. Typical variables to be used for that advanced identification are the number of tracks used to form the composite object, the overall charge, opening angle of the tracks, the impact parameter, or the jet mass.

In order to compensate for the missing energy due to the involved neutrino(s) in the τ decay, a kinematic fit of the event could help to increase the reconstruction performance. Also the W-boson reconstruction could benefit from this technique. Additionally, with this approach the explicit dependence of the LSP-mass reconstruction on the jet-energy scale could be substantially reduced. In exchange, a dependence on the center-of-mass energy is introduced. The center-of-mass energy, however, can be measured very precisely at the ILC to 10^{-4} [57]. Thus, a kinematic fit would also offer an independent cross-check of the systematic uncertainties in the LSP-mass reconstruction.

Once a proper τ identification is defined, one could make use of the reconstructed charge of the two involved leptons in the events. Neutralinos are Majorana particles and, therefore, they decay equally into $W^- + l^+$ and $W^+ + l^-$. In 50% of the events of pair-produced LSPs, both leptons carry the same charge. It could be worthwhile to study the additional cut on same-sign leptons. The signal selection efficiency would be reduced by a factor of two, but the effect on the LSP background comprising a Z boson and the Standard Model background is most likely much larger.

One striking feature of bRPV SUSY in the studied parameter range is the long lifetime of the LSP (cf. Figure 4.5). The lifetime information has not been exploited further in this analysis because it depends strongly on the LSP mass which would introduce a model dependency in the selection. However, especially in the region of the parameter space where the main Standard Model background is expected (around the W/Z-boson mass), displaced LSP decay vertices of a few millimeter are a powerful selection criterion, which could suppress Standard Model background events very efficiently.

8 Polarimetry

In the previous chapters, it has become clear that beam polarisation is a powerful tool in order to fully exploit the physics potential of the ILC. Therefore, we concentrate in the second part of this thesis on polarimetry and lay the focus especially on the polarimeter calibration.
In Section 8.1, we first introduce basic concepts of beam polarisation measurement. Thereby, we comment on the possibility of extracting the beam polarisation from collision data and discuss the need of dedicated polarimetry. In the subsequent Section 8.2, the precision goal of the polarisation measurement as well as the main source of measurement uncertainties at a ILC Compton polarimeter are discussed. Finally, in Section 8.3, we focus on the detector nonlinearity as one of the main contributions to the allowed error budget and describe the main sources of the nonlinear detector response.

8.1 Polarisation Measurement

As discussed in Section 3.3, beam polarisation needs to be measured to high precision in order to be able to extract observables of physical interest as accurate as possible. The actual quantity of interest is the so-called luminosity weighted polarisation at the IP

$$\langle \mathcal{P}_{e^\pm} \rangle_{\mathrm{IP}} = \frac{\int \mathcal{P}_{e^\pm}(t) L(t) \mathrm{d}t}{\int L(t) \mathrm{d}t}. \tag{8.1}$$

It is possible to extract the long-term average beam polarisation directly from collision data.

8.1.1 Polarisation Determination from Collision Data

In the so-called modified Blondel scheme [191], the absolute value of the electron and positron beam polarisation can be obtained from a known process, which is polarisation dependent. For all possible beam polarisation configurations $(\pm\mathcal{P}_{e^-}, \pm\mathcal{P}_{e^+})$, the total cross sections are measured. Assuming that the absolute value of the beam

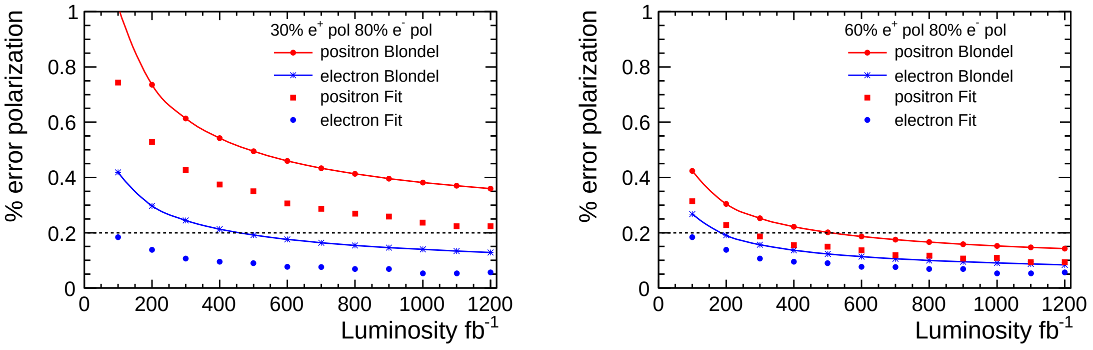

(a) $|\mathcal{P}_{e^+}| = 30\%, |\mathcal{P}_{e^-}| = 80\%$ **(b)** $|\mathcal{P}_{e^+}| = 60\%, |\mathcal{P}_{e^-}| = 80\%$

Figure 8.1: Achievable precision of the beam polarisation with the modified Blondel scheme and the angular fit method (see text for details) in the case of W-boson-pair production. A higher positron beam polarisation allows in most cases for a better precision in the determination of the beam polarisation. (a) and (b) differ in the absolute value of the positron polarisation. Taken from [193].

polarisation stays constant for helicity reversal, the absolute beam polarisation can be derived from [192]

$$\langle|\mathcal{P}_{e^\pm}|\rangle_{\text{IP}} = \sqrt{\frac{(\sigma_{-+}+\sigma_{+-}-\sigma_{--}-\sigma_{++})(\pm\sigma_{-+}\mp\sigma_{+-}+\sigma_{--}-\sigma_{++})}{(\sigma_{-+}+\sigma_{+-}+\sigma_{--}+\sigma_{++})(\pm\sigma_{-+}\mp\sigma_{+-}-\sigma_{--}+\sigma_{++})}}, \tag{8.2}$$

where $\sigma_{\pm\pm}$ denotes the measured cross section for a specific beam polarisation configuration (cf. Section 3.3).

A typical process to investigate for the polarisation determination is W-boson-pair production because of its large cross section at the ILC. It has been extensively studied in References [188, 193]. In addition to the modified Blondel scheme, which relies only on total cross section measurements, also differential cross sections have been investigated for extracting the beam polarisation. This method makes use of template fits in bins of the polar angle of the produced W bosons with respect to the beam axis. A comparison between both methods in terms of the achievable precision of the measured beam polarisation for the electron and positron beam are depicted in Figure 8.1. It shows that a sub-percent precision can be reached in both cases for large data samples. Thereby, the angular fit method performs significantly better than the modified Blonde scheme. However, it should be noted that in the case of the modified Blondel scheme in principle *all* polarisation dependent processes could be exploited and not only W-boson-pair production. A comparison of Figure 8.1a and 8.1b underlines the importance of a high positron beam polarisation.

In both figures, it is assumed that the total integrated luminosity is distributed equally among the four different beam polarisation configurations in order to obtain

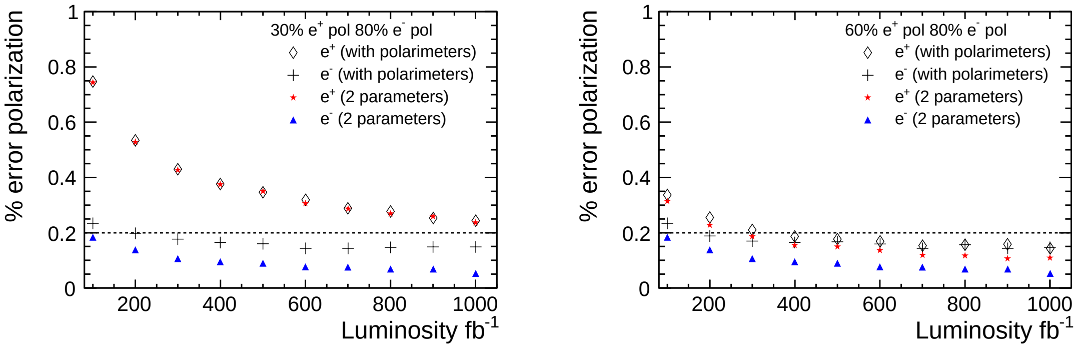

(a) $|\mathcal{P}_{e^+}| = 30\%, |\mathcal{P}_{e^-}| = 80\%$ **(b)** $|\mathcal{P}_{e^+}| = 60\%, |\mathcal{P}_{e^-}| = 80\%$

Figure 8.2: Comparison between the angular fit method assuming perfect helicity reversal and the more realistic polarimeter scheme (see text for details). For $\int Ldt > 400\,\text{fb}^{-1}$ the precision of the determination of the beam polarisation is limited in most of the cases by the systematic uncertainty of the polarimeter measurement. Taken from [193].

the corresponding cross sections $\sigma_{++}, \sigma_{-+}, \sigma_{+-}, \sigma_{--}$. However, for most analyses, both like-sign beam helicity configurations are disfavoured and, therefore, the smallest possible fraction of the luminosity should be spent on this configuration. Although in the angular fit method the helicity configuration "++" and "−−" can be avoided completely (in contrast to the modified Blondel scheme) it has been demonstrated that already a share of 2% of like-sign helicity configuration on the total integrated luminosity reduces the needed statistics for the same envisaged precision by a factor of two. A share of about 20% is already very close to the equal share situation (50%) [193].

Up to now, it has been assumed that the absolute polarisation of the beam stays the same before and after a helicity reversal and only the sign changes. Finally, in the angular fit method, this constraint can be relaxed, which is a much more realistic scenario. Leaving all four polarisation values ($\mathcal{P}_{e^\pm}^{\text{normal}}$, $\mathcal{P}_{e^\pm}^{\text{reversed}}$) as free fit parameters results in a very poor performance of the achievable precision in the determination of the beam polarisation. Assuming, however, that $\mathcal{P}_{e^\pm}^{\text{normal}}$ and $\mathcal{P}_{e^\pm}^{\text{reversed}}$ are equal up to a small value $\epsilon_{e^\pm}$,

$$|\mathcal{P}_{e^\pm}^{\text{normal}}| = |\mathcal{P}_{e^\pm}| + \epsilon_{e^\pm} \qquad\qquad |\mathcal{P}_{e^\pm}^{\text{reversed}}| = |\mathcal{P}_{e^\pm}| - \epsilon_{e^\pm}, \tag{8.3}$$

helps to restore the precision. Herein, $\epsilon_{e^\pm}$ has to be measured separately by polarimeters (see next section). $\epsilon_{e^\pm}$ comprises a systematic measurement uncertainty of 0.25%, which is propagated in the polarisation determination. It should be noted that a fast helicity reversal is necessary in order to ensure the assumptions in Equation (8.3) to be reasonable. Figure 8.2 shows the comparison of the ideal assumption of perfect helicity reversal (2 parameter fit) and the scenario incorporating a polarimeter measurement as described before. It is visible that in the polarimeter scenario the achievable precision is limited by the systematic uncertainty originating from $\delta\epsilon_{e^\pm}$ for $\int L\mathrm{d}t > 400\,\mathrm{fb}^{-1}$. Only the precision of the positron beam polarisation in the case of $\mathcal{P}_{e^+} = 30\%$ is still statistically limited.

Concluding, the collision data driven methods for determining the beam polarisation offer a very good precision. It is advantageous that the beam polarisation is exactly determined at the IP and that one obtains by default already the luminosity weighted polarisation. Depolarising effects due to beam collisions [194] are comprised as well as intra-bunch luminosity weighting. Unfortunately, this method is very slow. Only after years of ILC running, the precision on the determined polarisation is on the level of 0.2% and is finally limited by the polarimeter precision.

8.1.2 Need for Dedicated Polarimetry

The last section showed that there exist collision data driven methods for extracting the beam polarisation. However, as also discussed, in a realistic scenario, those methods rely on the input of an independent polarisation measurement. Therefore, this section outlines the principles of polarimetry.

8.1.2.1 Advantages of Compton Polarimetry

Polarimetry makes use of polarisation depended scattering processes. The two most commonly utilised processes in high energy accelerators are Møller scattering (e^--e^- scattering in a polarised target) and Compton scattering (γ-e scattering with polarised photons provided by a laser) [195]. Compton polarimetry has some clear advantages [69]:

- Compton scattering is well understood in QED, with radiative corrections less than 0.1% [196]
- Detector backgrounds can be measured and easily corrected by switching of the laser
- There is no thick target and therefore polarimetry data can be taken parasitic during a physics data run
- Compton scattering cross section is large such that statistical uncertainties of below 1% can be reached within a minute of data taking
- The laser polarisation can be changed very quickly on a pulse-by-pulse basis (in contrary to a polarised target)
- Uncertainties of laser polarisations can be controlled on a level of 0.1% [197]

For these reasons, Compton polarimetry is the technology chosen at the ILC.

8.1.2.2 Compton Polarimetry in Former Accelerators

Compton polarimetry has a long-standing history. In storage rings, transversal beam polarisation builds up automatically initiated by the Sokolov-Ternov effect [198]. For this reason, an independent polarisation measurement is essential in storage rings.

At LEP, a laser Compton polarimeter [199] was installed and a transverse polarisation of 57 ± 3% has been measured at a beam energy of 44.7 GeV [195].

HERA was equipped with two polarimeters. The so-called TPOL Compton polarimeter was dedicated to measure transversal polarisation of the lepton beam [200]. A second Compton polarimeter called LPOL [201] measured the longitudinal polarisation after a spin-rotator, which rotated the naturally transversal oriented polarisation vector of the beam into the longitudinal axis. In a recent reanalysis of the HERA II polarimeter data, the systematic uncertainty of the LPOL has been determined to 2.0% and for the TPOL to 1.9% [202].

The polarimeter which achieved the best precision up to now was operated at the Stanford Linear Collider (SLC) [203]. The collaboration has quoted a systematic uncertainty of the Compton polarimeter measurement of 0.5% [197].

8.1.2.3 Operating Principle of Compton Polarimeters

A detailed introduction to Compton polarimetry can be found in Reference [204]. In parts, we follow this description here:

The kinematics of Compton scattering is determined by the dimensionless variable

$$x = \frac{4E_0\omega_0}{m_e^2}\cos^2(\theta_0/2) \cong \frac{4E_0\omega_0}{m_e^2}, \tag{8.4}$$

where E_0 is the initial energy of the electron/positron, ω_0 the initial energy of the photon, m_e is the electron mass and θ_0 the crossing angle between the electron/-positron beam and the laser beam. Usually, the crossing angle is close to zero and can therefore be neglected.

The energies of the scattered electron and photon (E, ω) are related to the initial energies via energy conservation

$$E + \omega = E_0 + \omega_0 \cong E_0. \tag{8.5}$$

Since the photon is in the visible spectrum, it follows that ω_0 is negligible compared to the electron/positron energies of up to $E_0 = 250\,\text{GeV}$.

The spin dependent differential cross section can be formulated as

$$\frac{d\sigma}{dy} = \frac{2\sigma_0}{x}\Big(\underbrace{\frac{1}{1-y} + 1 - y - 4r(1-r)}_{\text{spin indep.}} + \underbrace{\mathcal{P}\lambda r x(1-2r)(2-y)}_{\text{spin dep.}}\Big). \tag{8.6}$$

Herein, $\mathcal{P}$ represents the electron/positron beam polarisation and λ the laser polarisation. y denotes the normalised energy of the scattered photon

$$y = \frac{\omega}{E_0}. \tag{8.7}$$

Further, the parameters σ_0 and r in Equation 8.6 are defined as

$$\sigma_0 = \pi r_0^2 = 0.2495\,b, \tag{8.8}$$

$$r = \frac{y}{x(1-y)}. \tag{8.9}$$

Figure 8.3a shows the energy dependent Compton cross section for the ILC parameters in dependence of the Compton-scattered electron/positron energy. The two different lines represent the $m_j = 1/2$ scattering mode, in which the head-on colliding incident photon and electron have the same helicity $\lambda\mathcal{P} = +1$ (blue line) and the $m_j = 3/2$ scattering mode, in which photon and electron helicity are opposite $\lambda\mathcal{P} = -1$ (red line). A clearly different behaviour can be observed, which is maximal at the Compton edge and vanishes as expected for unscattered particles ($E = E_0 = 250\,\text{GeV}$). The scattered Compton electrons are deflected due to the scattering process by only a few μrad in the whole energy range. Therefore, it is reasonable to exploit rather the energy of scattered particles than the scattering angle for reconstructing the Compton scattering process.

The Compton edge is the upper edge in the energy spectrum of the Compton-scattered photon or, due to energy conservation, the lower edge in the energy spectrum of the Compton-scattered electron/positron, respectively. Thus, it denotes the maximal energy transfer from the scattering electron to the involved photon. This point is kinematically determined and can be expressed as

$$\omega_{\max} = E_0\frac{x}{1+x} = E_{\min}. \tag{8.10}$$

Figure 8.3b illustrates the Compton endpoint energy of a Compton-scattered electron/positron in dependence of the initial lepton energy for incident green laser light, as it is foreseen at the ILC. Figure 8.3b shows a weak dependence of the position of the Compton edge from the beam energy, which changes only by a few GeV for the different discussed ILC staging scenarios (cf. Section 3.2). This is of relevance, since the position of the Compton edge is important for the alignment of a detector, as we will discuss later.

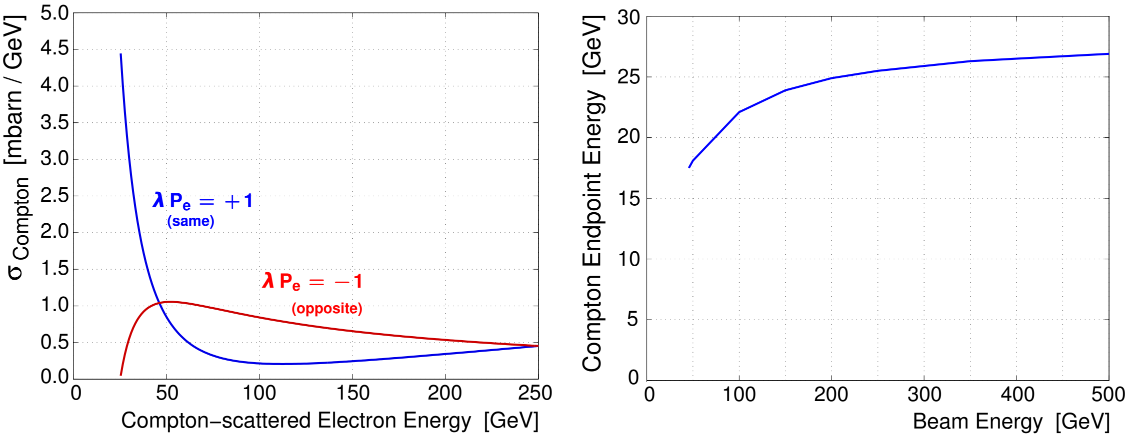

(a) **(b)**

Figure 8.3: (a) Differential Compton cross section of Compton-scattered leptons at $E_b = 250\,\mathrm{GeV}$ and $\omega = 2.33\,\mathrm{eV}$ (green laser). (b) Compton energy endpoint of Compton-scattered leptons in dependence of the beam energy. Taken from [205].

Between both helicity combinations an energy dependent asymmetry can be formed, which is usually denoted as analysing power:

$$\frac{d\mathcal{A}}{dE} = \frac{d\sigma^-/dE - d\sigma^+/dE}{d\sigma^-/dE + d\sigma^+/dE} \tag{8.11}$$

Herein, σ^+ (σ^-) indicates the cross section for the same (opposite) helicity configuration of photon and lepton. The total asymmetry can become rather small in a large analysed energy range. Therefore, it is highly desirable to define smaller energy intervals which feature a significantly larger analysing power. If the laser beam polarisation can be flipped between -1 and 1, it is possible to extract the average polarisation of the lepton beam

$$\mathcal{P}_i = \frac{1}{\mathcal{A}_i}\frac{\sigma^-_{m,i} - \sigma^+_{m,i}}{\sigma^-_{m,i} + \sigma^+_{m,i}} = \frac{1}{\mathcal{A}_i}\frac{N^-_{m,i} - N^+_{m,i}}{N^-_{m,i} + N^+_{m,i}}. \tag{8.12}$$

Herein, $\mathcal{A}_i$ indicates the analysing power in a certain energy interval

$$\mathcal{A}_i = \int_{E_i-\Delta/2}^{E_i+\Delta/2} \frac{d\mathcal{A}}{dE} dE, \tag{8.13}$$

$\sigma^{\pm}_{m,i}$ is the measured cross section in the corresponding energy interval for a given laser helicity ±1, and $N^{\pm}_{m,i} = \sigma^{\pm}_{m,i} \int L dt$ denotes the number of counted events correspondingly. The beam polarisation is determined in each polarimeter channel individually, which can be utilised in order to identify systematic effect. Finally, a weighted average of all $\mathcal{P}_i$ is calculated in order to obtain the beam polarisation [204].

It is important to note that the scattering process is unambiguously determined by the involved lepton *or* photon if the initial state is known. Therefore, in principle both objects, either the photon or the lepton, are suited to be used for detection. However, different operation modes of the polarimeter suggest different strategies: If the laser-bunch interaction rate is so small that only a single Compton-scattering process takes place per bunch crossing (single event mode), the energy of a single Compton-scattered photon can easily be analysed in a calorimeter such that a differential cross section measurement is possible. Additionally, the Compton-scattered leptons can also be examined in order to cross-check and eliminate systematic effects.

The statistical uncertainty of the polarisation measurement in the single event mode is obviously directly limited by the bunch crossing frequency. Especially in the case of a linear collider, which features small repetition rates (cf. Section 3.2), the single event mode is not sufficient in order to establish an acceptable statistical precision on short timescales. Therefore, at a linear collider, a polarimeter has to be operated in the multi-event mode. For an increased photon density, due to increased laser power for instance, in the order of 1000 scattering processes take place in parallel per bunch crossing. A calorimeter cannot disentangle the different photon energies anymore and, thus, in this case only the cross section weighted total energy sum can be obtained, and no energy resolved cross section measurement is accessible. Therefore, the analysing power is much smaller than in the differential case. Besides this, at the ILC one would expect a very large energy deposition in the calorimeter of $\mathcal{O}(10\,\text{TeV})$ per bunch crossing. Instead, in the multi-event mode, it is preferable to exploit the Compton-scattered leptons. The energy distribution of the leptons can be translated into a spatial distribution in a magnetic chicane such that an energy dependent event counting in corresponding detector channels is possible.

8.1.3 ILC Polarimeters

At the ILC, two Compton polarimeters operating in the multi-event mode are foreseen [56]. The upstream polarimeter is located in the beam delivery system (cf. Section 3.4.4) about 1800 m before the e^+/e^- interaction point, whereas the downstream polarimeter is located about 150 m behind. Since several magnets are situated between the polarimeters and the IP, the average polarisation vector of the particle bunches processes according to the T-BMT equation [206, 207]. In order to know the polarisation precisely at the IP, a dedicated spin transport simulation between the polarimeters and the IP is essential [194]. A detailed outline of both polarimeters can be found in Reference [205]. We summarise in the following the most important features.

8.1.3.1 Upstream Polarimeter

Figure 8.4a shows a schematic view of the upstream polarimeter. It consists of a magnetic chicane with four dipole magnets featuring all the same absolute magnetic field strength. Between dipoles 2 and 3 the Compton interaction point is situated, where about 1000 out of $\mathcal{O}(10^{10})$ leptons in a bunch undergo Compton scattering in the interaction with the laser beam. Dipoles 3 and 4 act as energy analyser of the scattered leptons making use of dispersion. The unscattered part of the lepton bunch is bent back to the original trajectory, whereas the energy spectrum of the Compton-scattered leptons is distributed on a transversal axis of 24 cm. At this, for the innermost detector channel, a clearance of about 2 cm to the main beam pipe is foreseen. This corresponds roughly to an observable part of the Compton energy spectrum ranging from the Compton edge up to an energy of 125 GeV. More energetic Compton-scattered electrons or positrons are too close to the unscattered leptons and cannot be detected at an acceptable background level.

The magnetic chicane is designed in such a way that it can be operated without changing the magnetic fields for all possible beam energies starting from the Z pole up to the full design energy. However, the fixed magnetic field strength makes it necessary to adjust the Compton IP laterally for each beam energy. In order to keep emittance growth induced by synchrotron radiation below 1%, the whole upstream polarimeter chicane is in total about 75 m long. [56].

In the foreseen operating mode, a statistical precision of the average polarisation of two measured bunch trains for both laser helicities is $\Delta\mathcal{P}/\mathcal{P} = 0.1\%$. The average polarisation of a single bunch with respect to its position within a bunch train can be determined to 1% already after 20 passed bunch trains [205]. In the 5 Hz scheme of the ILC, this corresponds to 4 s of data taking.

8.1.3.2 Downstream Polarimeter

The section of the beam line comprising the downstream polarimeter is depicted in Figure 8.4b. It allows for measuring the beam polarisation at a second point in the beam line. In order to study depolarising effects in e^+/e^- beam collisions, a second polarimeter behind the e^+/e^- IP is especially interesting. But also in the case of noncolliding beams during commissioning for instance, a second polarisation measurement is highly favourable in order to cross-calibrate the two polarimeters [194]. In Figure 8.4b, also a beam energy spectrometer is depicted (red), whereas the polarimeter is shown in blue.

The polarimeter chicane consists of six dipole magnets: The first two dipole magnets (1P+2P) offset the beam. Between the magnets 2P and 3P the Compton IP is located. The following two dipole magnets (3P+4P) provide a stronger magnetic

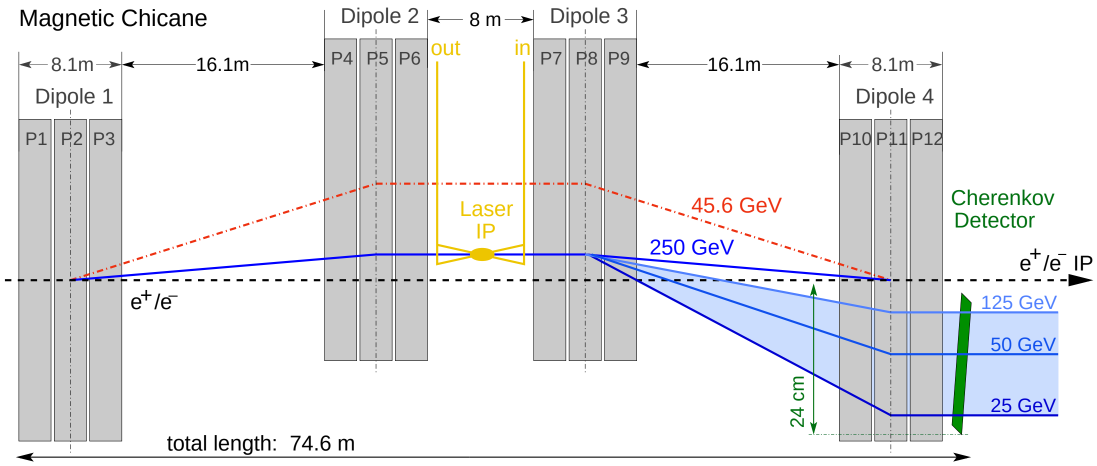

(a) Upstream polarimeter chicane.

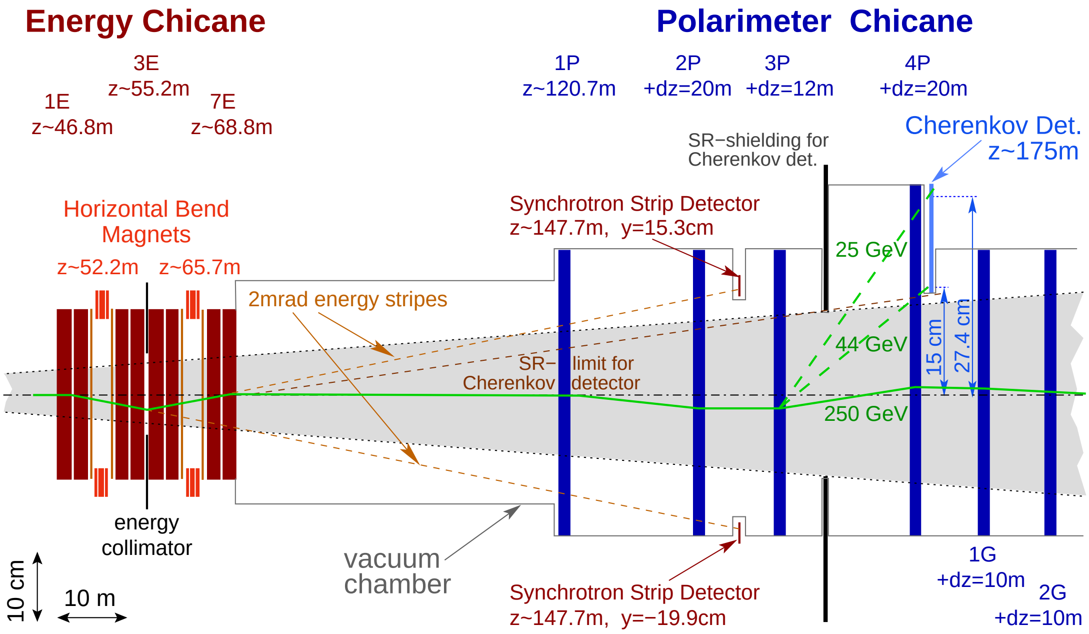

(b) Downstream energy chicane (red) and polarimeter chicane (blue).

Figure 8.4: Schematic view of upstream and downstream polarimeter. Taken from [205].

field compared to 1P and 2P, which results in an overcompensation of the deflection of the first two magnets. This helps to deflect the Compton-scattered leptons strong enough such that a large part of the Compton fan is separated from the synchrotron radiation fan originating from the e^+/e^- IP (grey area) and the energy chicane (dashed lines). Finally, the last two dipole magnets (1G+2G) bring the main beam back on the original trajectory. This modified chicane design has firstly been suggested in Reference [208].

The downstream polarimeter has a special laser design. Because of the highly disrupted beam after the collision and the, thereby, drastically reduced e^+/e^- density in the bunch, very intense lasers are necessary. Currently, three high intensity laser systems are foreseen, each operating at a maximal frequency of 5 Hz. For this reason, only three bunches per bunch train can be analysed. However, the achievable precision in the measurement of the polarisation at the downstream polarimeter is still $\Delta\mathcal{P}/\mathcal{P} < 1\%$ within one minute of data taking.

8.1.3.3 Cherenkov Detector

For detecting the Compton-scattered electrons or positrons, an array of Cherenkov detectors can be employed. This technique has also been used in the SLC polarimeter. A schematic picture of the arrangement of the Cherenkov detector channels is given in Figure 8.5a. In the current design, about 20 channels are foreseen for the upstream polarimeter [205]. The longitudinal displacement of the different Cherenkov detector channels along the beam line is necessary in order to avoid sharp edges in the beam pipe, which would introduce disturbing wake fields for the beam. Since the spatial distribution of the scattered electrons or positrons corresponds directly to their energy, the width of the Cherenkov detector channels represents the energy resolution of the spectrometer and, thus, defines Δ in Equation (8.13).

Figure 8.5b shows a cross section of a single Cherenkov detector channel. It is a gas-filled U-shaped pipe with a quadratic profile of $1 \times 1\,\mathrm{cm}^2$. The 15 cm long, horizontal part of the tube is located in the beam plane, in which also the Compton scattering takes place. An electron traversing the channel with an energy above the Cherenkov threshold produces Cherenkov light, which is reflected upwards at the end of the horizontal tube to a light sensor. Thereby, the amount of produced Cherenkov light is proportional to the number of traversing electrons or positrons in detector channel i, which is the relevant quantity for measuring $\mathcal{P}_i$ (see Equation (8.12)). At the other leg of the U-shaped tube, an LED system is foreseen, which allows for calibrating the light detector. This U-shaped design is advantageous, because thereby the sensitive photodetectors and other electronic components are not placed in the plane of the beam. As Cherenkov medium, the noninflammable gas C_4F_{10} is used, which features a rather high Cherenkov energy threshold of 10 MeV. This

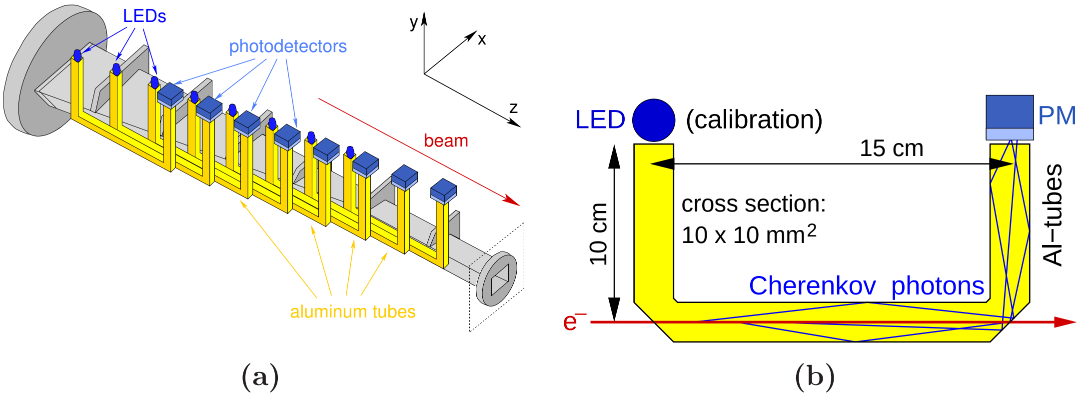

Figure 8.5: Schematic view of Cherenkov detector array (a) and U-shaped Cherenkov detector channel (b). Taken from [209].

threshold ensures the acceptance of the Compton electron signal and at the same time suppresses low-energetic (beam) background.

For the upstream polarimeter, a dedicated Monte-Carlo simulation exists. Figure 8.6 show the simulated distribution of scattered Compton electrons for the two helicity configurations of the laser binned in detector channels of the described size. In this simulation, a beam polarisation of $\mathcal{P}_{e^-} = 80\%$ has been chosen and ILC specific bunch parameters have been used. It is possible to evaluate the expected dynamic range of the polarimeter channels: At the Compton edge, about 75 and 200 Compton electrons are expected for $\lambda\mathcal{P} = -1$ and $\lambda\mathcal{P} = +1$, respectively, which marks the maximum absolute number. For higher energies (higher channel number) the absolute number of Compton electrons per channel is smaller, but the dynamic range to resolve gets larger. In channel 14, for instance, $\mathcal{O}(1)$ and $\mathcal{O}(60)$ scattered Compton electrons are expected for the different laser helicity configurations.

8.2 Design Goals and Error Budget

The envisaged precision of the polarimeters at the ILC amount to

$$\frac{\delta\mathcal{P}}{\mathcal{P}} = 0.25\%. \tag{8.14}$$

This is by a factor of two better than the already achieved precision of the polarimeter at the SLC [197]. In order to meet this design goal, the different contributions to $\delta\mathcal{P}/\mathcal{P}$ have to be well controlled and the following limits have to be fulfilled:

- uncertainty on laser polarisation control of $< 0.1\%$
- uncertainty on analysing power of $0.1\% - 0.2\%$

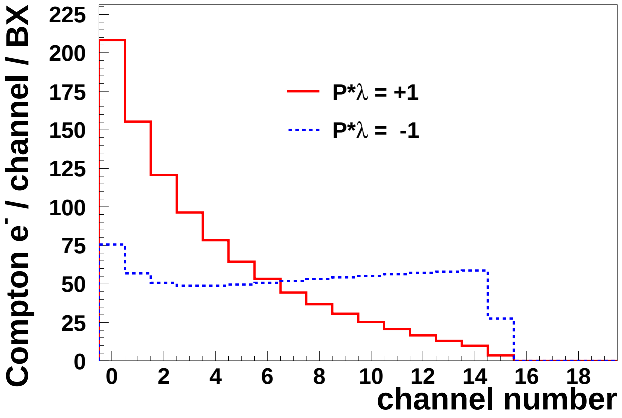

Figure 8.6: Number of Compton electron per polarimeter channel for different laser helicities obtained from a detailed polarimeter simulation [210].

- systematic error due to detector nonlinearity of 0.1%

In the following, we will comment on the introduced error budget and give some estimates how it can be achieved.

8.2.1 Laser Polarisation

The laser polarisation control on the level of 0.1% has already been demonstrated in the operation of the SLC polarimeter [197]. Therefore, it is a reasonable assumption that at the time of the construction of the ILC, laser systems will be on the market performing even better than at SLD in the 1990s.

8.2.2 Analysing Power

In order to determine the analysing power per detector bin, a very accurate alignment of the detector is necessary. Especially the determination of the position of the Compton edge is essential. For testing of the planned Cherenkov detector design shown in Figure 8.5b, a prototype consisting of two separated channels has been built. Figure 8.7a depicts a technical drawing of the prototype. The whole detector volume is filled with C_4F_{10} gas including the inner part of the visible U-shaped Cherenkov channels.

This prototype has already been operated in testbeam. The detector alignment has been studied in detail making use of different light distributions at the end of the detector channel, depending on the position of the beam. In Reference [209], it has

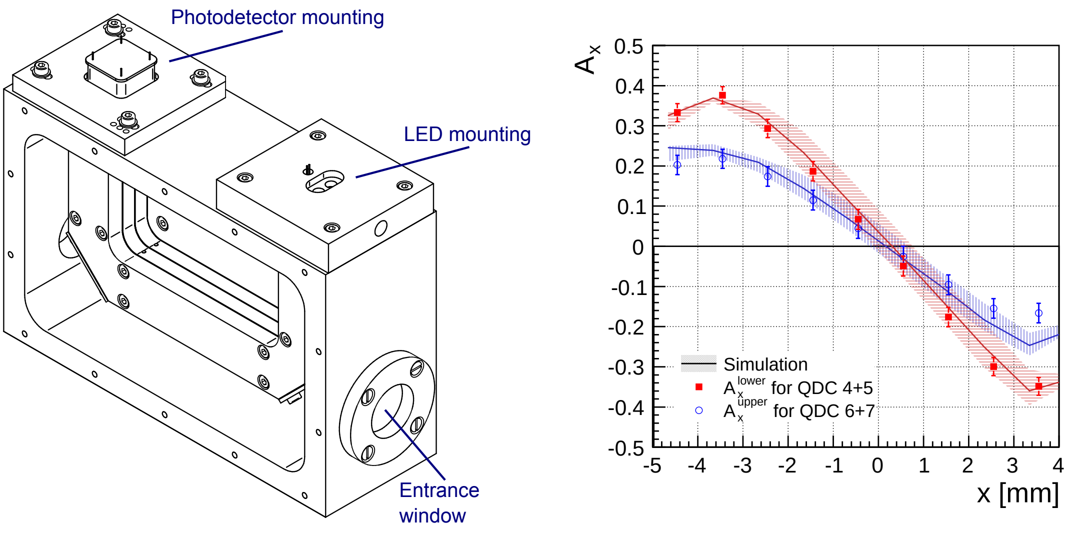

(a) (b)

Figure 8.7: (a) Technical drawing of the Cherenkov detector prototype. (b) Alignment study. The data points show the asymmetry A_x calculated from intra-channel light distribution in dependence of the horizontal beam position x. Solid lines indicate the result of a detailed Monte-Carlo simulation. The error bands correspond to a variation of the tilt angle $\alpha_y = \pm 0.1°$. From the light distribution an alignment of $0.1°$ seems feasible. Taken from [209].

been demonstrated that with the help of a segmented photodetector, asymmetries between different readout anodes can be formed, which show sensitivity to the detector alignment. Figure 8.7b illustrates the measured asymmetries A_x with respect to the horizontal beam position x. The solid lines in the figure depict the result of a detailed Monte-Carlo simulation of the light distribution within the detector channel. The error band indicates a variation of the tilt angle $\alpha_y = \pm 0.1°$, which is the rotation along the axis perpendicular to the horizontal plane. Figure 8.7b shows that alignment on this level is achievable even during a physics run using segmented photodetectors. An uncertainty in the tilt angle by $\pm 0.1°$ contributes to the polarisation measurement to about $0.05\% - 0.15\%$ depending on the distinct detector channel [209]. This shows that the design aim of $\Delta\mathcal{P}/\mathcal{P} = 0.1\%$ originating from alignment is achievable. However, further tests and more dedicated studies of the possible detector alignment are needed.

8.2.3 Detector Nonlinearity

The detector linearity is very essential in order to allow for an accurate polarisation determination. In a Monte-Carlo simulation, the effect of detector nonlinearities has

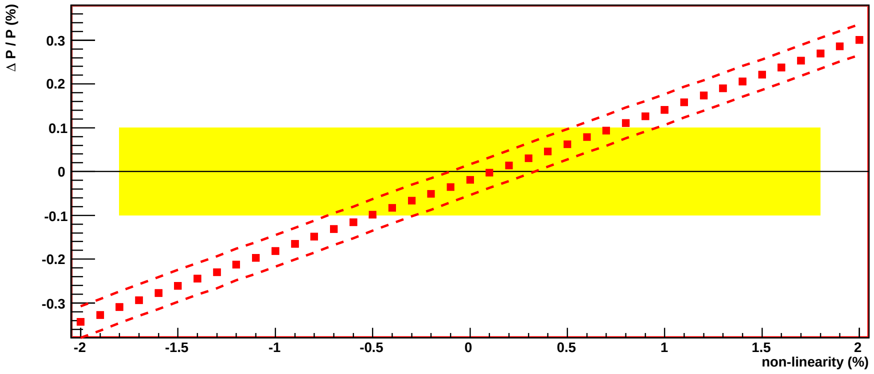

Figure 8.8: Impact of detector nonlinearity on polarisation uncertainty. An additional quadratic nonlinearity has been simulated. In order to keep $\Delta\mathcal{P}/\mathcal{P} < 0.1\%$ the detector nonlinearity has to be below 0.5%. Taken from [211].

been investigated [211] . To this end, a quadratic nonlinearity has been added to a linear response. Figure 8.8 shows the impact of different simulated nonlinearities on the total error budget of the polarisation determination. The yellow box indicates the area for which $\delta\mathcal{P}/\mathcal{P} \leqslant 0.1\%$. It can be read-off that the detector nonlinearity has to be below about 0.5% in order to meet this design goal.

The aim of this thesis is to develop a method to measure the detector nonlinearity and to calibrate the detector in order to achieve a linear response within the tolerances of the error budget. It is very important to note that no absolute calibration of the detector is necessary since the explicit proportionality factor in Equation (8.12) cancels out. Thus, *only* the linear response of the detector to the number of traversing Compton-scattered electrons/positrons in a polarimeter channel has to be ensured. For this reason, a differential nonlinearity measurement can be utilised for linearising the detector response which will be the topic of the subsequent chapter.

8.3 Sources of Detector Nonlinearity

The whole detector is already a very linear device. Nevertheless, two sources of nonlinearities can be identified:

8.3.1 Photomultiplier

As photodetectors for the Cherenkov detector design, classical photomultipliers are foreseen. A schematic picture of a photomultiplier is depicted in Figure 8.9a. These

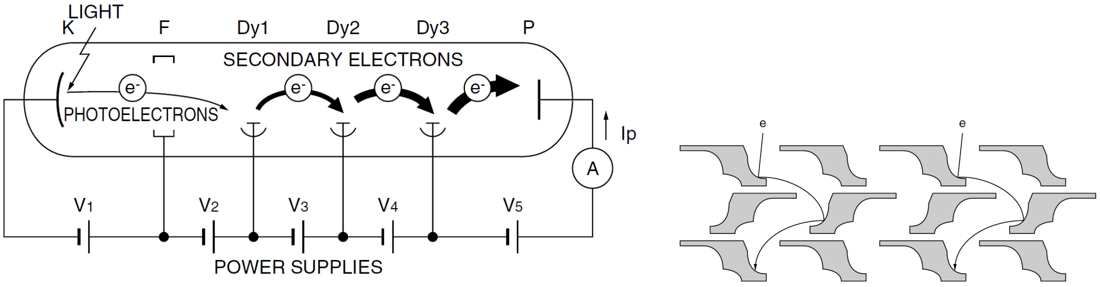

(a) **(b)**

Figure 8.9: (a) Schematic picture of a photomultiplier. Taken from [212]. (b) Cross section of three layers of photomultiplier dynodes. The arrangement of the dynodes allow for the use of segmented readout anodes, which can help for intra-polarimeter-channel alignment (see Section 8.2.2). Taken from [212].

devices consist of a photosensitive cathode behind a transparent entrance window. The material of the photocathode influences the wavelength sensitivity of the photodetector. For detecting Cherenkov light, UV sensitive cathodes are favorable.

An incident photon causes the emission of a photoelectron. Usual quantum efficiencies in the UV range for creating a photoelectron are in the order of 20%. The charge of a single electron is not sufficient in order to be detected. Therefore, the photoelectron gets multiplied in a system of dynodes, which are set on increasing voltage levels. Due to the strong electric field between the dynodes, the electrons get accelerated from one to the next dynode. When an accelerated electron hits a dynode, it causes that many new electrons are hit out. Typically, there are 8–10 dynode stages in one photomultiplier. The number of electrons finally reaching the anode is large enough in order to be detected. Typical gain factors of photomultipliers are $10^5 - 10^7$. Depending on the geometrical structure of the dynodes (see e.g. Figure 8.9b), it is possible to use segmented anodes for the readout, which allows for obtaining also spatial information on the incident photon.

Photomultipliers are known to be very linear measurement devices. However, effects which in particular can impair the linear response are short and intensive light pulses, as they are expected in the Compton polarimeters at the ILC. Very important for the linearity is the voltage divider circuit which defines the voltage levels of the individual dynodes. Figure 8.10a shows a typical voltage divider circuit for ten dynode stages and a four-fold segmented anode. If the photomultiplier is not exposed to light, current flows only in the voltage divider circuit (see upper part of Figure 8.10b). However, in the case of incident light, also photocurrent between the dynodes is present, which reduces the current in the voltage divider circuit (see lower part of Figure 8.10b). In order to ensure a stable potential of the dynodes, which is essential for the device linearity, the photocurrent has to be very small compared

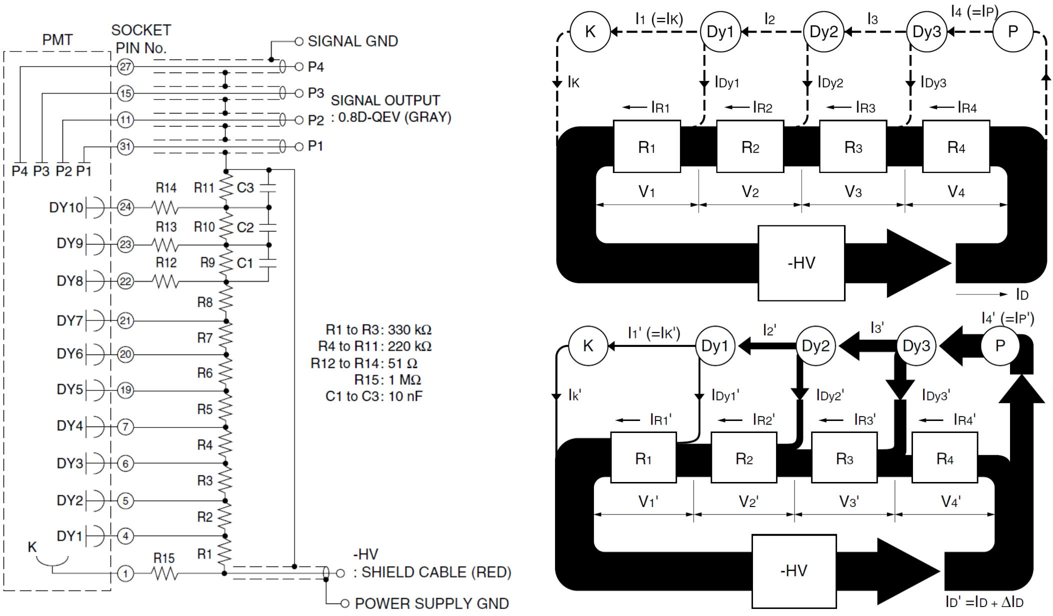

(a) (b)

Figure 8.10: (a) Schematics of the voltage divider E7083 by Hamamatsu. "K" indicates the photocathode, "P1"-"P4" the segmented anode, "DY1"-"DY10" are the photomultiplier dynodes. Taken from [212]. (b) Simplified picture of the (technical) current flow in a photomultiplier circuit without (top) and with (bottom) photomultiplier illumination. The voltage between two dynodes depend on the photocurrent ($V_i \neq V_i'$). If the incident light intensity is large, this can cause a significant nonlinear effect in the later dynode stages. Taken from [212].

to the voltage divider current. For pulsed light input, the average photocurrent may be small (depending on the pulse frequency), but the peak photocurrents can be very large such that the voltage divider circuit cannot supply the interelectrode currents at the later dynode stages anymore [212]. These effects obviously depend on the initial incident light intensity and, therefore, cause a nonlinear photomultiplier response. Additionally, in the case of intense light pulses, space charge effects of large electron clouds at later dynode stages can affect the linearity of the photomultiplier.

8.3.2 Charge-to-Digital Converter

A second source of nonlinear effects arises from the charge-to-digital converter (QDC). Such a device consists mainly out of two parts: The first part converts a charge signal into a voltage signal (QAC) by integrating the input charge using a capacitor. In order to protect the device from wrongly polarised input signals, a device internal current (pedestal current) is added in addition to the input current. The second part of a QDC comprises the actual digitisation of the voltage level of the capacitor (ADC).

There are diverse techniques used for the analog-to-digital conversion. They have all in common that a signal voltage is compared to a known reference voltage. A Wilkinson ADC, for instance, starts a voltage ramp at time $t = 0$ and compares the reference voltage in each clock step with the signal voltage. If the reference voltage exceeds the signal voltage, the voltage ramp is stopped and the counted number of clock-cycles corresponds to the digitised signal. A more evolved ADC is the flash ADC, which consists of a voltage divider chain with 2^n equal resistors, where n is the resolution of the ADC in bits. If a reference voltage is applied to the (ideal) voltage divider chain, the voltage drop between two consecutive resistors is equal. Thus, well defined reference voltages between the resistors can be compared to the signal voltage simultaneously. In this way, the matching comparators give directly the digitisation value within only one clock-cycle. Between these two extremes, many implementations of ADC are possible.

One potential source for nonlinear effects are unstable pedestal currents, which are negligible in modern QDCs. The main sources of QDC nonlinearities are expected to originate from the digitisation step. In the given examples, nonlinearities can arise from a nonlinear voltage ramp or small variations in the resistors of the voltage divider chain, for instance. However, these nonlinearities are very dependent on the actual ADC realisation.

It is expected that the main effect in the whole detector nonlinearity budget stems from the photomultiplier. In Reference [213], different methods of measuring the photomultiplier nonlinearity were examined. As a follow-up, in this thesis, we develop and investigate in detail a differential nonlinearity measurement which has not been further studied in Reference [213].

9 Differential Linearisation Method

We concentrate in this chapter on a differential linearisation method using two independent light pulses. Firstly, we give a formal definition of the integrated and differential nonlinearity in Section 9.1. Subsequently, in Section 9.2, we deduce a linearisation algorithm. After describing the implementation of a Monte-Carlo simulation in Section 9.3, we demonstrate the working principle of the linearisation method at one example in Section 9.4. The Monte-Carlo simulation is utilised for studying design parameters of a real measurements setup in Section 9.5 and, finally, hardware requirements are formulated in Section 9.6.

9.1 Definition of Nonlinearity

In almost every measurement process one encounters the problem that the quantity which is of physical interest is not directly accessible via a measurement device. The usual way of getting around this is to use a measurement device that internally converts the provided signal via some physical effect into another signal, which can be measured instead. In the case of a light intensity measurement, for instance, one possibility is to convert photons to electrical charge, which can be amplified, digitised and read out for further analysis. In order to give this data a physical meaning, it is necessary to know the translation from light to digitised data.

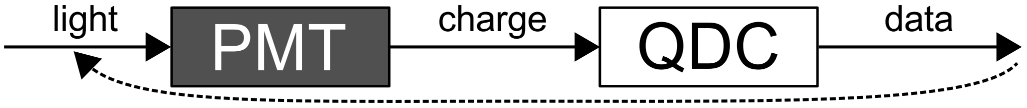

An ideal measurement device has a perfectly proportional response to the input signal, which means that the transfer function from the incoming to the measured signal is linear. However, this is of course in reality not the case due to diverse effects inside of the device. Any deviation from a linear transfer function is called nonlinearity (NL).

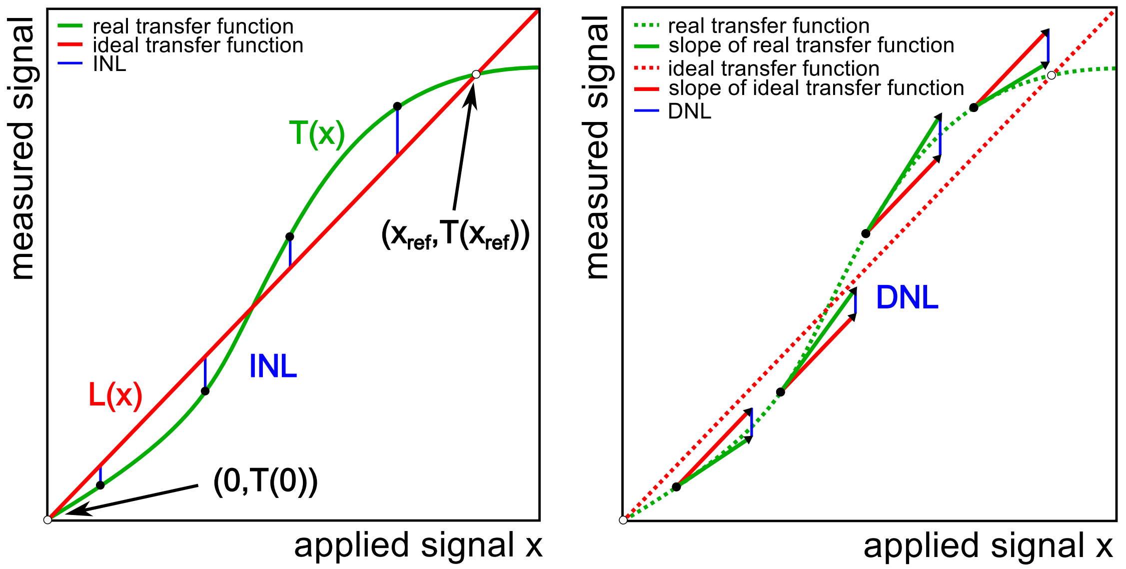

(a) INL **(b)** DNL

Figure 9.1: Schematic picture of different definitions of nonlinearity.

There are different ways of expressing nonlinearity: The **integrated nonlinearity** (INL) is the difference between the real response function $\mathrm{T}(x)$ and the ideal one $\mathrm{L}(x)$ (see Figure 9.1a).

$$\mathrm{INL}(x) = \mathrm{T}(x) - \mathrm{L}(x), \tag{9.1}$$

with

$$\mathrm{L}(x) = A_0 + B_{x_\mathrm{ref}} \cdot x. \tag{9.2}$$

Herein, A_0 describes the signal offset and B_{x_ref} is the proportionality factor. x denotes the actual input signal.

The parameters of $\mathrm{L}(x)$ are defined by two measurement points: $(0, \mathrm{T}(0))$ refers to the baseline measurement and is basically the response of the device when no signal is applied. $(x_\mathrm{ref}, \mathrm{T}(x_\mathrm{ref}))$ is the measurement of a reference signal. With this definitions, A_0 and B_{x_ref} become

$$\begin{aligned} A_0 &= \mathrm{T}(0), && (9.3)\\ B_{x_\mathrm{ref}} &= \langle \frac{\mathrm{d}}{\mathrm{dx}} \mathrm{T}(x) \rangle_{x \in \{0; x_\mathrm{ref}\}} && (9.4)\\ &= \frac{1}{x_\mathrm{ref}} \int_0^{x_\mathrm{ref}} \frac{\mathrm{d}}{\mathrm{dx}} \mathrm{T}(x)\,\mathrm{dx} && (9.5)\\ &= \frac{\mathrm{T}(x_\mathrm{ref}) - \mathrm{T}(0)}{x_\mathrm{ref}}. && (9.6) \end{aligned}$$

The angle brackets denote the average value in the given range.

The baseline measurement is usually performed before signal data taking and, therefore, all data can be corrected by the offset A_0. Thus, T can always be defined such that $\mathrm{T}(0) = 0$:

$$\mathrm{T}(x) \rightarrow \mathrm{T}'(x) = \mathrm{T}(x) - A_0 \tag{9.7}$$

For this reason, A_0 is neglected in the following . Note that from the definition of A_0 and B_{x_ref} it directly follows that the integrated nonlinearity vanishes at $x = 0$ and $x = x_\mathrm{ref}$.

Often, one is not interested in the absolute integrated nonlinearity, but in the relative one, defined as

$$\mathrm{INL}_\mathrm{rel}(x) = \frac{\mathrm{INL}(x)}{\mathrm{L}(x)} = \frac{\mathrm{T}(x) - \mathrm{L}(x)}{\mathrm{L}(x)} = \frac{\mathrm{T}(x)}{\mathrm{L}(x)} - 1. \tag{9.8}$$

Another quantity for quoting the nonlinearity is the so-called **differential nonlinearity**. It is a measure for the deviation of the slope of the real transfer function from the ideal one (see Figure 9.1b).

$$\mathrm{DNL}(x) = \frac{\mathrm{d}}{\mathrm{dx}}\big(\mathrm{T}(x) - \mathrm{L}(x)\big) = \frac{\mathrm{d}}{\mathrm{dx}}\mathrm{T}(x) - B_{x_\mathrm{ref}} \tag{9.9}$$

In the following, we will use this definition of nonlinearity for the derivation of a linearisation algorithm.

If no x dependency is given for INL or DNL, the given quantity usually refers to the maximum value of INL or DNL over the considered range of the measurement device:

$$\mathrm{INL} = \max_{0<x<x_\mathrm{ref}} |\mathrm{INL}(x)| \qquad\qquad \mathrm{DNL} = \max_{0<x<x_\mathrm{ref}} |\mathrm{DNL}(x)| \tag{9.10}$$

9.2 Data Linearisation

For an absolute calibration of a specific device or a data acquisition chain, x_ref sets the absolute calibration scale. In this case, x_ref is a precisely known calibration signal. For calibrations on the per-mil level, the uncertainty of the calibration signal must be in the per-mil range as well. This is especially challenging for photodetectors, like the ones used in a polarimeter. Absolute calibration sources that fulfill the needed specifications, such as nanosecond light pulses in the UV range, are rather complicated and thus not the preferred solution for a polarimeter.

However, for determining the beam polarisation, only the ratio of two light intensity measurements is of physical interest (see Equation 8.12). In this case, instead of an **absolute calibration**, it is sufficient to ensure a linear response of the light detector. The absolute proportionality factor cancels in the final result and is therefore not relevant. This means that the requirements for a calibration source are reduced, but it is still possible to advance to a per-mil level **linearisation**. x_{ref} defines in this case only the maximal expected signal and sets therefore the range for the linearisation. The absolute value of x_{ref} does not have to be known.

The aim in this thesis is to develop a method to linearise a light detector response without the necessity of having an absolutely calibrated calibration light source. In the following sections, we will show that a modified DNL measurement can be established in order to linearise the signal response.

9.2.1 Differential Nonlinearity Measurement

Determining $\mathrm{DNL}(x)$ essentially means to measure $\frac{\mathrm{d}}{\mathrm{dx}}\,\mathrm{T}(x)$. However, the differential quotient is only defined in the infinitesimal limit. Thus, there is no way of measuring this quantity in a real setup. It can be approximately replaced by the difference quotient:

$$\frac{\mathrm{d}}{\mathrm{dx}}\,\mathrm{T}(x) \approx \frac{\Delta\,\mathrm{T}(x)}{\Delta x} = \frac{\mathrm{T}(x+\Delta x) - \mathrm{T}(x)}{(x+\Delta x) - x} = \frac{\mathrm{T}(x+\Delta x) - \mathrm{T}(x)}{\Delta x} \tag{9.11}$$

Thereby, it is very important to choose Δx properly. For an analog-to-digital converter, this is usually the signal corresponding to the least significant bit (LSB) defined by the resolution of the device with respect to the full scale range (FSR)[1]. For an analog detection device, like a light detector, Δx has to be chosen small compared to the calibration range of the detector.

Within this thesis, x will be called **base signal**, which is a light pulse that can be varied in its intensity. Δx is called the **differential signal**, which is a constant and low-intensity light pulse. $\mathrm{T}(x)$ is the measured detector response when applying the base signal and $\mathrm{T}(x + \Delta x)$ is the measured signal when applying both, the base and differential signal, at the same time. It has to be pointed out that the exact size of Δx does not have to be known on an absolute scale, but it has only to be ensured that it is stable and reproducible. Hence, Equation (9.11) can be expressed independently of any absolute input signal:

$$\frac{\mathrm{d}}{\mathrm{dx}}\,\mathrm{T}(x) = \frac{\Delta\,\mathrm{T}(x)}{c} \propto \Delta\,\mathrm{T}(x), \tag{9.12}$$

where c is a constant.

---

[1] for a n bit device, e.g. $\mathrm{LSB} = \frac{\mathrm{FSR}}{2^n}$

In order to extract DNL(x), it is necessary to measure

$$\left(x_i, \frac{\mathrm{d}}{\mathrm{dx}}\,\mathrm{T}(x_i)\right) \propto (x_i, \Delta\,\mathrm{T}(x_i))\,. \tag{9.13}$$

However, for small integrated nonlinearities we can assume

$$x_i \precsim \mathrm{T}(x_i) \tag{9.14}$$

and, thus, it is possible to extract information about the nonlinearity also from data points

$$(\mathrm{T}(x_i), \Delta\,\mathrm{T}(x_i))\,. \tag{9.15}$$

With this final step, all dependencies on an absolute input signal x are eliminated and thus a DNL-like measurement which is independent of the calibration source is defined.

9.2.2 Linearisation Algorithm

In order to develop a linearisation algorithm, the following generic parametrisation of T(x) has been chosen:

$$\mathrm{T}(x) = (B_{x_\mathrm{ref}} + nl(x)) \cdot x \tag{9.16}$$

Herein, $nl(x)$ represents the nonlinearity, which modifies the constant B_{x_ref}. In this case, the correction factor that linearises the detector response has the following form

$$\mathrm{Corr}(x) = \frac{B_{x_\mathrm{ref}}}{B_{x_\mathrm{ref}} + nl(x)} \tag{9.17}$$

such that $\mathrm{T}(x) \cdot \mathrm{Corr}(x) = \mathrm{L}(x)$. In the following, it will be shown that Corr(x) can be determined from a set of data points as defined in (9.15).

From Equation (9.12) follows

$$\Delta\,\mathrm{T}(x) = c \cdot \frac{\mathrm{d}}{\mathrm{dx}}\,\mathrm{T}(x) = c \cdot \left(B_{x_\mathrm{ref}} + nl(x) + nl'(x) \cdot x\right) \tag{9.18}$$

and for the average we get

$$\langle \Delta\,\mathrm{T}(x) \rangle = c \cdot (B_{x_\mathrm{ref}} + \langle nl(x) + nl'(x) \cdot x \rangle). \tag{9.19}$$

By construction $\langle nl(x) + nl'(x) \cdot x \rangle_{x \in \{0; x_\mathrm{ref}\}} = 0$, because

$$\begin{aligned} \langle nl(x) + nl'(x) \cdot x \rangle &= \frac{1}{x_\mathrm{ref}} \int_0^{x_\mathrm{ref}} (nl(x) + nl'(x) \cdot x)\,\mathrm{dx} & (9.20)\\ &= \frac{1}{x_\mathrm{ref}} \left(\int_0^{x_\mathrm{ref}} nl(x)\,\mathrm{dx} + [nl(x) \cdot x]_0^{x_\mathrm{ref}} - \int_0^{x_\mathrm{ref}} nl(x)\,\mathrm{dx} \right) & (9.21)\\ &= \frac{1}{x_\mathrm{ref}} [\mathrm{INL}(x)]_0^{x_\mathrm{ref}} = 0. & (9.22) \end{aligned}$$

Thus, $B_{x_{\text{ref}}}$ can be derived by averaging $\Delta T(x)$ up to the factor c:

$$\langle \Delta\,\mathrm{T}(x) \rangle = c \cdot B_{x_{\text{ref}}} \tag{9.23}$$

The constant term (9.23) can now be subtracted from (9.18) in order to access the nonlinear contribution:

$$\Delta\,\mathrm{T}(x) - c \cdot B_{x_{\text{ref}}} \equiv \Delta\widehat{\mathrm{T}}(x) = (nl(x) + nl'(x) \cdot x) \tag{9.24}$$

Integration and division by x gives the nonlinearity $nl(x)$ up to the factor c:

$$\int \Delta\widehat{\mathrm{T}}(x)\,\mathrm{dx} = c \cdot nl(x) \cdot x \tag{9.25}$$

$$\frac{1}{x}\int \Delta\widehat{\mathrm{T}}(x)\,\mathrm{dx} = c \cdot nl(x). \tag{9.26}$$

From a discrete number of measured data points $(\mathrm{T}(x_i), \Delta\widehat{\mathrm{T}}(x_i))$ the LHS of Equation (9.26) can be approximated:

$$\frac{1}{x_j}\int_0^{x_j} \Delta\widehat{\mathrm{T}}(x)\,\mathrm{dx} \approx \frac{1}{x_j}\sum_{i=0}^{j} \frac{1}{2}\Big(\Delta\widehat{\mathrm{T}}(x_i) + \Delta\widehat{\mathrm{T}}(x_{i+1})\Big) \cdot (x_{i+1} - x_i) \tag{9.27}$$

$$= \sum_{i=0}^{j} \frac{1}{2}\Big(\Delta\widehat{\mathrm{T}}(x_i) + \Delta\widehat{\mathrm{T}}(x_{i+1})\Big) \cdot \frac{(x_{i+1} - x_i)}{x_j} \tag{9.28}$$

For small nonlinearities the following approximation holds:

$$\frac{1}{x_j}\int_0^{x_j} \Delta\widehat{\mathrm{T}}(x)\,\mathrm{dx} \approx \sum_{i=0}^{j} \frac{1}{2}\Big(\Delta\widehat{\mathrm{T}}(x_i) + \Delta\widehat{\mathrm{T}}(x_{i+1})\Big) \cdot \frac{(\mathrm{T}(x_{i+1}) - \mathrm{T}(x_i))}{\mathrm{T}(x_j)} \tag{9.29}$$

One should note that although LHS of Equation (9.29) is an explicit integration in x, it is possible to express this integration in the limit of small INL in terms of $\mathrm{T}(x)$ and $\Delta\widehat{\mathrm{T}}(x)$. The explicit x dependence is removed. The limit of validity of approximation (9.15) will be discussed in Section 9.5.4. Together with Equation (9.23), the correction factor $\mathrm{Corr}(x)$ can be approximately derived only from detector responses without having the knowledge of the absolute scale of the input calibration signal, which has been the aim of this procedure.

Alternatively, the data points (9.15) can be fitted with a polynomial and the obtained function can be processed in a similar way. In this case, we get a continuous function describing the nonlinearity as well as the correction factor.

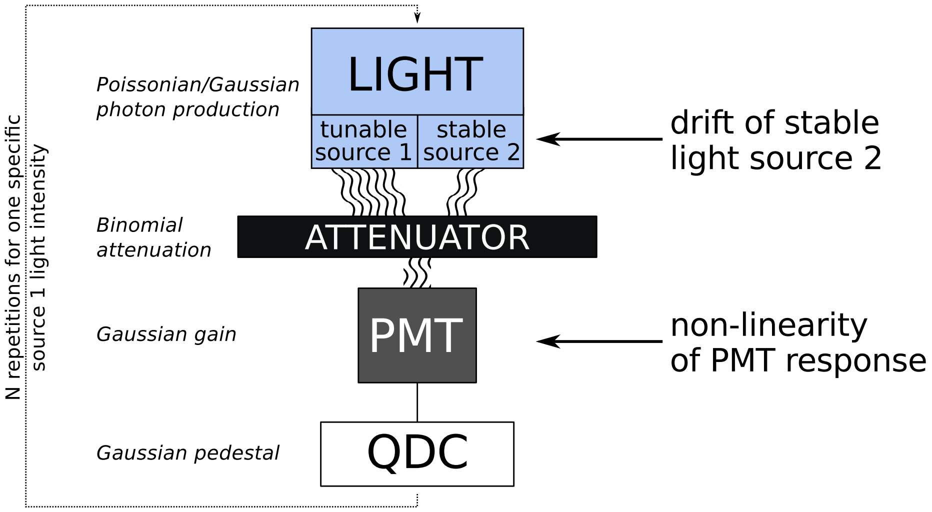

Figure 9.2: Schematic picture of the implemented Monte-Carlo simulation. See text for details.

Although the absolute integrated nonlinearity $\mathrm{INL}(x)$ cannot be determined with this method because of the unknown constant c, it is possible to calculate the relative integrated nonlinearity (see Equation (9.8))

$$\mathrm{INL}_{\mathrm{rel}}(x) = \frac{(B_{x_{\mathrm{ref}}} + nl(x)) \cdot x}{B_{x_{\mathrm{ref}}} \cdot x} - 1 = \frac{nl(x)}{B_{x_{\mathrm{ref}}}}. \tag{9.30}$$

The last term in this equation contains only quantities, which are extractable from the data points (9.15) whereas the unknown factor c cancels.

9.3 Monte-Carlo Simulation

In order to demonstrate the functionality of the proposed method as well as to quantify some requirements for a real setup, a Monte-Carlo simulation has been implemented. Figure 9.2 gives a schematic overview of the different parts of the simulation.

In the first part, two independent light sources are simulated, where N_{base} denotes the in average produced number of photons for the base pulse and N_{diff} for the differential pulse. N_{diff} is chosen to be small compared to N_{base}. The actual event-by-event produced number of photons is Gaussian distributed for a sufficiently large number of photons. In order to extract the DNL, as proposed in the section before, two pulses have to be simulated: The first pulse contains only the base pulse of source 1

$$N_{\mathrm{pulse\,1}} = \mathcal{G}(N_{\mathrm{base}}, \sigma_{N_{\mathrm{base}}}), \tag{9.31}$$

the second pulse is a superimposition of the pulses of source 1 and source 2

$$N_{\mathrm{pulse}\,2} = \mathcal{G}(N_{\mathrm{base}}, \sigma_{N_{\mathrm{base}}}) + \mathcal{G}(N_{\mathrm{diff}}, \sigma_{N_{\mathrm{diff}}}). \tag{9.32}$$

Herein, $\mathcal{G}(\mu, \sigma)$ represents a Gaussian random number with the mean at μ and a width of σ. Since the impact of a drifting differential pulse is of particular interest, N_{diff} can be systematically increased or lowered during one simulation run.

As a second element, an attenuator is simulated, which reduces the comparably large number of photons of the light source to a small level entering the photodetector. The attenuation follows a binomial statistics. Assuming a transmission factor $\mathcal{T}$, we get for the diminished number of photons

$$N^{\mathrm{att}}_{\mathrm{pulse}\,1,2} = \mathcal{B}(N_{\mathrm{pulse}\,1,2}, \mathcal{T}), \tag{9.33}$$

where $\mathcal{B}(N, p)$ is a binomial distributed random number, with N being the number of total trials and p the success probability. The calculation of a binomial random number is very resource consuming. Therefore, we use an approximation (compare Reference [214]). If

$$\left| \frac{1}{\sqrt{N_{\mathrm{pulse}\,1,2}}} \left(\sqrt{\frac{1-\mathcal{T}}{\mathcal{T}}} - \sqrt{\frac{\mathcal{T}}{1-\mathcal{T}}} \right) \right| < 0.1, \tag{9.34}$$

the Binomial distribution (9.33) can be approximated by a Gaussian distribution

$$N^{\mathrm{att}}_{\mathrm{pulse}\,1,2} = \mathcal{G}\left(\mathcal{T} \cdot N_{\mathrm{pulse}\,1,2}, \sqrt{\mathcal{T}(1-\mathcal{T}) \cdot N_{\mathrm{pulse}\,1,2}} \right). \tag{9.35}$$

In the next step, the photomultiplier (PMT) response is simulated. Each photon arriving at the photodetector is converted into a photoelectron carrying an elementary charge e^-. Any quantum efficiency in the conversion process can be assigned to the attenuation step before. The photoelectron is amplified by a specific gain g, which is allowed to fluctuate with some width σ_g. Therefore, the charge of the two pulses at the end of the photomultiplier becomes

$$Q_{\mathrm{pulse}\,1,2} = N^{\mathrm{att}}_{\mathrm{pulse}\,1,2} \cdot e^- \cdot \mathcal{G}(g, \sigma_g). \tag{9.36}$$

In this step, also the nonlinearity enters. In the simulation, a nonlinear transfer function $\mathrm{T}(x)$ is used in order to translate the up to now perfectly linear charge response into a nonlinear response. $\mathrm{T}(x)$ is a normalised function, defined in the range $x \in [0; 1]$. In the simulation a random transfer function is generated, which features a specific input nonlinearity (see Appendix C for details). The nonlinear response is eventually calculated via

$$Q^{\mathrm{NL}}_{\mathrm{pulse}\,1,2} = \mathrm{T}\left(\frac{Q_{\mathrm{pulse}\,1,2}}{Q_{\mathrm{max}}} \right) \cdot Q_{\mathrm{max}}, \tag{9.37}$$

Number of photons (base pulse)[t]	$N_{\text{base}} = 12000 - 400000$	$\sigma_N = 27\sqrt{N}$
Number of photons (diff. pulse)[t]	$N_{\text{diff}} = 2200$	
Transmission coefficient[d]	$\mathcal{T} = 0.0025775$	—
PMT gain[d]	$g = 2.7 \times 10^5$	$\sigma_g/g = 1\%$
QDC resolution[d]	$\sigma_{\text{QDC}} = 25\,\text{fC}$	—
Pedestal QDC counts[m]	$\text{Cnt}_{\text{ped}} = 225$	$\sigma_{\text{Cnt}_{\text{ped}}} = 1.32209$

Table 9.1: Input parameters used for the Monte-Carlo simulation. The superscript t indicates parameters which have been tuned in order to match measurements in a real setup, d denotes parameters which are estimated based on values in data sheets, and m marks parameters extracted from an independent measurement. Parameters which are not listed in this table are varied in different simulation runs.

where Q_{max} defines the upper end of the expected dynamic range.

Finally, the charge-to-digital converter (QDC) translates the charges into a 12 bit number Cnt taking into account the resolution of the digitiser σ_{QDC}. Additionally, a Gaussian smeared baseline signal (pedestal) is added:

$$\text{Cnt}_{\text{pulse}\,1,2} = (\text{int})\left(\mathcal{G}(\text{Cnt}_{\text{ped}}, \sigma_{\text{Cnt}_{\text{ped}}}) + Q^{\text{NL}}_{\text{pulse}\,1,2}\right)/\sigma_{\text{QDC}} \tag{9.38}$$

The resulting output is filled into different one-dimensional histograms. For one specifically chosen N_{base}, the whole chain is repeated N times and then set to the next larger value of N_{base}. The procedure is repeated in s steps, until the base pulse intensity has scanned the full predefined range.

The whole simulation is implemented within the ROOT framework [176] and is based on the ROOT random generator `TRandom3`.

All for the simulation introduced input parameters have either been taken from the manuals of certain measurement devices or tuned in order to reproduce comparable signal shapes with respect to measurements in a real setup. Table 9.1 shows the set of the used parameters.

9.4 Example Case

The produced Monte-Carlo data is provided in the same data format as real data. Therefore, it is possible to develop an analysis code which is also applicable to real data. In the following, we present an example, in which a relative INL of 0.8% has been simulated.

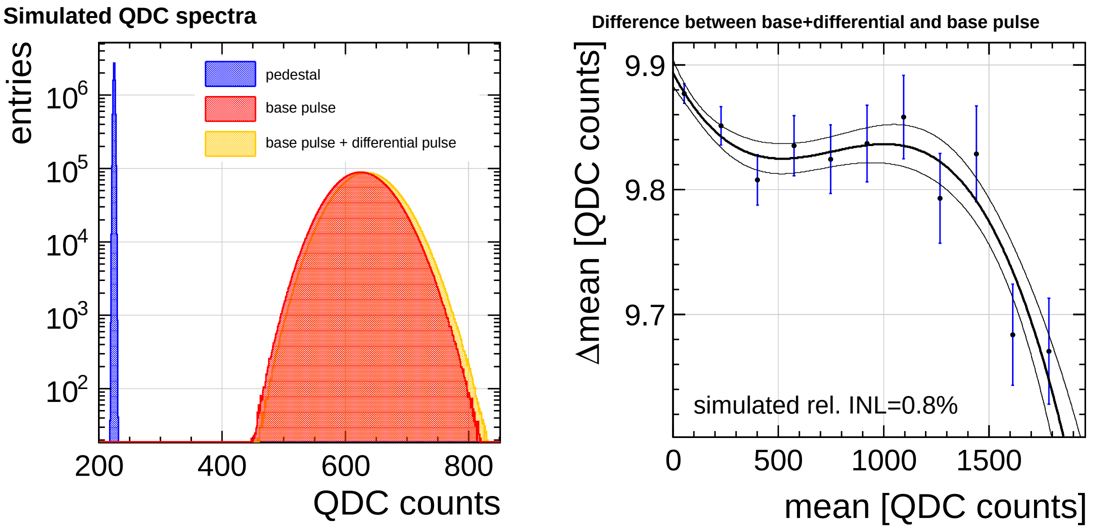

(a) (b)

Figure 9.3: Result of a typical simulation run. (a) Simulated QDC spectrum for one specific N_{base} of pedestal only (blue), base pulse (red) and base pulse + differential pulse (orange). For each configuration, $N = 10^7$ events have been simulated. (b) Differences between the mean values of pulse 1 and pulse 2 in dependence of the mean position of pulse 1. The black lines indicate the fit of a higher order polynomial to the data points and the corresponding error band.

Figure 9.3a shows a typical resulting QDC spectrum for $N = 10^7$ repetitions of one specific light intensity configuration. The pedestal peak (blue) is very sharp compared to the "light" peaks (red, orange). This reflects very accurately the situation in real data. For each light intensity configuration the arithmetic means as well as the corresponding errors are extracted from the distribution of the pedestal signal, the pulse 1 signal, and the pulse 2 signal. Also more evolved methods of mean extraction have been studied, like fits of a Gaussian or a Poissonian to the spectrum, but only for very small signals, a noticeable deviation from the arithmetic mean has been observed.

Figure 9.3b depicts the difference between the means of the pulse 1 signal and the pulse 2 signal in dependence of the pedestal corrected mean of the pulse 1 signal. Any deviation from a constant can be attributed to nonlinear contributions. These data points are fitted with polynomials of the order 1 to 10 and the fit with the smallest χ^2/ndf is chosen for further data processing. The fitted polynomial as well as the corresponding error bands are indicated by the black lines in Figure 9.3b. The error bands have been derived from the covariance matrix of the parameter of the fit function.

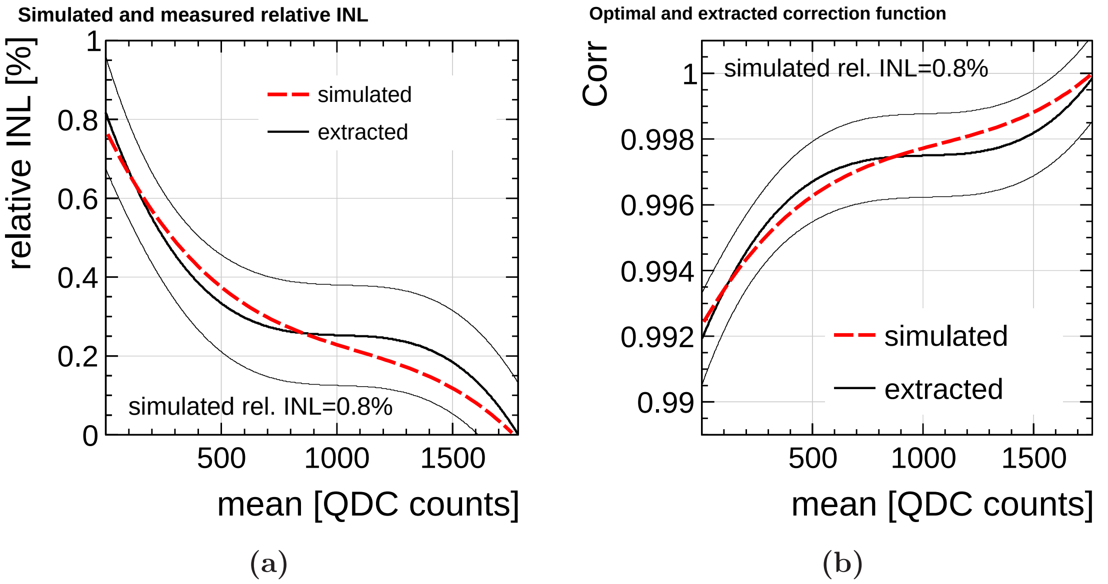

(a)

(b)

Figure 9.4: (a) Calculated relative INL from a fit to the data points in Figure 9.3b including the error band. The red dashed line indicates the simulated nonlinearity. (b) Extracted and ideal correction function.

From the fit of the data points, the relative INL can be derived by following a similar procedure as described in Section 9.2.2. This is shown in Figure 9.4a. By construction of this method, the last taken data point defines the reference point, which sets the final slope of the linearised data. For this reason, the relative INL vanishes at the right end of the horizontal axis. In the same plot, also the simulated nonlinearity is shown as red dashed line. A comparison of both curves clearly indicates that the simulated and measured nonlinearity agree very well within the error band.

Based on this measured relative INL, it is possible to construct a correction function, as depicted in Figure 9.4b. Again, by definition, the very last data point is used as reference and, thus, this point is uncorrected (multiplication with 1) whereas in the remaining range the data points are scaled correspondingly to the measured relative INL. The optimal correction function, derived from the simulated nonlinearity, is drawn as a red dashed line.

Finally, we can study the performance of the correction algorithm. Therefore, an independent new data set is produced, which is based on the same nonlinear transfer function that has been used for determining the correction function. Figure 9.5a shows the uncorrected data set in dependence of the simulated true number of photons. The upper part of the graph depicts the absolute measured signal with respect to the input light intensity. No deviation from a perfect linear function can be recognised. However, in the lower part the relative deviation is plotted and actually a maximum relative INL of 0.8% is present. In Figure 9.5b, the same data

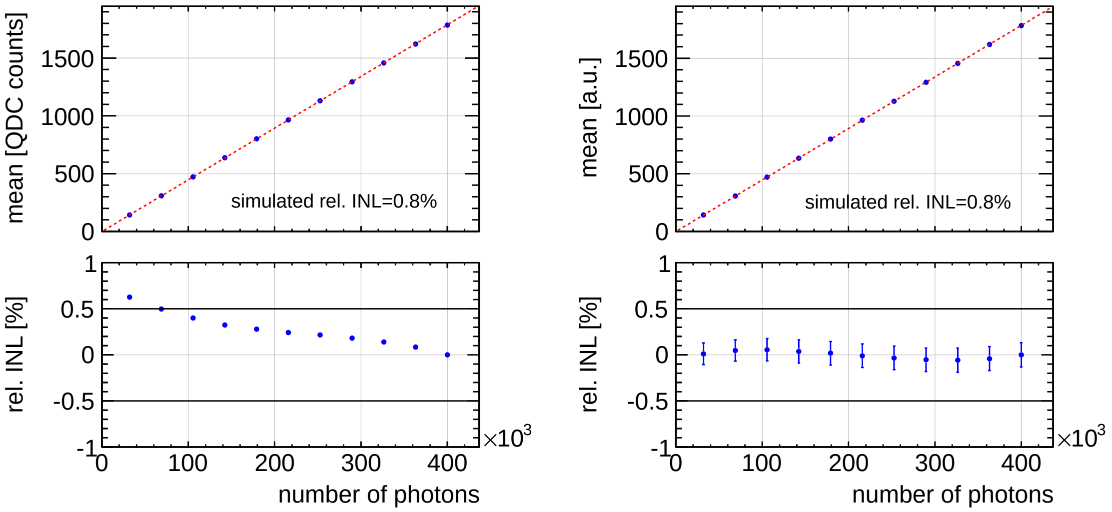

(a) Uncorrected data. **(b)** Corrected data.

Figure 9.5: Comparison between uncorrected and corrected data. The upper half of the figure shows the detector signal in dependence of the simulated number of photons. The relative deviation from a linear function is depicted in the lower parts. The corrected data is clearly within the 0.5% nonlinearity bounds.

set is shown after the data points have been multiplied with the correction function. The data points are clearly linearised and the relative INL is now in the whole range below 0.5%, which is the design goal in order to meet the precision requirements of the polarisation measurement (see Section 8.2.3).

9.5 Optimisation Study

After having demonstrated that the proposed method indeed allows one to linearise data without any absolute calibration, we now turn to the question of how the variation of different measurement parameters determine the linearisation power of this method. Therefore, we have scanned different simulation parameters and analysed the resulting maximal relative INL on truth level.

The important quantity for the polarisation measurement is the difference between the signals of two light intensities (see Equation (8.12)). Since $\mathrm{INL}_{\mathrm{rel}}(x)$ can also change sign within the analysed range, the largest INL between two points is not given by

$$\max_{0<x<x_{\mathrm{ref}}} \left|\mathrm{INL}_{\mathrm{rel}}(x)\right| , \tag{9.39}$$

but rather

$$\max_{0<x<x_{\mathrm{ref}}} \mathrm{INL}_{\mathrm{rel}}(x) - \min_{0<x<x_{\mathrm{ref}}} \mathrm{INL}_{\mathrm{rel}}(x). \tag{9.40}$$

Thus, this quantity is more suited to judge the linearisation power and, therefore, used in the following.

In order to study the effect of different parameters on the described method more systematically, 200 random nonlinearities have been produced at each scan step, all featuring a fixed relative INL (see Appendix C). One Monte-Carlo sample is produced to extract a correction function and a second independent Monte-Carlo sample is linearised with the derived correction function. The linearised sample is then examined for the maximal relative INL as defined in Equation (9.40). From the 200 results for each single scan point the mean and RMS is calculated and finally displayed.

In the following, we always consider two scenarios for the randomly generated nonlinearities: In the first scenario, the randomly generated transfer functions comprise relative INLs of 0.8% without any extremum in the analysed range (see Figure C.1). The other scenario features rather large relative INLs of 2.0% with one extremum in the analysed range (see Figure C.2). Therefore, the scenarios define one slightly optimistic and one rather pessimistic example case.

9.5.1 Influence of Data Point Statistics

As a first parameter, we focus on the needed data statistics per data point. This determines the size of the error bars of the difference between the pulse 1 and pulse 2 signal. In turn, this influences heavily the uncertainty band of the resulting fit. Figures 9.6 and 9.7 show two examples for a simulated nonlinearity of $\mathrm{INL}_{\mathrm{rel}} = 0.8\%$ and $\mathrm{INL}_{\mathrm{rel}} = 2.0\%$ for $N = 10^5$ and $N = 10^7$ events per data point. It is obvious that the quality of the fit improves with more events per data point. In Figure 9.6a, the best fit would even be compatible with a constant, which would indicate no present nonlinearity. Thus, a high data statistics is very essential in order to resolve small nonlinearities. Additionally, also the number of available points s within the analysed range is related to the fit quality, which will be discussed in Section 9.5.3.

In Figure 9.8, a scan of N is presented for the two introduced scenarios. It shows $\mathrm{INL}_{\mathrm{max}} - \mathrm{INL}_{\mathrm{min}}$ in dependence of the simulated data statistics per data point before (red) and after (green) the linearisation. It is clear that for very limited statistics per data point the determined correction function cannot linearise the data anymore and, thus, the resulting $\mathrm{INL}_{\mathrm{max}} - \mathrm{INL}_{\mathrm{min}}$ after the application of the correction function is even larger than before the correction.

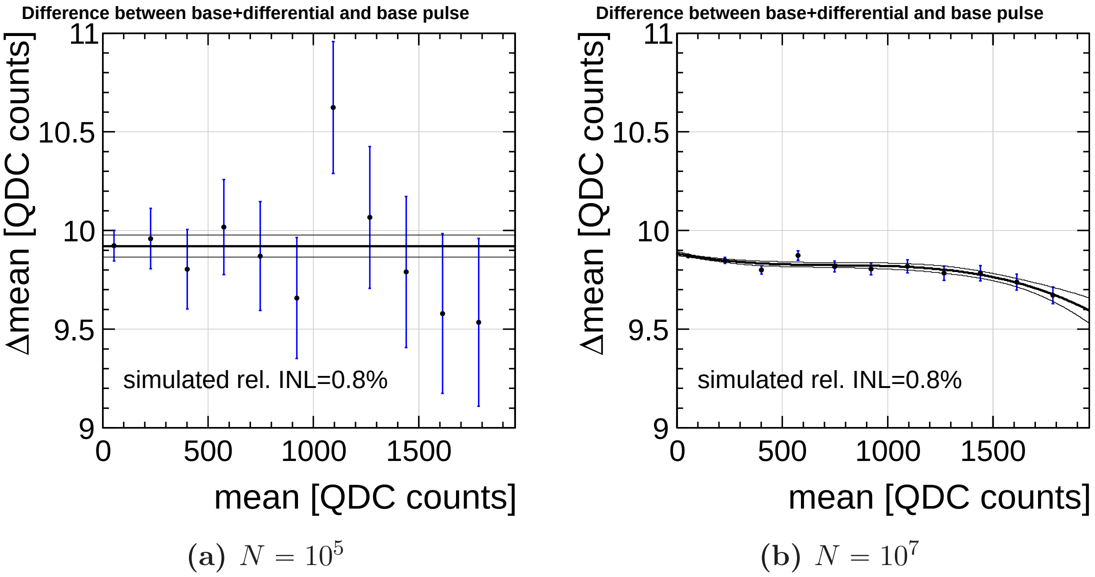

(a) $N = 10^5$ **(b)** $N = 10^7$

Figure 9.6: Differences between the mean values of pulse 1 and pulse 2 in dependence of the mean of pulse 1 for a simulated relative INL of 0.8% and different number of events N per data point. A rather high statistics is needed in order to allow for a reliable fit.

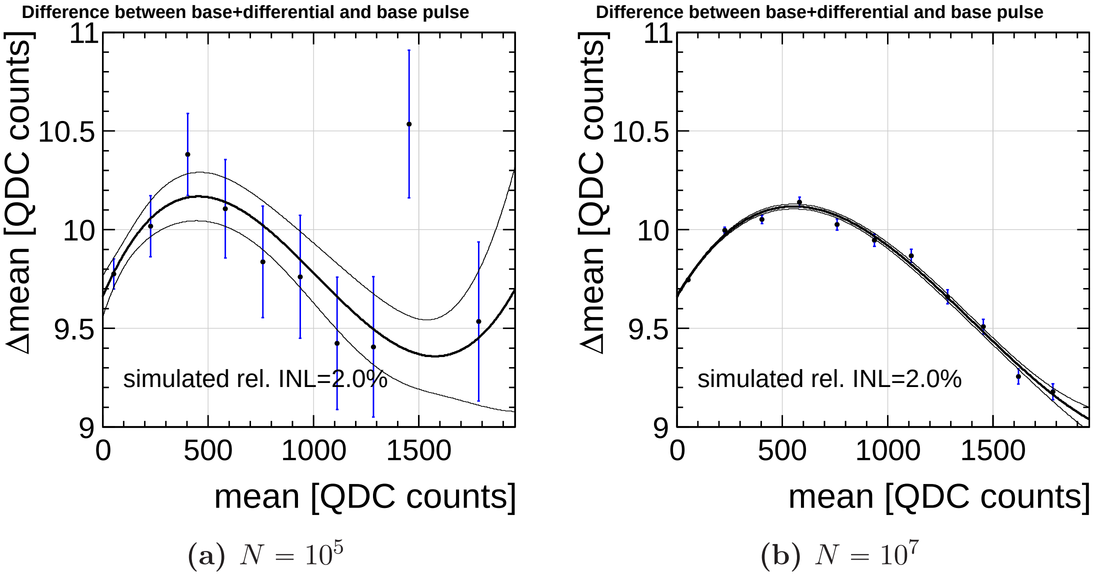

(a) $N = 10^5$ **(b)** $N = 10^7$

Figure 9.7: Differences between the mean values of pulse 1 and pulse 2 in dependence of the mean of pulse 1 for a simulated relative INL of 2.0% and different number of events N per data point. A rather high statistics is needed in order to allow for a reliable fit.

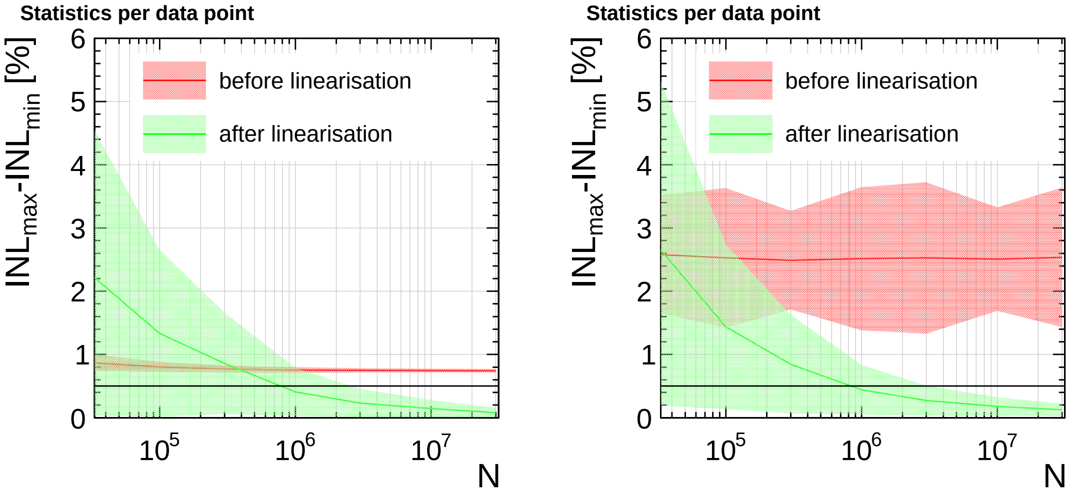

(a) simulated $\mathrm{INL_{rel}} = 0.8\%$ **(b)** simulated $\mathrm{INL_{rel}} = 2.0\%$

Figure 9.8: $\mathrm{INL_{max}} - \mathrm{INL_{min}}$ in dependence of the taken number of events N for one single light intensity configuration. A large statistics is needed in order to be able to obtain a reliable correction function from the data points.

The horizontal black solid line in Figure 9.8 indicates the 0.5% limit, which has to be achieved in order to fulfill the precision requirements of the future polarimeters (see Section 8.2.3). From both figures one can read off that for $N > 3 \times 10^6$ events per data point the upper end of the RMS band drops below this limit.

9.5.2 Light Pulse Spread

As listed in Table 9.1, the spread for the number of initially emitted photons in the standard simulation is larger than for an ideal Poissonian emitter and is tuned to real measurements (cf. Figure 9.9a and 9.9b). For comparison, also a purely Poissonian light source has been simulated, as depicted in Figure 9.9c Thereby, the width of the original photon distribution naturally affects the width of the resulting QDC spectra σ. This, in turn, effects directly the size of the error on the mean δm, since

$$\delta m = \frac{\sigma}{\sqrt{N}}. \tag{9.41}$$

From Figure 9.9 one can read off that the width of the resulting QDC spectra is reduced by almost a factor of two for a purely Poissonian light source. For this reason, a Poissonian light source would allow for the same linearisation quality as the baseline light source, but with only a quarter of the data statistics.

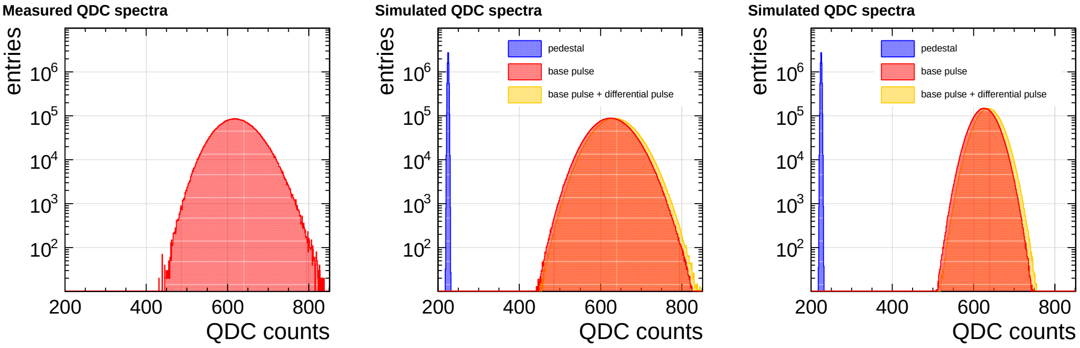

(a) Measured QDC spectrum.

(b) Baseline light source ($\sigma_N = 27\sqrt{N}$).

(c) Poissonian light source ($\sigma_N = \sqrt{N}$).

Figure 9.9: QDC spectra assuming different widths for the photon multiplicity distribution ((b) and (c)). The comparison to the measured spectrum in a real setup (a) shows that (b) describes the baseline light source very well.

9.5.3 Base Pulse Scanning Steps

As a further parameter, we study the influence of the number of scanning steps s within the analysed signal range. Figures 9.10 and 9.11 demonstrate the impact of s on the resulting fit to the data points for a simulated relative INL of 0.8% and 2.0%. It is clear that more data points within the analysed range constrain the fit more strongly and help to obtain a more reliable result. Therefore, the whole linearisation method profits from an increased number of scanning steps.

In Figure 9.12, $\mathrm{INL}_{\mathrm{max}} - \mathrm{INL}_{\mathrm{min}}$ is plotted in dependence of the number of scanning steps within the analysed range for both scenarios. In the first scenario (cf. Figure 9.12a), already very few data points are sufficient to linearise the data well. This originates from the fact that small nonlinearities without an extremum in the analysed range can often already be well parametrised by a straight line neglecting all higher order contributions. For the other scenario (cf. Figure 9.12b), the linearisation quality rapidly increases for $s \geqslant 4$ and then stays rather constant. This can be understood from the fact that all randomly generated transfer function $\mathrm{T}(x)$ are forth order polynomials, adding a linear, quadratic, and cubic nonlinear term to the purely linear behaviour. This transfer functions are therefore described by four parameters (see Appendix C) and for $s \geqslant 4$ enough data points are available in order to describe the polynomial properly. Even though in a real setup it is rather unlikely that higher orders than cubic nonlinear terms play an important role, the precise functional description of the INL is unknown. For this reason, it is advisable to take as many data points as possible within the analysed range. As baseline for the measurements $s = 20$ is chosen.

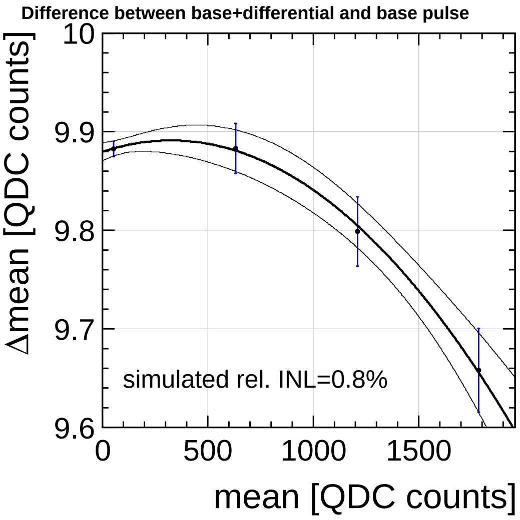

(a) $s = 4$ **(b)** $s = 30$

Figure 9.10: Differences between the mean values of pulse 1 and pulse 2 in dependence of the mean of pulse 1 for a simulated relative INL of 0.8% and different number of scanning steps s within the analysed range. More steps help to improve the resulting fit.

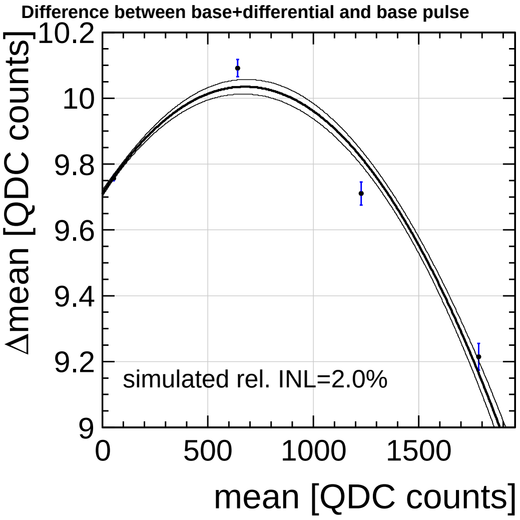

(a) $s = 4$ **(b)** $s = 30$

Figure 9.11: Differences between the mean values of pulse 1 and pulse 2 in dependence of the mean of pulse 1 for a simulated relative INL of 2.0% and different number of scanning steps s within the analysed range. More steps help to improve the resulting fit.

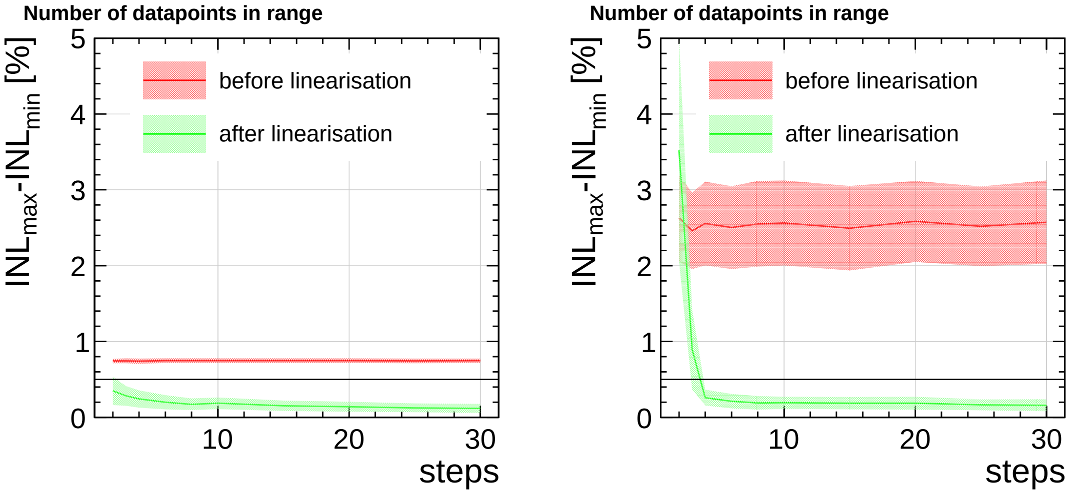

(a) simulated $\mathrm{INL}_{\mathrm{rel}} = 0.8\%$ **(b)** simulated $\mathrm{INL}_{\mathrm{rel}} = 2.0\%$

Figure 9.12: $\mathrm{INL}_{\mathrm{max}} - \mathrm{INL}_{\mathrm{min}}$ in dependence of the number of scanning steps within the analysed range. More data points allow for a better linearisation of the signal.

9.5.4 Limits of Small-INL-Approximation

As described in Section 9.2.2, the linearisation method is a approximate method. It relies on the assumption that the measured difference between the mean values of the signal of pulse 1 and pulse 2 does not change significantly with respect to the measured response of pulse 1 compared to the perfect linear response of pulse 1 (see Equation (9.14)). For large nonlinearities this is no longer true. With the Monte-Carlo simulation we can analyse the maximal tolerable nonlinearity.

Figure 9.13 shows $\mathrm{INL}_{\mathrm{max}} - \mathrm{INL}_{\mathrm{min}}$ for different simulated nonlinearities in the described scenarios. The linearisation method works up to nonlinearities of up to $\mathrm{INL}_{\mathrm{rel}} = 7\%$ in scenario 1 and up to $\mathrm{INL}_{\mathrm{rel}} = 3.5\%$ in scenario 2. This is much larger than the expected nonlinearity of typical photomultipliers and therefore it demonstrates that the proposed linearisation method is well suited for the intended case of application.

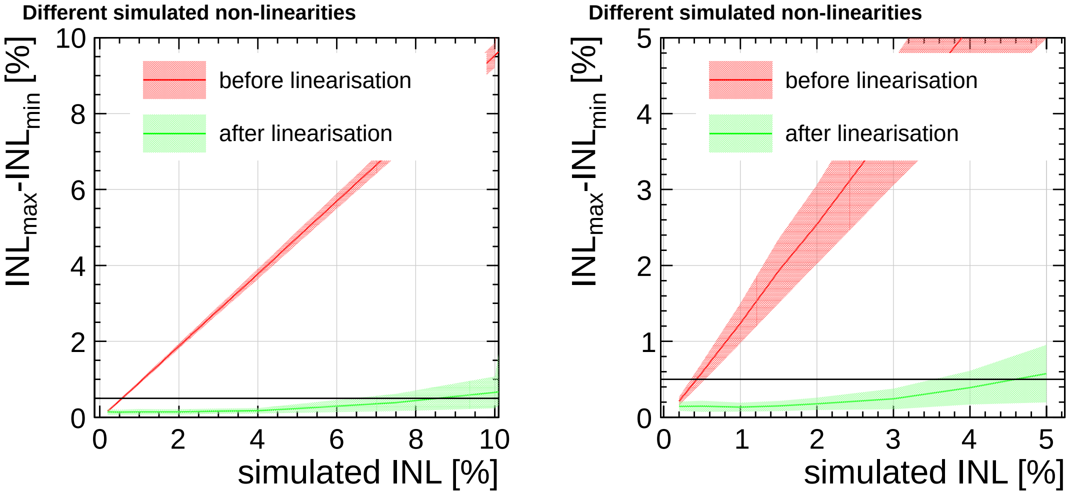

(a) one extremum in analysed range **(b)** no extremum in analysed range

Figure 9.13: $\mathrm{INL}_{\mathrm{max}} - \mathrm{INL}_{\mathrm{min}}$ in dependence of the simulated relative INL. The proposed linearisation method still works for a relative INL of up to 3.5%.

9.5.5 Stability of Differential Pulse

Finally, we study the impact of a drifting differential pulse. In the simulation, there is the possibility to change the light intensity of the additional differential pulse during the scan of the analysed range. Since the linearisation method heavily relies on the stability of the differential pulse (it is the measure of the derivative), it is an important question how much drifting is acceptable. Figures 9.14 and 9.15 show the comparison of the uncorrected and the corrected data for a simulated $\mathrm{INL}_{\mathrm{rel}} = 0.8\%$ and $\mathrm{INL}_{\mathrm{rel}} = 2.0\%$ and a simulated drift of 0.2% and 2.0%.

In the case of a 0.2% drift, no significant reduction of the linearisation quality is recognisable (see Figures 9.14a and 9.15a). For a drift of 2.0%, however, the linearisation method fails because the nonlinearity after the linearisation exceeds the acceptable limit of 0.5%. As an interesting observation from a comparison of Figure 9.14b and 9.15b, one should note that the linearised data features in both cases the same shape and slope. This indicates that it is still possible to correct for the actual simulated nonlinearity, but one picks up an additional first order nonlinear effect from the pulse intensity drift.

The determined dependence of $\mathrm{INL}_{\mathrm{max}} - \mathrm{INL}_{\mathrm{min}}$ of the differential pulse intensity drift for the two scenarios is depicted in Figure 9.16. It shows that drifts between $0.5 - 1.0\%$ are acceptable for the differential light pulse.

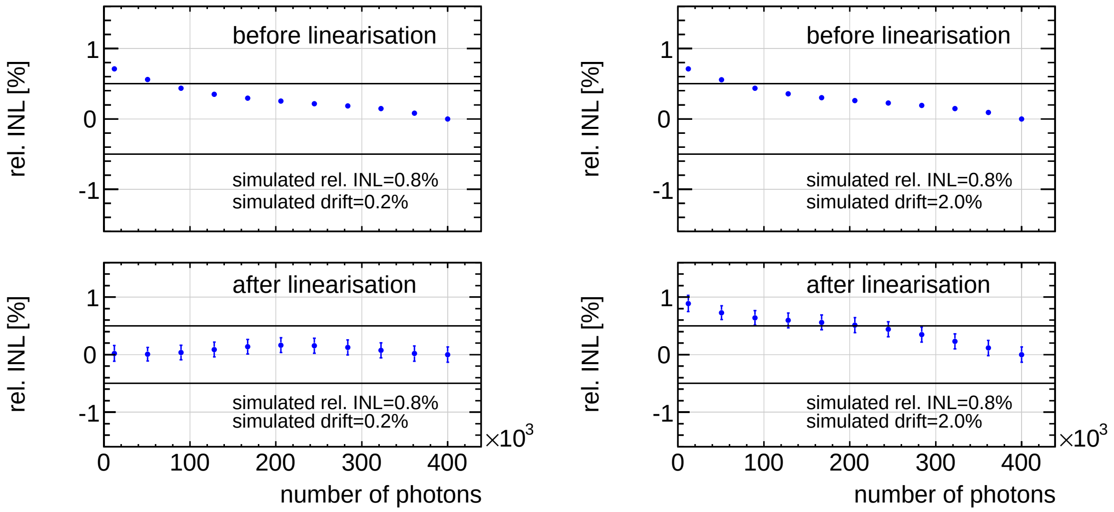

(a) drift = 0.2%

(b) drift = 2%

Figure 9.14: Comparison between uncorrected and corrected data for a simulated relative INL of 0.8% and different simulated intensity drifts of the differential pulse.

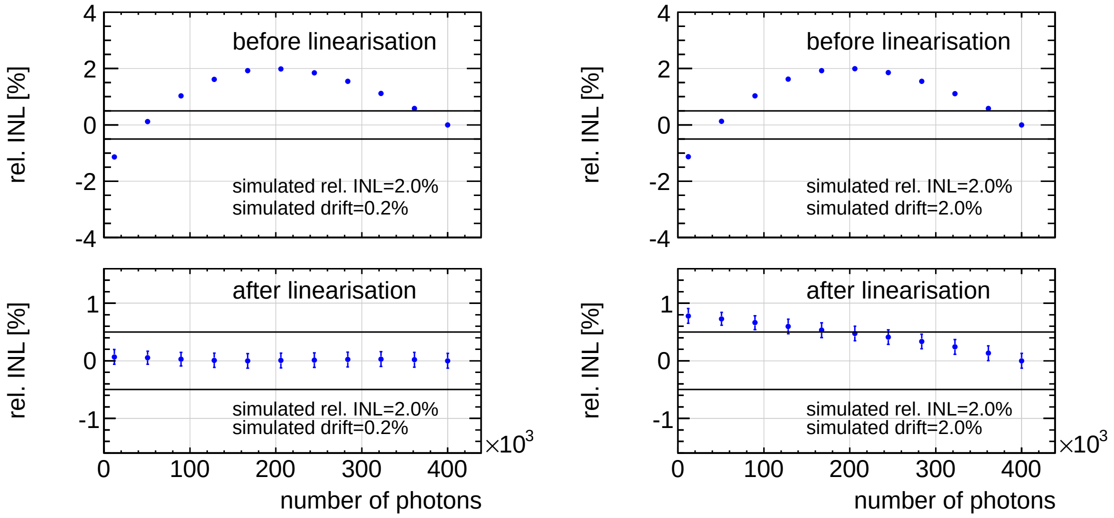

(a) drift = 0.2%

(b) drift = 2%

Figure 9.15: Comparison between uncorrected and corrected data for a simulated relative INL of 2.0% and different simulated intensity drifts of the differential pulse.

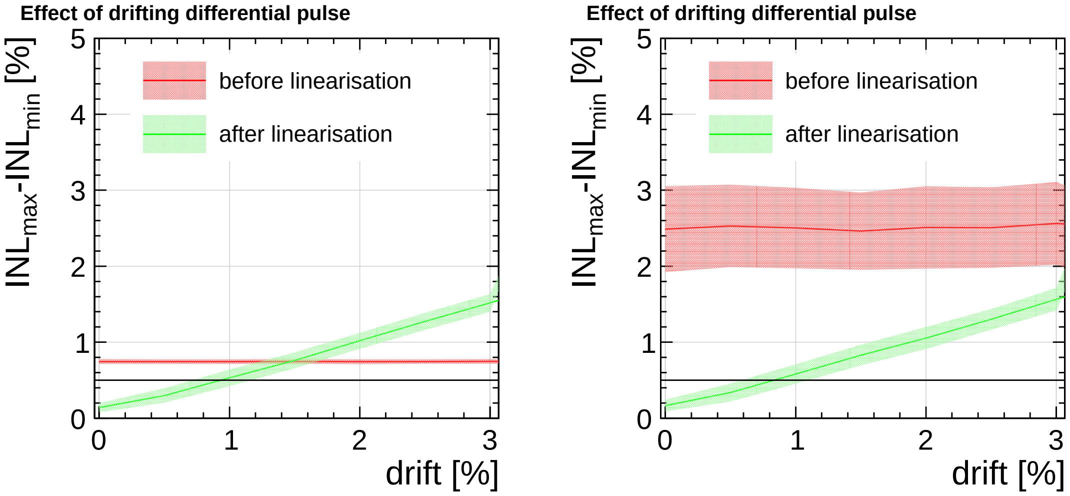

(a) simulated $\mathrm{INL}_{\mathrm{rel}} = 0.8\%$

(b) simulated $\mathrm{INL}_{\mathrm{rel}} = 2\%$

Figure 9.16: $\mathrm{INL}_{\mathrm{max}} - \mathrm{INL}_{\mathrm{min}}$ in dependence of different simulated intensity drifts of the differential light pulse.

9.6 Hardware Requirements

After having introduced the linearisation method and discussed the most important parameters of the measurement, we can now formulate the requirements for an experimental setup. Even though for this linearisation method no absolutely calibrated light source is necessary, there are still a few requirements that have to be met in order to make this light source applicable in the planned Compton polarimeters.

General design. The light source must consist of two independent sources, which can be triggered and adjusted in its light intensity independently.

Stability of differential pulse. The light intensity of the source providing the differential light pulses must not drift for more than 0.5% (see Section 9.5.5).

Dynamic range of base signal. The light source providing the base pulses has to be adjustable in its light intensity over the whole dynamic range of the planned Compton polarimeters in order to be able to probe the differential nonlinearity within this range.

Those requirements are essential for making the linearisation method possible at all. Additionally, there are some more requirements, which are important in order to meet the conditions of the actual polarisation measurement.

Wavelength. The light sensors at the Compton polarimeters detect Cherenkov light, whose wavelength intensity distribution peaks in the UV range. Therefore, the calibration light source should emit light in this wavelength range as well.

Short pulses. An ILC bunch with a longitudinal bunch length of 300 μm (cf. Table 3.2) traversing the Compton polarimeters creates a Cherenkov light pulse of only $t = 1$ fs. This is much shorter than the usual transit time of the electron avalanche in a photomultiplier. Therefore, the light pulse of the calibration source should be as short as possible, but at least as short as the photomultiplier transit time, which is of the order of 10 ns [212].

Applicable in detector design. The light source should ideally be very small such that it can be integrated in the existing polarimeter design (cf. Section 8.1.3.3).

The realisation of a real measurement setup is the topic of the next chapter.

10 Differential Nonlinearity Measurement and Results

In this chapter, we present the experimental realisation of the differential nonlinearity measurement. Therefore, we first introduce the measurement setup in Section 10.1. In the subsequent Section 10.2, the development of a suitable LED pulse driver is described. Various tests of the measurement setup and, in particular, of the LED driver are presented in Section 10.3. Finally, we perform differential nonlinearity measurements in Section 10.4 and evaluate the nonlinearity of a photomultiplier and its readout chain. In this section, we also confirm experimentally that the proposed linearisation method is able to linearise an independent dataset. In Section 10.5, we conclude this part of the thesis with an outlook on the application of the calibration method in the ILC polarimeters.

10.1 Measurement Setup

The schematic overview of the measurement setup is depicted in Figure 10.1. It consists of a light tight test box hosting the light source and the photomultiplier. In addition to that, the figure also shows the read-out electronics, voltage supplies, and the steering computer. A picture of the workplace in the laboratory is given in Figure 10.2a. In the following paragraphs we introduce the different parts in more detail.

10.1.1 Measurement Box

The light tight measurement box is the core part of the measurement setup. The box itself is made out of aluminum and the inside walls are coated matt black in order to suppress light reflections inside of the box originating from the light source. All slits, which are there design related, are filled with modelling clay and covered with aluminum tape. The lid of the box is removable such that the inner setup can easily be reached. During measurements, 14 thumbscrews press the lid onto the box and a layer of Thorogummite ensures light-tightness between the parts.

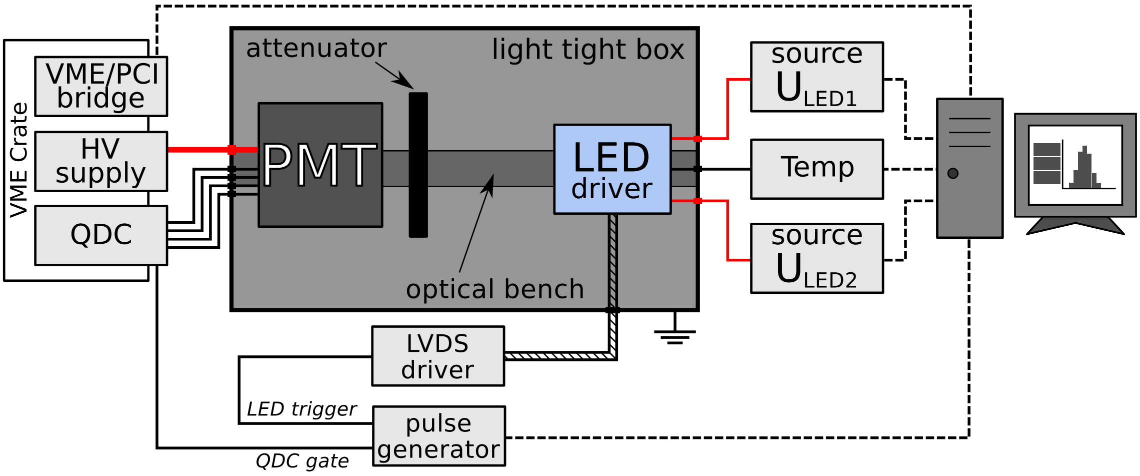

Figure 10.1: Schematic overview of the measurement setup. Solid (dashed) lines depict analog (digital) data flow and red lines indicate supply and steering voltages.

Inside of the box, an optical bench is installed. Different holding structures have been fabricated for the photomultiplier and the LED driver circuit, which acts as light source. A detailed description of the LED driver is given in Section 10.2. Figure 10.2b shows a picture of the optical bench. The LED driver (left) is mounted on a cross-table, which can be adjusted in both transversal directions with respect to the optical axis. This is especially important for highly directed light sources in order to be able to scan the light sensitive area of the photomultiplier. In our setup, however, we use only the central position. The mounting for the photomultiplier is visible on the right-hand side of Figure 10.2b.

In front of the photomultiplier mounting, a filter unit is located, as shown in Figure 10.2c. A variable number of neutral density filters can be clamped between the aluminum mask and the black plastic mounting. Most of the measurements have been performed with filter *8* featuring a transmission coefficient of about 3% for a wavelength of $\lambda \approx 400\,\mathrm{nm}$. All filters in use have been spectrometrically characterised at the LZH[1] (see Reference [213] for details).

Photomultiplier and light source are contacted from the outside via cable lead-throughs for pin plugs and LEMO connectors preventing light entering from the outside. At the same time the metal box acts as grounding plate for the different measurement and voltage supply devices. The inner part of the box is therefore well shielded from electromagnetic noise. The whole measurement box is placed on a layer of foam in order to damp vibrations.

---

[1] Laser Zentrum Hannover

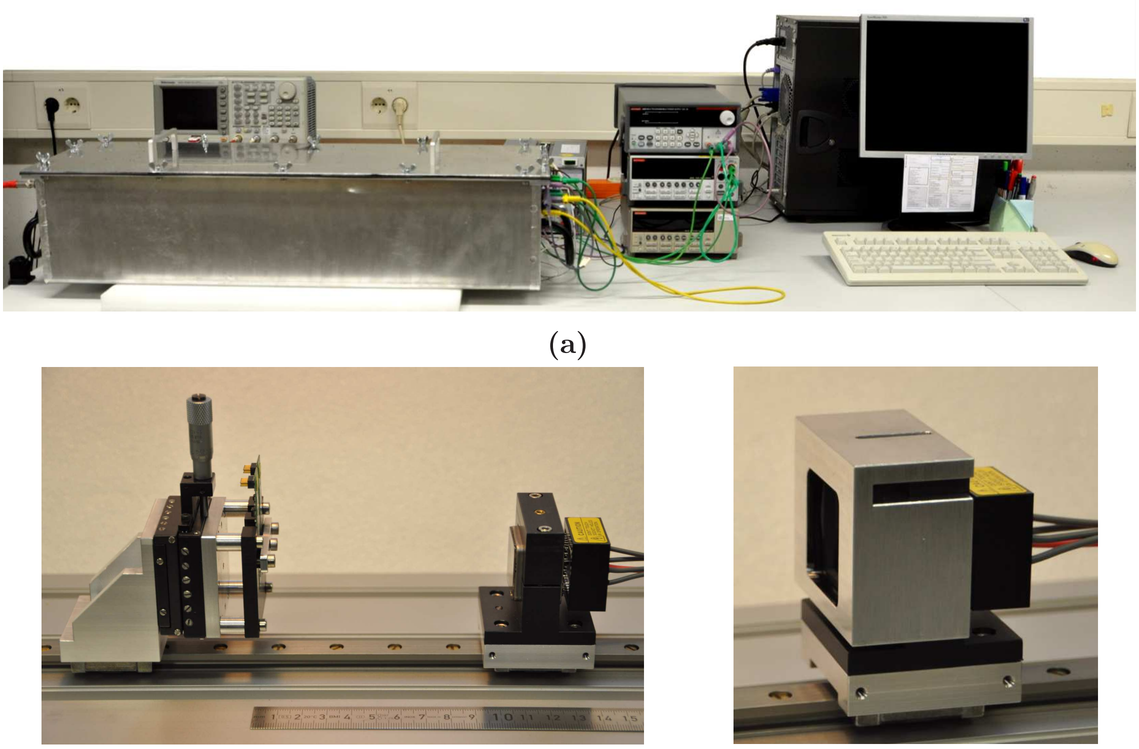

(a)

(b)

(c)

Figure 10.2: (a) Picture of the measurement setup. The VME crate as well as the LVDS driver is not visible in this picture. (b) Picture of optical bench with mounted LED driver (left) and photomultiplier (right). (c) Completed photomultiplier assembly with filter unit in front of the photomultiplier. A variable number of neutral density filters can be clamped between the aluminum structure and the black plastic holder in order to attenuate the light signal reaching the photomultiplier.

10.1.2 Instrumentation

As photodetector, the photomultiplier `Hamamatsu R5900-03-M4` is used, contacted with the appropriate photomultiplier socket `Hamamatsu E7083` (cf. Figure 8.10a). This photomultiplier features ten dynode stages and a four-fold segmented anode readout.

For the operation of the photomultiplier, a VME crate is used (cf. Figure 10.1). VME is a standardised multi-purpose data bus, which is widely spread in high-energy physics.

The VME system used in our setup comprises a QDC for the photomultiplier readout, a high voltage source for the photomultiplier, and a VME/PCI bridge, which establishes the data link between the VME bus and the PCI bus of the steering computer via an optical link. In principle, the used module `CAEN 2718` allows for data transfer rates of up to 70 MByte/s [215]. However, this rate is highly constrained by the actual measurement device operated via the VME bus and the readout software.

For the high voltage source, the VME module `CAEN V6533` has been chosen. It provides six high voltage output channels, three with positive and another three with negative output voltage of up to 4 kV. In this setup, typically voltages between 600 V and 800 V are chosen. The voltage ripple at a working point of $V = 1\,\mathrm{kV}$ and $A = 500\,\mu\mathrm{A}$ amounts to 5 mV [216] and is therefore negligible with respect to photomultiplier gain modulations. Also the long-term stability of the HV source of $\pm 0.02\%$ after one week at constant temperature ensures a very stable operation of the photomultiplier. For a photomultiplier with $n = 10$ dynode stages, one expects for the relative change in the photomultiplier gain approximately [217]

$$\frac{\Delta g}{g} = n\frac{\Delta V}{V} = 0.2\%. \tag{10.1}$$

This gain variation is acceptable on time scale of weeks.

The charge-to-digital conversion is performed by a `CAEN V965A` QDC [218]. This device has eight input channels, expecting a negative input signal. The resolution of the digitisation is 12 bit for two possible input ranges: In the high range, signals up to $\sim 900\,\mathrm{pC}$ can be processed, with a digitisation resolution of 200 fC. The low range has a by a factor of eight increased sensitivity, resulting in an input range of only up to $\sim 100\,\mathrm{pC}$. This corresponds to a digitisation resolution of 25 fC. Both digitisations are performed simultaneously such that both ranges are available for later analyses. We will always refer to the low range in the presented results.

The digitisation of all eight channels takes about $2.8\,\mu\mathrm{s}$, which leads in the end to a total dead time of the QDC of about $3.5\,\mu\mathrm{s}$. This dead time limits the maximum signal rate to 285 kHz, which is much higher than the foreseen signal rates of $\mathcal{O}(10\,\mathrm{kHz})$ for the test measurements. However, the available QDC is not fast enough for the final operation in the ILC polarimeters.

The INL and DNL of the described QDC module have been extensively investigated in Reference [213]. Therein, it has been shown that the QDC nonlinearity has only a sub-per-mil effect on the mean position of a signal-like QDC spectrum and will therefore not be explicitly corrected in the data analysis. However, it should be mentioned that the introduced linearisation method measures the nonlinearity of the whole DAQ chain comprising also possible QDC effects.

The QDC gate is provided by a programmable dual-channel function generator `Tektronix AFG 3102` [219]. Its time resolution for produced pulses amounts to 10 ps and the jitter is 200 ps. Limiting for the gate is the rise/fall time of $\leqslant 5\,\mathrm{ns}$.

In order to fulfill the gate condition of the QDC of a gate signal being at minimum 15 ns above the threshold, the gate pulse width should not be much below 25 ns. The second channel of `AFG 3102` is synchronised with the first one and can therefore be used as trigger signal for the light source. It is possible to delay channel two with respect to channel one in order to compensate for different signal path lengths.

The LED trigger pulse is converted into an LVDS[2] trigger signal, which is required by the light source. LVDS is less error-prone than a "normal" trigger signal since two mirrored signals are used to transmit the trigger information. At the LVDS receiver both signals are compared in order to restore the original trigger pulse. In this procedure, signal distortions on the way from the transmitter to the receiver cancel out.

The light source itself requires two steering voltages modulating the light intensities of the two LEDs. For this, we use two programmable voltage source: The KEITHLEY sourcemeter `Model 2410` features a voltage setting precision of $0.02\% + 2.4\,\mathrm{mV}$ and a read-back precision of $0.015\% + 1\,\mathrm{mV}$ [220]. The other device is a KEITHLEY DC power supply `Model 2200-32-3` with an attributed setting precision of $0.03\% + 3\,\mathrm{mV}$ and a read-back precision of $0.02\% + 3\,\mathrm{mV}$ [221] in the corresponding range. Both precisions are sufficient for steering voltages between 6 V and 10 V. The rise/fall time of the devices are quoted as $< 35\,\mathrm{ms}$. For this reason, data taking is paused for two seconds after a change in the LED supply voltage such that the targeted voltage level is definitely reached.

Finally, also the temperature is monitored using a temperature dependent, calibrated platinum resistor (`Pt1000`). From a resistance measurement, the actual temperature can be deduced. In our setup, the resistance is measured by a KEITHLEY electrometer `Model 6514`. It measures the resistance with a test current of 0.9 mA on a precision of $0.20\% + 10\mathrm{cnts}$.

All parts of the DAQ chain are controlled by a computer. Figure 10.1 visualises the complete data flow. Solid lines indicate analog signals, dashed lines represent digital data, and red lines show voltage supplies.

10.1.3 Software

In order to bring together all parts of the DAQ chain, the software framework `PolDAQ` has been developed. Based on the work done for [222] and [213], the existing software has been rearranged and considerably extended. The whole framework including the device drivers are written in C++.

For steering and read-out of the VME devices, the hardware registers of the VME modules are directly read and written via a CAEN software library. All the other

---

[2] Low Voltage Differential Signal

devices implement the SCPI[3] interface, which consists of a set of standardised ASCII commands for read and write operations. The SCPI hardware drivers have been designed in such a way that they are independent of the actual transport layer. For the physical communication, a USB module, an RS-232 module, as well as an Ethernet module is available and can be employed depending on the available hardware interface of the specific device. If needed in the future, the framework can be easily extended by further communication modules and devices. A logger class allows for logging any changes of the device state to a text file.

The raw data of the QDC is persistently stored as ROOT histograms [176], whereas all slow control data is saved as n-tuples.

This presented software framework allows for completely automatised measurements. For every measurement, specific programs are available. They are collected in the software package `PolCalib`. The measurement programs are configured by ASCII configuration files such that measurement parameters can easily be modified or measurements can be repeated under equal conditions.

10.2 LED Driver

A very important piece in the whole setup is the light source. For this reason, we describe in this part the development of an appropriate light source, which fulfills the requirements defined in Section 9.6.

For the light source, an LED driver has been developed, which is based on the calibration light source of the CALICE tile hadron calorimeter [223]. It is equipped with two UV-LEDs (`LEDTRONICS SML0603-395-TR` [224]) which feature a peak intensity at $\lambda = 395\,\mathrm{nm}$, but with a rather large spectral width of a few 10 nm. Its directional characteristic is almost an Lambertian radiator. A schematic overview of the circuit is given in Figure 10.3a. It consists basically of a large resistor $R = 5\,\mathrm{k}\Omega$, a parallel circuit of a small resistor $R_p = 51\,\Omega$ and the LED, and a capacitor $C = 150\,\mathrm{pF}$. In parallel to this, a transistor (`Infineon BFR183W`) can open and close the ground connection.

The light pulse generation can be subdivided into three phases: In the first phase, the transistor is opened and the capacitor is charged via the resistors up to the externally provided voltage U_{LED} (Figure 10.3b). When the transistor gets closed, the charged capacitor starts to discharge (Figure 10.3c). As the LED is now oriented in forward direction and its resistance is small for large currents in the beginning of the capacitor discharge, the LED path of the parallel circuit is chosen by the main current. Thus, the LED emits light. Without the parallel resistor, the light pulse

---

[3] Standard Commands for Programmable Instruments

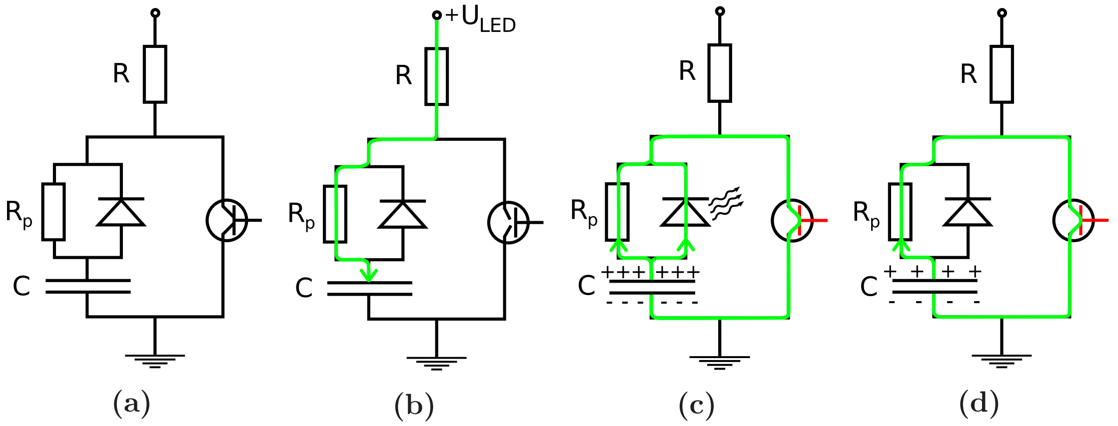

Figure 10.3: (a) Schematic picture of the LED driver circuit. (b) Stage 1: If the transistor is opened, capacitor C is charged by an external voltage supply. (c) Stage 2: The transistor is closed and the capacitor discharges mainly via the LED, because the LED resistance is small compared to R_p. Light is emitted. (d) Stage 3: The voltage has dropped below the operating point of the LED and light emission is stopped. The light pulse gets quenched.

would be rather long. However, as the parallel circuit allows for a second current route, the voltage at the capacitor quickly drops below the operating voltage of the LED and the LED stops emitting light (Figure 10.3d). This limits the length of the light pulse and, thus, generates very short pulses. The external voltage defines herein the light intensity of the LED pulse.

In our LED source, two replications of the described LED circuit are placed on one board, triggered by the same trigger pulse, but allowing for two independent steering voltages U_{LED1} and U_{LED2}. In order to further stabilise the input voltages, large capacitors (10 μF, 10 nF) are connected in parallel to the actual voltage inputs. The full schematics of the circuit can be found Appendix D.

Figure 10.4a shows a picture of the designed LED driver board. It is eye-caching that the dimensions of the board are rather small ($50 \times 8.5\,\mathrm{mm}^2$). The two UV-LEDs are located on the bottom side of the board, whereas the remaining electronic components are placed on top. This design has been chosen such that the driver is applicable within the Cherenkov detector design (cf. Figure 8.5b). In a final polarimeter Cherenkov detector assembly, one LED board is foreseen for each of the staggered Cherenkov detector channels, which sets the constraint of the tolerable width of the board.

As LEDs are rather temperature dependent devices, two temperature sensors are located on the board. An analog temperature sensitive resistor (`Pt1000`) is placed directly opposite the LEDs on the top side. A second, digital temperature sensor

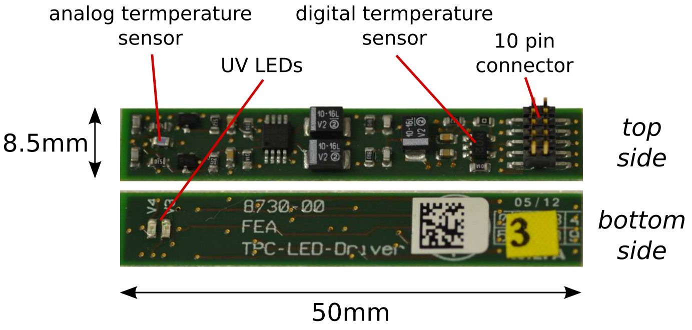

(a)

pin allocation			
U_{LED1}	**10**	**9**	GND
+3.3 V	**8**	**7**	T_{analog}
LVDS+	**6**	**5**	LVDS-
T_{digital}	**4**	**3**	GND
U_{LED2}	**2**	**1**	GND

(b)

Figure 10.4: (a) Picture of the developed LED driver. (b) Connector pin allocation.

(`DS18B20U`) is present at the other end of the board, which provides a 12-bit digitised temperature, read out via a 1-wire bus. For the slow control data, only the analog signal has been recorded.

The whole board is connected via a 10-pin connector. In Table 10.4b, the pin allocation is given, where pin 1 denotes the bottom right pin in the top view of the board. LVDS+ and LVDS- are the two LVDS trigger inputs. The board needs a supply voltage of +3.3 V.

10.3 Characterisation Measurements

In this section, we investigate the properties of the LED driver and the setup, and test whether the design criteria are fulfilled.

10.3.1 Pulse Length

For the visualisation of the LED light pulses, the photomultiplier is connected directly to an oscilloscope. As input impedance of the oscilloscope 50 Ω is chosen such that it is equal to the input impedance of the QDC `V965A`, which is used later for the precision measurements. The photomultiplier is operated at a high voltage of $U_{\mathrm{HV}} = -700\,\mathrm{V}$. Figure 10.5a shows the waveforms recorded with the oscilloscope for different LED voltages U_{LED}. In this measurement, only LED 1 of the LED driver board is used and the voltage of the second LED is set to 0 V. The displayed pulse shapes are obtained from averaging 5120 recorded waveforms per LED voltage. In Figure 10.5a, also the RMS of the waveforms is included as error band, but it is too small to be visible.

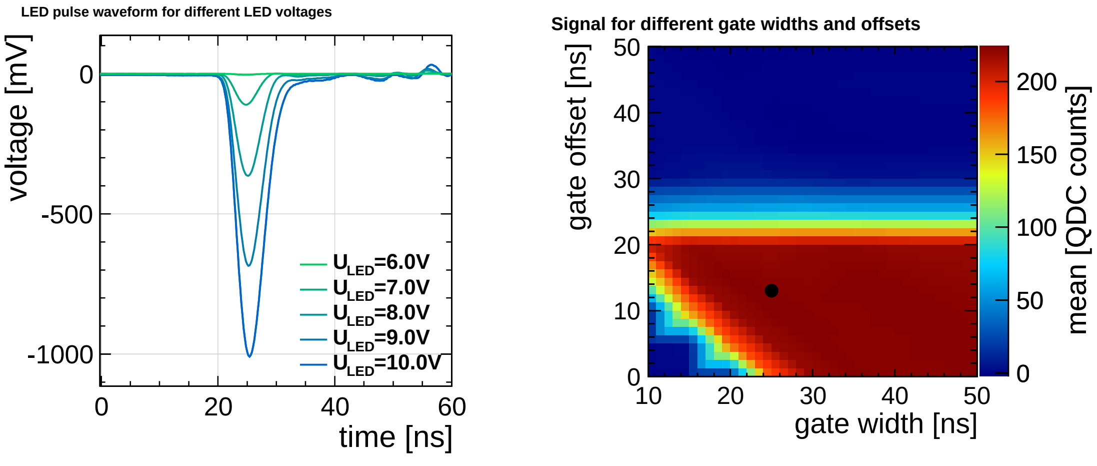

(a)

(b)

Figure 10.5: (a) Waveform taken with the oscilloscope of LED pulses for different LED voltages U_{LED}. (b) Gate scan for the QDC measurements. U_{LED} is set to 7 V. The used gate is marked with a black dot in the figure. Note that the signal measurement at the QDC is delayed by additional 10 ns compared to the direct oscilloscope measurement because of QDC internal signal processing.

It is striking that the light pulses are very short. With the developed LED driver circuit pulse lengths well below 10 ns can be achieved, which fulfills the design criteria (see Section 9.6). However, it can also be observed that especially for larger light intensities afterpulses and signal under- and overshoots are present, which can be attributed to the photomultiplier.

For the measurement with the QDC, it is important to define a proper gate in order to measure the full signal, but to exclude noisy afterpulse effects. Therefore, the photomultiplier is now connected to the QDC and the gate width as well as the gate offset are scanned with respect to the LED trigger pulse. At this, the LED voltage is fixed at $U_{\text{LED}} = 7\,\text{V}$. The result is shown in Figure 10.5b. On the z-axis, the pedestal corrected mean of the QDC spectra of $N = 10^5$ pulses digitised in the low range (cf. Section 10.1.2) is depicted. It should be mentioned that the signal measurement by the QDC is additionally delayed compared to the direct oscilloscope measurement because of the internal signal processing of the QDC. Therefore, the direct comparison of the time axis between Figure (a) and (b) is not possible. Without a gate offset, no signal is observed for gate widths smaller than 20 ns, which indicates that the arriving photomultiplier signal is delayed by about this time with respect to the LED trigger pulse. For $t_{\text{gate}} > 30\,\text{ns}$ the whole signal is selected. Figure 10.5a shows that the length of the light pulses is below 10 ns, which would in principle allow for a comparably small gate. For $t_{\text{gate}} = 10\,\text{ns}$ and $t_{\text{offset}} = 18\,\text{ns}$, the whole pulse corresponding to $U_{\text{LED}} = 7\,\text{V}$ is already located within the

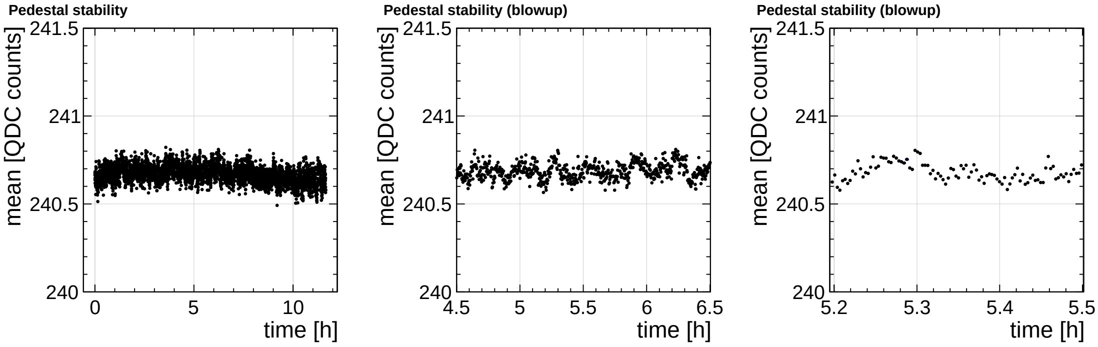

(a) **(b)** **(c)**

Figure 10.6: Fluctuations of the pedestal signal over (a) 12 hours, (b) 2 hours, and (c) 20 minutes. The error bars are too small to be visible in the figure.

gate. However, the used QDC should not be operated with gates much smaller than $t_{\text{gate}} = 25\,\text{ns}$ as explained in Section 10.1.2. Additionally, we observe an increasing pulse width for larger light pulses, which disfavours a too sharp gate configuration and finally suggests the following gate configuration for the measurements

$$t_{\text{gate}} = 25\,\text{ns}, \tag{10.2}$$

$$t_{\text{offset}} = 13\,\text{ns}. \tag{10.3}$$

In this case, the offset is set such that the data taking starts about 5 ns before the signal arrives.

10.3.2 Pedestal Correction Scheme

The QDC pedestal and photomultiplier dark current has to be measured beforehand in order to subtract it from the actual signal measurements. To this end, the photomultiplier is switched on, but all LED voltages are set to 0 V. In this configuration, $N = 10^5$ dark events are measured and the mean of the QDC spectrum is used to correct the signal measurements. Figure 10.6a shows the fluctuations of the pedestal signal over 12 hours, which is the usual time scale for a high-precision DNL measurement of a photomultiplier. The error bars are too small to be visible in the figure. We observe pedestal fluctuations of the order of 0.2 QDC counts.

Figures 10.6b and 10.6c are blow-ups of Figure 10.6a focusing on different time scales. Especially in Figure 10.6b an oscillating behaviour of the pedestal signal is observable with a period length of about 20 minutes. The origin of this oscillation is not entirely clear, but can be most probably attributed to fluctuations in the QDC pedestal current. The figures demonstrate clearly that only one pedestal measurements in the very beginning of a 12 h lasting signal measurement run is not sufficient. Instead, the pedestal signal has to be measured continuously also between signal measurements in order to allow for an accurate pedestal correction.

In the applied pedestal correction scheme, each measurement of $N = 10^5$ signal events is preceded by a measurement of $N = 10^5$ dark events, which is then used to correct the corresponding signal measurement.
Since the resulting statistical uncertainty is too large for only $N = 10^5$ events in most of the measurements (cf. Section 9.5.1), depending on the demanded precision, either 10 or 100 repetitions of pedestal and signal measurement are performed. The individual pedestal-corrected values are finally averaged.

10.3.3 Dynamic Range

Figure 10.7 depicts the intensity reach of the LED driver board for different filter configurations. The nominal transmission coefficients of the filters are given in the caption of the figure. The LED voltage is tuned from $U_{\mathrm{LED}} = 6\,\mathrm{V}$ up to $U_{\mathrm{LED}} = 10\,\mathrm{V}$. $N = 10^6$ events are recorded per step and the pedestal corrected mean of the QDC spectrum is displayed in the figure.

In order to calibrate the photomultiplier in the correct regime, the LED light intensity should be comparable with the expected light intensity at the polarimeters. We can estimate the expected light intensity from Figure 8.6. The polarimeter simulation shows that up to 200 Compton electrons per bunch crossing traverse a single Cherenkov detector channel. From detailed Monte-Carlo simulations of the Cherenkov detector prototype it is known that about 6.5 photoelectrons are created in the photomultiplier per Compton electron taking into account the typical Cherenkov wavelength spectrum and a typical photomultiplier quantum efficiency [209]. The photomultiplier gain is estimated to $g = 3 \times 10^5$, which is a typical value for photomultipliers operated at $U_{\mathrm{HV}} = -700\,\mathrm{V}$. With these assumptions, we expect a photomultiplier anode charge of 312.2 fC per Compton electron, which corresponds to 12.5 QDC counts digitised in the low range of the used QDC. For up to 200 Compton electrons per detector channel, the dynamic range can be estimated to reach up to 2500 QDC counts.

A comparison with the intensity scan presented in Figure 10.7 illustrates that the configuration with filter *8* adjusts the LED driver intensity range exactly in the right order of magnitude. However, it should be noted that with different filter configurations the intensity range of the LED driver board can easily be adapted to any needed range. Even larger intensity ranges are possible by replacing the 3% filter by a more transparent one. Therefore, there is lots of room for adjustment to the specific needs. Hence, the designed LED driver board fulfills completely the envisaged dynamic range requirements.

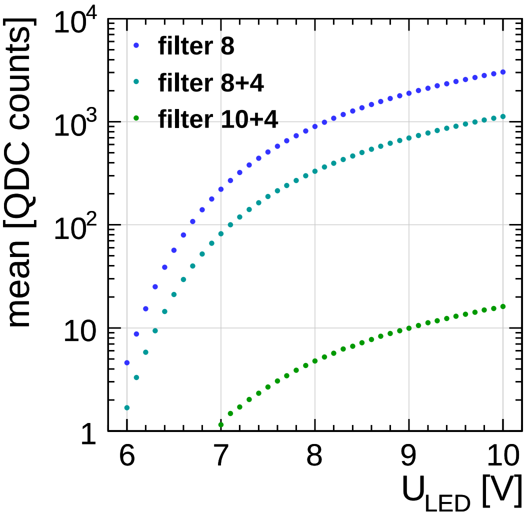

Figure 10.7: Intensity reach of the LED driver board for different filter configurations. The transmission coefficients for $\lambda \approx 400\,\mathrm{nm}$ have been measured to 3.7×10^{-1} (filter *4*), 2.7×10^{-2} (filter *8*), and 5.0^{-4} (filter *10*) [213].

10.3.4 Absolute Signal Stability

It has already been pointed out that the signal stability is an essential criterion for the light source. In the foreseen DNL measurement, which is discussed later in this chapter, three different time scales are of importance. A total scan of the dynamic range takes about 12 hours for the current choice of the trigger rate. Each data point is measured within 36 minutes, which is the average of 100 individual measurements according to the pedestal correction scheme. Each single set of base pulse and base + differential pulse measurements takes, in turn, about 22 seconds.

Since LEDs are temperature dependent devices, we present the warm-up behaviour of the setup with respect to the signal stability in this section.

10.3.4.1 Photomultiplier and LED Effects

In order to decouple warm-up effects originating from the photomultiplier and the LED, we perform a long-term measurement of the pedestal subtracted mean position of the QDC spectrum shown in Figure 10.8. Each 12-hours measurement is interrupted by a six hours break where either the LED voltage (a,b,c) or the photomultiplier high voltage (d,e,f) is switched off. Before break "a", the LED and the photomultiplier have already been operated for 12 hours. The data points drawn in the figure correspond to the mean position averaged over $N = 10 \times 10^5$ events.

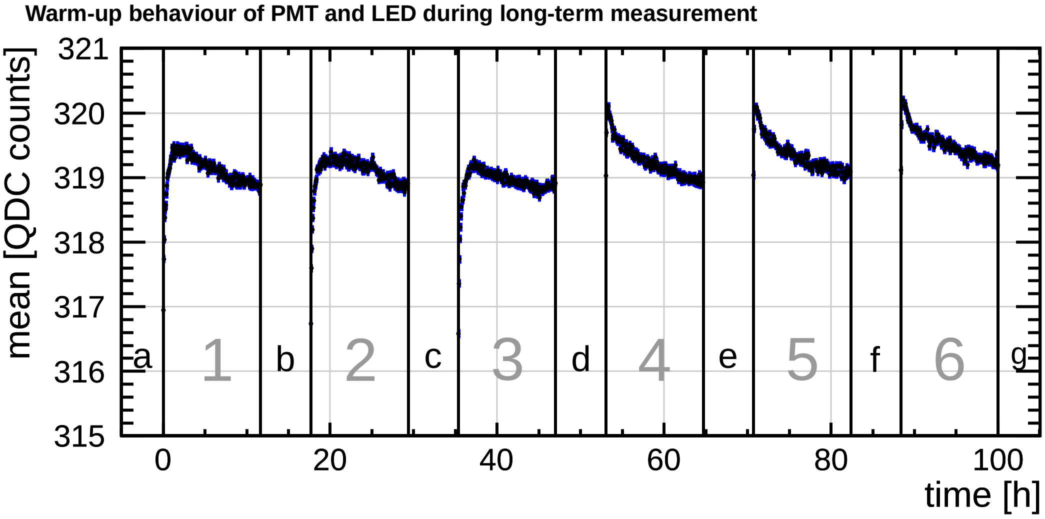

Figure 10.8: Long-term measurement of the pedestal corrected mean position of the QDC spectrum for one fixed LED voltage. Between each 12 hours measurement either the LED voltage (a,b,c) or the photomultiplier high voltage (d,e,f) are set to zero. Therefore, measurements 1-3 show the warm-up behaviour of the LED and 4-6 of the photomultiplier.

The LED voltage is set to $U_{\mathrm{LED}} = 7\,\mathrm{V}$ and the photomultiplier high voltage is set to $U_{\mathrm{HV}} = -700\,\mathrm{V}$. Since in this run the second LED of the LED driver board is used, the measured mean position differs from the measurements presented so far, where always the first LED has been used.

In the measurements 1-3, the effects originating from turning on the LED can be studied. It is visible that there are two competing behaviours: Shortly after switching on the LED there is a rather steep increase of the mean position, which then passes into a falling slope on longer time scales. The fast rise happens within the first 40 minutes after turning on the LED.

In contrary, measurements 4-6 show the effects from turning on the photomultiplier. Here, the same long-term falling behaviour is observed, but no fast signal rising as seen before. Therefore, the falling behaviour can clearly be attributed to the warm-up of the photomultiplier. It is observable in all six measurements, because it takes only place when the photocathode is illuminated *and* the photomultiplier is powered up. On very long time-scales, a slight increase of the mean position is visible comparing the end-points of measurements 4, 5, and 6. These effects can only arise from the LED, since only the LED had been switched on over this long period. This very long-term increase is determined to $1.42 \times 10^{-3}\%/\,\mathrm{h}$ and is therefore negligible on time scales of a DNL measurement of a photomultiplier.

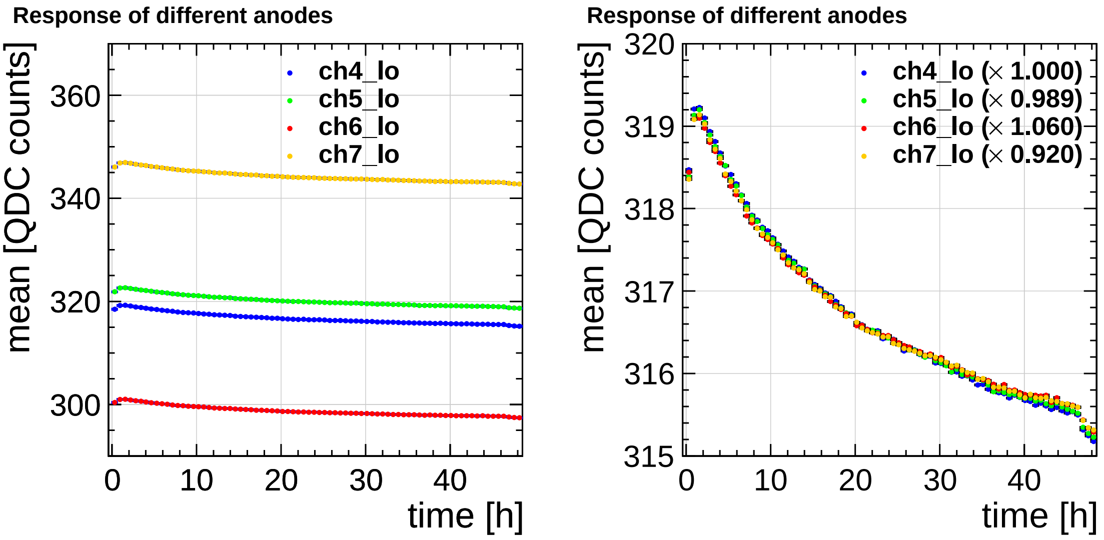

(a) **(b)**

Figure 10.9: Long-term measurement of the pedestal corrected mean position of the QDC spectrum for one fixed LED voltage after one month of full time measurements. (a) The anode responses of all four anodes of the segmented photomultiplier `Hamamatsu R5900-03-M4` are displayed. The different absolute scales originate from different anode sensitivities and inhomogeneous light distribution on the photomultiplier. (b) They can be overlayed by scaling. After 6 hours warm-up time, the mean position drift over 12 hours is less than 0.5%.

Concluding, we find that the LED warm-up is only relevant in the first 40 minutes after turning on the LED and then gets negligible. However, the photomultiplier effect is relevant on time scales of a DNL measurement. Therefore, these data suggest that a warm-up of the LED and the photomultiplier should be performed at least a few hours before the actual measurement. At this, the photomultiplier has to be illuminated with light. For the DNL measurements, we always warm-up the system six hours before starting the main measurement.

The measurement shown in Figure 10.8 has been the very first measurement of a measurement campaign lasting for about one month of full time data taking. At the very end, a second very long-term measurement of the mean position under equal conditions has been performed. For the whole month, the measurement box has not been opened and the setup has not been modified. The result of the second long-term measurement is depicted in Figure 10.9. In order to reduce fluctuations, we average over 100 pedestal corrected mean positions of QDC spectra originating from $N = 10^5$ light pulses.

In contrary to Figure 10.8, Figure 10.9 contains the mean positions of all four anodes of the segmented photomultiplier `Hamamatsu R5900-03-M4`. It is possible to rescale the anode signals in order bring them to overlap as shown in Figure 10.9b. The obtained scaling factors account for any inhomogeneous illumination and different anode sensitivities of the photomultiplier, which can differ by up to 10% [212]. Since for the targeted DNL measurement the distinction between the different anodes is not relevant, we will present only the signal measured with one anode in the following.

From Figure 10.9b it can be observed that the falling slope is steeper compared to Figure 10.8. This effect is not further investigated. Nevertheless, we can derive a conservative estimate for the mean drift over 12 hours after 6 hours of warm-up, which amounts to

$$\frac{318.0 - 316.7}{318.0} = 0.41\%. \tag{10.4}$$

Thus, with this setup, the design criterion of a pulse stability below 0.5% can be achieved during a DNL measurement. For a longer warm-up time, the drift can be further reduced. After 20 hours of warm-up, the drift is below 0.2%, for instance.

10.3.4.2 LED Voltage Changes

For the targeted DNL measurement, not only the signal stability for one fixed LED voltage is relevant, also the effect of sudden LED voltage changes are of interest. This is especially important for the base pulse, which scans the dynamic range during a DNL measurement. Therefore, we study now the time dependence of the pedestal corrected mean position when the LED voltage jumps between $U_{\mathrm{LED}} = 6.5\,\mathrm{V}$, $U_{\mathrm{LED}} = 7.0\,\mathrm{V}$, and $U_{\mathrm{LED}} = 7.5\,\mathrm{V}$. The result is depicted in Figure 10.10. Herein, the bottom row shows blow-ups of the first figure. For each data point $N = 10^5$ light pulses are recorded.

We find a similar LED behaviour as discussed in the section before. The mean position stabilises about 40 minutes after the new voltage level has been set. Before, a rather steep slope can be observed. This behaviour is found for voltage increases ($6.5\,\mathrm{V} \rightarrow 7.0\,\mathrm{V}$, $7.0\,\mathrm{V} \rightarrow 7.5\,\mathrm{V}$) as well as for voltage decreases ($7.5\,\mathrm{V} \rightarrow 6.5\,\mathrm{V}$). Thereby, the sign of the slope depends on the sign of the voltage change.

We can now discuss this result in the light of the envisaged DNL measurement:
Not too large drifts of the base pulse are unproblematic on the time scale of the 100 individual DNL measurements, since the DNL is not expected to change drastically for small changes of the base pulse. The final averaging of the 100 individual DNL measurements does not distort the nonlinearity measurement.
However, drifts of the base pulse on the time scale of a single set of base and

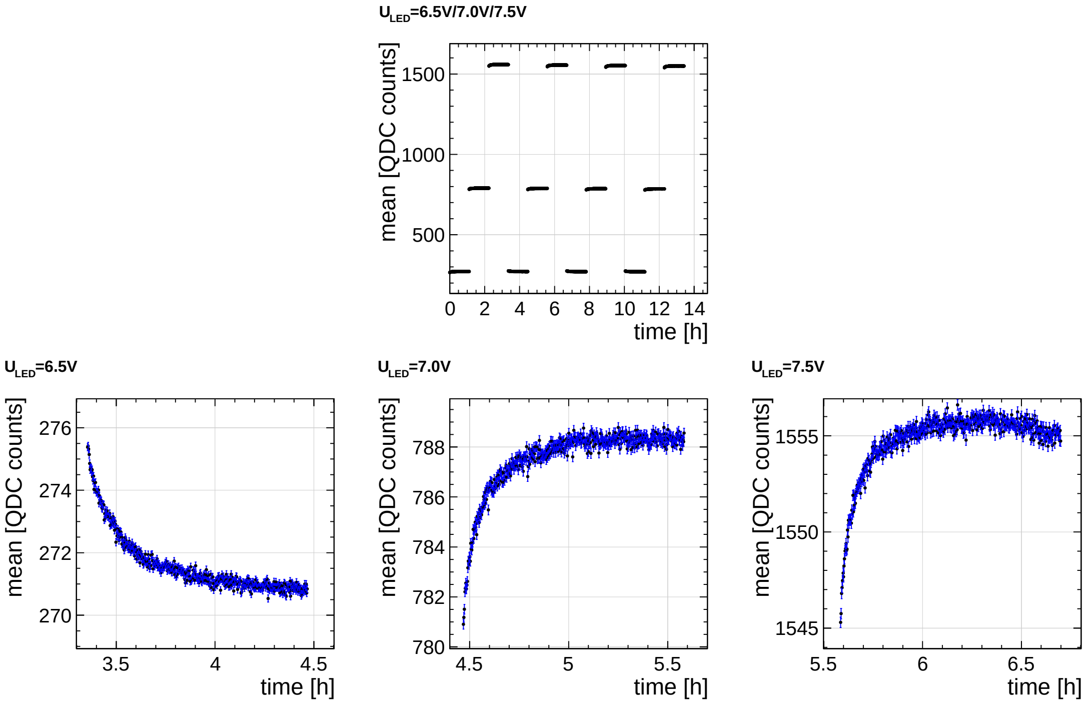

Figure 10.10: Pedestal corrected mean position of the QDC spectra for jumping LED voltages $U_{\mathrm{LED}} = 6.0\,\mathrm{V}$, $U_{\mathrm{LED}} = 6.5\,\mathrm{V}$, and $U_{\mathrm{LED}} = 7.0\,\mathrm{V}$. The lower plots are blow-ups of the upper plot. About 40 minutes after a voltage change a stable mean position is reached.

base + differential pulse measurements are relevant. The measured DNL, which is the difference between the base + differential pulse response and the base pulse response, is in this case dependent of the scan direction. After the voltage has been decreased, we observe a falling signal slope (cf. bottom left part of Figure 10.10). Under the assumption of a constant differential pulse, the derived difference between the base + differential pulse measurement and the base pulse measurement is reduced due to the base pulse drift. Thus, the measured DNL appears smaller than it actually is. In turn, for increasing voltage, the measured DNL is larger. However, this effect can be canceled out if DNL measurements are performed in both scan directions and the results are averaged.

Furthermore, from Figure 10.10, it is clear that large voltage jumps should be avoided in a DNL measurement. For the base pulse scan in the DNL measurement, we choose voltage steps of 0.2 V.

10.3.5 Independence of the Board LEDs

Up to now, only measurements with one LED of the driver board have been presented. In this section, we test the independence of the two LEDs on one driver board. To this end, we perform measurements with different combinations of input voltages U_{LED1} and U_{LED2}. First, we take 200 measurements of the mean position of the QDC spectra for $N = 10^5$ light pulses with only LED 1 set to U_{LED1}. U_{LED2} is set to zero. The obtained average from the pedestal corrected mean positions is called in the following base signal $\langle \text{mean}_1 \rangle$. In a second step, LED 2 is additionally switched on and another 200 measurements of $N = 10^5$ combined light pulses of LED 1 and LED 2 are taken. The obtained average is denoted as $\langle \text{mean}_{1+2} \rangle$. Finally, the difference between the two measurements can be determined as $\langle \Delta\text{mean} \rangle = \langle \text{mean}_{1+2} - \text{mean}_1 \rangle$. In order to test the independence of the LEDs, also measurements are taken in which LED 2 is masked such that only photons emitted from LED 1 can reach the photomultiplier.

The quantitative results are summarised in Table 10.1. In the first configuration (I), only LED 1 is set to a voltage different from zero. Therefore, the first and second measurements are equal, which results in a vanishing $\langle \Delta\text{mean} \rangle$, as expected.
In the next configuration (II), LED 2 is set to $U_{\text{LED2}} = 6.5\,\text{V}$ in the second measurement. We observe that the switched on second LED 2 implicates a rise of the measured mean position of $\langle \text{mean}_{1+2} \rangle$ by 217 QDC counts. This increase is not exactly equal to the pure signal of LED 1, which features the same voltage, however, it lies in the same order of magnitude. In many prestudies it has already been observed before that the resulting light output differs for individual LEDs even if they are set to the same LED voltage. Therefore, the different values of $\langle \text{mean}_1 \rangle$ and $\langle \Delta\text{mean} \rangle$ are not unusual. However, this measurement does not confirm the independence of

	U_{LED1} [V]	U_{LED2} [V]	$\langle \mathrm{mean}_1 \rangle$	$\langle \mathrm{mean}_{1+2} \rangle$	$\langle \Delta \mathrm{mean} \rangle$
I	6.5	0.0	276.2160 ± 0.0096	276.2319 ± 0.0096	0.016 ± 0.014
II	6.5	6.5	276.7555 ± 0.0096	493.879 ± 0.012	217.124 ± 0.015
III	0.0	[6.5]	-0.1812 ± 0.0044	0.1648 ± 0.0044	0.3460 ± 0.0063
IV	6.5	[6.5]	239.6099 ± 0.0091	321.943 ± 0.010	82.333 ± 0.014

Table 10.1: Different configurations of LED voltages and maskings in order to test the independence of LED 1 and LED 2. Brackets indicate that the corresponding LED is masked such that no light can reach the photomultiplier. The mean values are pedestal corrected and averaged over 200 measurements of each 10^5 light pulses. The values are given in units of QDC counts. From configuration IV it can be deduced that cross-talk between the LEDs on one driver board is present.

LED 1 and LED 2.
In order to really study this independence, LED 2 is now masked, indicated by the brackets in Table 10.1. Configuration III proofs that the masking blocks efficiently the emitted light from LED 2. Apart from very small fluctuations, the observed signal is close to 0 in both measurements.
Configuration IV finally repeats the measurements as in configuration II, but LED 2 is now blocked. $\langle \mathrm{mean}_1 \rangle$ in this configuration is slightly smaller compared to the value obtained in configuration I and II, since the distance between photomultiplier and LED driver board has not been exactly the same due to the modification of the setup for the masking. When LED 2 is set to $U_{\mathrm{LED2}} = 6.5\,\mathrm{V}$ in the second measurement of this configuration, the resulting signal should not change. However, we observe that the signal increases by 82 QDC counts. This can only be interpreted as cross-talk between the two LEDs on the LED driver board. It is important to note that in configuration III no cross-talk is observable, which suggests that the observed effect does not increases the signal absolutely, but only enhances an already present signal.

The reason for this cross-talk needs further investigation. It has been tried to place a grounding wire between the nearly located LEDs on the board in order to reduce possible electromagnetic cross-talk. This, however, has not shown any improvement. Also changes of the circuit (cf. Appendix D) like, for instance, removing the coupling capacitors to the transistor base (C10, C11) or a stronger decoupling of the LVDS receiver by changing R10 to $1.5\,\mathrm{k}\Omega$ and R11 to $270\,\Omega$ [225] has had no effect on the observed cross-talk.

In order to ensure the independence of the two light pulses for the DNL measurement, the setup has finally been modified such that two independent LED drivers are used for the different light pulses as depicted in Figure 10.11. In this setup, only one LED per LED driver board is used, whereas the second LED on each board is set

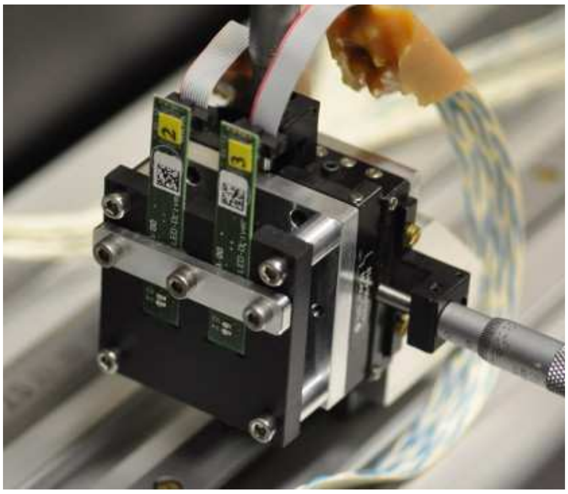

Figure 10.11: Holding structure for two LED driver boards. In this setup, only one of the two LEDs per board is used.

to 0 V. It has been ensured that both cable paths in the modified setup are equal in order to preserve the light pulse coincidence.

10.3.6 Pulse-by-Pulse Stability

For the proposed measurement of the DNL, the pulse by pulse stability is of particular importance. To this end, we perform a measurement equivalent to configuration I of the previous section for different LED voltages U_{LED1} and further investigate the long-term stability of Δmean. In order to achieve a very accurate measurement, the pedestal correction scheme is applied as described in Section 10.3.2. For each data point, $N = 10^5$ light pulses are recorded and the photomultiplier is operated at a high voltage of $U_{\mathrm{HV}} = -700\,\mathrm{V}$. The results of this differential stability measurement are shown exemplarily for $U_{\mathrm{LED1}} = 6\,\mathrm{V}$, $U_{\mathrm{LED1}} = 7\,\mathrm{V}$, and $U_{\mathrm{LED1}} = 8\,\mathrm{V}$ in Figure 10.12. The absolute mean positions for the corresponding voltage levels can be read off Figure 10.7 and amounts to 4.4, 216, and 878 QDC counts. This explains the increasing spread of the data points for the different LED voltages.

In Figure 10.13, the corresponding pull distribution of Δmean is presented, which is defined as the distribution of

$$\frac{\Delta\mathrm{mean}_i - \mu}{\sigma_{\Delta\mathrm{mean}_i}}, \tag{10.5}$$

where $\Delta\mathrm{mean}_i$ are the individually determined differences between two consecutive pedestal corrected mean positions extracted from $N = 10^5$ light pulses. $\sigma_{\Delta\mathrm{mean}_i}$ are the corresponding uncertainties of the data points and μ is the average of all

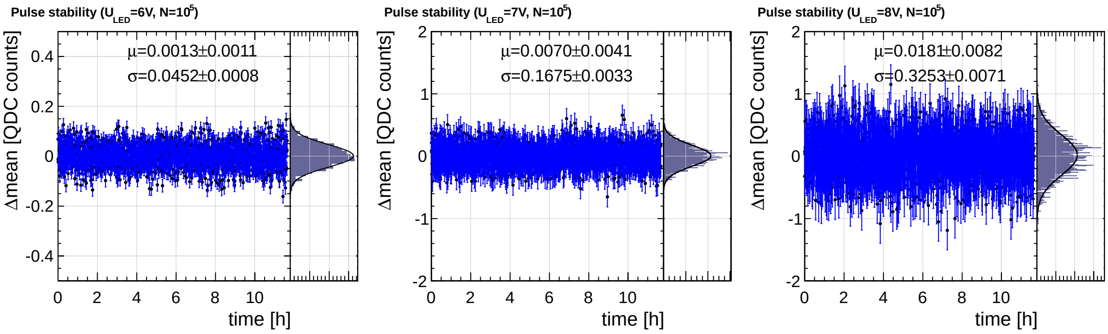

(a) **(b)** **(c)**

Figure 10.12: Δmean for to consecutive measurements of $N = 10^5$ light pulses for fixed LED voltages (a) $U_{\mathrm{LED1}} = 6\,\mathrm{V}$, (b) $U_{\mathrm{LED1}} = 7\,\mathrm{V}$, and (c) $U_{\mathrm{LED1}} = 8\,\mathrm{V}$. Note the different scales of the y-axis.

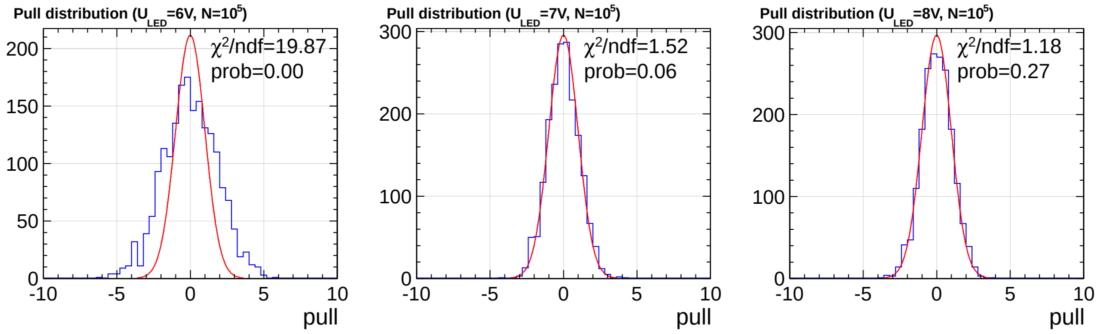

(a) **(b)** **(c)**

Figure 10.13: Pull distributions for measured Δmean for the LED voltages (a) $U_{\mathrm{LED1}} = 6\,\mathrm{V}$, (b) $U_{\mathrm{LED1}} = 7\,\mathrm{V}$, and (c) $U_{\mathrm{LED1}} = 8\,\mathrm{V}$.

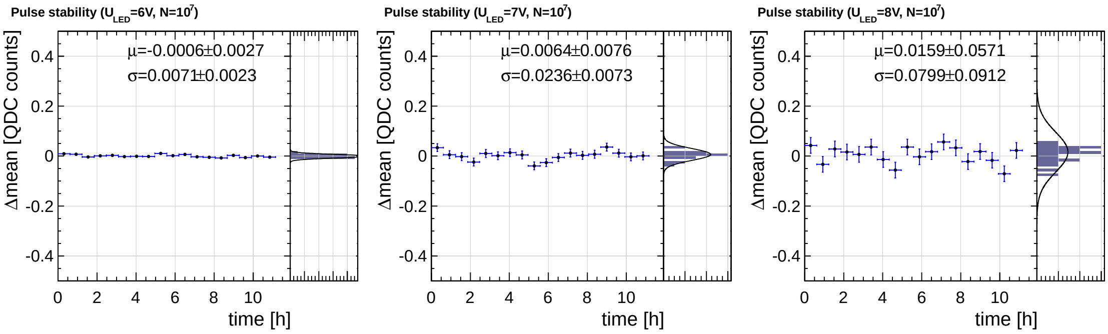

(a) (b) (c)

Figure 10.14: Δmean averaged over 100 data points for the LED voltages (a) $U_{\mathrm{LED1}} = 6\,\mathrm{V}$, (b) $U_{\mathrm{LED1}} = 7\,\mathrm{V}$, and (c) $U_{\mathrm{LED1}} = 8\,\mathrm{V}$.

$\Delta\mathrm{mean}_i$ quoted in Figure 10.12. For properly described data point errors, the pull distribution should be a Gaussian centered at $\mu_{\mathrm{pull}} = 0$ and a width $\sigma_{\mathrm{pull}} = 1$. In order to test this hypothesis, a Gaussian with the described properties is fitted to the distributions in Figure 10.13 and the χ^2/ndf as well as the fit probability is quoted. It is obvious that in the case of $U_{\mathrm{LED1}} = 7\,\mathrm{V}$ (Figure 10.13b) and $U_{\mathrm{LED1}} = 8\,\mathrm{V}$ (Figure 10.13c) the pull distribution follows very well the expected behaviour. For $U_{\mathrm{LED1}} = 6\,\mathrm{V}$, however, deviations can be observed (Figure 10.13a). These deviations originate from the very small signal at this voltage level corresponding to only a few QDC counts. In this case, in a considerably large fraction of the 10^5 triggered light pulses an empty event is observed. This of course affects the RMS of the QDC spectrum, which is used as data point error. As soon as the signal is large enough such that the fraction of empty events is small, this effect vanishes. This is already the case for $U_{\mathrm{LED1}} \geqslant 6.2\,\mathrm{V}$.

In order to achieve the envisaged precision in the DNL measurement, the uncertainty of the data points derived from $N = 10^5$ light pulses is much too large, as it has already been discussed in Section 9.5.1. To this end, we average over 100 individual measurements as shown in Figure 10.14. Thus, the spread of the data points gets small enough in order to be able to determine very small nonlinearities later on. It should be noticed that Δmean is very stable in time and consecutive pulses are well reproducible. The projections of the data points to the y-axis show a good compatibility of the mean value of the distribution with 0.

Finally, with this introduced measurement, we can also test the stability of a differential light pulse on top of a base pulse. For this purpose, the first LED voltage is set to $U_{\mathrm{LED1}} = 7\,\mathrm{V}$ and the second LED voltage to $U_{\mathrm{LED2}} = 6\,\mathrm{V}$. Δmean is determined by the measurements of $\mathrm{mean}_{1+2} - \mathrm{mean}_1$. The resulting data points are depicted in Figure 10.15a. It is clear that the data points are no longer centered around zero, but around the signal corresponding to the light pulse of LED 2 at $U_{\mathrm{LED2}} = 6\,\mathrm{V}$,

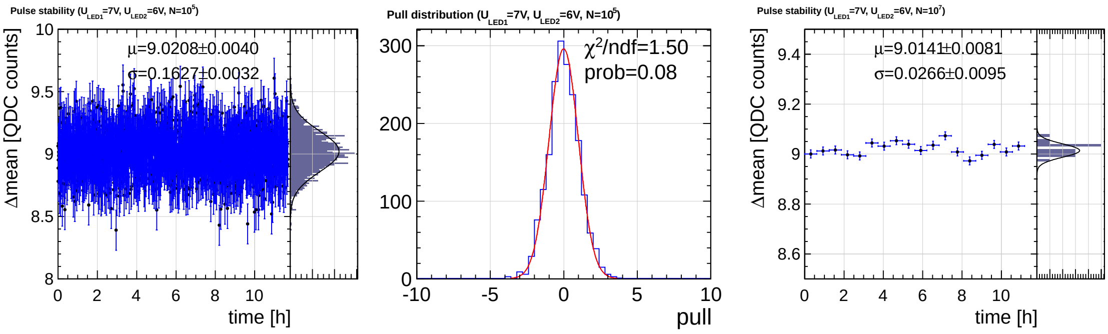

(a) **(b)** **(c)**

Figure 10.15: Stability of the differential light pulse of LED 2. $U_{\mathrm{LED1}} = 7\,\mathrm{V}$ and $U_{\mathrm{LED2}} = 6\,\mathrm{V}$ are chosen. (a) Δmean determined from raw data of $N = 10^5$ light pulses. (b) Corresponding pull distribution. (c) Averaged Δmean over 100 data points.

which are about 9 QDC counts. LED 2 has a slightly larger light yield compared to LED 1. The corresponding pull distribution is shown in Figure 10.15b and looks very adequate. The finally averaged data points are presented in Figure 10.15c, which proof a very stable differential pulse over time.

10.3.7 Concluding Remarks

As demonstrated in this section, all the characterisation measurements show that the designed LED driver as well as the proposed measurement setup meet very well the requirements for a DNL measurement which have been defined in Section 9.6:

Our setup consists of two independent light sources (cf. Section 10.3.5), which provide light pulses in the UV range well below 10 ns (cf. Section 10.3.1). Both LEDs easily cover the demanded light intensity range (cf. Section 10.3.3). It has been shown that filters can be used to adapt the intensity range of the LED to the needed dynamic range of the detector. In extensive studies it has been proven that the differential pulse stability is on absolute and differential levels in agreement with the design tolerances (cf. Section 10.3.4.1 and 10.3.6). In order to cancel drift effects originating from the base pulse drifts, the DNL measurement should be performed in both scan directions (cf. Section 10.3.4.2).

10.4 Nonlinearity Determination and Data Linearisation

The studies of the last section enable us to use the proposed setup for performing DNL measurements in this section.

10.4.1 DNL Measurements

The last measurement of Section 10.3.6 is already very close to the proposed DNL measurement. The only difference is that LED 1 is no longer kept fixed, but its intensity scans the dynamic range under study. In the following paragraphs, we show the results of different setup configurations in order to disentangle effects arising from the LED driver and the remaining setup.

10.4.1.1 Default Setup

In the default configuration we perform a DNL measurement, where the LED which provides the base pulse is scanned from $U_{\text{LED1}} = 6.4\,\text{V}$ to $U_{\text{LED1}} = 10\,\text{V}$. For each scan step we average over 100 determined mean positions of the QDC spectra resulting from $N = 10^5$ light pulses each, according to the described pedestal correction scheme. The voltage of the LED providing the differential signal is set to $U_{\text{LED2}} = 6\,\text{V}$.

The result is shown as blue data points in Figure 10.16a. On the x-axis, the mean position of the base pulse is displayed, whereas the y-axis shows the difference between the photomultiplier response of LED 1+LED 2 and LED 1. Repeating the measurement and reversing the scan direction gives the green data points in Figure 10.16a. Note that the data points of this run are taken in reversed order (right to left). It shows a very similar shape compared to the first measurement, but is slightly offset and differs in the slope. This dependence of the DNL measurements on the scan direction originates from the drift of the base pulse as discussed in Section 10.3.4.2. In order to cancel this effect, both data sets are averaged and displayed as black data points in Figure 10.16a. One observes a flat behaviour for small light intensities corresponding to mean positions of less than 1500 QDC counts. This indicates a very linear response of the setup in this range. As described in Section 9.2.2, from the measured Δmean the relative integrated nonlinearity can be derived. Therefore, the data points are fitted with a higher order polynomial, indicated as solid lines. The calculated relative INL is shown in Figure 10.16b. It underlines the conclusion that for small light intensities the nonlinearity is not changing significantly and, thus, in this regime the nonlinearity is small. At the end of the studied range the

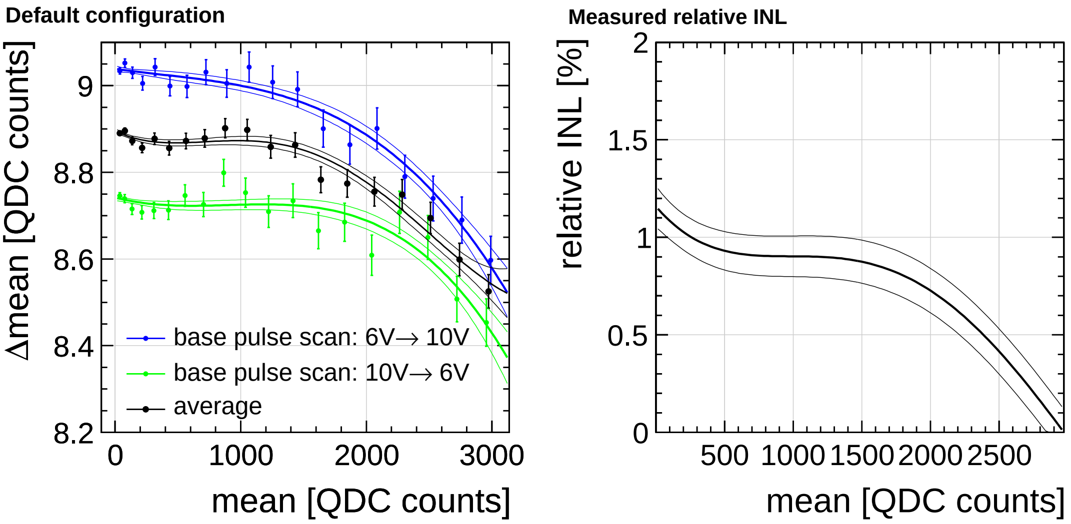

(a)

(b)

Figure 10.16: (a) Measured Δmean in the default configuration for different scan directions of the base pulse. (b) Determined relative INL.

nonlinearity converges to zero, which is due to the fact that the extracted mean position of the most intensive base pulse defines the reference point for the ideal linear response (see Section 9.1).

10.4.1.2 Exchanged LED Driver Setup

In order to exclude systematic effects of one specific LED, we repeat the measurement with exchanged LED driver boards and keep all other parameters unchanged. The results are shown in Figure 10.17a. It can be observed that the effective signal increase because of the differential light pulse is between $\Delta\text{mean} = 4.2 - 4.6$ QDC counts and, therefore, significantly smaller compared to the default configuration. This is due to the different light yields of the specific LEDs as mentioned earlier. Nevertheless, we find exactly the same behaviour as in the default configuration. These data suggest that the light intensity of the differential LED pulse does not affect the measured DNL significantly and already a larger differential pulse as in the default setup is sufficient to resolve the nonlinearity of the setup.

We again observe a difference between the two scan directions of the base pulse and, therefore, average the data points in order to cancel this effect. Comparing Figure 10.16a with Figure 10.17a proves that the visible effect with respect to the scan direction is indeed related to the base pulse drift and not to the differential pulse. This effect is equal on the absolute level in both measurements, although the differential light pulse intensity differs by about a factor of two between the measurements.

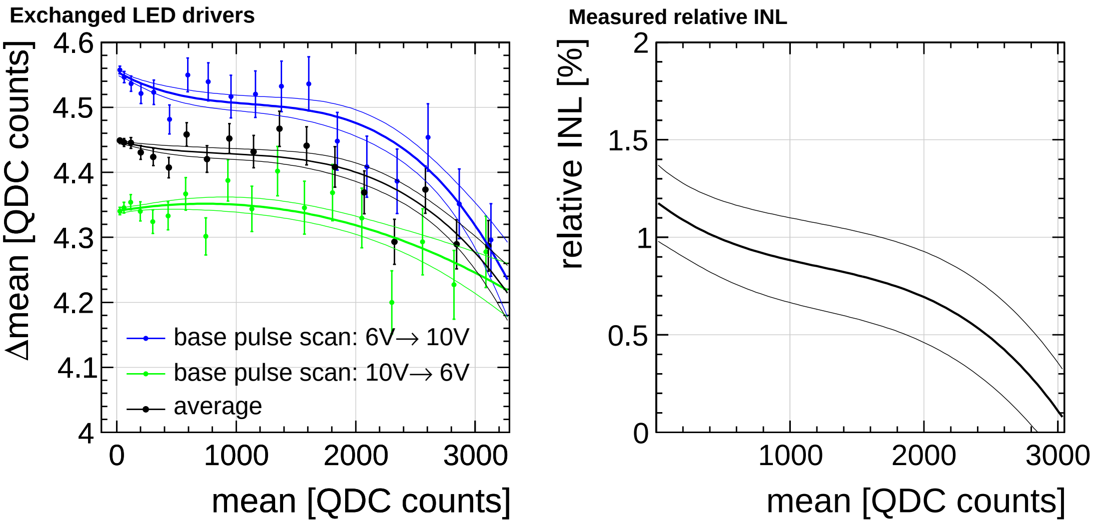

(a) (b)

Figure 10.17: (a) Measured Δmean in the exchanged LED driver configuration for different scan directions of the base pulse. The absolute scale is changed since different LEDs feature a different light yield at the same LED voltage. (b) Determined relative INL.

In Figure 10.17b, the derived nonlinearity from the averaged Δmean data points is depicted. A direct comparison of both extracted nonlinearities in the different configurations is displayed in Figure 10.19a. Both results agree very well within the errors.

10.4.1.3 Filter Setup

Finally, we change the operating range of the LED drivers in the default configuration by introducing an additional filter (filter *4*), which reduces the light intensity by a factor of about three (cf. Figure 10.7). The voltage level of LED 2, which provides the differential light pulse, is increased in order to compensate for the additionally introduced losses. This causes a signal increase Δmean due to the differential light pulse which is comparable to the default setup. In Figure 10.18a, the result of this configurations is presented. Note the reduced range of the x-axis, which is a direct result of the additional filter. The findings are again consistent with the measurements before. The derived relative nonlinearity is shown in Figure 10.18b and we find a overall nonlinearity of about 0.3%.

In order to make a reasonable comparison between all three configurations possible, the nonlinearities are calculated based on the same (reduced) range. Therefore, the last nine data points in the default and exchanged LED driver setup are neglected.

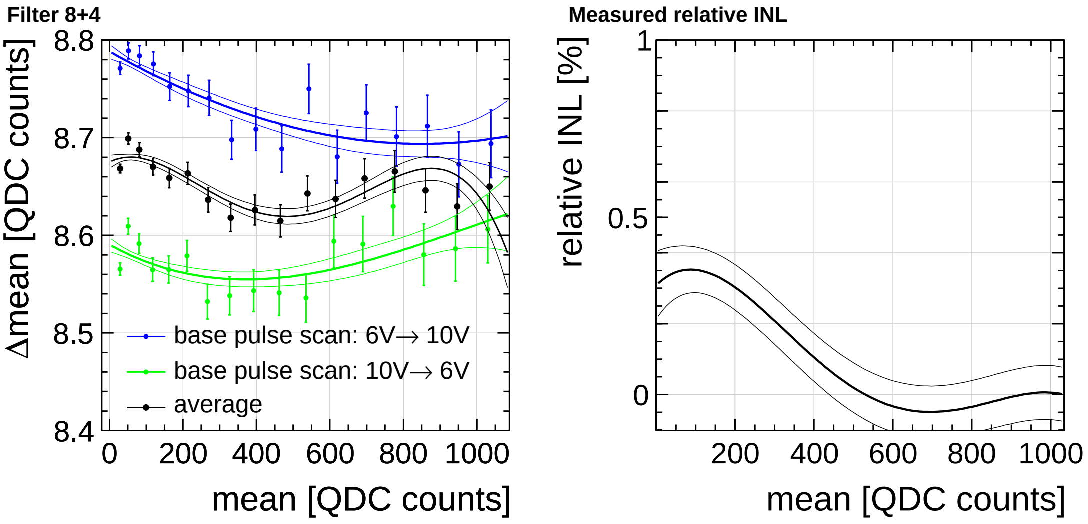

(a) (b)

Figure 10.18: (a) Measured Δmean in the default configuration with an additional filter for different scan directions of the base pulse. The additional filter reduces the intensity range of the LED driver. The voltage of LED 2 is tuned such that the response of the differential light pulse is comparable to the default configuration. (b) Determined relative INL.

Figure 10.19b shows the comparison between the different configurations. All results agree very well for light intensities corresponding to more than 500 QDC counts and we find for all measurements, a very small nonlinearity in this range. In the lower range small deviations can be observed, which can be traced back to an inaccurate functional description of the data points in the default and exchanged LED configuration. The larger error bands for the default and exchanged LED configuration arise mainly from the reduced number of data points for the fit.

Finally, from the measurements with these different configurations, we can conclude that the measured effects in Δmean can only originate from the measurement setup itself (photomultiplier, DAQ) and not from the LED driver. Thus, it allows us to use this method to linearise data.

10.4.2 Data Linearisation

For the data linearisation, a correction function has to be determined. As illustration, Figure 10.20a depicts the reconstructed signal response based on the relative nonlinearity shown in Figure 10.16b. Note that in the figure the nonlinearity is multiplied by a factor of ten in order to make the qualitative nonlinear behaviour

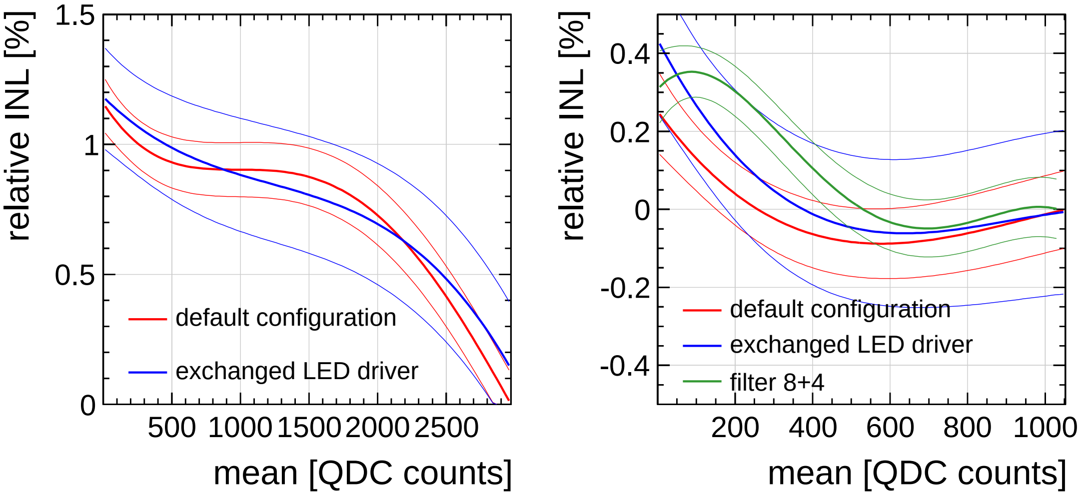

(a) (b)

Figure 10.19: Comparison between the determined nonlinearities in the large intensity range (a) and reduced intensity range (b). The nonlinearity in the reduced intensity range for the default and exchanged LED driver configuration has been derived by ignoring data points larger than 1100 QDC counts in order to get comparable results.

of the setup visible. The shape of the reconstructed nonlinearity is well in agreement with the expectation because the response flattens for larger input signal. In Figure 10.20b, the correction function is depicted, which has been derived from the nonlinearity measurement in the default setup.

For the test of the linearisation, a completely independent data set is used. Since there is no absolute calibration of the data available, it is also not possible to examine the power of the linearisation method on absolute scales. However, we can compare the measured Δmean in the raw data with the calculated Δmean after applying the correction function to the extracted mean positions. It has to be pointed clearly out that each measured mean position of the QDC spectra is corrected individually ($\text{mean}_{1,i}$, $\text{mean}_{1+2,i}$) and not Δmean. The comparison is displayed in Figure 10.20, where the red data points indicate the raw data and the green points the linearised data set. In both cases, a constant is fitted to the data points and the compatibility of the fit with the data points is quoted in terms of χ^2/ndf. For the raw data, we obtain $\chi^2/ndf = 6.4$, which clearly disfavours the hypothesis of a constant value describing Δmean over the whole range. In contrary, after linearisation, χ^2/ndf becomes 1.1. This shows that the linearity of the data set has significantly improved.

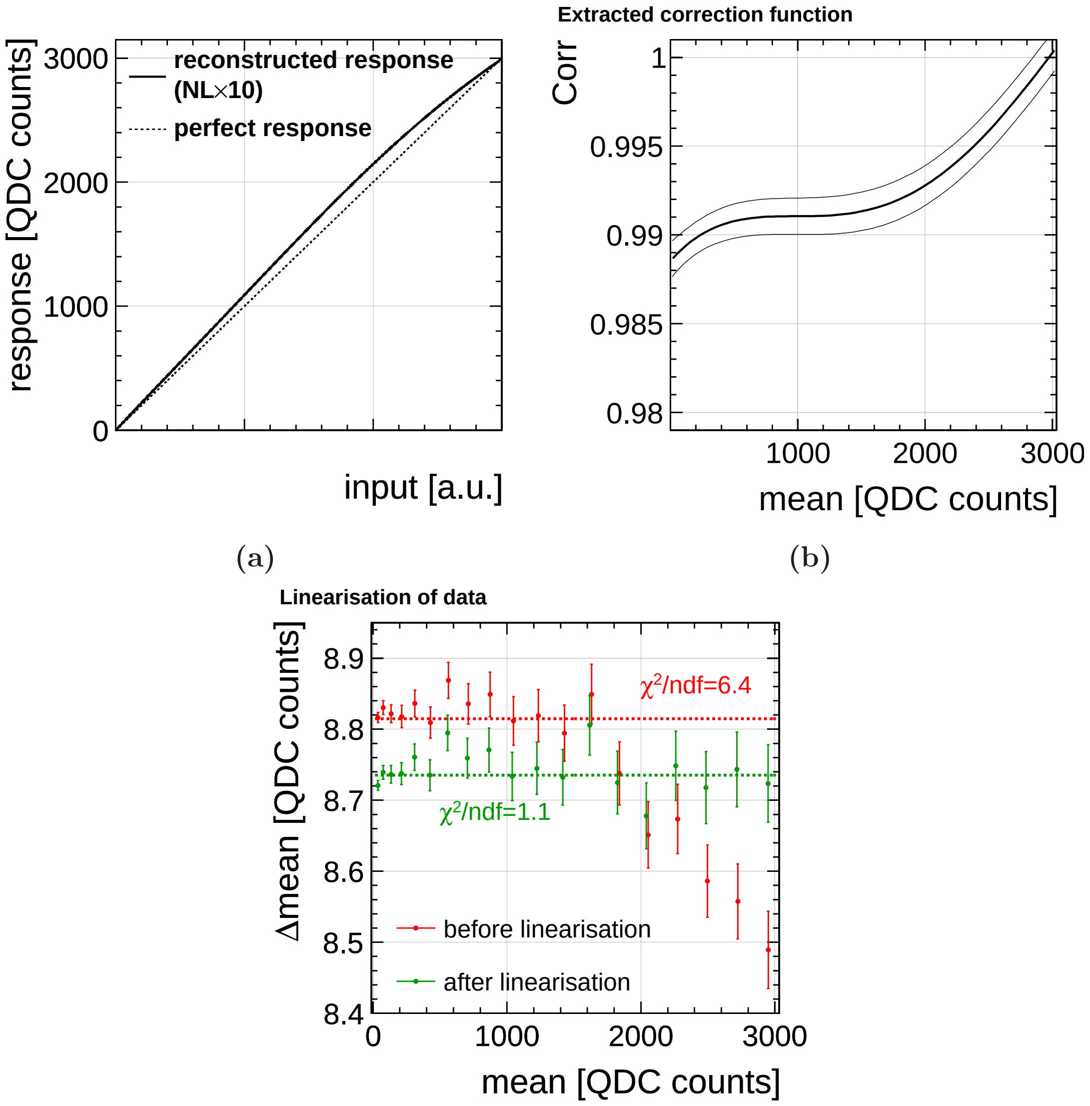

(a)

(b)

(c)

Figure 10.20: (a) Visualisation of the measured nonlinearity of Figure 10.16b. The nonlinearity is magnified by a factor of ten in order to make the qualitative shape visible. The absolute scale is not accessible with the presented method. (b) Correction function derived from Figure 10.16b. (c) Independent data set before (red) and after (green) linearisation.

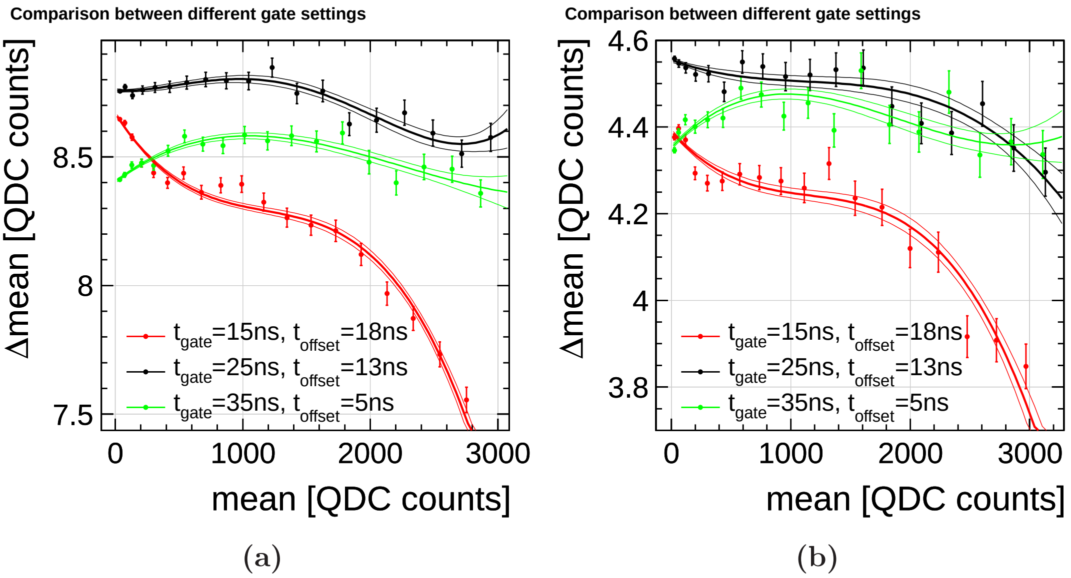

Figure 10.21: Dependence of the measured Δmean of the chosen gate in the default configuration (a) and in the exchanged LED driver configuration (b).

10.4.3 Gate Dependence

Finally, we investigate the dependence of the measured nonlinearity with respect to the chosen gate. For that purpose, three gate scenarios have been defined:

$$t_{\text{gate}} = 15\,\text{ns}, \quad t_{\text{offset}} = 18\,\text{ns} \tag{10.6}$$
$$t_{\text{gate}} = 25\,\text{ns}, \quad t_{\text{offset}} = 13\,\text{ns} \tag{10.7}$$
$$t_{\text{gate}} = 35\,\text{ns}, \quad t_{\text{offset}} = 5\,\text{ns} \tag{10.8}$$

Herein, (10.7) is the standard configuration used for the measurements presented up to now. In addition to this, a smaller and a larger gate is introduced. It should be noted that the chosen gate length in (10.6) is shorter than the minimal recommended gate in the QDC manual. This can in principle introduce additional nonlinear effects to the measurement originating from the QDC gate. The offset of the gate definitions is chosen in such a way that the signal of a light pulse corresponding to $U_{\text{LED}} = 7\,\text{V}$ is within the gate according to Figure 10.5b.

The resulting DNL measurement is depicted in Figure 10.21. We observe a strong dependence of the measured Δmean with respect to the used gate in the default (Figure 10.21a) as well as the exchanged LED configuration (Figure 10.21b). It is eye-catching that in both configurations qualitatively the same behaviour is visible: For the smallest gate (red), a steeply falling slope is measured, whereas with increasing gate the slope flattens out.

In order to investigate this effect, the time-dependent photomultiplier response to a light pulse is further analysed. Therefore, Figure 10.22a shows a fine-granular gate scan, in which the gate length (signal integration time) is increased in $\Delta t_{\text{gate}} = 1\,\text{ns}$ steps starting at $t_{\text{gate}} = 10\,\text{ns}$. For the default scan, the gate offset is set to $t_{\text{offset}} = 0\,\text{ns}$. U_{LED1} has been set to 7 V. The measured mean position of the signal in dependence of the closing time of the gate is plotted as black data points. Additionally, also the integrated signal for the base light pulse overlayed with the differential light pulse ($U_{\text{LED2}} = 6\,\text{V}$) is displayed as red data points. The integrated signal starts rising at around $t_{\text{gate}} = 20\,\text{ns}$ and reaches then a plateau as expected for a pulse integration. However, a blow-up of the same measurement (see Figure 10.22b) shows that the mean position varies slightly with the integration time also within the plateau. This originates from over- and undershoots of the time dependent signal reaching the QDC. The coloured horizontal lines in the figures show the closing time of the different defined gate scenarios using the same colour code as in Figure 10.21.

In the lower panel of Figure 10.22a, the differential signal response is depicted. The black data points show Δmean in a default scan, whereas the orange data points illustrate the effect of a gate offset by $t_{\text{offset}} = 18\,\text{ns}$ (corresponding to gate scenario (10.6)). Both measurements are compatible within the errors and, thus, the gate offset does not affect the measured Δmean in this configuration.

It is important to note that Δmean starts rising simultaneously with the base pulse and then stays rather constant. This indicates that the measurable additional signal due to the differential light pulse coincides with the signal of the pure base light pulse. On smaller scales (see Figure 10.22b), the measured Δmean varies and clearly depends on the signal integration time. This can be related to nonlinear effects introduced by the already mentioned under-/overshoots visible also in the absolute signal. Although for low light intensities, t_{offset} of the defined gate scenarios has no effect on the measured Δmean, however, the chosen gate length t_{gate} clearly has.

In Figure 10.22c, the same measurement is shown for a base pulse at $U_{\text{LED1}} = 10\,\text{V}$. It is visible that for the larger light intensity, the measured signal starts rising already by about $2 - 3\,\text{ns}$ earlier compared to Figure 10.22a. In the blow-up in the upper panel of Figure 10.22d, we can additionally observe that the integrated signal does not reach a proper plateau anymore. Eye-catching is the visible bump around $t_{\text{gate}} = 46\,\text{ns}$, which can be attributed to photomultiplier afterpulses triggered by the larger light intensity. For the measured Δmean in the lower panel of Figure 10.22c, we again observe a simultaneous rise with respect to the signal of the base pulse. Since the measured signal rises earlier, this time, a gate offset of $t_{\text{offset}} = 18\,\text{ns}$ (according to (10.6)) already cuts into the rising edge, which results in a lowered measured Δmean compared to the standard gate scan with $t_{\text{offset}} = 0\,\text{ns}$. This is clearly visible by comparing the orange and black data points in the lower panel of Figure 10.22c. Furthermore, due to the various (nonlinear) effects after the main

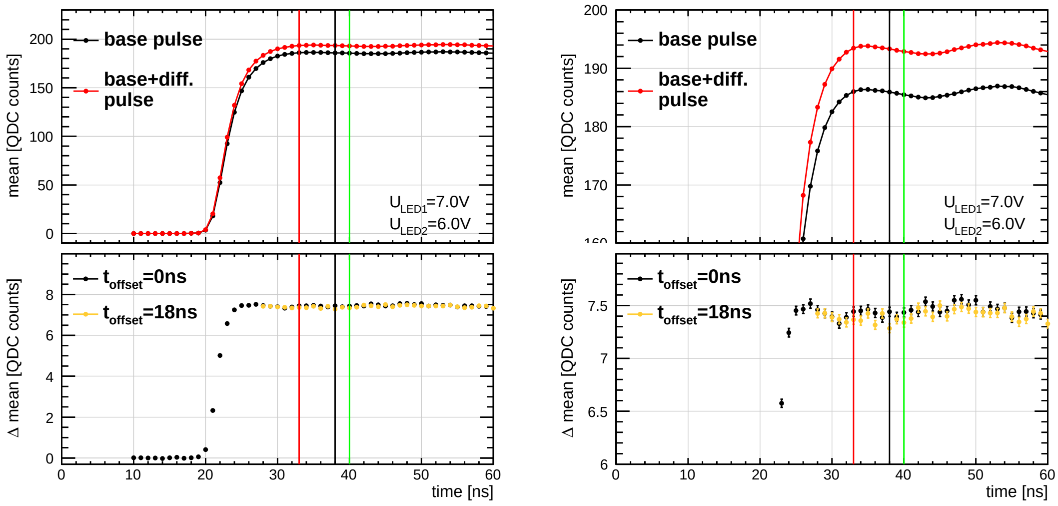

(a) $U_{\mathrm{LED1}} = 7\,\mathrm{V}$, full scale y-axes **(b)** $U_{\mathrm{LED1}} = 7\,\mathrm{V}$, zoomed y-axes

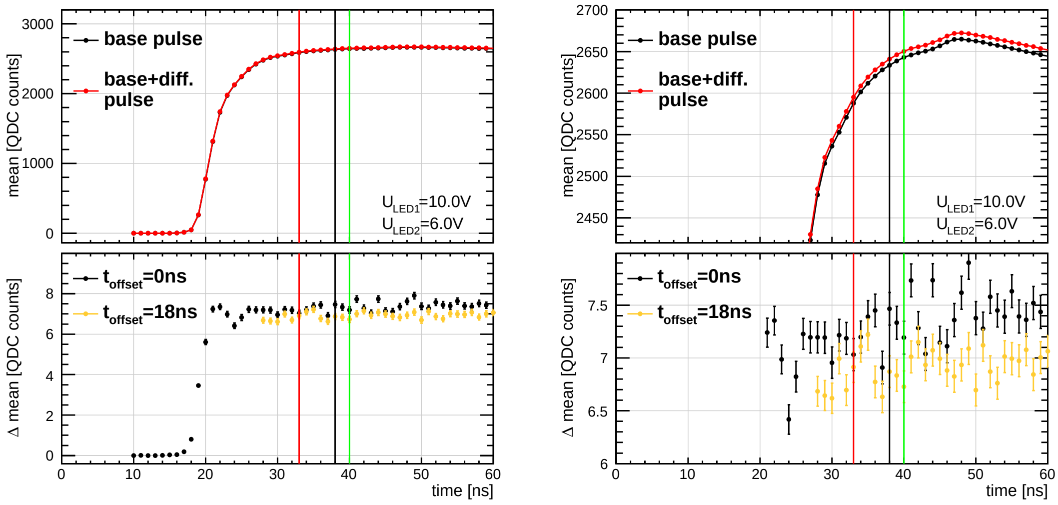

(c) $U_{\mathrm{LED1}} = 10\,\mathrm{V}$, full scale y-axes **(d)** $U_{\mathrm{LED1}} = 10\,\mathrm{V}$, zoomed y-axes

Figure 10.22: Top panels: Integrated signal in dependence of the integration time for the base pulse with $U_{\mathrm{LED1}} = 7\,\mathrm{V}/10\,\mathrm{V}$ (black) and an additional differential pulse with $U_{\mathrm{LED2}} = 6\,\mathrm{V}$. Bottom panels: Measured Δmean for different gate offsets. Coloured horizontal lines indicate different gate definitions.

light pulse (afterpulses, under-/overshoots), a strong dependence of the measured Δmean with respect to the actual integration time is observed.

Thus, the steeply falling behaviour of Δmean in Figure 10.21 for increasing light intensity in the smallest gate configuration (10.6) originates from the gate offset, which causes a cut into the actual signal. This effect increases with increasing light intensity, since we observe a continuous shift towards earlier signal pulses for larger base pulses. Therefore, it is an obvious consequence that in this gate definition the nonlinearity of the measured (integrated) signal increases significantly. The other studied gate scenarios do not show such a large discrepancy and the differences can be traced back to different integration times incorporating different nonlinear effects after the actual main pulse.

Summarising, we observe that the choice of the gate has a clear impact on the measured nonlinearity. This is reasonable taking into account the presented analysis of the time-dependent signal response. Therefore, we come to the conclusion that it is very important to perform the linearisation measurements under exactly the same condition as those for which the linearisation is aimed for.

10.5 Results

In the following paragraphs we give an overview of the most important achievements of this part of the thesis and compare the presented measurement method to other approaches studied in the same context. Finally, we comment on a possible calibration strategy applicable to the ILC polarimeters.

10.5.1 Achievements

We have presented the development of a setup for measuring the photomultiplier nonlinearities as proposed in Chapter 9. The properties of the setup as well as the developed LED driver have been extensively studied. It has been demonstrated that the LED driver is very well suited as a light source, producing short and stable light pulses. The observation of cross-talk between the two LEDs on the same driver board still needs further investigation. However, in the used setup this problem has been resolved by the use of a second independent LED driver board. Smaller modifications of the driver board could resolve this problem, as it will be mentioned later.

Finally, it has been possible to measure the nonlinearity of the photomultiplier in diverse configurations, using filters and exchanged hardware. We have obtained in all configurations consistent results such that systematic effects of the LED driver board can be ruled out. In the large light intensity range we have measured $\mathrm{INL}_{\mathrm{rel}} = 1.0 \pm 0.1\%$ in the middle of the dynamic range. This rather large nonlinearity is mainly driven by nonlinear effects arising from short and very intense light pulses at the upper end of the dynamic range, which defines the slope of the linear response. Leaving out the high intensity range and only considering smaller light intensities, gives $\mathrm{INL}_{\mathrm{rel}} = 0.4 \pm 0.1\%$ at maximum.

It has been demonstrated that this nonlinearity measurement can be utilised in order to correct a completely independent data set recorded under equal conditions. The corrected response shows afterwards a much more linear behaviour, which underlines the performance of this method. Finally, it has been observed that the integration time of the signal significantly influences the measured nonlinearity such that it is crucial to perform the linearisation measurements under the right conditions.

10.5.2 Comparison to Other Calibration Methods

In Reference [213], an earlier work on the measurement of photomultiplier nonlinearities is presented, focusing on different measurement methods:

In the “Pulse Length Method”, the nonlinearity of the photomultiplier response is determined by light pulses varied in their pulse length. In this method, an LED is pulsed directly with a constant voltage of $-5\,\mathrm{V}$ and the pulse length is increased in 5 ns steps from 30 ns to 150 ns. For each step $N = 10^7$ light pulses are recorded. This method assumes that the amount of light reaching the photomultiplier is proportional to the actual pulse length. Any deviation of the photomultiplier signal response from linear dependence of the pulse time is identified as nonlinearity of the photomultiplier. With this procedure a relative INL of $(0.5 \pm 0.05)\%$ has been found where a similar photomultiplier as in this thesis was in use. However, this photomultiplier has been operated at a larger high voltage of $U_{\mathrm{HV}} = -800\,\mathrm{V}$ and, therefore, the results cannot be compared directly. Furthermore, in the analysis of the time-dependent photomultiplier in this thesis we observed that the response to light pulses of different intensities has a strong influence on the nonlinear behaviour of photomultipliers. For this reason, it is to question whether the “Pulse Length Method” with its constant light intensity is suited to calibrate photomultipliers, which are going to be exposed to very short light signals of different intensities as it is the case in the planned polarimeters.

As a further method, the so-called “E158 Method” is discussed in Reference [213]. It uses two different LEDs which are pulsed directly with a voltage of $-5\,\mathrm{V}$, but with two different pulse lengths $t_1 = 50\,\mathrm{ns}$ and $t_2 = 150\,\mathrm{ns}$. By the use of different combinations of filters a differential nonlinearity has been extracted from the measurement of the response to LED 1, LED 2, and LED 1+LED 2 for each filter combination. The obtained results lie in the same range as determined with the “Pulse Length

Method". However, the used pulse lengths are one to two orders of magnitudes away from the actual light pulse lengths as expected at the ILC Compton polarimeters.

Therefore, the differential photomultiplier calibration method presented in this thesis, tests the linear response of the photomultiplier in a completely different operating range, which is much closer to the real measurement conditions in the polarimeters.

10.5.3 Implications on the Polarimeters at the ILC – Calibration Strategy

The planned Compton polarimeter at the ILC (see Section 8.1.3) consists of about 20 Cherenkov detector channels. According to Figure 8.6, a different number of Compton-scattered electrons/positrons is expected in the individual channels for the two different helicity configurations of the laser. Therefore, each channel features an individual dynamic range. Instead of operating all photomultipliers at the same high voltage, it could be beneficial to adapt the gain of the installed photomultipliers in each Cherenkov detector channel individually in such a way that the expected signal is stretched over the whole digitisation range of the QDC. Correspondingly, the light intensities of the LED driver boards, which are also located within each Cherenkov detector channel (see Figure 8.5b), need to be adapted to the same dynamic range. Although it has been shown in Figure 10.7 that the LED driver can cover a very large intensity range solely by tuning the LED voltage, it is however preferable to adjust the maximal light output with an appropriately chosen filter. In this way, the full voltage range is still available for the base pulse scan and fine tuning of the differential pulse.

Before commissioning of the polarimeters, the nonlinearity of each installed photomultiplier should be characterised to high precision. During operation a floating calibration scheme is conceivable, making use of the ILC specific beam structure: Between each bunch train at the ILC in the 5 Hz scheme, there is no signal in the Cherenkov detectors for about 199 ms. This time could be used for calibration measurements. In the current setup it would take about 12 hours for a full scan of the dynamic range in the needed precision. However, there is room for optimisation: In the current measurement, there are a lot of safety delays between LED voltages changes, which can easily be reduced. By increasing the QDC readout by a factor of two and switching to a more evolved LED trigger scheme (see Figure 10.23) it would be possible to measure 11940 DNL data points per second. Thereby, we assume that 80% of the inter-train time can be used for calibration purposes.

In this scheme, it would take about 14 minutes to acquire the envisaged number of measurements of $N = 10^7$ per scan step. Thus, a whole scan of the dynamic range consisting of 20 steps could be done in one direction in less than 5 h. However, as it has been already explained in Section 10.4.1, it is beneficial to perform scans always

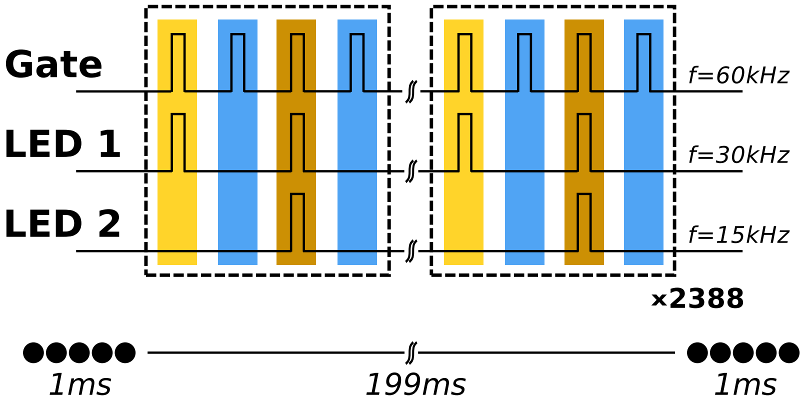

Figure 10.23: Possible trigger scheme for DNL measurements at the ILC. Between two bunch trains 2985 measurements of pedestal (blue), base light pulse (yellow), and base+differential (orange) pulse could be performed. This scheme allows for operating each LED with a constant frequency between the bunch trains. During a traversing bunch train both LEDs must not trigger.

in both directions in order to cancel drift effects. This can easily be incorporated in the floating calibration scheme. In order to implement the proposed floating scheme, a small modification of the LED driver board is necessary such that both LEDs can be triggered independently. As a side benefit, this could also solve the observed interdependence of the LEDs on one LED driver board. Finally, this scheme would allow for monitoring the time development of the nonlinearity of the setup on the time scales of some hours. As analysed in the “Pulse Length Method” in Reference [213], a noticeable change in the measured nonlinearity becomes visible on the time scale of a week. However, the nonlinearities determined with the differential pulse method of this thesis seem rather stable. Between the measurements displayed in Figure 10.19a, two weeks of full time operation of the photomultiplier have passed. Within the errors, no deviation can be identified. The determined nonlinearity in the filter configuration in Figure 10.19b has been measured four weeks after the default configuration. Here, small deviation can be observed. However, those deviations can most probably be attributed to the limited number of data points used for the determination of the nonlinearity in the default configuration for the reduced range in Figure 10.19b.

It has been shown that the precision in the determination of the nonlinearity derived in the differential pulse method is in the order of 0.1%. Therefore, the allowed error budget attributed to the uncertainty originating from the nonlinearity of the setup at the ILC Compton polarimeters is satisfied. Thus, it could be demonstrated that the investigated DNL method is well applicable in the future ILC Compton polarimeters.

11 Conclusions

The Standard Model of Particle Physics is a very convincing theory, however, due to several shortcomings it cannot be the final description of nature. Physics beyond the Standard Model is needed in order to give answers to the hierarchy problem, the evidence for dark matter, or the observation of neutrino masses and mixing, for instance. Supersymmetry could be one possible solution for solving the shortcomings of the Standard Model.

Therefore, we have investigated in this thesis a supersymmetric model with bilinearly broken R parity, which allows for an elegant introduction of neutrino masses and mixing into the Standard Model. At this, neutralinos mix with neutrinos and, thus, neutralinos can be utilised as probes of the neutrino sector at colliders. In particular, the decay of the lightest neutralino into Standard Model particles gives access to neutrino mixing parameters. As a study case, we focused on the determination of the atmospheric mixing angle θ_{23}, which is on tree level defined as the ratio of the two neutralino branching ratios $\mathrm{BR}(\widetilde{\chi}_1^0 \to W\mu)/\,\mathrm{BR}(\widetilde{\chi}_1^0 \to W\tau)$.

In order to study the neutralino decays, we have conservatively assumed only direct $\widetilde{\chi}_1^0$-pair production, as further SUSY production modes would just increase the number of available neutralino candidates for the study. For this production mode, a simplified model has been defined which reduces the large number of SUSY parameters. In the case of the neutralino being a bino, two relevant parameters have been identified, namely $m_{\widetilde{\chi}_1^0}$ as well as $m_{\widetilde{e}_R}$. The remaining masses have been set to the multi-TeV scale, which is consistent with the current limits of LHC SUSY searches. The bRPV parameters of the model have been fitted to neutrino-oscillation data and are therefore fixed.

For one specific benchmark point ($m_{\widetilde{\chi}_1^0} = 98.5\,\mathrm{GeV}$, $m_{\widetilde{e}_R} = 280.0\,\mathrm{GeV}$) a full detector simulation at a center-of-mass energy of $\sqrt{s} = 500\,\mathrm{GeV}$ has been performed, taking into account a highly detailed ILD model as well as realistic ILC beam parameters. The choice of the benchmark point is conservative, since the neutralino mass is chosen to be close to the W/Z-boson mass, which is the region where the main Standard Model background is localised.

We have developed a model-independent event selection for disentangling the LSP decays $\widetilde{\chi}_1^0 \to W\mu$ and $\widetilde{\chi}_1^0 \to W\tau$. In the $\mu\mu$ selection class the LSP mass could be measured with an uncertainty of $\delta(m_{\widetilde{\chi}_1^0}) = (40(\mathrm{stat.}) \oplus 35(\mathrm{syst.}))\,\mathrm{MeV}$ for an integrated luminosity of $\int L\mathrm{d}t = 500\,\mathrm{fb}^{-1}$. The obtained selection efficiencies at the benchmark point have been used to estimate the signal significance in the parameter plane of the simplified model. It has been shown that for the $\mu\mu$ selection class, for instance, the bRPV $\tilde{\chi}_1^0$ decay can be observed on a 5σ-level for selectron masses of $m_{\tilde{e}_R} = 1.5 - 2.0\,\mathrm{TeV}$ and a large range of LSP masses. An increased positron beam polarisation to 60% extends the sensitivity reach in the selectron mass parameter of up to 200 GeV.

The ratio $\mathrm{BR}(\tilde{\chi}_1^0 \to W\mu)/\,\mathrm{BR}(\tilde{\chi}_1^0 \to W\tau)$ could be determined to a precision of 2.9% for an integrated luminosity of $\int L\mathrm{d}t = 500\,\mathrm{fb}^{-1}$. This result has been reinterpreted as measurement of the atmospheric neutrino mixing angle, which results in a final experimental uncertainty of $\delta\sin^2(\theta_{23})/\sin^2(\theta_{23}) = 1.5\%$. Depending on the knowledge of the remaining SUSY particle spectrum, additional parametric uncertainties between $7 - 17\%$ have to be considered due to loop corrections. Thus, the determination of the atmospheric mixing angle is completely limited by these uncertainties. However, the achievable precision is sufficient in order to be comparable with results of current neutrino oscillation experiments. An agreement could indicate that bRPV SUSY is the realised mechanism which introduces neutrino masses and mixings. Furthermore, this completely independent neutrino parameter measurement could help to resolve the octant discrimination of θ_{23} in the case of nonmaximal mixing.

This study has demonstrated the benefits of beam polarisation in order to suppress backgrounds and enhance signal processes. At this, the precise knowledge of the beam polarisation is as important as the luminosity or beam energy. Therefore, two Compton polarimeters per beam measure the beam polarisation with an envisaged precision of 0.25%. In order to achieve this design goal, the detector linearity of the used Cherenkov detectors have to be better than 0.5%, which makes necessary a precise measurement of the detector nonlinearity, especially of the involved photomultipliers.

In the second part of this thesis, we have developed a differential linearisation method for a photomultiplier and its associated readout chain. The linearisation method utilises two LED light pulses: a tuneable base light pulse, which can scan the whole dynamic range of the photodetector and an additional constant light pulse, which probes the differential detector response in dependence of the base pulse detector response. It has been deduced that for this proposed method, the requirements for the light source is considerably reduced since no absolutely calibrated light source is necessary.

We have demonstrated the working principle of the linearisation method in a Monte-Carlo simulation and have studied the design criteria for a real measurement setup. Based on this results, an LED driver and a test stand have been developed. In extensive test measurements, it has been proven that all the design criteria are fulfilled: It could be shown that the light pulses are well below 10 ns and that the required light intensity range is covered. The drift of the signal response is below 0.5% on time scales of a typical linearisation measurement. For LED voltage changes, a trailing intensity response has been observed, which suggests to perform DNL measurements always in two scan directions in order to average out possible systematic effects.

Finally, the relative nonlinearity of the photomultiplier has been measured in different setups with the proposed differential method. All configurations have shown consistent results such that systematic LED driver effects could be ruled out. Depending on the analysed dynamic range of the photomultiplier, we find relative nonlinearities of 1.0% ± 0.1% for larger light intensities and 0.4% ± 0.1% in a reduces intensity range. This measurement has been used to calculate a correction function which has been applied to an independent data set. It could be shown that the linearity of this data set has significantly improved after the linearisation.

The design of the LED driver as well as the developed method is well suited to be used in the Cherenkov detectors of the ILC polarimeters even during a physics run. The time in-between two bunch trains can be used for continuous calibration measurements such that a complete DNL measurement data set can be obtained for one scan direction in approximately five hours . This, in turn, allows for a sliding nonlinearity monitoring and correction during the ILC data taking.

Here ends one high precision story at the ILC, but there are many more to discover.

Acknowledgements

Finally, I would like to thank a few people who played an important role for me in the last years and who made this work possible:

First of all, I want to thank *Jenny List* for giving me the chance to do my PhD in her group and for offering me two very interesting topics. I am very grateful for all the enlightening discussions over the last three and a half years. I have really learned a lot and I always felt very well advised. I am especially thankful for the unreserved support during the last weeks of the thesis writing.

Furthermore, I would like to thank *Peter Schleper*, *James Brau*, *Caren Hagner*, and *Georg Steinbrück* for agreeing to be part of my PhD committee.

Connected to this thesis, there are a few people I want to thank:

- *Werner Porod*, for many enlightening discussions about bRPV SUSY and for providing my with a tailored `SPheno` version for the simplified model study
- *Florian Staub*, who advised me in setting up `Sarah` properly and helped with debugging the bRPV model file.
- the DESY electronics group, especially *Mathias Reinecke*, for designing the LED driver and for his patience in explaining all kinds of questions about electronics to me
- the ILC software team, in particular *Frank Gäde*, who has always been willing to support me in case of software related problems
- *Bernd Bayer*, who constructed the mechanical part of the measurement setup

Without your help, this thesis would not have been possible. Thank you so much!

I would also like to thank my two mentors, *Karsten Büßer* and *Marcel Stanitzki*, for always giving me good advises and for having an open door for questions, discussions, or simply a chat.

I am very grateful to all my colleagues of the *FLC* group for the very friendly and productive working atmosphere. In particular, I would like to thank

- *Hale Sert*, for being such a nice office mate

- *Annika Vauth*, for sharing the lab with me and for many inspiring discussions
- *Klaus Zenker*, for being a virtuoso on the trumpet and for his willingness to play music together
- *Andrea Schrader*, for helping me with all kinds of administrative issues and for just being the "good soul" of the FLC group
- *Moritz Beckmann*, for our countless discussions about physical, political, and private topics. I found in you not just an office mate, but also a good friend.
- *Madalina Chera*, for our extended whiteboard discussions, your friendly manner, and especially for our friendship

During my time at DESY, I shared the office with quite some people: *Daniela Käfer*, *Christoph Bartels*, *Christian Helebrant*. You all made the office a place I liked to be. Thank you for this!

A big thank goes to my friends, who accepted my limited time over the last months. In particular, I would like to mention *Patrick*. Thank you for being such a longstanding friend.

Of course, I want to give thanks to my family. In particular I want to mention my *mother* and *Wolfgang*, who have always unreservedly supported me and my *father* and *Petra*, who have always believed in me.
Without your love, your support, and your confidence I would certainly not have achieved all of this. It helps a lot to know that you are always there for me!

Finally, my biggest thank goes to *Julia*. Not just for your tireless proof-reading of this thesis, but for all the great years together with you! I am so grateful that we met each other and that I can always count on you.

A Spinors

In supersymmetry spinors play an important role. For this reason, we introduce the different types of spinors and their transformation properties in this chapter. Thereby, we follow very closely the introduction in Reference [36].

A.1 Helicity and Chirality

Let us start with the Dirac equation

$$E\Psi = (\alpha \cdot \mathbf{p} + \beta m)\Psi, \tag{A.1}$$

with

$$\alpha = \begin{pmatrix} \sigma & 0 \\ 0 & -\sigma \end{pmatrix} \qquad \text{and} \qquad \beta = \begin{pmatrix} 0 & \mathbf{1} \\ \mathbf{1} & 0 \end{pmatrix}, \tag{A.2}$$

where σ are the Pauli matrices. This choice of representation determines the γ matrices to

$$\gamma = \begin{pmatrix} 0 & -\sigma \\ \sigma & 0 \end{pmatrix} \qquad \text{and} \qquad \gamma_5 = \begin{pmatrix} \mathbf{1} & 0 \\ 0 & -\mathbf{1}. \end{pmatrix}. \tag{A.3}$$

Herein, Ψ is a four-component Dirac spinor, which can be written as

$$\Psi = \begin{pmatrix} \psi \\ \chi \end{pmatrix}, \tag{A.4}$$

with ψ and χ being two-component Weyl spinors. One has to note that ψ and χ are different objects. They transform differently under Lorentz transformation, as will be shown in a moment.

In this nomenclature, Equation (A.1) can be decomposed into

$$(E - \sigma \cdot \mathbf{p})\psi = m\chi \tag{A.5}$$

$$(E + \sigma \cdot \mathbf{p})\chi = m\psi. \tag{A.6}$$

The result is a system of coupled equations. In the massless limit ($m \to 0$, $E \to |\mathbf{p}|$), however, the equations decouple and one can easily derive

$$\frac{\sigma \cdot \mathbf{p}}{|\mathbf{p}|}\psi = +\psi \qquad \text{and} \qquad \frac{\sigma \cdot \mathbf{p}}{|\mathbf{p}|}\chi = -\chi, \tag{A.7}$$

which means that ψ and χ are eigenstates of the operator $\sigma \cdot \mathbf{p}/|\mathbf{p}|$ with the eigenvalues ± 1. This is called the "helicity" of the fermion.

In the general, massive case one can find that ψ and χ are eigenstates of γ_5, which is also called the "chirality" of a spinor.

$$\gamma_5 \begin{pmatrix} \psi \\ 0 \end{pmatrix} = + \begin{pmatrix} \psi \\ 0 \end{pmatrix} \qquad \text{and} \qquad \gamma_5 \begin{pmatrix} 0 \\ \chi \end{pmatrix} = - \begin{pmatrix} 0 \\ \chi \end{pmatrix} \tag{A.8}$$

By definition the eigenvalue $+1$ is referred to as "right-handed" and -1 to "left-handed". Thus, ψ represents the right-handed and χ the left-handed part of the Dirac spinor.

One can define an operator $P_{\mathrm{R,L}}$ which projects out the specific part of the Dirac spinor

$$P_{\mathrm{R}} = \left(\frac{1+\gamma_5}{2}\right) = \begin{pmatrix} 1 & 0 \\ 0 & 0 \end{pmatrix} \tag{A.9}$$

$$P_{\mathrm{L}} = \left(\frac{1-\gamma_5}{2}\right) = \begin{pmatrix} 0 & 0 \\ 0 & 1 \end{pmatrix}. \tag{A.10}$$

A.2 Transformation Properties of Weyl Spinors

A.2.1 Lorentz Transformation

In Reference [226, p. M.6], it is shown that ψ and χ are two different representations of the Lorentz group and, thus, have different Lorentz transformations properties. We assume a general, infinitesimal Lorentz transformation consisting of a three-dimensional rotation

$$E \to E' = E, \quad \mathbf{p} \to \mathbf{p}' = \mathbf{p} - \epsilon \times \mathbf{p}, \tag{A.11}$$

where ϵ are infinitesimal rotation parameters, and an infinitesimal Lorentz boost

$$E \to E' = E - \eta \cdot \mathbf{p}, \quad \mathbf{p} \to \mathbf{p}' = \mathbf{p} - \eta E, \tag{A.12}$$

where the vector η parametrises the boost. Then, the spinors transform like

$$\psi \to \psi' = (1 + i\epsilon \cdot \sigma/2 - \eta \cdot \sigma/2)\psi = V\psi \tag{A.13}$$

$$\chi \to \chi' = (1 + i\epsilon \cdot \sigma/2 + \eta \cdot \sigma/2)\chi = W\chi \tag{A.14}$$

It can be shown that $W = V^{-1\dagger} = V^{\dagger^{-1}}$. As one can see, both Weyl spinors behave equally under three-dimensional rotation, but differently under Lorentz boosts. It is very essential to know the transformation properties of ψ-type and χ-type spinors in order to distinguish them from each other.

A.2.2 Transformation of χ-type Spinor into ψ-type Spinor

In a next step, we want to find a recipe for the transformation of a χ-type spinor into a ψ-type spinor. For this purpose, we complex conjugate Equation (A.14)

$$\chi^{*\prime} = (1 - i\epsilon \cdot \sigma^*/2 + \eta \cdot \sigma^*/2)\chi^* \tag{A.15}$$

and make use of the properties of the Pauli matrices $\sigma_1^* = \sigma_1$, $\sigma_2^* = -\sigma_2$, $\sigma_3^* = \sigma_3$. In order to arrive at a global minus sign in front of σ, we multiply (A.15) with σ_2 and make use of the anti-commuting property $\{\sigma_1, \sigma_2\} = \{\sigma_3, \sigma_2\} = 0$.

$$\sigma_2\chi^{*\prime} = \sigma_2(1 - i\epsilon \cdot \sigma^*/2 + \eta \cdot \sigma^*/2)\chi^* \tag{A.16}$$

$$= (1 + i\epsilon \cdot \sigma/2 - \eta \cdot \sigma/2)\sigma_2\chi^* \tag{A.17}$$

$$= V\sigma_2\chi^* \tag{A.18}$$

This last line let us draw a very important conclusion: It tells us that $\sigma_2\chi^*$ transforms as a ψ-type spinor, referring to (A.13). Therefore, we can define a ψ-type spinor derived from a χ-type spinor

$$\psi_\chi \equiv i\sigma_2\chi^*. \tag{A.19}$$

The factor i is introduced by convention, but does not change the transformation behaviour. Equivalently, it can be shown that a similar expression for χ_ψ can be obtained, which reads

$$\chi_\psi \equiv -i\sigma_2\psi^*. \tag{A.20}$$

A.3 Construction of Four-Spinors

A.3.1 Majorana Fermions

With Equations (A.19) and (A.20) we are now able to describe correctly transforming four-spinors by only using one type of Weyl spinor. This leaves us with the interesting possibility to use only one Weyl spinor twice in one Dirac spinor, which halves its number of degrees of freedom:

$$\Psi_{\mathrm{M}}^{\psi} = \begin{pmatrix} \psi \\ -i\sigma_2\psi^* \end{pmatrix} \tag{A.21}$$

If we introduce the charge conjugation operator

$$C_0 = -i\gamma^2 = \begin{pmatrix} 0 & i\sigma_2 \\ -i\sigma_2 & 0 \end{pmatrix} \tag{A.22}$$

we can probe the behaviour of that kind of spinor under charge conjugation:

$$\Psi_{\mathrm{M,C}}^{\psi} = C_0(\Psi_{\mathrm{M}}^{\psi})^* = \Psi_{\mathrm{M}}^{\psi}. \qquad (\text{note that } \sigma_2^2 = \mathbf{1}) \tag{A.23}$$

As we see, the particle, described by Ψ_{M}^{ψ} is its own anti-particle. It is a so-called Majorana fermion. Thereby, the charge-self-conjugate property accounts for the reduced number of degrees of freedom. The spinor Ψ_{M}^{χ} , which can be constructed analogously, has the same properties.

A.3.2 Dirac Fermions

In context of supersymmetry, each Standard Model fermion is accompanied by two complex scalar particles – one per each chirality state. That is the reason, why Weyl spinors are of fundamental importance in the theoretical formulation of supersymmetry. Hereby, usually χ-type/ left-type spinors are used (which stresses the importance of left-type spinors for the electroweak interaction). However, Standard Model fermions of course hold a right component as well. Fortunately we already know, how to re-express right spinors by left-spinors.

Let us consider the Dirac spinor of an electron field, for instance:

$$\Psi^{(e)} = \begin{pmatrix} \psi^{(e^-)} \\ \chi^{(e^-)} \end{pmatrix} \equiv \begin{pmatrix} e_R \\ e_L \end{pmatrix} \tag{A.24}$$

We can now use the left-transforming component of the charge conjugate of e^- to write down a general electron Dirac spinor – this time using only left-type Weyl spinors. This is possible because the degrees of freedom of a Dirac spinor (in contrast to a Majorana spinor) comprise the charge conjugate state of e^-.

$$\Psi^{(e)} = \begin{pmatrix} i\sigma_2\chi^{(e^+)^*} \\ \chi^{(e^-)} \end{pmatrix} \equiv \begin{pmatrix} \chi^{(e^+)^{\mathrm{c}}} \\ \chi^{(e^-)} \end{pmatrix} \equiv \begin{pmatrix} \overline{e}_L \\ e_L \end{pmatrix} \tag{A.25}$$

B Les Houches Input Files

B.1 mSUGRA Point

```
Block MODSEL  # Select model
 1     1      # mSUGRA

Block SMINPUTS         # Standard Model inputs
 1      1.27934000E+02 # alpha_em^-1(MZ)^MSbar
 2      1.16639000E-05 # G_mu [GeV^-2]
 3      1.18470000E-01 # alpha_s(MZ)^MSbar
 4      9.11876000E+01 # m_Z(pole)
 5      4.19000000E+00 # m_b(m_b), MSbar
 6      1.72700000E+02 # m_t(pole)
 7      1.77682000E+00 # m_tau(pole)

Block MINPAR  # Input parameters
 1    220     # m0
 2    250     # m12
 3    10      # tanb
 4    1       # sign(mu)
 5    -300    # A0

Block SPhenoInput       # SPheno specific input
 1    0       # error level
 2    0       # if =1, then SPA conventions are used
11    1       # calculate branching ratios
12    0       # write only branching ratios larger than this value
22    500     # c.m.s. energy
23    0.8     # value gives degree of polarisation for e- beam
24   -0.3     # value gives degree of polarisation for e+ beam
90      1     # add R-parity
91      1     # fit neutrino data
93      1     # calculate cross-sections
```

B.2 Generic Model Point

```
 BLOCK MODSEL
 1    0         # MSSM (0=(general MSSM), 1=(mSUGRA MSSM), ...)
 3    0         # MSSM (0=(MSSM), 1=(NMSSM), ...)
 4    0         # generic RPV (0=(no RPV), 1=(RPV?))
                # see BLOCK SPHENOINPUT for actual bRPV switch

BLOCK SMINPUTS
 1    1.27931432E+02  # alpha_em^-1(MZ)^MSbar
 2    1.16639000E-05  # G_mu [GeV^-2]
 3    1.19000000E-01  # alpha_s(MZ)^MSbar
 4    9.12000000E+01  # m_Z(pole)
 5    4.20000000E+00  # m_b(m_b), MSbar
 6    1.73300000E+02  # m_t(pole)
 7    1.77710000E+00  # m_tau(pole)

BLOCK MINPAR
 3    10        # tanb
 4    1         # sign(mu)

BLOCK EXTPAR
 1     100.15   # M1
 2     3500     # M2
 3     3500     # M3

11    -3750     # ATOP
12     0        # ABOT
13     0        # ATAU

23     3500     # MU
26     3500     # M_A, pole mass

31     3000     # M_eL
32     3000     # M_muL
33     3000     # M_tauL
34     247.5    # M_eR
35     3000     # M_muR
36     3000     # M_tauR

41     3000     # M_q1L
42     3000     # M_q2L
```

```
43      3000      # M_q3L
44      3000      # M_uR
45      3000      # M_cR
46      3000      # M_tR
47      3000      # M_dR
48      3000      # M_sR
49      3000      # M_bR

BLOCK SPHENOINPUT
 1      -1        # Error level
 2       0        # SPA Convention
11       1        # Branching ratios
12       0        # write only branching ratios larger than this value
13       1        # h -> V V* without folding
22     500        # c.m.s. energy
23     0.8        # value gives degree of polarisation for e- beam
24    -0.3        # value gives degree of polarisation for e+ beam
90       1        # add R-parity
91       1        # fit neutrino data
93       1        # calculate cross-sections
```

C Nonlinear Transfer Function for the NL Simulation

The transfer function $\mathrm{T}(x)$ is used to nonlinearise a detector signal in the MC simulation. In order to minimise any bias of a chosen transfer function on the nonlinearity analysis, this transfer function can be randomly generated. $\mathrm{T}(x)$ is defined for $x \in [0;1]$ and is a normalised fourth-order polynomial parametrised as

$$\mathrm{T}(x) = \frac{f(x) \cdot x}{f_{\max}}, \tag{C.1}$$

with

$$f(x) = a + bx + cx^2 + dx^3 \tag{C.2}$$

and

$$f_{\max} = f(1) = a + b + c + d. \tag{C.3}$$

The relative integrated nonlinearity of $\mathrm{T}(x)$ is

$$\mathrm{INL_{rel}} = \frac{\mathrm{T}(x) - x}{x} = \frac{f(x)}{f_{\max}} - 1 \tag{C.4}$$

and, thus, the maximum relative nonlinearity can be derived by determining the extrema of this function.

$$\frac{\mathrm{d}}{\mathrm{dx}} \mathrm{INL_{rel}}(x) \propto \frac{\mathrm{d}}{\mathrm{dx}} f(x) = b + 2cx + 3dx^2 \overset{!}{=} 0 \tag{C.5}$$

$$\Rightarrow x_{1,2} = \frac{1}{3d} \left(-c \pm \sqrt{c^2 - 3bd} \right) \tag{C.6}$$

In addition to the two extrema, also the relative integrated nonlinearity at the borders of the defined range of $\mathrm{T}(x)$ are of interest. By definition, $\mathrm{INL_{rel}}(1)$ vanishes and $\mathrm{INL}_{\mathrm{rel}}(0) = a/f_{\max} - 1$. As long as $x_{1,2}$ are located in the defined range of $\mathrm{T}(x)$, the maximal relative integrated nonlinearity becomes

$$\mathrm{INL}_{\mathrm{rel}} = \max_{x \in \{0, x_1, x_2\}} \mathrm{INL}_{\mathrm{rel}}(x). \tag{C.7}$$

In order to find a random transfer function $\mathrm{T}(x)$ with a given $\mathrm{INL}_{\mathrm{rel}}$, the parameters of $\mathrm{T}(x)$ are randomly varied between $[0; 1]$ for a and $[-1; 1]$ for b, c, d until the aspired nonlinearity is reached within a certain tolerance.

Figure C.1 (Figure C.2) show a set of 100 transfer functions $\mathrm{T}(x)$ and the corresponding $\mathrm{INL}_{\mathrm{rel}}(x)$, which all feature no (one) extremum in the defined range and a relative integrated nonlinearity of about 0.8% (2%).

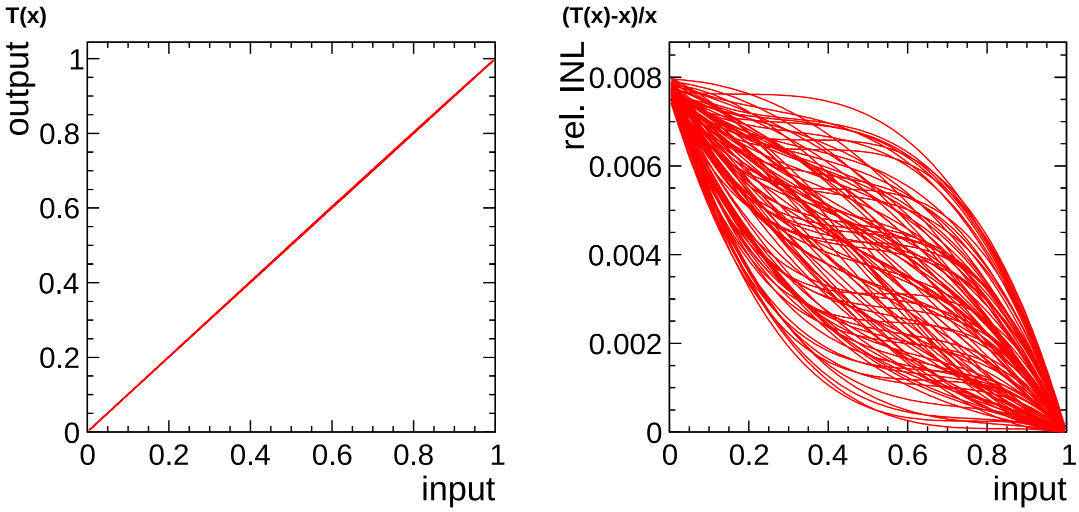

Figure C.1: Family of curves all featuring a maximal relative integrated nonlinearity of $\mathrm{INL}_{\mathrm{rel}} = 0.8\%$ and no extremum in the defined range.

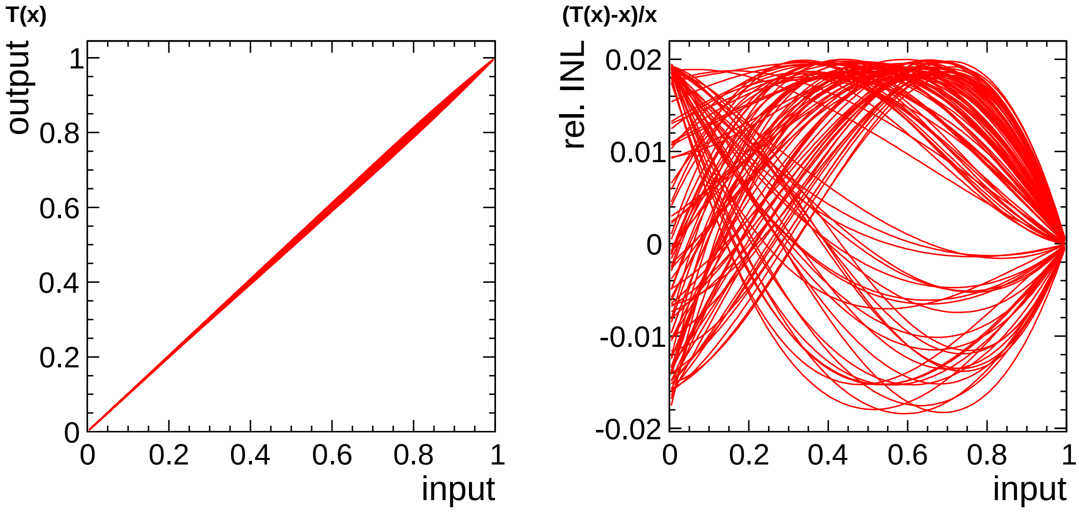

Figure C.2: Family of curves all featuring a maximal relative integrated nonlinearity of $\mathrm{INL}_{\mathrm{rel}} = 2.0\%$ and one extremum in the defined range.

D LED Driver Circuit

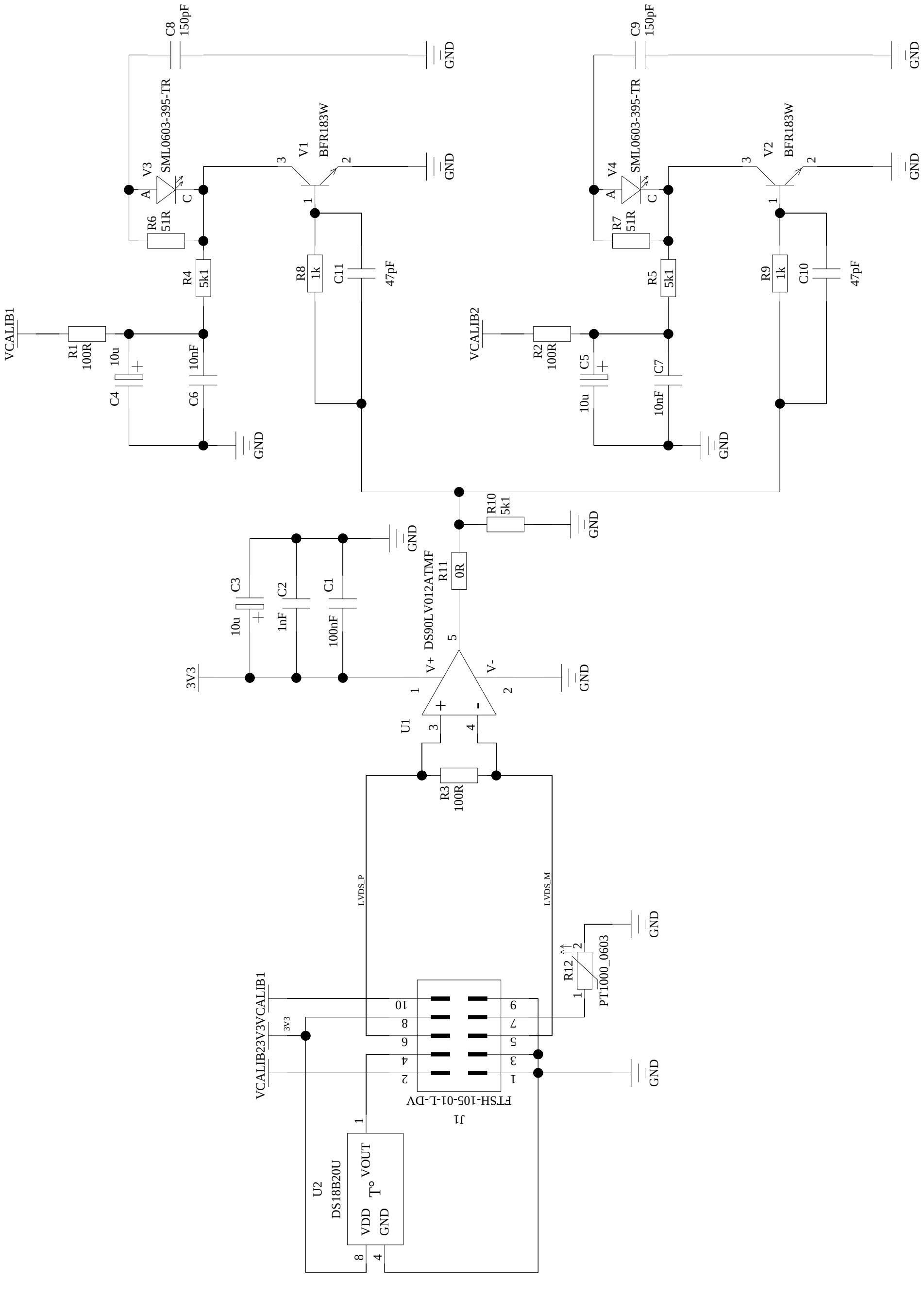

Bibliography

[1] B. Vormwald, “Bilinear R Parity Violation at the ILC - Neutrino Physics at Colliders”, PoS **EPS-HEP2013**, 034 (2013).

[2] B. Vormwald and J. List, “Bilinear R Parity Violation at the ILC - Neutrino Physics at Colliders”, (accepted by EPJ-C, 2013), arXiv:`1307.4074 [hep-ex]`.

[3] H. Baer, T. Barklow, et al., “The International Linear Collider Technical Design Report - Volume 2: Physics”, (2013), arXiv:`1306.6352 [hep-ph]`.

[4] Y. Gershtein, M. Luty, et al., “New Particles Working Group Report of the Snowmass 2013 Community Summer Study”, (2013), arXiv:`1311.0299 [hep-ex]`.

[5] Particle Data Group. “Review of Particle Physics (RPP)”, Phys.Rev. **D86**, 010001 (2012).

[6] C. Yang and R. Mills, “Conservation of Isotopic Spin and Isotopic Gauge Invariance”, Physical Review **96**, 191–195 (1954).

[7] E. Noether, “Invariante Variationsprobleme”, Gött. Nachr., 235–257 (1918).

[8] H. Fritzsch, M. Gell-Mann, and H. Leutwyler, “Advantages of the color octet gluon picture”, Physics Letters B **47**, 365–368 (1973).

[9] S. Glashow, “Partial Symmetries of Weak Interactions”, Nucl.Phys. **22**, 579–588 (1961).

[10] A. Salam and J. C. Ward, “On a Gauge Theory of Elementary Interactions”, Nuovo Cim. **19**, 165–170 (1961).

[11] A. Salam and J. Ward, “Electromagnetic and weak interactions”, Physics Letters **13**, 168–171 (1964).

[12] S. Weinberg, “A Model of Leptons”, Physical Review Letters **19**, 1264–1266 (1967).

[13] J. Goldstone, “Field Theories with Superconductor Solutions”, Nuovo Cim. **19**, 154–164 (1961).

[14] J. Goldstone, A. Salam, and S. Weinberg, “Broken Symmetries”, Physical Review **127**, 965–970 (1962).

[15] P. Higgs, “Broken symmetries, massless particles and gauge fields”, Physics Letters **12**, 132–133 (1964).

[16] P. Higgs, “Broken Symmetries and the Masses of Gauge Bosons”, Physical Review Letters **13**, 508–509 (1964).

[17] F. Englert and R. Brout, “Broken Symmetry and the Mass of Gauge Vector Mesons”, Physical Review Letters **13**, 321–323 (1964).

[18] G. Hooft, “Renormalizable Lagrangians for massive Yang-Mills fields”, Nuclear Physics B **35**, 167–188 (1971).

[19] G. Aad, T. Abajyan, et al., “Observation of a new particle in the search for the Standard Model Higgs boson with the ATLAS detector at the LHC”, Physics Letters B **716**, 1–29 (2012), arXiv:`1207.7214`.

[20] S. Chatrchyan, V. Khachatryan, et al., “Observation of a new boson at a mass of 125 GeV with the CMS experiment at the LHC”, Physics Letters B **716**, 30–61 (2012), arXiv:`1207.7235`.

[21] ATLAS Collaboration. “Measurements of the properties of the Higgs-like boson in the two photon decay channel with the ATLAS detector using 25 fb^{-1} of proton-proton collision data”, (2013), ATLAS-CONF-2013-012.

[22] CMS Collaboration. “Measurement of the properties of a Higgs boson in the four-lepton final state”, (2013), CMS-HIG-13-002. arXiv:`1312.5353 [hep-ex]`.

[23] ATLAS Collaboration, “Search for a heavy narrow resonance decaying to eμ, eτ, or $\mu\tau$ with the ATLAS detector in pp collisions at the LHC”, Physics Letters B **723**, 15–32 (2013), arXiv:`1212.1272`.

[24] K. Begeman, A. Broeils, and R. Sanders, “Extended rotation curves of spiral galaxies: Dark haloes and modified dynamics”, Mon.Not.Roy.Astron.Soc. **249**, 523 (1991).

[25] E. W. Kolb and M. S. Turner, *The early universe*, Frontiers in physics (Addison-Wesley, Reading, Mass, 1990), p. 547.

[26] W. Tucker, P. Blanco, et al., “1E 0657-56: A Contender for the Hottest Known Cluster of Galaxies”, The Astrophysical Journal **496**, L5–L8 (1998).

[27] D. Clowe, M. Bradač, et al., “A Direct Empirical Proof of the Existence of Dark Matter”, The Astrophysical Journal **648**, L109–L113 (2006), arXiv:`astro-ph/0608407 [astro-ph]`.

[28] P. Peebles and B. Ratra, “The Cosmological constant and dark energy”, Rev.Mod.Phys. **75**, 559–606 (2003), arXiv:`astro-ph/0207347 [astro-ph]`.

[29] Planck Collaboration, P. A. R. Ade, et al., “Planck 2013 results. XVI. Cosmological parameters”, 67 (2013), arXiv:`1303.5076`.

[30] S. P. Martin, “A Supersymmetry Primer”, (1997), arXiv:`hep-ph/9709356 [hep-ph]`.

[31] U. Amaldi, W. de Boer, and H. Fürstenau, "Comparison of grand unified theories with electroweak and strong coupling constants measured at LEP", Physics Letters B **260**, 447–455 (1991).

[32] S. Coleman and J. Mandula, "All Possible Symmetries of the S Matrix", Physical Review **159**, 1251–1256 (1967).

[33] R. Haag, J. T. Łopuszański, and M. Sohnius, "All possible generators of supersymmetries of the S-matrix", Nuclear Physics B **88**, 257–274 (1975).

[34] D. J. Gross, "The role of symmetry in fundamental physics.", Proceedings of the National Academy of Sciences of the United States of America **93**, 14256–9 (1996).

[35] J. Wess and B. Zumino, "Supergauge transformations in four dimensions", Nuclear Physics B **70**, 39–50 (1974).

[36] I. J. R. Aitchison, "Supersymmetry and the MSSM: An Elementary Introduction", (2005), arXiv:`hep-ph/0505105 [hep-ph]`.

[37] M. Drees, P. Roy, and R. M. Godbole, *Theory and phenomenology of sparticles: an account of four-dimensional N=1 supersymmetry in high energy physics* (World Scientific, Hackensack, NJ, 2004), p. 555.

[38] H. Pagels and J. R. Primack, "Supersymmetry, Cosmology and New TeV Physics", Phys.Rev.Lett. **48**, 223 (1982).

[39] W. Buchmüller, L. Covi, et al., "Gravitino Dark Matter in R-Parity Breaking Vacua", JHEP **0703**, 037 (2007), arXiv:`hep-ph/0702184 [hep-ph]`.

[40] S. Bobrovskyi, W. Buchmuller, et al., "Broken R-Parity in the Sky and at the LHC", JHEP **1010**, 061 (2010), arXiv:`1007.5007 [hep-ph]`.

[41] S. Bobrovskyi, W. Buchmuller, et al., "Quasi-stable neutralinos at the LHC", JHEP **1109**, 119 (2011), arXiv:`1107.0926 [hep-ph]`.

[42] S. Bobrovskyi, F. Brummer, et al., "Searching for light higgsinos with b-jets and missing leptons", JHEP **1201**, 122 (2012), arXiv:`1111.6005 [hep-ph]`.

[43] S. Bobrovskyi, J. Hajer, and S. Rydbeck, "Long-lived higgsinos as probes of gravitino dark matter at the LHC", JHEP **1302**, 133 (2013), arXiv:`1211.5584 [hep-ph]`.

[44] S. Bobrovskyi, "Gravitinos and hidden supersymmetry at the LHC", DESY-THESIS-2012-032.

[45] J. Hajer, "Long-lived neutralinos as probes of gravitino dark matter", DESY-THESIS-2013-031.

[46] S. Dimopoulos and D. Sutter, "The supersymmetric flavor problem", Nuclear Physics B **452**, 496–512 (1995).

[47] H. E. Haber, "Supersymmetry, Part I (Theory)", **010001**, 1–49 (2012).

[48] P. Buchmueller, O. and de Jong, “Supersymmetry, Part II (Experiment)”, **010001**, 1–36 (2012).

[49] I. Linear, C. Steering, et al., “Final International Technology Recommendation Panel Report”, (2004).

[50] ILC Collaboration. “ILC Reference Design Report: ILC Global Design Effort and World Wide Study”, (2007), arXiv:`0712.1950 [physics.acc-ph]`.

[51] ILC. “International Linear Collider Reference Design Report Volume 2: Physics at the ILC”, (2007), arXiv:`0709.1893 [hep-ph]`.

[52] N. Phinney, N. Toge, and N. Walker, “ILC Reference Design Report Volume 3 - Accelerator”, (2007), arXiv:`0712.2361 [physics.acc-ph]`.

[53] T. Behnke et al., “ILC Reference Design Report Volume 4 - Detectors”, (2007), arXiv:`0712.2356 [physics.ins-det]`.

[54] T. Behnke, J. E. Brau, et al., “The International Linear Collider Technical Design Report - Volume 1: Executive Summary”, (2013), arXiv:`1306.6327 [physics.acc-ph]`.

[55] C. Adolphsen, M. Barone, et al., “The International Linear Collider Technical Design Report - Volume 3.I: Accelerator & in the Technical Design Phase”, (2013), arXiv:`1306.6353 [physics.acc-ph]`.

[56] C. Adolphsen, M. Barone, et al., “The International Linear Collider Technical Design Report - Volume 3.II: Accelerator Baseline Design”, (2013), arXiv:`1306.6328 [physics.acc-ph]`.

[57] T. Behnke, J. E. Brau, et al., “The International Linear Collider Technical Design Report - Volume 4: Detectors”, (2013), arXiv:`1306.6329 [physics.ins-det]`.

[58] M. Aicheler, M. Aicheler, et al., “A Multi-TeV Linear Collider Based on CLIC Technology”, (2012) doi:`10.5170/CERN-2012-007`, CERN-2012-007.

[59] M. Tigner, “A possible apparatus for electron clashing-beam experiments”, Nuovo Cim. **37**, 1228–1231 (1965).

[60] F. Richard, *From LEP and SLC to ILC*, Lecture, 2013.

[61] PLUTO Collaboration. “Evidence for Gluon Bremsstrahlung in e+ e- Annihilations at High-Energies”, Phys.Lett. **B86**, 418 (1979).

[62] D. Barber, U. Becker, et al., “Discovery of Three Jet Events and a Test of Quantum Chromodynamics at PETRA Energies”, Phys.Rev.Lett. **43**, 830 (1979).

[63] TASSO Collaboration. “Evidence for Planar Events in e+ e- Annihilation at High-Energies”, Phys.Lett. **B86**, 243 (1979).

[64] ALEPH Collaboration, DELPHI Collaboration, L3 Collaboration, OPAL Collaboration, SLD Collaboration, LEP Electroweak Working Group, SLD Electroweak Group, SLD Heavy Flavour Group. "Precision electroweak measurements on the Z resonance", Phys.Rept. **427**, 257–454 (2006), arXiv:`hep-ex/0509008 [hep-ex]`.

[65] LHC Higgs Cross Section Working Group. "Handbook of LHC Higgs Cross Sections: 3. Higgs Properties", (2013) doi:`10.5170/CERN-2013-004`, CERN-2013-004. arXiv:`1307.1347 [hep-ph]`.

[66] K. Fujii, D. J. Miller, and A. Soni, *Linear collider physics in the new millennium*, Advanced series on directions in high energy physics (World Scientific, New Jersey, 2005), p. 499.

[67] N. Walker, *Accelerator ILC*, Lecture, 2013.

[68] CERN, *Powering CERN*, 2013.

[69] G. Moortgat-Pick, T. Abe, et al., "Polarized positrons and electrons at the linear collider", Physics Reports **460**, 131–243 (2008), arXiv:`hep-ph/0507011 [hep-ph]`.

[70] A. Tsytrinov, J. Kalinowski, et al., "Sneutrino Identification in Lepton Pair Production at ILC with Polarized Beams", Phys.Lett. **B718**, 94–99 (2012), arXiv:`1207.6234 [hep-ph]`.

[71] A. Ushakov, V. Kovalenko, et al., "Simulations of the ILC positron source with 120 GeV electron drive beam", (2013), LC-REP-2013-019.

[72] M. Pivi, L. Wang, et al., "Recommendation for Mitigations of the Electron Cloud Instability in the ILC", Conf.Proc. **C110904**, 1063–1065 (2011).

[73] H. Li, R. Pöschl, et al., "HZ Recoil Mass and Cross Section Analysis in ILD", 1–37 (2012), arXiv:`1202.1439`.

[74] D. Asner, T. Barklow, et al., "ILC Higgs White Paper", (2013), arXiv:`1310.0763 [hep-ph]`.

[75] M. Carena, H. Haber, et al., "Distinguishing a minimal supersymmetric standard model Higgs boson from the SM Higgs boson at a linear collider", Physical Review D **65**, 055005 (2002), arXiv:`hep-ph/0106116 [hep-ph]`.

[76] G. Degrassi, S. Di Vita, et al., "Higgs mass and vacuum stability in the Standard Model at NNLO", JHEP **1208**, 098 (2012), arXiv:`1205.6497 [hep-ph]`.

[77] K. Seidel, F. Simon, et al., "Top quark mass measurements at and above threshold at CLIC", Eur.Phys.J. **C73**, 2530 (2013), arXiv:`1303.3758 [hep-ex]`.

[78] P. Doublet, F. Richard, et al., "Determination of Top-quark Asymmetries at the ILC", 1–7 (2012), arXiv:`1202.6659`.

[79] O. Kittel, G. Moortgat-Pick, et al., "Measurement of CP asymmetries in neutralino production at the ILC", Eur.Phys.J. **C72**, 1854 (2012), arXiv:`1108.3220 [hep-ph]`.

[80] K. Desch, J. Kalinowski, et al., "SUSY parameter determination in combined analyses at LHC / LC", JHEP **0402**, 035 (2004), arXiv:`hep-ph/0312069 [hep-ph]`.

[81] M. Berggren, F. Brümmer, et al., "Tackling light higgsinos at the ILC", 1–27 (2013), arXiv:`1307.3566`.

[82] J. N. Bahcall and R. Davis, "Solar Neutrinos - a Scientific Puzzle", Science **191**, 264–267 (1976).

[83] B. T. Cleveland, T. Daily, et al., "Measurement of the Solar Electron Neutrino Flux with the Homestake Chlorine Detector", The Astrophysical Journal **496**, 505–526 (1998).

[84] N. Schmitz, *Neutrinophysik*, German (Teubner, Stuttgart, 1997).

[85] Borexino Collaboration. "Direct Measurement of the Be-7 Solar Neutrino Flux with 192 Days of Borexino Data", Phys.Rev.Lett. **101**, 091302 (2008), arXiv:`0805.3843 [astro-ph]`.

[86] SNO Collaboration. "The Sudbury neutrino observatory", Nucl.Instrum.Meth. **A449**, 172–207 (2000), SNO-STR-99-025. arXiv:`nucl-ex/9910016 [nucl-ex]`.

[87] SNO Collaboration. "Measurement of the rate of $\nu_e + d \rightarrow p + p + e^-$ interactions produced by B-8 solar neutrinos at the Sudbury Neutrino Observatory", Phys.Rev.Lett. **87**, 071301 (2001), UPR-0240E. arXiv:`nucl-ex/0106015 [nucl-ex]`.

[88] KamLAND Collaboration. "Precision Measurement of Neutrino Oscillation Parameters with KamLAND", Phys.Rev.Lett. **100**, 221803 (2008), arXiv:`0801.4589 [hep-ex]`.

[89] Super-Kamiokande Collaboration. "Evidence for oscillation of atmospheric neutrinos", Phys.Rev.Lett. **81**, 1562–1567 (1998), BU-98-17, ICRR-REPORT-422-98-18, UCI-98-8, KEK-PREPRINT-98-95, LSU-HEPA-5-98, UMD-98-003, SBHEP-98-5, TKU-PAP-98-06, TIT-HPE-98-09. arXiv:`hep-ex/9807003 [hep-ex]`.

[90] K2K Collaboration. "Measurement of Neutrino Oscillation by the K2K Experiment", Phys.Rev. **D74**, 072003 (2006), arXiv:`hep-ex/0606032 [hep-ex]`.

[91] MINOS Collaboration. "Observation of muon neutrino disappearance with the MINOS detectors and the NuMI neutrino beam", Phys.Rev.Lett. **97**, 191801 (2006), arXiv:`hep-ex/0607088 [hep-ex]`.

[92] T2K Collaboration. "Measurement of Neutrino Oscillation Parameters from Muon Neutrino Disappearance with an Off-axis Beam", Phys.Rev.Lett. **111**, 211803 (2013), arXiv:`1308.0465 [hep-ex]`.

[93] OPERA Collaboration. “OPERA: An appearance experiment to search for $\nu_\mu \rightarrow \nu_\tau$ oscillations in the CNGS beam. Experimental proposal”, (2000), CERN-SPSC-2000-028.

[94] OPERA Collaboration. “New results on $\nu_\mu \rightarrow \nu_\tau$ appearance with the OPERA experiment in the CNGS beam”, JHEP **1311**, 036 (2013), arXiv:`1308.2553 [hep-ex]`.

[95] DOUBLE-CHOOZ Collaboration. “Indication for the disappearance of reactor electron antineutrinos in the Double Chooz experiment”, Phys.Rev.Lett. **108**, 131801 (2012), arXiv:`1112.6353 [hep-ex]`.

[96] DAYA-BAY Collaboration. “Observation of electron-antineutrino disappearance at Daya Bay”, Phys.Rev.Lett. **108**, 171803 (2012), arXiv:`1203.1669 [hep-ex]`.

[97] RENO Collaboration. “Observation of Reactor Electron Antineutrino Disappearance in the RENO Experiment”, Phys.Rev.Lett. **108**, 191802 (2012), arXiv:`1204.0626 [hep-ex]`.

[98] K. Abe, J. Adam, et al., “Observation of Electron Neutrino Appearance in a Muon Neutrino Beam”, 8 (2013), arXiv:`1311.4750`.

[99] G. L. Fogli, E. Lisi, et al., “Global analysis of neutrino masses, mixings, and phases: Entering the era of leptonic CP violation searches”, Physical Review D **86**, 013012 (2012), arXiv:`1205.5254`.

[100] M. Gonzalez-Garcia, M. Maltoni, et al., “Global fit to three neutrino mixing: critical look at present precision”, JHEP **1212**, 123 (2012), arXiv:`1209.3023 [hep-ph]`.

[101] D. V. Forero, M. Tórtola, and J. W. F. Valle, “Global status of neutrino oscillation parameters after Neutrino-2012”, Physical Review D **86**, 073012 (2012), arXiv:`1205.4018`.

[102] F. Capozzi, G. L. Fogli, et al., “Status of three-neutrino oscillation parameters, circa 2013”, 11 (2013), arXiv:`1312.2878`.

[103] LBNE Collaboration. “Long-Baseline Neutrino Experiment (LBNE) Project - Conceptual Design Report”, (2012).

[104] C. Berger, *Elementarteilchenphysik: von den Grundlagen zu den modernen Experimenten*, German (Springer, Berlin, 2001).

[105] E. Majorana, “Theory of the Symmetry of Electrons and Positrons”, Nuovo Cim. **14**, 171–184 (1937), RX-888.

[106] P. Minkowski, “$\mu \rightarrow e\gamma$ at a rate of one out of 10^9 muon decays?”, Physics Letters B **67**, 421–428 (1977).

[107] M. Gell-Mann, P. Ramond, and R. Slansky, “Complex Spinors and Unified Theories”, Conf.Proc. **C790927**, 315–321 (1979), arXiv:`1306.4669 [hep-th]`.

[108] R. Mohapatra and G. Senjanović, “Neutrino Mass and Spontaneous Parity Nonconservation”, Physical Review Letters **44**, 912–915 (1980).

[109] R. Mohapatra and G. Senjanović, “Neutrino masses and mixings in gauge models with spontaneous parity violation”, Physical Review D **23**, 165–180 (1981).

[110] T. Yanagida, “Horizontal Symmetry and Masses of Neutrinos”, Prog.Theor.Phys. **64**, 1103 (1980).

[111] J. Casas and A. Ibarra, “Oscillating neutrinos and $\mu \to e, \gamma$”, Nuclear Physics B **618**, 171–204 (2001).

[112] B. Allanach, A. Dedes, and H. Dreiner, “R-parity violating minimal supergravity model”, Physical Review D **69**, 115002 (2004), arXiv:`hep-ph/0309196 [hep-ph]`.

[113] J. Romão and J. Valle, “Neutrino masses in supersymmetry with spontaneously broken R-parity”, Nuclear Physics B **381**, 87–108 (1992).

[114] B. Mukhopadhyaya, S. Roy, and F. Vissani, “Correlation between neutrino oscillations and collider signals of supersymmetry in an R-parity violating model”, Physics Letters B **443**, 191–195 (1998), arXiv:`hep-ph/9808265 [hep-ph]`.

[115] S. Choi, E. Chun, et al., “Neutrino oscillations and R-parity violating collider signals”, Physical Review D **60**, 075002 (1999), arXiv:`hep-ph/9903465 [hep-ph]`.

[116] J. W. F. Valle, “Super-gravity unification with bilinear R-parity violation”, 1–11 (1998), arXiv:`hep-ph/9808292 [hep-ph]`.

[117] M. Hirsch, M. Díaz, et al., “Neutrino masses and mixings from supersymmetry with bilinear R-parity violation: A theory for solar and atmospheric neutrino oscillations”, Physical Review D **62**, 113008 (2000), arXiv:`hep-ph/0004115 [hep-ph]`.

[118] W. Porod, M. Hirsch, et al., “Testing neutrino mixing at future collider experiments”, Physical Review D **63**, 115004 (2001), arXiv:`hep-ph/0011248 [hep-ph]`.

[119] M. Hirsch, M. Díaz, et al., “Erratum: Neutrino masses and mixings from supersymmetry with bilinear R-parity violation: A theory for solar and atmospheric neutrino oscillations [Phys. Rev. D 62, 113008 (2000)]”, Physical Review D **65**, 119901 (2002).

[120] ATLAS Collaboration. “Search for supersymmetry at $sqrts = 7$ TeV in final states with large jet multiplicity, missing transverse momentum and one isolated lepton with the ATLAS detector”, (2012), ATLAS-CONF-2012-140.

[121] ATLAS Collaboration. "Search for strongly produced superpartners in final states with two same sign leptons with the ATLAS detector using 21 fb-1 of proton-proton collisions at sqrt(s)=8 TeV.", (2013), ATLAS-CONF-2013-007.

[122] ATLAS Collaboration. "Search for a heavy narrow resonance decaying to $e\mu$, $e\tau$, or $\mu\tau$ with the ATLAS detector in $\sqrt{s} = 7$ TeV pp collisions at the LHC", Phys.Lett. **B723**, 15–32 (2013), CERN-PH-EP-2012-326. arXiv:`1212.1272`.

[123] ATLAS Collaboration. "Search for pair production of massive particles decaying into three quarks with the ATLAS detector in $\sqrt{s} = 7$ TeV pp collisions at the LHC", JHEP **1212**, 086 (2012), arXiv:`1210.4813 [hep-ex]`.

[124] ATLAS Collaboration. "Search for massive particles in multijet signatures with the ATLAS detector in $\sqrt{s} = 8$ TeV pp collisions at the LHC", (2013), ATLAS-CONF-2013-091.

[125] CMS Collaboration. "Search for RPV SUSY resonant second generation slepton production in same-sign dimuon events at sqrt(s) = 7 TeV", (2013), CMS-PAS-SUS-13-005.

[126] CMS Collaboration. "Search for RPV supersymmetry with three or more leptons and b-tags", (2012), CMS-PAS-SUS-12-027.

[127] CMS Collaboration. "Search for top squarks in R-parity-violating supersymmetry using three or more leptons and b-tagged jets", Phys.Rev.Lett. **111**, 221801 (2013), CMS-SUS-13-003, CERN-PH-EP-2013-093. arXiv:`1306.6643 [hep-ex]`.

[128] CMS Collaboration. "Search for RPV SUSY in the four-lepton final state", (2013), CMS-PAS-SUS-13-010.

[129] CMS Collaboration. "Search for electroweak production of charginos, neutralinos, and sleptons using leptonic final states in pp collisions at 8 TeV", (2013), CMS-PAS-SUS-13-006.

[130] CMS Collaboration. "Search for electroweak production of charginos and neutralinos in final states with a Higgs boson in pp collisions at 8 TeV", (2013), CMS-PAS-SUS-13-017.

[131] ATLAS Collaboration. "Search for direct production of charginos and neutralinos in events with three leptons and missing transverse momentum in $21\,\mathrm{fb}^{-1}$ of pp collisions at $\sqrt{s} = 8\,\mathrm{TeV}$ with the ATLAS detector", (2013), ATLAS-CONF-2013-035.

[132] ATLAS Collaboration. "Search for electroweak production of supersymmetric particles in final states with at least two hadronically decaying taus and missing transverse momentum with the ATLAS detector in proton-proton collisions at $\sqrt{s} = 8$ TeV", (2013), ATLAS-CONF-2013-028.

[133] ATLAS Collaboration. "Search for chargino and neutralino production in final states with one lepton, two b-jets consistent with a Higgs boson, and missing transverse momentum with the ATLAS detector in 20.3 fb^{-1} of $\sqrt{s} = 8$ TeV pp collisions", (2013), ATLAS-CONF-2013-093.

[134] ATLAS Collaboration. "Search for direct-slepton and direct-chargino production in final states with two opposite-sign leptons, missing transverse momentum and no jets in 20/fb of pp collisions at sqrt(s) = 8 TeV with the ATLAS detector", (2013), ATLAS-CONF-2013-049.

[135] ATLAS Collaboration. "Search for supersymmetry in events with four or more leptons in 21 fb^{-1} of pp collisions at $\sqrt{s} = 8\,\text{TeV}$ with the ATLAS detector", (2013), ATLAS-CONF-2013-036.

[136] ATLAS Collaboration. "Search for long-lived, heavy particles in final states with a muon and a multi-track displaced vertex in proton-proton collisions at sqrt(s) = 8TeV with the ATLAS detector.", (2013), ATLAS-CONF-2013-092.

[137] H. Baer, V. Barger, and P. Huang, "Hidden SUSY at the LHC: the light higgsino-world scenario and the role of a lepton collider", JHEP **1111**, 031 (2011), arXiv:`1107.5581 [hep-ph]`.

[138] C. Bartels, M. Berggren, and J. List, "Characterising WIMPs at a future e^+e^- Linear Collider", Eur.Phys.J. **C72**, 2213 (2012), arXiv:`1206.6639 [hep-ex]`.

[139] T. Schwetz, M. Tórtola, and J. W. F. Valle, "Global neutrino data and recent reactor fluxes: status of three-flavour oscillation parameters", 15 (2011), arXiv:`1103.0734`.

[140] M. Thomson, "Particle Flow Calorimetry and the PandoraPFA Algorithm", Nucl.Instrum.Meth. **A611**, 25–40 (2009), arXiv:`0907.3577 [physics.ins-det]`.

[141] I. Knowles and G. Lafferty, "Hadronization in Z^0 decay", J.Phys. **G23**, 731–789 (1997), arXiv:`hep-ph/9705217 [hep-ph]`.

[142] J. S. Marshall and M. A. Thomson, "The Pandora Particle Flow Algorithm", (2013), arXiv:`1308.4537`.

[143] GLD Concept Study Group, "GLD Detector Outline Document", (2006), arXiv:`physics/0607154 [physics]`.

[144] The LDC Working Group, "Detector Outline Document for the Large Detector Concept",

[145] The ILD Concept Group, "The International Large Detector: Letter of Intent", 163 (2010), arXiv:`1006.3396`.

[146] L. Linssen, A. Miyamoto, et al., "Physics and Detectors at CLIC: CLIC Conceptual Design Report", (2012), arXiv:`1202.5940`.

[147] I. Valin, C. Hu-Guo, et al., "A reticle size CMOS pixel sensor dedicated to the STAR HFT", JINST **7**, C01102 (2012).

[148] L. Greiner, E. Anderssen, et al., “A MAPS based vertex detector for the STAR experiment at RHIC”, Nucl.Instrum.Meth. **A650**, 68–72 (2011).

[149] T. A. Collaboration, “Impact parameter resolution data 2011”, ATL-COM-PHYS-2012-471.

[150] O. Biebel, B. Boden, et al., “Performance of the OPAL jet chamber”, Nucl.Instrum.Meth. **A323**, 169–177 (1992).

[151] A. Savoy-Navarro, “Development of semiconductor tracking: The future linear collider case”, Nucl.Instrum.Meth. **A636**, S73–S78 (2011).

[152] J. Fuster, S. Heinemeyer, et al., “Forward tracking at the next e+ e- collider. Part I. The Physics case”, JINST **4**, P08002 (2009), arXiv:`0905.2038 [hep-ex]`.

[153] A. Munnich, “Simulation studies for a high resolution time projection chamber at the International Linear Collider”, (2007).

[154] F. Sauli, “GEM: A new concept for electron amplification in gas detectors”, Nucl.Instrum.Meth. **A386**, 531–534 (1997).

[155] Y. Giomataris, P. Rebourgeard, et al., “MICROMEGAS: A High granularity position sensitive gaseous detector for high particle flux environments”, Nucl.Instrum.Meth. **A376**, 29–35 (1996).

[156] LCTPC Collaboration, “Report to the Desy PRC 2010 by the LCTPC Collaboration”, (2010).

[157] J.-C. Brient, P. Dauncey, et al., “CALICE Report to the Calorimeter R&D Review Panel”, 77 (2007), arXiv:`0707.1245`.

[158] H. Abramowicz, A. Abusleme, et al., “Forward Instrumentation for ILC Detectors”, JINST **5**, P12002 (2010), arXiv:`1009.2433 [physics.ins-det]`.

[159] C. Grah and A. Sapronov, “Fast luminosity measurement and beam parameter determination”, (2007), EUROTEV-REPORT-2007-006.

[160] CALICE Collaboration. “Design and Electronics Commissioning of the Physics Prototype of a Si-W Electromagnetic Calorimeter for the International Linear Collider”, JINST **3**, P08001 (2008), arXiv:`0805.4833 [physics.ins-det]`.

[161] CALICE Collaboration. “First Stage Analysis of the Energy Response and Resolution of the Scintillator ECAL in the Beam Test at FNAL”, 1–15 (2010).

[162] CALICE Collaboration. “Response of the CALICE Si-W Electromagnetic Calorimeter Physics Prototype to Electrons”, J.Phys.Conf.Ser. **160**, 012065 (2009), arXiv:`0811.2354 [physics.ins-det]`.

[163] CALICE collaboration. “Construction and Commissioning of the CALICE Analog Hadron Calorimeter Prototype”, JINST **5**, P05004 (2010), arXiv:`1003.2662 [physics.ins-det]`.

[164] T. C. Collaboration, “First results of the CALICE SDHCAL technological prototype”, (2012).

[165] W. Kilian, T. Ohl, and J. Reuter, “WHIZARD: Simulating Multi-Particle Processes at LHC and ILC”, Eur.Phys.J. **C71**, 1742 (2011), arXiv:`0708.4233 [hep-ph]`.

[166] M. Moretti, T. Ohl, and J. Reuter, “O’Mega: An Optimizing Matrix Element Generator”, 29 (2001), arXiv:`hep-ph/0102195 [hep-ph]`.

[167] M. Berggren, “Tuning PYTHIA”, (2010).

[168] L. Garren, *StdHep Manual*, 2006.

[169] F. Gaede, T. Behnke, et al., “LCIO - A persistency framework for linear collider simulation studies”, 1–5 (2003), arXiv:`physics/0306114 [physics]`.

[170] P. M. de Freitas, “Detector Simulation with MOKKA and Geant4: Present and Future”, (2003).

[171] GEANT4. “GEANT4: A Simulation toolkit”, Nucl.Instrum.Meth. **A506**, 250–303 (2003).

[172] J. Allison, K. Amako, et al., “Geant4 developments and applications”, IEEE Trans.Nucl.Sci. **53**, 270 (2006), SLAC-PUB-11870.

[173] M. Drees and R. M. Godbole, “Resolved photon processes”, Pramana **41**, 83–123 (1993), BU-TH-92-5, TIFR-TH-92-70. arXiv:`hep-ph/9302256 [hep-ph]`.

[174] F. Gaede, “Marlin and LCCD: Software tools for the ILC”, Nucl.Instrum.Meth. **A559**, 177–180 (2006).

[175] LCFI Collaboration. “The LCFIVertex package: vertexing, flavour tagging and vertex charge reconstruction with an ILC vertex detector”, Nucl.Instrum.Meth. **A610**, 573–589 (2009), arXiv:`0908.3019 [physics.ins-det]`.

[176] R. Brun and F. Rademakers, “ROOT: An object oriented data analysis framework”, Nucl.Instrum.Meth. **A389**, 81–86 (1997).

[177] F. Staub, “From Superpotential to Model Files for FeynArts and CalcHep/-CompHep”, Comput.Phys.Commun. **181**, 1077–1086 (2010), arXiv:`0909.2863 [hep-ph]`.

[178] F. Staub, “Automatic Calculation of supersymmetric Renormalization Group Equations and Self Energies”, Comput.Phys.Commun. **182**, 808–833 (2011), arXiv:`1002.0840 [hep-ph]`.

[179] I. Wolfram Research, *Mathematica Edition: Version 8.0*, 2010.

[180] W. Porod, “SPheno, a program for calculating supersymmetric spectra, SUSY particle decays and SUSY particle production at e+ e- colliders”, Comput.Phys.Commun. **153**, 275–315 (2003), arXiv:`hep-ph/0301101 [hep-ph]`.

[181] W. Porod and F. Staub, "SPheno 3.1: Extensions including flavour, CP-phases and models beyond the MSSM", Comput.Phys.Commun. **183**, 2458–2469 (2012), arXiv:`1104.1573 [hep-ph]`.

[182] F. Staub, private communication, 2011.

[183] C. Uhlemann and N. Kauer, "Narrow-width approximation accuracy", Nuclear Physics B **814**, 195–211 (2009), arXiv:`0807.4112`.

[184] P. Z. Skands, B. Allanach, et al., "SUSY Les Houches accord: Interfacing SUSY spectrum calculators, decay packages, and event generators", JHEP **0407**, 036 (2004), arXiv:`hep-ph/0311123 [hep-ph]`.

[185] B. Allanach, C. Balazs, et al., "SUSY Les Houches Accord 2", Comput.Phys.Commun. **180**, 8–25 (2009), arXiv:`0801.0045 [hep-ph]`.

[186] M. Cacciari and G. P. Salam, "Dispelling the myth for the jet-finder", Physics Letters B **641**, 57–61 (2006), arXiv:`hep-ph/0512210 [hep-ph]`.

[187] M. Cacciari, G. P. Salam, and G. Soyez, "FastJet User Manual", Eur.Phys.J. **C72**, 1896 (2012), arXiv:`1111.6097 [hep-ph]`.

[188] A. Rosca, "Measurement of the beam polarisation at the ILC using the WW annihilation data", (2013), LC-REP-2013-009.

[189] S. Catani, Y. Dokshitzer, et al., "New clustering algorithm for multijet cross sections in e^+e^- annihilation", Physics Letters B **269**, 432–438 (1991).

[190] W. Porod, private communication, 2013.

[191] A. Blondel, "A scheme to measure the polarization asymmetry at the z pole in LEP", Physics Letters B **202**, 145–148 (1988).

[192] K. Moenig, "The use of Positron Polarization for precision Measurements", (2000), LC-REP-2013-009.

[193] I. Marchesini, "Triple Gauge Couplings and Polarization at the ILC and Leakage in a Highly Granular Calorimeter", (2011), DESY-THESIS-2011-044.

[194] M. Beckmann, "Spin Transport at the International Linear Collider and its Impact on the Measurement of Polarization", (2013), DESY-THESIS-2013-053.

[195] A. Chao and M. Tigner, *Handbook of accelerator physics and engineering* (World Scientific, Singapore, 1998).

[196] M. L. Swartz, "Complete order-α^3 calculation of the cross section for polarized Compton scattering", Physical Review D **58**, 014010 (1998), arXiv:`hep-ph/9711447 [hep-ph]`.

[197] K. Abe, K. Abe, et al., "High-Precision Measurement of the Left-Right Z Boson Cross-Section Asymmetry", Physical Review Letters **84**, 5945–5949 (2000), arXiv:`hep-ex/0004026 [hep-ex]`.

[198] A. A. Sokolov and I. M. Ternov, “On Polarization and Spin Effects in the Theory of Synchrotron Radiation”, Soviet Physics Doklady **8**, 1203 (1964).

[199] M. Placidi and R. Rossmanith, “e^+e^- polarimetry at LEP”, Nucl.Instrum.Meth. **A274**, 79 (1989).

[200] D. Barber, H. Bremer, et al., “The HERA polarimeter and the first observation of electron spin polarization at HERA”, Nucl.Instrum.Meth. **A329**, 79–111 (1993).

[201] M. Beckmann, A. Borissov, et al., “The Longitudinal polarimeter at HERA”, Nucl.Instrum.Meth. **A479**, 334–348 (2002), arXiv:`physics/0009047 [physics]`.

[202] B. Sobloher, R. Fabbri, et al., “Polarisation at HERA - Reanalysis of the HERA II Polarimeter Data”, (2012), DESY-11-259, POL2000-2011-002. arXiv:`1201.2894 [physics.ins-det]`.

[203] SLD Collaboration. “The Scanning Compton polarimeter for the SLD experiment”, (1996), SLAC-PUB-7319, C96-09-09.5. arXiv:`hep-ex/9611005 [hep-ex]`.

[204] V. Gharibyan, N. Meyners, and P. Schuler, “The TESLA Compton polarimeter”, (2001), LC-DET-2001-047.

[205] S. Boogert, M. Hildreth, et al., “Polarimeters and Energy Spectrometers for the ILC Beam Delivery System”, JINST **4**, P10015 (2009), arXiv:`0904.0122 [physics.ins-det]`.

[206] L. Thomas, “The Kinematics of an electron with an axis”, Phil.Mag. **3**, 1–21 (1927).

[207] V. Bargmann and V. L. Telegdi, “Precession of the Polarization of Particles Moving in a Homogeneous Electromagnetic Field”, Physical Review Letters **2**, 435–436 (1959).

[208] K. Moffeit, T. Maruyama, et al., *Proposal to Modify the Polarimeter Chicane in the ILC 14 mrad Extraction Line*, tech. rep. March (Stanford Linear Accelerator Center (SLAC), Menlo Park, CA, Apr. 2007), pp. 1–17.

[209] C. Bartels, J. Ebert, et al., “Design and Construction of a Cherenkov Detector for Compton Polarimetry at the ILC”, JINST **7**, P01019 (2012), arXiv:`1011.6314 [physics.ins-det]`.

[210] J. List, private communication, 2013.

[211] K. O. Eyser, C. Helebrant, et al., “Simulation studies and detector scenarios for an ILC polarimeter”, eConf **C0705302**, MDI03 (2007), arXiv:`0709.2859 [physics.ins-det]`.

[212] Hamamatsu, *Photomultiplier Tubes and Assemblies for Scintillation Counting and High Energy Physics.*

[213] C. Helebrant, “In Search of New Phenomena using Polarization — HERA and ILC”, (2009), DESY-THESIS-2009-049.

[214] G. E. P. Box, J. S. Hunter, and W. G. Hunter, *Statistics for experimenters: design, innovation, and discovery*, 2nd ed, Wiley series in probability and statistics (Wiley-Interscience, Hoboken, N.J, 2005), p. 633.

[215] CAEN, *Technical Information Manual V2718*, 2009.

[216] CAEN, *Technical Information Manual V6533*, 2012.

[217] W. R. Leo, *Techniques for Nuclear and Particle Physics Experiments*, 2nd Edition (Springer-Verlag, 1994).

[218] CAEN, *Technical Information Manual V965A*, 2007.

[219] Tektronix, *Serie AFG3000 Manual.*

[220] KEITHLEY, *Datasheet Model 2410 High-Voltage SourceMeter.*

[221] KEITHLEY, *Datasheet Model 2200-32-3 Programmable DC Power Supply.*

[222] U. Velte, “Aufbau eines Teststandes für Photodetektoren und Teststrahlmessungen für die Strahlpolarisationsmessung am ILC”, (2008), DESY-THESIS-2009-005.

[223] M. Reinecke, “Towards a full scale prototype of the CALICE Tile hadron calorimeter”, IEEE Nucl.Sci.Symp.Conf.Rec. **2011**, 1171–1176 (2011).

[224] LEDTRONICS, *Datasheet SML0603-395-TR.*

[225] M. Reinecke, private communication, 2013.

[226] I. J. R. Aitchison and A. J. G. Hey, *Gauge theories in particle physics: a practical introduction*, 4th ed (CRC Press, Boca Raton, FL, 2012), p. 1.